Underwater Acoustic Communications: Algorithms for Delay-Scale Spread Wideband Channels

A Thesis

Submitted for the Degree of

Doctor of Philosophy

in the **Faculty of Engineering**

by

Arunkumar K. P.

under the Guidance of

Prof. Chandra R. Murthy
and
Dr. Muralikrishna P.

Electrical Communication Engineering
Indian Institute of Science
Bangalore – 560 012, INDIA

June 2022

To

My Family

Acknowledgments

I value my time with *Prof. Chandra R. Murthy*, my thesis advisor, as one of the best moments in my carrier and academics alike. I am indebted to him for all the productive hours we spent discussing on different problems dealt with in this thesis. His ability to drive research, while viewing our own work from a distance and being mindful of the needed details, is a take away for me. Never once have I been delayed or halted working on any problem waiting for an input from him – as an advisor he has been very responsive, and patient up to a remarkable degree. I picked up a significant lot from him about the praxis of technical writing and presenting ideas in a cogent manner.

I am grateful to *Dr. Muralikrishna P.*, my co-advisor, who, despite his tight schedules and responsibilities as a project director at Naval Physical Oceanographic Laboratory (NPOL), Kochi, was kind enough to spare his time to attend all my annual research reviews and suggest a few problems to consider. I thank him for the generous support and reassurance he often extended.

I thank my organization, Defence Research and Development Organisation (DRDO), and my parent laboratory, Naval Physical Oceanographic Laboratory (NPOL), Kochi, for letting me pursue a doctoral degree at the Indian Institute of Science (IISc), Bangalore. In particular, I wish to thank *Ms. Manjula Rani P.* who, as my group head at NPOL, encouraged me to pursue the doctoral program and *Mr. S. K. Shenoy*, who was then the Director of NPOL, for permitting me to join the program. I would like to thank my colleague *Mr. Nissar K. E.* who instilled enough confidence in me to undertake the program despite my lack of prior exposure to the field of wireless communications. I am grateful to *Ms. Pradeepa R.*, who, as my division head and project director, valued the

program and granted me occasional leaves from work to visit IISc for my research.

I thank IISc for providing an excellent intellectual ambience. I am thankful to the institute faculty who taught me various courses and prepared me to undertake academic research. Courses taught by *Prof. B. Sundar Rajan, Prof. A. Chockalingam, Prof. Neelesh B. Mehta and Prof. Himanshu Tyagi* exposed me to the fundamentals of digital wireless communication theory and practice. I thank *Mr. R. Srinivas Murthy*, *Ms. Suma T. C.* and *Ms. Rajani B.* for their prompt administrative support during my course work and visits to the campus.

I thank the members of the Signal Processing for Communication (SPC) laboratory at the Electrical Communication Engineering (ECE) Department of the institute who were great companions during my short visits to the campus. I am grateful to *Chirag Ramesh* for taking care of our poster presentation at the SPAWC 2022 venue in Finland, on my behalf, when I could not travel. My special thanks are due to *Sai Thoota* and *Saurabh Khanna* who were always forthcoming in matters ranging from interesting friendly talks to useful technical discussions. Good times with *Anubabh Chowdhury* and *Yashvanth L.* were a welcome change amid the hectic last mile run towards my thesis submission. I wish to thank *Akshay, Ashok, Chandrasekhar, Chethan, Chirag, Dheeraj, Geethu, Lekshmi, Mohit, Niladri, Pradip, Ramu, Ribhu, Rubin, and Sangeeta* for pleasant individual interactions at random occasions during my visits.

I thank my spouse *Devi* without whose priceless support, understanding and patience, I could not have managed life between research, office work, and my family. I thank my son *Adi* for taking good care of himself and letting me focus on my research without hassles. I am grateful to my mother *Anandavally* and mother-in-law *Rema* who cared and supported my family throughout my Ph.D. I would also like to thank my brother *Anoop*, and his family, occasional visits to whose home in Bangalore during the period of my residential course work helped ward off homesickness.

Publications and Preprints

1. Arunkumar K. P., Chandra R. Murthy, and Venkatesh Elango, "Joint Sparse Channel Estimation and Data Detection for Underwater Acoustic Communications Using Partial Interval Demodulation", IEEE 17th International Workshop on Signal Processing Advances in Wireless Communications (SPAWC), Edinburgh, UK, July 2016.

2. Arunkumar K. P. and Chandra R. Murthy, "Iterative Sparse Channel Estimation and Data Detection for Underwater Acoustic Communications Using Partial Interval Demodulation", IEEE Transaction on Signal Processing, vol. 66, no. 19, October 2018.

3. Arunkumar K. P. and Chandra R. Murthy, "Variational Soft Symbol Decoding for Sweep Spread Carrier Based Underwater Acoustic Communications", IEEE 20th International Workshop on Signal Processing Advances in Wireless Communications (SPAWC), Cannes, France, July 2019.

4. Arunkumar K. P. and Chandra R. Murthy, "Soft Symbol Decoding in Sweep-Spread-Carrier Underwater Acoustic Communications: A Novel Variational Bayesian Algorithm and Its Analysis", IEEE Transaction on Signal Processing, vol. 68, March 2020.

5. Arunkumar K. P. and Chandra R. Murthy, "Orthogonal Delay Scale Space Modulation: A New Technique for Wideband Time-Varying Channels", IEEE Transactions

on Signal Processing, vol. 70, pp. 2625-2638, June 2022.[1]

6. Arunkumar K. P., Chandra R. Murthy, and P. Muralikrishna, "Variable Bandwidth Multicarrier Communications: A New Waveform for the Delay-Scale Channel", IEEE 23rd International Workshop on Signal Processing Advances in Wireless Communications (SPAWC), Oulu, Finland, July 2022.[2]

7. Arunkumar K. P., Chandra R. Murthy, and P. Muralikrishna, "A METHOD AND A SYSTEM FOR GENERATING A SIGNAL FOR WIRELESS COMMUNICATION", Indian Patent Application No. 202241059394, filing date October 18, 2022, Applicants: (1) Indian Institute of Science, C V Raman Road, Bangalore - 560012, Karnataka, India, and (2) Chairman, Defence Research & Development Organisation, Ministry of Defence, Govt of India, DRDO Bhawan, Rajaji Marg, New Delhi 110011.

[1]Listed in the IEEE ComSoc's *Best Readings in Orthogonal Time Frequency Space (OTFS) and Delay Doppler Signal Processing* for June 2022 (Topic: Alternative Time-Frequency Transformation-based Modulation.)

[2]Won the best student paper award at SPAWC 2022.

Abstract

In wideband wireless communication systems, the relative motion of the transmitter, receiver, or scatterers in the medium causes the Doppler effect, which stretches or compresses the transmitted waveforms, resulting in inter-symbol interference and a consequent severe performance degradation. To counter this, specialized transmitter and receiver architectures are needed for energy- and spectrally-efficient communications in channels characterized by path-dependent delays and time-scales. In this thesis, we develop and evaluate improved receiver side signal processing algorithms for two existing modulation schemes used in wideband Underwater Acoustic (UWA) communications. We also propose new modulation schemes suited for wideband delay and scale spread UWA channels.

In the first part of the thesis, for the well known Orthogonal Frequency Division Multiplexing (OFDM) waveform, we develop a two-stage iterative algorithm at the receiver that alternates between sparse channel estimation and data detection. Specifically, we consider the sequence of observations from partial interval demodulators (PIDs) using a partial-length Fast Fourier Transform (FFT). We show that the PID outputs help in tracking the channel by providing additional measurements to estimate the Inter-Carrier Interference (ICI) due to the Doppler spread. We also derive the Cramér-Rao lower bound on the mean squared error in channel estimation, and empirically show that the two-stage algorithm meets the bound at high SNR.

Next, we develop a new Bayesian-inspired data detection algorithm in the context of sweep spread carrier (S2C) communication – a practically successful waveform used in some commercial underwater acoustic modems. The existing schemes for data detection – based on the gradient heterodyne receiver – are only effective when the path delay and

Doppler spread are moderate. Based on the principle of variational Bayes' inference, we present a new variational soft symbol decoding (VSSD) algorithm. In harsh UWA channels where the existing S2C receivers completely fail, or must compromise on the data rate to maintain the bit error rate (BER) performance, the VSSD algorithm successfully recovers the data symbols, even at low signal-to-noise ratios (SNRs).

We then turn to developing a new modulation scheme for the wideband doubly spread channel, namely, Orthogonal Delay Scale Space (ODSS), from first principles. The scheme pre-processes the information symbols using a 2D ODSS transform, which performs a discrete Fourier transform on the frequency axis and inverse Mellin transform on the Mellin variable axis, to obtain the transformed symbols in the delay-scale domain. These transformed symbols are mounted onto ODSS modulation waveforms to generate the signal to be transmitted. The pre-processing step spreads the symbols in the delay-scale domain, which in turn improves the bit error rate compared to Orthogonal Time Frequency Space (OTFS) and OFDM in wideband time-varying channels. More importantly, since the ODSS modulation renders the channel matrix near-diagonal, it performs well even under low-complexity subcarrier-by-subcarrier equalization in the delay-scale domain followed by symbol recovery in the Mellin-Fourier domain.

Finally, we develop a novel Variable Bandwidth Multicarrier (VBMC) waveform comprising of multiple subcarriers that are constructed from chirp pulses. The chirps occupy progressively increasing, frequency-dependent bandwidth from the lower to upper frequency edge of the communication band. Due to this, the subcarriers maintain their near mutual orthogonality even after passing through a delay and scale spread channel. We compare the performance of VBMC with existing waveforms using a generic framework for modeling delay-scale spread channels that we develop for the first time in this thesis.

Overall, this thesis develops advanced receiver processing techniques and novel modulation schemes that greatly outperform the state-of-the-art in wideband delay-scale spread channels, while matching their performance in more benign channels.

Contents

List of Figures

Notation

Acronyms

AUV	Autonomous Underwater Vehicle
ASV	Autonomous Surface Vehicle
AWGN	Additive White Gaussian Noise
BER	Bit Error Rate
BPSK	Binary Phase Shift Keying
CP	Cyclic Prefix
FFT	Fast Fourier Transform
FID	Full Interval Demodulator
GradH	Gradient Heterodyne Receiver
ICI	Inter Carrier Interference
IFFT	Inverse Fast Fourier Transform
i.i.d.	Independent and Identically Distributed
ISFFT	Inverse Symplectic Fast Fourier Transform
MF	Matched Filter
ML	Maximum Likelihood
MMSE	Minimum Mean Squared Error
MRC	Maximum Ratio Combining
MSE	Mean Squared Error
MVR	Minimum Variance Recovery
NMSE	Normalized Mean Squared Error
pGradH	Path based Gradient Heterodyne Receiver

ODSS	Orthogonal Delay Scale Space
OFDM	Orthogonal Frequency Division Multiplexing
OTFS	Orthogonal Time Frequency Space
OMP	Orthogonal Matching Pursuit
PAPR	Peak to Average Power Ratio
PID	Partial Interval Demodulator
PSD	Power Spectral Density
QAM	Quadrature Amplitude Modulation
QPSK	Quadrature Phase Shift Keying
RF	Radio Frequency
S2C	Sweep Spread Carrier
SBL	Sparse Bayesian Learning
SFFT	Symplectic Fast Fourier Transform
SINR	Signal to Interference plus Noise Ratio
SNR	Signal to Noise Ratio
SOFAR	Sound Ranging And Fixing
UWA	Underwater Acoustic
UWB	Ultra Wideband
VB	Variational Bayes'
VBMC	Variable Bandwidth Multicarrier
VSSD	Variational Soft Symbol Decoder
WSSUS	Wide-Sense Stationary Uncorrelated Scattering

Chapter 1

Introduction

Acoustic waves are the de facto carriers of the wireless communication signals undersea. Electromagnetic waves do not travel far in sea waters due to heavy attenuation caused by sea water's high electrical conductivity and dielectric constant. Therefore, light and radio waves do not present even a slightest possibility of use as carriers for conveying information across useful distances. Sound waves, on the other hand, can travel far in seas. Sound travels even up to thousands of kilometers in deep seas under certain propitious channel conditions: systems such as the Sound Fixing And Ranging (SOFAR) favor a long range propagation. Yet, compared to the terrestrial wireless radio channels, underwater acoustic communication channel is much harsher due to a variety of factors: limited available acoustic bandwidth, drastic transmission loss and attenuation due to absorption that increases with frequency, high levels of ambient sea-noise, reverberation, and temporal variations happening on different time scales. The significantly lower speed of sound wave propagation in water (about 1500 m/s) puts the latency of deep space radio wave communication between the earth and moon at par with acoustic communication across a much smaller distance of about 5.5 km in deep sea. Underwater acoustic communication, therefore, inherits the demerits of both terrestrial and deep space wireless radio channels. Also, the underwater acoustic communication system's receiver noise is dominated by the ambient noise whose spectral level is much higher than an RF receiver noise. Furthermore, sea noise is not white over the receiver band. The operating frequency of

acoustic communications and the usable bandwidth are also much smaller than its RF counterpart. Therefore, the data rates and quality of service (QoS) of underwater acoustic communications are inferior compared to their radio wave counterpart in terrestrial wireless communications.

The acoustic propagation loss, also known as the transmission loss, is an intricate function of the wave frequency, medium conditions and the source-receiver geometry. Sound propagation is predominantly influenced by the variation of sound speed with water depth (sound-speed profile) which causes the sound rays to refract downward or upward often leading to formation of "shadow zones" where sound signals do not reach at all. Under certain channel conditions, sound waves get severely attenuated due to their interaction with sea surfaces (both top and bottom) limiting the distances across which they can effectively serve as carriers in a single hop from a source to receiver. Shallow water environments such as fjords present an even tougher channel for acoustic communications due to dense multipath propagation and heavy losses encountered by the sound wave during every boundary interaction. Also, most underwater acoustic channels cannot be modeled as a wide-sense stationary uncorrelated scattering (WSSUS) process. Underwater channels exhibit both long and short term temporal variations – this variability of transmission properties can be on the scale of several months (seasonal variation), several days and hours (such as due to tides and factors depending on time of the day), minutes (due to internal waves), a few seconds (due to surface waves) as well as milliseconds (such as due to reflections, scattering).

A major contributor of time variation in acoustic channel is the relative motion between the transmitter and receiver. The low speed of sound ($c = 1500$ m/s) causes the relative Doppler factor, v/c, in an underwater channel to be far greater than in radio frequency channels, where v is the speed of a communication receiver relative to the transmitter. A low speed underwater target moving at $v = 5$ km/h speed has a Doppler factor which is $\frac{3\times10^8}{1500} \times \frac{5}{1000} = 1000$ times that of an aircraft traveling at $v = 1000$ km/h and communicating over a radio frequency (RF) channel. As acoustic signals are transmitted at far lower frequency bands compared to RF, the signaling bandwidth is

often a significant fraction of the center frequency. These aspects make the underwater channel characteristically *wideband* for moderate and high data rate communications. The precise effect of the Doppler, due to source-receiver relative motion, is to *time-scale* the transmitted waveform. Unlike in narrowband channels, the effect of Doppler cannot be approximated by a frequency-shift in wideband channels. In multi-carrier communications, the time-scaling leads to a non-uniform shift in frequency of the subcarriers across the communication band. Inter-carrier interference (ICI) is pronounced in the commonly used communication frameworks such as the Orthogonal Frequency Division Multiplex (OFDM) and Orthogonal Time-Frequency Space (OTFS) modulation schemes when communicating over such wideband doubly selective underwater acoustic channels.

Significant delay and time-scale spread distortions due to multiple propagation paths render the underwater acoustic channel doubly-selective, making it highly varying in both time and frequency. This necessitates the need for developing bespoke signal processing and modulation schemes for wideband underwater acoustic communications, which is the overarching goal of this thesis. In the next section, we present the delay-scale channel model that applies to wideband underwater acoustic communications.

1.1 Wideband delay-scale spread channel model

A transmitted signal undergoes three changes when passing through a delay-scale propagation channel: (a) amplitude change due to path loss and fading, (b) delay, τ, corresponding to the length of the path traversed, and (c) time-scaling by a factor, $\alpha = \frac{c-v}{c+v}$, due to Doppler effect, where v is the velocity of a scatterer and c is the speed of the wave in the propagation medium. Multiple propagation paths can result in a continuum of delay and scale parameters, i.e., $\tau \in [\tau_l, \tau_h]$ and $\alpha \in [\alpha_l, \alpha_h]$. Such a *doubly-spread* propagation channel is characterized by the wideband spreading function, $h(\tau, \alpha)$, that corresponds to the amplitude gain of the time-scaled and delayed copy of the transmitted signal reaching the receiver along a reflected path. The received signal is a superposition of the amplitude-scaled, time-scaled, and delayed versions of the transmitted signal, $s(t)$,

given by [25]

$$r_s(t) = \iint h(\tau, \alpha)\sqrt{\alpha} s\left(\alpha(t-\tau)\right) d\tau d\alpha, \tag{1.1}$$

where we have omitted the limits of integration for notational brevity.

The underwater channel can be often represented by a discrete multipath structure with N_p paths where each path, p ($p = 1, 2, \ldots, N_p$), is associated with a gain ($h_p \in \mathbb{C}$), delay ($0 \leq \tau_p \in \mathbb{R}$) and Doppler scale ($0 < \alpha_p \in \mathbb{R}$). The channel response due to a collection of discrete set of reflectors associated with the multipath parameter triples $(h_p, \tau_p, \alpha_p), p = 1, 2, \ldots, N_p$, is given by

$$h(\tau, \alpha) = \sum_{p=1}^{N_p} h_p \delta(\tau - \tau_p)\delta(\alpha - \alpha_p). \tag{1.2}$$

The signal after propagating through the discrete delay-scale channel is obtained by substituting $h(\tau, \alpha)$, from (1.2), into (1.1) to get

$$r_s(t) = \sum_{p=1}^{N_p} h_p \sqrt{\alpha_p} s\left(\alpha_p(t-\tau_p)\right). \tag{1.3}$$

The transmitted waveform $s(t)$ is usually an up-converted (modulated) version of a baseband waveform $s_B(t)$: the spectrum, $S(f)$, of $s(t)$ is the frequency shifted version of the spectrum of the baseband signal, $S_B(f)$, of $s_B(t)$, i.e., $S(f) = S_B(f - f_c)$, where the f_c is the carrier frequency (band center frequency). The baseband version, $r_{s,B}(t)$, of the received waveform $r_s(t)$ is obtained by down-conversion[1]. Proceeding from equation (1.3), we can show that the spectrum, $R_{s,B}(f)$, of $r_{s,B}(t)$ is related to the spectrum of $s_B(t)$ as

$$R_{s,B}(f) = \sum_{p=1}^{N_p} h_p \sqrt{\alpha_p} S_B\left(\frac{f}{\alpha_p} + f_c\left(\frac{1}{\alpha_p} - 1\right)\right) e^{-j2\pi(f+f_c)\tau_p} \tag{1.4}$$

Consider a multicarrier communication setup using N pulsed sinusoidal subcarriers, each of duration $T > \tau_{\max}$, at frequencies $f_k = k\Delta f, k = 0, 1, \ldots, N-1$, where $\Delta f = 1/T$

[1]The baseband received signal is given by: $r_{s,B}(t) = \sum_{p=1}^{N_p} h_p \sqrt{\alpha_p} s_B\left(\alpha_p(t-\tau_p)\right) e^{j2\pi f_c((\alpha_p - 1)t - \tau_p)}$.

is the subcarrier spacing and $\tau_{\max} \triangleq \tau_h - \tau_l$ is the channel delay spread. The noiseless received symbol at a subcarrier frequency f_m is given by

$$R_{s,B}(f_m) = \sum_{n=0}^{N-1} H_{m,n} s_n, \tag{1.5}$$

where the inter-symbol mixing factor, $H_{m,n}$ is given by

$$H_{m,n} = \frac{T}{2} \sum_{p=1}^{N_p} h_p \sqrt{\alpha_p} \text{sinc}\left(n - \frac{m}{\alpha_p} - f_c T \left(\frac{1}{\alpha_p} - 1\right)\right) e^{-j2\pi(f_m + f_c)\tau_p}. \tag{1.6}$$

In the absence of Doppler ($\alpha_p = 1, p = 1, 2, \ldots, N_p$), we observe that

$$H_{m,n} = \left(\frac{T}{2} \sum_{p=1}^{N_p} h_p e^{-j2\pi(f_m + f_c)\tau_p}\right) \delta[m - n], \tag{1.7}$$

where $\delta[m-n]$ is the discrete Kronecker delta function. Since $H_{m,n} = 0$ for $m \neq n$, we have

$$R_{s,B}(f_m) = H_{m,m} s_m, \tag{1.8}$$

which signifies no inter-carrier interference (ICI) in the absence of Doppler. In other words, time-scaling due to Doppler results in nonzero ICI.

The high delay spread of the underwater acoustic channels, ranging from tens to hundreds of milliseconds, results in a low coherence bandwidth ($\propto \frac{1}{\tau_{\max}}$). Communication at even moderate data rates would require a signaling bandwidth which far exceeds the coherence bandwidth of the underwater channel, making it highly *frequency selective*. The bandwidth of an underwater acoustic communication system also has to be a significant fraction of the operating frequency to support data transfer at moderate rates across a few kilometers. For example, a signaling bandwidth in excess of $B = 10$ kHz is needed to send 1000 symbols across a channel of delay spread, $\tau_{\max} = 100$ ms, at a rate of $10,000$ symbols per second, using a multicarrier modulation scheme with each symbol occupying a bandwidth of at least $W = \frac{1}{\tau_{\max}} = 10$ Hz. In practice, the optimum frequency band for communication across a distance of about $R_{\max} = 8$ km in deep ocean, turns out to

be around $f_c = 10$ kHz. The signaling bandwidth, in this case, is 100% of the center frequency, rendering the underwater acoustic communication system truly *wideband*.

To appreciate the effect of time-scaling in wideband communications, as opposed to frequency shifting in narrowband communications, consider an underwater vehicle moving at a speed of $v = 1.5$ m/s (3 knots). The Doppler time-scale factor for this case is $\alpha = 1 \pm v/c = 1 \pm 10^{-3}$. In a multicarrier communication, the time-scale will cause a subcarrier at $f_l = 5$ kHz ($f_h = 15$ kHz) to shift by an amount $\delta f_l \approx \pm 5$ Hz ($\delta f_h \approx \pm 15$ Hz). The subcarrier at the upper band edge thus experiences a three-fold Doppler shift in frequency compared to the subcarrier at the lower band edge. Such non-uniform shift in frequency of the subcarriers across the frequency band is a characteristic feature of the time-scaling phenomenon in wideband multicarrier underwater acoustic communications. This is in contrast with RF communications, say, from an aircraft traveling at $v = 278$ m/s (1000 km/h) in the band 400-420 MHz. The Doppler scale factor, in this scenario, is $\alpha = 1 \pm v/c = 1 \pm \frac{278}{3\times 10^8} < 1 \pm 10^{-6}$. The subcarriers experience a frequency shift of about 410 ± 10 Hz, showing only about $\pm 2.5\%$ variation in Doppler shift across the frequency band. The RF communication can be essentially regarded as narrowband ($B/f_c < 0.05$) for a signal frame of duration, $T \ll 25$ ms, and hence the Doppler may be modeled by a frequency shift in this scenario. The wideband acoustic communication, therefore, exhibit a Doppler factor which about 1000-fold larger than the narrowband RF communication.

The contributions of this thesis are a result of the research efforts to improve the performance of underwater acoustic communications which is particularly affected by the three canonical properties of the underwater acoustic propagation channel – its *wideband* nature, *delay* spread, and *Doppler-scale* spread. The wideband channel model in (1.1) is, therefore, central to the development of communication algorithms developed in this work. In the next section, we present a summary of these contributions.

1.2 Summary of contributions and techniques

In this section, we briefly describe the main contributions of this thesis. They are as follows:

1. Exploiting channel sparsity, viz., a small number of delay and Doppler parameters, while estimating the channel, we develop an iterative algorithm to improve the data symbol detection performance in a cyclic prefix orthogonal frequency division modulation (CP-OFDM) system. The proposed receiver side algorithm involves iterating between channel estimation and data detection taking into account the effect of multiple path-dependent time-scaling on the received signal. Unlike the traditional CP-OFDM systems based on the full interval demodulation (FID) receiver, we propose to combine the observations from *partial interval demodulators* (PID) which we show is effective in tackling the time-variations caused by the Doppler spread. Theoretically, we show that the PID outputs track the time-varying channel better by providing additional measurements to estimate the inter-carrier interference due to Doppler spread compared to FID. The Cramer–Rao lower bound on the mean squared error in channel estimation is derived, and it is shown empirically that the proposed two-stage algorithm meets the bound at high signal-to-noise ratio. The performance of the algorithm is validated through benchmark channel models, a ray tracing theory based acoustic channel simulator, and on real-world measured channel data available in the public domain.

2. We develop an improved data detection algorithm in the context of a practically successful modulation scheme in the underwater environment, namely, the sweep spread carrier (S2C) communication. S2C modulation finds use in some commercial modems and relies on the use of high bandwidth chirp waveforms commonly used in sonar systems. The existing schemes for data detection – based on the gradient heterodyne receiver – are only effective when the path delay and Doppler spread are moderate. Based on the principle of variational Bayes' inference, we propose a new variational soft symbol decoding (VSSD) algorithm for a general linear channel model. In benign underwater channels with moderate delay and Doppler spreads, the VSSD algorithm is shown to be equivalent to the existing receivers for S2C communications. The VSSD algorithm outperforms the minimum mean squared error (MMSE) data detection in both uncoded and coded communications when

applied to the benchmark i.i.d. Gaussian multiple-input multiple-output (MIMO) channel. Even with channel estimation errors, the VSSD algorithm is shown to retain its performance advantage over the MMSE receiver. The performance of the algorithm is validated in both simulated and measured underwater acoustic channels. In UWA channels where the existing S2C receivers completely fail, or must compromise on the data rate to maintain the bit error rate (BER) performance, the proposed VSSD algorithm recovers the data symbols at a signal-to-noise ratio (SNR) which is significantly lower than the MMSE decoder.

3. Thirdly, we develop a new modulation scheme for the wideband doubly spread channel — Orthogonal Delay Scale Space (ODSS) — which is similar to the recently proposed Orthogonal Time Frequency Space (OTFS). While OTFS is designed for narrowband channels characterised by delay and Doppler-frequency spread, ODSS is developed for the wideband delay and Doppler scale spread channels such as the underwater acoustic channels and the ultra wideband (UWB) channels. Unlike the narrowband channels, for which time contractions or dilations due to Doppler effect can be approximated by frequency-shifts, the Doppler effect in wideband channels result in frequency-dependent non-uniform shift of signal frequencies across the band. We derive the ODSS transmission and reception schemes from first principles. In the process, we introduce the notion of ω-convolution in the delay-scale space that parallels the twisted convolution used in the time-frequency space. The pre-processing 2D transformation from the Fourier-Mellin domain to the delay-scale space in ODSS, which plays the role of inverse simplectic Fourier transform (ISFFT) in OTFS, improves the bit error rate performance compared to OTFS and Orthogonal Frequency Division Multiplexing (OFDM) in wideband time-varying channels. Furthermore, since the channel matrix is rendered near-diagonal, ODSS retains the advantage of OFDM in terms of its low-complexity receiver structure.

4. We propose a waveform, which we call the Variable Bandwidth Multicarrier (VBMC) waveform, comprising multiple subcarriers that are constructed from chirp pulses used in radars and sonars, and resemble the whistles of bottlenose dolphins and the

songs of beluga whales who use them for both near and long range communications underwater. We design the subcarrier chirps of VBMC to occupy progressively increasing, frequency-dependent bandwidth from the lower to upper frequency edge of the communication band. The variable bandwidth design of the VBMC subcarriers is key to handling the multiple and time-scaling distortions caused by multipath Doppler on wideband waveforms. Due to this, the subcarriers of the VBMC waveform maintain their near mutual orthogonality even after passing through a delay and scale spread channel, resulting in low inter-carrier interference, and thereby facilitating a low complexity subcarrier-by-subcarrier decoding at the receiver. We relate VBMC with other similar waveforms in the literature. In particular, we observe that VBMC is a candidate modulation waveform that satisfies the ODSS design criteria for time-scale spread channels. Numerical simulation of the bit error rate over delay-scale channels shows that the VBMC waveform outperforms the widely used Cyclic Prefix Orthogonal Frequency Division Multiplexing (CP-OFDM) and the recently developed Orthogonal Time-Frequency Space (OTFS) waveforms.

5. We develop a generic framework for comparing the communication performance of different waveforms over a delay-scale spread channel. We use the well known continuous time Shannon basis for representing the transmitted signal, which allows us to accurately generate delayed and scaled versions of bandlimited signals as they pass through the channel. We introduce and describe the construction of a modulation dictionary whose columns are the subcarriers of a multicarrier waveform. The framework we develop here allows us to systematically model the delay-scale channel as a linear transformation that can be used to design and evaluate various waveforms for communications on a level playing field. Using this framework, we analyze the performance of a variety of waveforms – those developed in this thesis, the ones widely used in practice, and a few emerging waveforms found in the literature – over a delay-scale spread channel.

1.3 Organization of the thesis

We dedicate a chapter each to the three contributions listed in Section 1.2.

Chapter 2 presents the receiver side iterative symbol detection and sparse channel estimation for PID based CP-OFDM communications. After describing the theory, and analyzing the working of the proposed algorithm, extensive numerical evaluation of the communication performance based on both simulated and measured real world underwater acoustic channels is presented.

Chapter 3 presents the new VSSD receiver for the S2C communications. A mathematical model for S2C communications over delay and scale spread channels is first developed, and the limitations of the state-of-the-art gradient heterodyne based S2C receivers are elicited. The VSSD algorithm for data detection is presented, and its convergence property to a local optimum is then analyzed. Numerical results are presented showing the efficacy of the newly proposed variational Bayesian inference based data symbol decoder in the S2C communications framework.

Chapter 4 develops a new modulation scheme, ODSS, that is well suited for delay and scale spread wideband channels. We develop the transmitter and receiver side signal processing for the ODSS communication scheme and derive the conditions that need to be satisfied while designing the waveform for ODSS. We throughly evaluate the performance of ODSS and numerically illustrate its merits relative to existing waveforms.

In Chapter 5, we propose another new waveform, VBMC, that results in a low complexity single-tap equalizer based receiver. This chapter also develops a generic framework for comparing the communication performance of different waveforms over a delay-scale spread channel. We present the results of numerical simulations to show the performance advantage of VBMC over the widely used CP-OFDM and the recent OTFS schemes as well as other waveforms found in the literature.

We conclude with a discussion of possible directions of future work in Chapter 6.

Chapter 2

Iterative Sparse Channel Estimation and Data Detection

In this chapter, we present an iterative scheme for sparse-channel recovery and data detection in cyclic-prefix orthogonal frequency division multiplex (CP-OFDM) communication over doubly-spread underwater acoustic channels. We consider the sequence of observations from partial interval demodulators (PIDs), and cast them into an observation model amenable for sparse channel recovery. We propose a two-stage iterative algorithm for channel estimation and data detection. In the first stage, we recover the channel from pilot only observations and estimate the unknown data symbols from the post-combined PID outputs. In the second stage, we use the data symbols estimated in the first stage to reconstruct the dictionary matrix corresponding to a full interval demodulator, re-estimate the channel using the entire observations including the data subcarriers, and use it to detect the unknown data symbols from the PID outputs. We also propose a computationally attractive algorithm for sparse signal recovery, based on the minimum variance principle, that may be of independent interest. Theoretically, we show that the PID outputs help in tracking the time-varying channel better by providing additional measurements to estimate the ICI due to Doppler spread compared to full interval demodulation. Also, we derive the Cramér-Rao lower bound on the mean squared error in channel estimation, and empirically show that the proposed two-stage algorithm meets

the bound at high SNR. Numerical studies on simulated channels and publicly available experimental channel data in WATERMARK show that the proposed algorithm considerably improves data detection performance, in terms of bit error rate, over that from a traditional full length demodulator output, in highly Doppler distorted scenarios.

2.1 Introduction

Orthogonal frequency division multiplexing (OFDM) achieves high data rates, even in doubly-distorted channels with large delay spreads, due to its better resilience to inter symbol interference (ISI). However, the orthogonality between subcarriers is lost due to frequency offsets and the Doppler distortion introduced by the channel, leading to inter carrier interference (ICI). The Doppler distortion is particularly severe in multipath channels prevalent in underwater acoustic (UWA) communications, because different paths can potentially have different Doppler shifts, leading to Doppler spread [72]. This makes the problem of channel estimation and data detection particularly challenging. On the other hand, the UWA channel is known to be sparse in the lag-Doppler domain, because there are typically only a few significant multipath components in the channel. Therefore, it is pertinent to develop techniques that exploit the underlying structure in the channel to jointly estimate the channel and data symbols in the presence of severe ICI, which is the goal of this chapter.

Sparsity based channel recovery techniques are well known to produce significantly improved channel estimates, and hence lead to better symbol detection on data subcarriers [14, 36, 53, 73]. UWA channels typically have large delay and Doppler spreads but have only a few dominant paths [53]. This has been used in [14] to characterize the channel impulse response by using a path-based model, thereby facilitating channel estimation using sparse signal recovery techniques.

In [34], an equalization scheme was proposed where an iterative receiver progressively increases the so-called ICI span parameter to improve the channel estimate in severe ICI conditions. Both [14] and [34] require additional pilots to estimate the channel in high Doppler spread environments. An alternative approach to ICI mitigation using several

partial interval demodulators (PID), instead of a full interval demodulator (FID), was proposed in [106]. The authors also develop a recursive algorithm to compute the weights for combining the output of PIDs so as to make the post-combined channel matrix close to diagonal. While [106] used non-overlapping rectangular windows over time for PID and applied coherent detection, [7] extended the decomposition to other forms of windowing and applied differentially coherent data detection. The authors propose a stochastic gradient algorithm to estimate the combiner weights. However, the inherent sparsity of the channel is not exploited in [106] and [7].

In this chapter, we consider a cyclic-prefix OFDM (CP-OFDM) system [11, 106]. We propose a two-stage iterative approach for channel estimation and data detection. We exploit channel sparsity to estimate the path-dependent delay, Doppler and amplitude parameters of the channel from pilot-only observations of the PID outputs. An approximate dictionary, initially constructed using only the pilot symbols, is used to initiate the channel recovery. We refine the dictionary using estimates of the data symbols and iterate between channel estimation and data detection. The data symbols detected at the end of the first stage are then used to initialize a second stage that makes use of the entire observation vector, consisting of both pilot and data subcarriers, at the output of the FID. The second stage iteratively bootstraps the channel estimation using the detected data symbols to construct the dictionary matrix for the FID output, thereby reducing the channel estimation error, and ultimately leading to better data detection performance. Our specific contributions are as follows:

1. We reformulate problem of estimating the doubly-spread channel from the PID outputs in a manner that is amenable to sparsity-based channel estimation.

2. We propose a two-stage iterative framework that recovers the channel and detects the data symbols. For sparse channel recovery, we present an improved low complexity algorithm based on the minimum variance principle, that may be of independent interest. The algorithm refines the initial estimate produced by the Orthogonal Matching Pursuit (OMP) algorithm, and is observed to converge within a single

iteration. Its performance is better than OMP and is comparable to the computationally intensive Sparse Bayesian Learning (SBL) algorithm.

3. We analytically show that using the PID outputs increases the effective number of measurements compared to using only the FID output. Further, in the context of ℓ_1 based sparse signal recovery, we show that our scheme minimizes a joint cost function of the channel estimation and data detection error, and establish its convergence.

4. We derive a lower bound on the mean square error (MSE) in channel estimation, and numerically show that the bound corresponding to the PID outputs is strictly better than that corresponding to the FID outputs.

5. Through extensive numerical studies, using synthesized and measured channels, we demonstrate that the BER of the proposed scheme is considerably lower than the existing methods, in highly Doppler spread scenarios.

2.2 System Model

2.2.1 Transmitted and Received Signal

We consider a CP-OFDM system as in [106]. Let T denote the OFDM symbol duration and T_g the guard interval (duration of the cyclic prefix). When using a carrier frequency f_c and K subcarriers, the kth subcarrier is at frequency

$$f_k = f_c + k/T,\ k = -K/2, \ldots, K/2 - 1. \tag{2.1}$$

The transmitted symbol at the kth subcarrier is denoted by $s[k]$. The disjoint sets of data subcarriers S_D, pilot subcarriers S_P, and null subcarriers[1] S_N partition the K available

[1]The null subcarriers are not crucial for the performance, but they are useful for estimating the ICI, since the doubly-spread channel is no longer diagonal in the frequency domain. They can also be used to estimate the noise variance.

subcarriers. The transmitted signal is given by

$$\tilde{x}(t) = \frac{1}{\sqrt{T}}\mathrm{Re}\left\{\left[\sum_{k\in S_D\cup S_P} s[k]e^{j2\pi\frac{k}{T}t}\right]e^{j2\pi f_c t}\right\}, \quad t\in[-T_g, T]. \tag{2.2}$$

At the receiver, the signal is resampled by a factor $\hat{a}$ corresponding to a coarse Doppler estimate, leading to a baseband received signal $\tilde{z}(t)$ given by [14, 51, 56, 106, 107]

$$\tilde{z}(t) = \sum_{p=1}^{N_p} A_p \tilde{x}\left((1+b_p)\,t - \tau_p\right) + \tilde{n}\left(\frac{t}{1+\hat{a}}\right). \tag{2.3}$$

where A_p and τ_p are the amplitude and delay, respectively, of the p^{th} path, N_p is the number of significant paths in the channel, and $\tilde{n}(t)$ is the additive noise. The above assumes that the path amplitudes are constant within the OFDM symbol duration T, and that the time variation of the path delays due to Doppler rate a_p can be approximated as $\tau_p - a_p t$, as in [14]. The resampled signal is equivalent to a received signal obtained through a channel with Doppler rate $b_p = \left(\frac{a_p-\hat{a}}{1+\hat{a}}\right)$. Note that, in this work, the effect of Doppler spread is modeled as a corresponding path dependent time compression/dilation.

We use the above $\tilde{z}(t)$ to formulate the input-output model and the sparse channel recovery model pertaining to the PID output as follows. We divide the OFDM symbol interval $[0, T]$ into M consecutive partial intervals of duration T/M each. The output $z_k^{(m)}$ on the k^{th} subcarrier, upon performing demodulation for the m^{th} partial interval, $(m-1)\frac{T}{M} \le t \le m\frac{T}{M}, m = 1, 2, \cdots, M$, is given by

$$z_k^{(m)} = \sum_{p=1}^{N_p} A_p \sum_{l\in S_D\cup S_P} \varrho_{k,l}^{(p)}[m]e^{-j2\pi f_l\tau_p}s[l] + \eta_k^{(m)}, \tag{2.4}$$

where $\eta_k^{(m)}$ is the additive noise, and

$$\varrho_{k,l}^{(p)}[m] \;=\; \mathrm{sinc}\left(\frac{\beta_{k,l}^{(p)}T}{M}\right)e^{j\pi\beta_{k,l}^{(p)}(2m-1)\frac{T}{M}}, \tag{2.5}$$

$$\beta_{k,l}^{(p)} = (l-k)\frac{1}{T} + b_p f_l. \tag{2.6}$$

The above equations combine the models in [14] and [106]. The channel model in the above is the same as in [14], which used only the FID outputs and did not consider PID. On the other hand, [106] used the PID outputs but did not parameterize the channel in the delay-Doppler plane as in [14].

2.2.2 Input-Output Data Model

By stacking the received symbols across all the subcarriers into $\mathbf{z}^{(m)} \in \mathbb{C}^K$, the data symbols into $\mathbf{s} \in \mathbb{C}^K$, and the noise into $\mathbf{v}^{(m)} \in \mathbb{C}^K$, we get the channel input-output equation as:

$$\mathbf{z}^{(m)} = \mathbf{H}^{(m)}\mathbf{s} + \mathbf{v}^{(m)}, \tag{2.7}$$

for $m = 1, \ldots, M$, where the channel matrix $\mathbf{H}^{(m)}$ can be expressed as

$$\mathbf{H}^{(m)} = \sum_{p=1}^{N_p} A_p \mathbf{\Lambda}_p^{(m)} \mathbf{\Gamma}_p.$$

Here, $\mathbf{\Lambda}_p^{(m)}$ is a $K \times K$ matrix with $(k,l)^{\text{th}}$ entry $[\mathbf{\Lambda}_p]_{k,l}^{(m)} = \varrho_{k,l}^{(p)}[m]$, and $\mathbf{\Gamma}_p$ is a $K \times K$ diagonal matrix with $(k,k)^{\text{th}}$ entry $[\mathbf{\Gamma}_p]_{k,k} = e^{-j2\pi f_k \tau_p}$.

The output from a FID is obtained by summing up all $\mathbf{z}^{(m)}, m = 1, 2, \cdots, M$: $\mathbf{z} = \sum_{m=1}^{M} \mathbf{z}^{(m)} = \mathbf{H}\mathbf{s} + \mathbf{v}$, where $\mathbf{H}$ is the channel matrix corresponding to the FID output given by $\mathbf{H} = \sum_{m=1}^{M} \mathbf{H}^{(m)}$, and $\mathbf{v} = \sum_{m=1}^{M} \mathbf{v}^{(m)}$.

If the additive noise in (2.3) is zero mean circularly symmetric white Gaussian distributed, then the noise in FID output is also zero mean Gaussian with covariance $N_0\mathbf{I}$, where N_0 is the variance of each component of $\mathbf{v}$ and $\mathbf{I}$ is the $K \times K$ identity matrix. The noise in (2.7) is not white, but it is also zero mean Gaussian distributed with covariance given by:

$$E\left[\eta_k^{(m)} \eta_l^{(m)*}\right] = \frac{N_0}{M} e^{-\frac{j2\pi(k-l)(2m-1)}{2M}} \operatorname{sinc}\left(\frac{k-l}{M}\right), \tag{2.8}$$

and $E\left[\eta_k^{(m_1)} \eta_l^{(m_2)*}\right] = 0$ for $m_1 \neq m_2$.

It is straightforward to see that when $b_p = 0$, the channel matrix $\mathbf{H}$, as seen by the FID, is diagonal. When b_p's are nonzero and high, due to heavy Doppler spread, the channel matrix is no longer diagonal and this results in the mixing of the symbols at the output corresponding to each subcarrier. Within a partial interval, $b_p t$ can be approximated by $b_p t_m$, where $t_m \triangleq (2m-1)\frac{T}{2M}$ is the mid-point of the m^{th} partial interval [106]. Then, we can write the channel matrices as

$$\mathbf{H}^{(m)} = \mathbf{J}^{(m)} \sum_{p=1}^{N_p} A_p \mathbf{\Gamma}_p^{(m)}, \tag{2.9}$$

where $\mathbf{\Gamma}_p^{(m)}$ is a diagonal matrix whose $(k,k)^{\text{th}}$ entry is given by $[\mathbf{\Gamma}_p]_{k,k}^{(m)} = e^{-j2\pi f_k(\tau_p - b_p t_m)}$, and $\mathbf{J}^{(m)}$ is a matrix with $(k,l)^{\text{th}}$ element $J_{k,l}^{(m)} = \frac{1}{M} e^{-\frac{j2\pi(k-l)(2m-1)}{2M}} \text{sinc}\left(\frac{k-l}{M}\right)$, for $k, l = 1, 2, \ldots, K$. Henceforth, we consider the data model for the PID outputs expressed by (2.7), where the channel matrix is given by (2.9) and the noise vector is zero-mean with a covariance matrix given by (2.8).

2.2.3 Sparse Channel Recovery Model

In the formulation above, the channel matrix $\mathbf{H}^{(m)}$ is defined by N_p triplets (A_p, b_p, τ_p). In this section, we cast the problem of estimating these N_p triplets as a sparse channel recovery problem, given the sequence of PID outputs $\mathbf{z}^{(m)}, m = 1, 2, \ldots, M$. To this end, we construct a dictionary consisting of the signals parameterized by a representative selection of possible parameter values [14]. Since parameter values that are not part of the solution will have the corresponding coefficient as zero and a large number of parameter values are needed to construct an accurate dictionary, the vector of coefficients is sparse, thus making sparse vector recovery algorithms applicable. The representative values of (b_p, τ_p) are chosen as

$$\tau_p \in \left\{ \frac{T}{\lambda K}, \frac{2T}{\lambda K}, \ldots, \frac{N_\tau T}{\lambda K} \right\}, \tag{2.10}$$

$$b_p \in \{-b_{\max}, -b_{\max} + \Delta b, \ldots, b_{\max}\}. \tag{2.11}$$

The time resolution for τ_p is chosen as a multiple, λ, of the sampling time T/K, with N_τ candidate delays such that $\frac{N_\tau T}{\lambda K}$ is larger than the maximum delay spread of the channel. For b_p, we consider $N_b = 2b_{\max}/(\Delta b) + 1$ candidate Doppler rates. Defining the coefficient vector corresponding to all delays associated with Doppler scale b_i as $\mathbf{x}_A^{(i)} = \left[A_1^{(i)}, \ldots, A_{N_\tau}^{(i)}\right]^T$, the stacked coefficient vector corresponding to all candidate delays and Doppler rates is given by

$$\mathbf{x} = \left[\left(\mathbf{x}_A^{(1)}\right)^T, \ldots, \left(\mathbf{x}_A^{(N_b)}\right)^T\right]^T. \tag{2.12}$$

Hence, (2.7) now takes the form:

$$\mathbf{z}^{(m)} = \mathbf{A}^{(m)}\mathbf{x} + \mathbf{v}^{(m)}, \tag{2.13}$$

$$\text{where } \mathbf{A}^{(m)} = \mathbf{J}^{(m)}\left[\mathbf{\Gamma}_1^{(m)}\mathbf{s}, \ldots, \mathbf{\Gamma}_N^{(m)}\mathbf{s}\right], \tag{2.14}$$

for $m = 1, \ldots, M$, with $N = N_\tau N_b$ representing the total number of grid points used in the delay-Doppler plane.

Although the channel vector $\mathbf{x}$ is sparse, the construction of the dictionary matrix $\mathbf{A}^{(m)}$ requires knowledge of the transmitted symbol vector $\mathbf{s}$, which is unknown at the receiver. In the next section, we propose a two-stage iterative algorithm to recover the channel vector $\mathbf{x}$ and the data vector $\mathbf{s}$.

2.3 Channel Estimation and Data Detection

Our proposed two stage algorithm works as follows. In stage 1, we use PID measurements from only the pilot subcarriers to estimate the channel, and subsequently use the estimated channel to detect the unknown data symbols. In stage 2, we use the FID outputs on both the data and pilot subcarriers, with the data symbols initialized using the outcome of stage 1, to further reduce the channel estimation error and improve the data detection performance. Figure 2.1 shows a block diagram for the proposed approach.

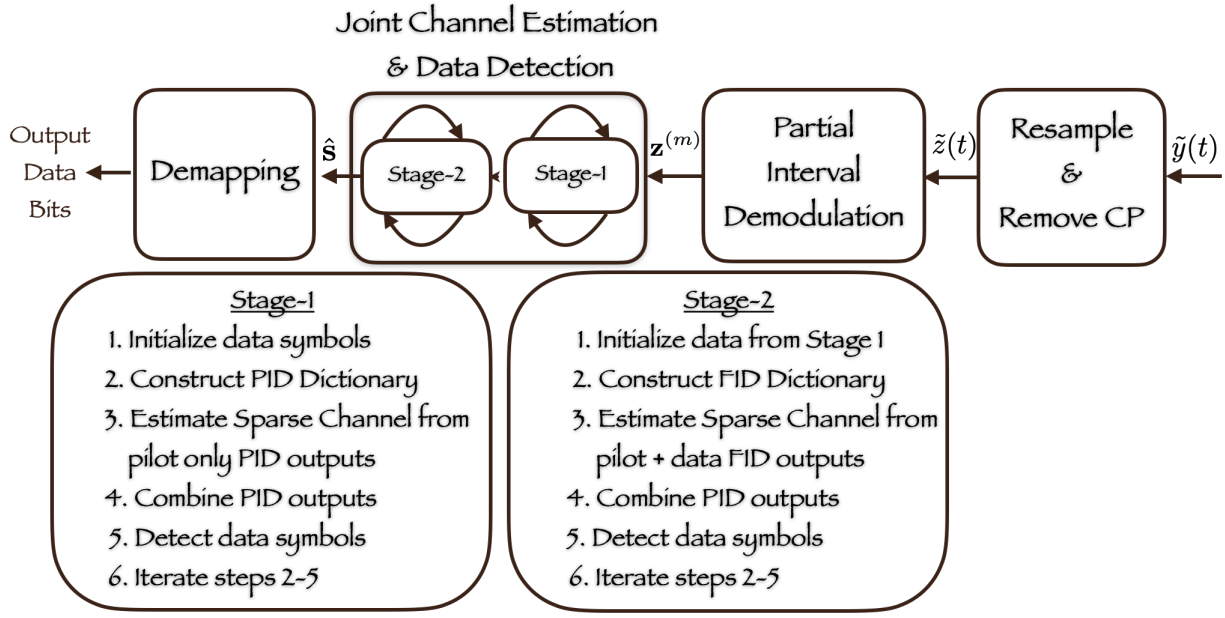

Figure 2.1: Block diagram of the receiver processing chain and the dual stage algorithm for iterative channel estimation and data detection.

2.3.1 Stage 1

We start by constructing a vector $\hat{\mathbf{s}} \in \mathbb{C}^K$ by placing the known pilot symbol at the pilot subcarrier locations and zeros at the null subcarrier locations. Further, we initialize the unknown data symbols at subcarrier locations S_D to zero.[2] By defining $\mathbf{z}_{S_P}^{(m)} \in \mathbb{C}^{|S_P|}$ to be a sub-vector of $\mathbf{z}^{(m)} \in \mathbb{C}^K$ that collects the symbols corresponding to the pilot subcarrier locations S_P, from (2.13) we have,

$$\mathbf{z}_{S_P}^{(m)} = \hat{\mathbf{A}}_{S_P}^{(m)} \mathbf{x} + \mathbf{e}_{S_P}^{(m)}, \tag{2.15}$$

where

$$\hat{\mathbf{A}}_{S_P}^{(m)} = \mathbf{I}_{S_P} \mathbf{J}^{(m)} \left[\mathbf{\Gamma}_1^{(m)} \hat{\mathbf{s}}, \ldots, \mathbf{\Gamma}_N^{(m)} \hat{\mathbf{s}} \right] \in \mathbb{C}^{|S_P| \times N}, \tag{2.16}$$

[2]We find in our simulation studies that a random initialization of the data symbols also works equally well.

$\mathbf{I}_{S_P} \in \mathbb{R}^{|S_P| \times K}$ is the submatrix of the $K \times K$ identity matrix consisting of its rows indexed by S_P, and $\mathbf{e}_{S_P}^{(m)} \triangleq \Delta\mathbf{A}_{S_P}^{(m)}\mathbf{x} + \mathbf{v}_{S_P}^{(m)}$ is the effective noise that includes the dictionary estimation error given by:

$$\Delta\mathbf{A}_{S_P}^{(m)} = \mathbf{I}_{S_P}\mathbf{J}^{(m)}\left[\mathbf{\Gamma}_1^{(m)}(\mathbf{s}-\hat{\mathbf{s}}), \ldots, \mathbf{\Gamma}_N^{(m)}(\mathbf{s}-\hat{\mathbf{s}})\right]. \tag{2.17}$$

The error $\mathbf{s} - \hat{\mathbf{s}}$ affects $\mathbf{z}_{S_P}^{(m)}$ in as much as there is ICI captured by the matrix $\mathbf{J}^{(m)}$. Note that, the presence of null subcarriers around each pilot subcarrier mitigates the ICI.

To recover the sparse channel vector $\mathbf{x}$ in (2.15), we propose an improved algorithm that bootstraps from the channel estimate produced by OMP and refines this estimate. We call our proposed algorithm the Minimum Variance Recovery (MVR) algorithm, and provide its details in Section 2.3.3.

Once the sparse channel vector $\mathbf{x}$ is recovered, the channel matrix $\hat{\mathbf{H}}^{(m)}$ for each PID output is constructed using (2.9). The estimates $\hat{\mathbf{H}}^{(m)}, m = 1, 2, \ldots, M$, are then weighted and combined so as to make the post-combined channel matrix close to diagonal, as follows:

$$\hat{\mathbf{H}}_{k,:} = \sum_{m=1}^{M} w_k^{(m)*}\hat{\mathbf{H}}_{k,:}^{(m)}, \tag{2.18}$$

where the weights $\mathbf{w}_k = \left[w_k^{(1)}, \cdots, w_k^{(M)}\right]^T \in \mathbb{C}^M$ are chosen for each subcarrier k to minimize the interference from other subcarriers as $\mathbf{w}_k = \hat{\mathbf{R}}_{\mathbf{z}_k}^{-1}\hat{\mathbf{h}}_{k,k} / \|\hat{\mathbf{R}}_{\mathbf{z}_k}^{-1}\hat{\mathbf{h}}_{k,k}\|_2$, with $\hat{\mathbf{h}}_{k,l} \triangleq \left[\hat{H}_{k,l}^{(1)}, \cdots, \hat{H}_{k,l}^{(M)}\right]^T$ and $\hat{\mathbf{R}}_{\mathbf{z}_k} \triangleq \sum_{l=1}^{K}\hat{\mathbf{h}}_{k,l}\hat{\mathbf{h}}_{k,l}^H + \frac{N_0}{M}\mathbf{I}_M$ [106]. The post-combined observation $\tilde{z}_k$ is obtained by weighting and adding the k^{th} entry, $z_k^{(m)}$, of $\mathbf{z}^{(m)}$:

$$\tilde{z}_k = \sum_{m=1}^{M} w_k^{(m)*} z_k^{(m)}. \tag{2.19}$$

Figure 2.2 contrasts an instance of the channel matrix obtained by simply summing up the PID outputs with that obtained by their weighted combination. The latter is clearly closer to diagonal than the former, which simplifies the subsequent data detection step, described next.

Since the weights in (2.18) are normalized to have unit 2-norm, it follows from (2.8)

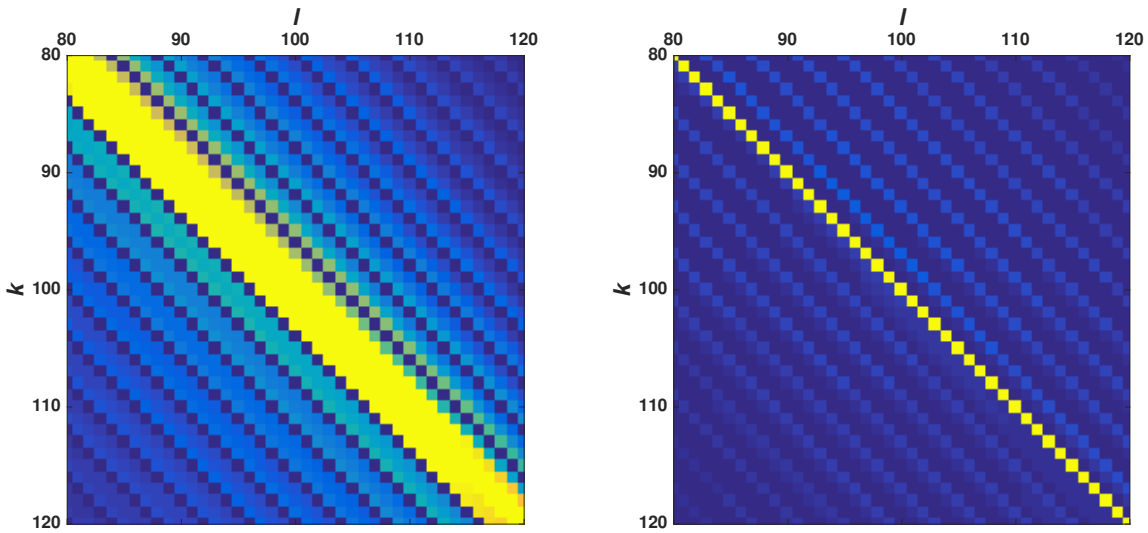

Figure 2.2: Left: Channel matrix seen at FID output. Right: Post-combined channel matrix at (combined) PID output. (k, l) are (row, column) indices of the channel matrix. Only indices from 80-120 are shown for clarity. Bright yellow indicates high magnitude while dark black indicates low magnitude. These matrices are obtained for the CP-OFDM system I in Table 2.3, Section 2.5, and residual Doppler spread in $[-b_{\max}, b_{\max}]$, where $b_{\max} = 5 \times 10^{-4}$.

and (2.19) that the variance of the noise at the post-combiner output is $E\{|\tilde{\eta}_k|^2\} = N_0$. A minimum mean square error (MMSE) receiver is applied for data demodulation, as follows:

$$\hat{\mathbf{s}} = \text{dec}\left[\left(\hat{\mathbf{H}}^H\hat{\mathbf{H}} + N_0\mathbf{I}\right)^{-1}\hat{\mathbf{H}}^H\tilde{\mathbf{z}}\right] \tag{2.20}$$

where $\tilde{\mathbf{z}} \in \mathbb{C}^K$ is obtained by stacking $\tilde{z}_k, k = 1, \ldots, K$, and $\text{dec}(\cdot)$ is the hard-thresholding operation to the signal constellation. We find in our simulation studies that zeroing out all but diagonal entries of the post-combined channel matrix, $\hat{\mathbf{H}}$, has negligible effect on data detection accuracy. On the positive side, this approximation significantly reduces the computational complexity involved in the matrix inversion in (2.20). Using this approximation, the unknown data symbols are estimated as follows:

$$\hat{s}_k \approx \text{dec}\left[\frac{\hat{H}^*_{k,k}}{|\hat{H}_{k,k}|^2 + N_0}\tilde{z}_k\right], k \in S_D, \tag{2.21}$$

where $\hat{H}_{k,k}$ is the kth diagonal entry of $\hat{\mathbf{H}}$. Using $\hat{\mathbf{s}}$, we reconstruct the dictionary matrix $\hat{\mathbf{A}}_{S_P}^{(m)}$, for $m = 1, 2, \cdots, M$, and iterate through channel estimation and data symbol detection.

In stage 1, the channel vector is recovered using only the pilot subcarriers in the output of the PID, and the data symbols are detected from the post-combined demodulator output. The detection of data symbols helps in accurately estimating the ICI, which in turn helps in reducing $\|\Delta\mathbf{A}_{S_P}^{(m)}\mathbf{x}\|_2$ in (2.17), leading to better channel estimates. However, the observations on the data subcarriers are not used for channel estimation in stage 1. In stage 2, we make use of the measurements from both data and pilot subcarriers for channel estimation.

2.3.2 Stage 2

We start by constructing the dictionary matrix corresponding to the FID as:

$$\mathbf{A} = \sum_{m=1}^{M} \mathbf{A}^{(m)}, \tag{2.22}$$

using the data symbols $\hat{\mathbf{s}}$ estimated at the end of stage 1. Then we proceed to re-estimate the channel vector from:

$$\mathbf{z} = \sum_{m=1}^{M} \mathbf{z}^{(m)} = \mathbf{A}\mathbf{x} + \mathbf{v}, \tag{2.23}$$

as in stage 1, but now using the full set of observations including data subcarriers at the output of the FID. From the estimated channel vector, we construct the post-combined channel matrix $\hat{\mathbf{H}}$, and the corresponding post-combined measurement $\tilde{\mathbf{z}}$, using (2.18) and (2.19) respectively, and apply the MMSE receiver in (2.21) for data demodulation using the PID outputs, as in stage 1. Further, we iterate between channel estimation and data detection until convergence or till a fixed number of iterations (N_{iter}) have elapsed.

Algorithm 1: Minimum Variance Recovery

1: Threshold: $\gamma = \sigma\sqrt{\frac{m}{n}}$

2: Initial support: $\mathbb{S} = \{i \in [1, 2 \dots n] : |\hat{\mathbf{x}}_{0,i}| > \gamma\}$

3: Initial solution: $\hat{\mathbf{x}}_{\mathbb{S}} = \mathbf{A}^{\dagger}_{:,\mathbb{S}}\mathbf{z}$, $\hat{\mathbf{x}}_{\mathbb{S}^c} = 0$

4: Cardinality: $k = |\mathbb{S}|$

5: Measurement covariance: $\mathbf{R} = \sum_{i\in\mathbb{S}} |\hat{x}_i|^2 \mathbf{a}_i\mathbf{a}_i^H + \delta I$

6: Weight vector: $\mathbf{w}_i = \frac{\mathbf{R}^{-1}\mathbf{a}_i}{\mathbf{a}_i^H\mathbf{R}^{-1}\mathbf{a}_i}$

7: Minimum variance signal: $\tilde{\mathbf{x}} = \mathbf{W}^H\mathbf{z}$

8: $\mathbb{S}$ = Set of indices of the largest k entries of $|\tilde{\mathbf{x}}|$

9: Update solution: $\hat{\mathbf{x}}_{\mathbb{S}} = \mathbf{A}^{\dagger}_{:,\mathbb{S}}\mathbf{z}$, $\hat{\mathbf{x}}_{\mathbb{S}^c} = 0$

10: Output: $\hat{\mathbf{x}}$

2.3.3 Minimum Variance Recovery (MVR) Algorithm

The proposed MVR algorithm, given in Algorithm 1, is inspired by the minimum variance spectrum estimation principle [43] and works by refining the channel estimate produced by OMP. We construct an estimate of the measurement covariance matrix from a thresholded[3] version of the sparse channel estimate provided by OMP, and use it to compute an adaptive minimum variance weight vector. We use the weight vector to re-estimate each entry of the channel vector, and update the solution to contain the indices of the k largest entries of the minimum variance solution, where k is the cardinality of the thresholded version of the initial channel estimate. This form of support update helps to minimize the leakage of interference from other nonzero coefficients while identifying the location of a nonzero coefficient in the sparse channel vector. Finally, a refined solution vector is constructed using the updated support. We note that, in the context of synthetic aperture radar imaging, an algorithm similar in flavor called the iterative adaptive algorithm has been proposed in [99].

In Figure 2.3, we show the phase transition curves of OMP, SBL and MVR on the

[3]The thresholding operation sets the coefficients whose magnitude is smaller than the threshold to zero. Empirically, we find that performance is insensitive to the value of the threshold, so its choice is not critical.

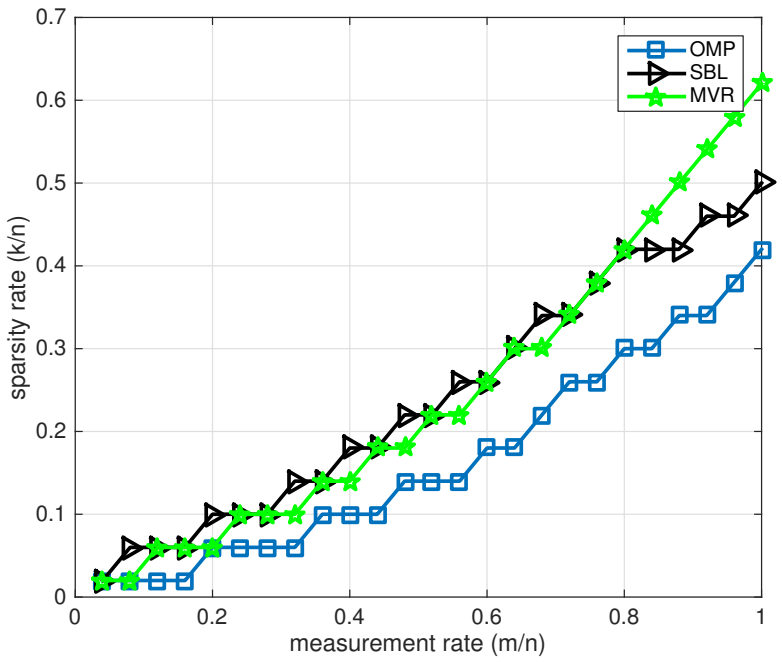

Figure 2.3: OMP, SBL & MVR phase transition curves at SNR = 30 dB.

m/n-k/n plane. At all operating points below the curve, the signal to reconstruction error ratio (SRR) exceeds 15 dB for at least 90% of the 1000 trial runs, where m is the number of measurements, k is the number of nonzero entries in the sparse vector and $n = 50$ is the ambient dimension of the sparse vector. The $m \times k$ measurement matrices are drawn independent and identically distributed (i.i.d.) from a standard Gaussian distribution with i.i.d. entries. The sparse vector is generated with k nonzeros at uniformly random locations and with i.i.d. entries, uniformly distributed on $[-2, -1] \cup [1, 2]$. The additive noise is zero mean Gaussian with a standard deviation chosen to achieve a signal to noise ratio (SNR) of 30 dB. The phase transition curves of SBL and MVR nearly coincide, and are superior to OMP. However, SBL is a computationally demanding algorithm and it takes a large number of iterations to converge. For the MVR algorithm, while steps from lines 5 to 9 in Algorithm 1 can be iterated multiple times, we find, in our simulations, that the channel estimation error reduces significantly in just one pass of the algorithm. Thus, MVR offers a computationally attractive alternative to SBL with comparable performance for our application. Empirically, we have observed a similar relative performance behavior at other SNRs also.

Table 2.1: Split-up of Computational Complexity.

Computation	**Stage 1**	**Stage 2**
Dictionary Matrix	$\mathcal{O}(M\|S_P\|KN)$	$\mathcal{O}(K^2N)$
OMP (per iteration)	$\mathcal{O}(M\|S_P\|N)$	$\mathcal{O}(KN)$
SBL (per iteration)	$\mathcal{O}(M^2\|S_P\|^2N)$	$\mathcal{O}(K^2N)$
MVR	$\mathcal{O}(M^2\|S_P\|^2N)$	$\mathcal{O}(K^2N)$
Channel Matrix	$\mathcal{O}(K^2\hat{N}_p)$	$\mathcal{O}(K^2\hat{N}_p)$
Combining Weights	$\mathcal{O}\left(KM^3\right)$	$\mathcal{O}(KM^3)$
Post-Combined Channel Matrix	$\mathcal{O}(K^2M)$	$\mathcal{O}(K^2M)$
Data Demodulation	$\mathcal{O}(K)$	$\mathcal{O}(K)$

Table 2.2: Overall Computational Complexity.

	Total Complexity (Stage 1 + Stage 2)
OMP	$\mathcal{O}\left((K^2(\hat{N}_p+M)+KM^3)(N_{\text{iter,I}}+N_{\text{iter,II}})+(K+\hat{N}_p)NM\|S_P\|N_{\text{iter,I}}\right)$
SBL	$\mathcal{O}\left((K^2(\hat{N}_p+M)+KM^3)(N_{\text{iter,I}}+N_{\text{iter,II}})+(K+\kappa M\|S_P\|N)NM\|S_P\|N_{\text{iter,I}}\right)$
MVR	$\mathcal{O}\left((K^2(\hat{N}_p+M)+KM^3)(N_{\text{iter,I}}+N_{\text{iter,II}})+(K+M\|S_P\|N)NM\|S_P\|N_{\text{iter,I}}\right)$

2.3.4 Computational Complexity

Table 2.1 shows the computational complexity, based on floating point operation (FLOP) count for matrix-vector operations [37, 93], per iteration, of stage 1 and stage 2. Note that the near-diagonal nature of the post-combined channel matrix was utilized to reduce the computational complexity of data demodulation in stage 1. We iterate OMP for $\hat{N}_p$ times, where $\hat{N}_p$ is an integer exceeding the number of paths, SBL for a fixed number of times, κ, and MVR just once. The overall computational complexity when using OMP, SBL and MVR is given in Table 2.2, where $N_{\text{iter,I}}$ and $N_{\text{iter,II}}$ are used to denote the number of stage 1 and stage 2 iterations, respectively.

In the proposed algorithm, the construction of dictionary matrices in (2.14) consumes most of the CPU time, especially for large K and N. Also, the dictionary matrix must be recomputed in every iteration during stage 1 and stage 2 since the data symbols get

updated after the data detection step. We perform a recursive update of the dictionary matrix during the ν^{th} iteration according to

$$\mathbf{A}^{(m)}(\nu) = \mathbf{A}^{(m)}(\nu-1) + \Delta\mathbf{A}^{(m)}(\nu), \tag{2.24}$$

where $\Delta\mathbf{A}^{(m)}(\nu) = \mathbf{J}^{(m)}\left[\mathbf{\Gamma}_1^{(m)}\Delta\mathbf{s}^{(\nu)}, \ldots, \mathbf{\Gamma}_N^{(m)}\Delta\mathbf{s}^{(\nu)}\right]$ and $\Delta\mathbf{s}^{(\nu)} = \mathbf{s}^{(\nu)} - \mathbf{s}^{(\nu-1)}$ is the change in the data symbols between iterations. As the iteration progresses, $\Delta\mathbf{s}^{(\nu)}$ will contain many zero elements and the corresponding columns of $\Delta\mathbf{A}^{(m)}(\nu)$ will be all zero vectors. Thus, only the columns of $\mathbf{A}^{(m)}(\nu)$ corresponding to the nonzero entries in $\Delta\mathbf{s}^{(\nu)}$ need to be computed, making the dictionary update fast.

2.4 Analysis

Recall that the PID outputs are obtained from the same OFDM receiver output as the FID outputs. Yet, using the PID outputs in stage 1 leads to better data detection performance. First, we analyze this behavior and show that using the PID leads to a larger number of effective measurements compared to the FID, which explains its better performance.

2.4.1 Effective Number of Measurements

We compare the number of linearly independent rows in the measurement matrices corresponding to the PID and the FID outputs for pilot only measurements in the stage 1. It is easy to see that:

$$\text{rank}\left(\sum_{m=1}^{M}\mathbf{A}_{S_P}^{(m)}\right) \leq \text{rank}\left(\tilde{\mathbf{A}}_{S_P}\right) \leq \min\left(M|S_P|, N\right), \tag{2.25}$$

where $\tilde{\mathbf{A}}_{S_P}$ is the augmented matrix obtained by vertically stacking $\mathbf{A}_{S_P}^{(m)}, m = 1, 2, \cdots, M$. Therefore, there are at least as many linearly independent pilot only measurements at the output of the PID, whose sensing matrix is $\tilde{\mathbf{A}}_{S_P}$, as the FID, whose sensing matrix is

$\mathbf{A}_{S_P} \triangleq \sum_{m=1}^{M} \mathbf{A}_{S_P}^{(m)}$. We proceed to show that it is possible to obtain strictly more linearly independent measurements from the PIDs than from the FID.

In the first iteration of stage 1, we set all the entries of $\hat{\mathbf{s}}$, except pilot locations, to zero. If all the pilot symbols are equal to, say, s_0, then, the dictionary matrix constructed in the first iteration of stage 1 is given by:

$$\mathbf{A}_{S_P}^{(m)} = s_0 \mathbf{I}_{S_P} \mathbf{J}^{(m)} \mathbf{I}_{S_P}^T \mathbf{I}_{S_P} \mathbf{\Gamma}^{(m)}, \tag{2.26}$$

where,

$$\mathbf{\Gamma}^{(m)} \triangleq \left[\mathbf{\Gamma}_1^{(m)} \mathbf{1}_K \ldots \mathbf{\Gamma}_{N_\tau N_b}^{(m)} \mathbf{1}_K \right], \tag{2.27}$$

$\mathbf{1}_K \in \mathbb{R}^K$ is a column vector of K ones and $\mathbf{I}_{S_P}$ is as defined after (2.16). The matrix $\mathbf{\Gamma}^{(m)}$ can be decomposed as:

$$\begin{aligned} \mathbf{\Gamma}^{(m)} &= \mathbf{\Gamma}_b^{(m)} \otimes \mathbf{\Gamma}_\tau, & (2.28) \\ \mathbf{\Gamma}_b^{(m)} &= e^{j2\pi \mathbf{f}\mathbf{b}^T t_m} \in \mathbb{C}^{K \times N_b}, & (2.29) \\ \mathbf{\Gamma}_\tau &= e^{-j2\pi \mathbf{f}\tau^T} \in \mathbb{C}^{K \times N_\tau}, & (2.30) \end{aligned}$$

where $\otimes$ denotes the Khatri-Rao product,[4] $e^{\mathbf{B}}$ finds elementwise exponentiation of a matrix $\mathbf{B}$, and

$$\begin{aligned} \mathbf{f} &= [f_1, \ldots, f_K]^T \in \mathbb{R}^K, & (2.31) \\ \tau &= \left[\frac{T}{\lambda K}, \frac{2T}{\lambda K}, \ldots, \frac{N_\tau T}{\lambda K} \right]^T \in \mathbb{R}^{N_\tau}, & (2.32) \\ \mathbf{b} &= [-b_{\max}, -b_{\max} + \Delta b, \ldots, b_{\max}]^T \in \mathbb{R}^{N_b}. & (2.33) \end{aligned}$$

It readily follows from (2.28) and the definition of the Khatri-Rao product that,

$$\mathbf{I}_{S_P} \mathbf{\Gamma}^{(m)} = \mathbf{I}_{S_P} \mathbf{\Gamma}_b^{(m)} \otimes \mathbf{I}_{S_P} \mathbf{\Gamma}_\tau. \tag{2.34}$$

[4]The Khatri-Rao product is formed by taking the row-wise Kronecker products of $\mathbf{\Gamma}_b^{(m)} \in \mathbb{C}^{K \times N_b}$ and $\mathbf{\Gamma}_\tau \in \mathbb{C}^{K \times N_\tau}$.

Let $\tilde{\mathbf{\Gamma}}_{S_P} \in \mathbb{C}^{M|S_P| \times N_\tau N_b}$ and $\tilde{\mathbf{\Gamma}}_{b,S_P} \in \mathbb{C}^{M|S_P| \times N_b}$ denote the augmented matrices obtained by vertically stacking $\mathbf{I}_{S_P}\mathbf{\Gamma}^{(m)}, m = 1, \ldots, M$, and $\mathbf{I}_{S_P}\mathbf{\Gamma}_b^{(m)}, m = 1, \ldots, M$, respectively. Similarly, let $\tilde{\mathbf{\Gamma}}_{\tau,S_P} \in \mathbb{C}^{M|S_P| \times N_\tau}$ be the augmented matrix obtained by vertically stacking $\mathbf{I}_{S_P}\mathbf{\Gamma}_\tau$ M-times. We then have:

$$\tilde{\mathbf{\Gamma}}_{S_P} = \tilde{\mathbf{\Gamma}}_{b,S_P} \otimes \tilde{\mathbf{\Gamma}}_{\tau,S_P}. \tag{2.35}$$

We now state two properties of the Khatri-Rao product that are useful in the sequel. We denote k-rank($\mathbf{B}$) to be the row Kruskal-rank[5] of a matrix $\mathbf{B}$.

Lemma 2.4.1. *The rank (k-rank) of the Khatri-Rao product of two matrices, both having at least one of the columns with all its entries nonzero, is never less than the rank (k-rank) of the two matrices, i.e., if $\mathbf{B} \in \mathbb{C}^{r\times p}$ and $\mathbf{C} \in \mathbb{C}^{r\times q}$ are two matrices such that for some $n \in \{1, 2, \ldots, p\}$ and $n' \in \{1, 2, \ldots, q\}$, we have $[\mathbf{B}]_{m,n} \neq 0$ and $[\mathbf{C}]_{m,n'} \neq 0$ for every $m \in \{1, 2, \ldots, r\}$, then:*

$$\begin{aligned} \text{rank}\,(\mathbf{B} \otimes \mathbf{C}) &\geq \max\left(\text{rank}\,(\mathbf{B}), \text{rank}\,(\mathbf{C})\right), & (2.36)\\ k\text{-rank}\,(\mathbf{B} \otimes \mathbf{C}) &\geq \max\left(k\text{-rank}\,(\mathbf{B}), k\text{-rank}\,(\mathbf{C})\right). & (2.37) \end{aligned}$$

Proof. The Khatri-Rao product $\mathbf{B} \otimes \mathbf{C} \in \mathbb{C}^{r\times pq}$ houses a submatrix (and another submatrix) whose rows are scaled versions of the rows of $\mathbf{B} \in \mathbb{C}^{r\times p}$ (respectively $\mathbf{C} \in \mathbb{C}^{r\times q}$) and hence its rank, and the k-rank, must be at least that of $\mathbf{B} \in \mathbb{C}^{r\times p}$ ($\mathbf{C} \in \mathbb{C}^{r\times q}$). The results follow. □

Lemma 2.4.2. *If $\mathbf{B} \in \mathbb{C}^{r\times p}$ and $\mathbf{C} \in \mathbb{C}^{r\times q}$ then*

$$k\text{-rank}\,(\mathbf{B} \otimes \mathbf{C}) \geq \min\left(k\text{-rank}\,(\mathbf{B}) + k\text{-rank}\,(\mathbf{C}) - 1, r\right). \tag{2.38}$$

Proof. Let $\mathcal{R}$ denote a set of $r_k = k\text{-rank}\,(\mathbf{B} \otimes \mathbf{C}) + 1$ indices of the rows of $\mathbf{B} \otimes \mathbf{C}$ that are linearly dependent. It follows from the definition of k-rank that there exists a

[5]The row Kruskal-rank (k-rank) of a matrix is r if every subset of its r rows is linearly independent and at least one subset of $r + 1$ rows is linearly dependent.

vector $\mathbf{d} \in \mathbb{C}^{r_k}$ with all entries nonzero such that $\mathbf{d}^T (\mathbf{B}_{\mathcal{R}} \otimes \mathbf{C}_{\mathcal{R}}) = \mathbf{0}$, where $\mathbf{B}_{\mathcal{R}} = \mathbf{I}_{\mathcal{R}}\mathbf{B}$ and $\mathbf{C}_{\mathcal{R}} = \mathbf{I}_{\mathcal{R}}\mathbf{C}$. Therefore, we have $\mathbf{B}_{\mathcal{R}}^T \mathbf{D} \mathbf{C}_{\mathcal{R}} = \mathbf{0} \in \mathbb{C}^{p \times q}$ where $\mathbf{D} = \operatorname{diag}(\mathbf{d})$. $\mathbf{D}$ is non-singular since all entries of $\mathbf{d}$ are nonzero and hence, by the Sylvester inequality, $\mathbf{0} = \operatorname{rank}\left(\mathbf{B}_{\mathcal{R}}^T \mathbf{D} \mathbf{C}_{\mathcal{R}}\right) \geq \operatorname{rank}(\mathbf{B}_{\mathcal{R}}) + \operatorname{rank}(\mathbf{C}_{\mathcal{R}}) - r_k \implies r_k \geq \operatorname{rank}(\mathbf{B}_{\mathcal{R}}) + \operatorname{rank}(\mathbf{C}_{\mathcal{R}})$. The rows of $\mathbf{B}_{\mathcal{R}}$ and $\mathbf{C}_{\mathcal{R}}$ are dependent by construction, and hence appending more rows to these matrices cannot increase their k-rank: $\operatorname{rank}(\mathbf{B}_{\mathcal{R}}) \geq k\text{-rank}(\mathbf{B}_{\mathcal{R}}) \geq k\text{-rank}(\mathbf{B})$ and $\operatorname{rank}(\mathbf{C}_{\mathcal{R}}) \geq k\text{-rank}(\mathbf{C}_{\mathcal{R}}) \geq k\text{-rank}(\mathbf{C})$. Thus, we find $r_k = k\text{-rank}(\mathbf{B} \otimes \mathbf{C}) + 1 \geq k\text{-rank}(\mathbf{B}) + k\text{-rank}(\mathbf{C})$, from which the result follows. □

All entries of the matrices $\mathbf{I}_{S_P} \mathbf{\Gamma}_b^{(m)}$ and $\mathbf{I}_{S_P} \mathbf{\Gamma}_\tau$, in (2.35), have unit magnitude and therefore satisfy the conditions in Lemma 2.4.1. Also, it is straightforward to see that

$$\operatorname{rank}\left(\tilde{\mathbf{\Gamma}}_{\tau,S_P}\right) = \operatorname{rank}\left(\mathbf{I}_{S_P}\mathbf{\Gamma}_\tau\right), \tag{2.39}$$

$$k\text{-rank}\left(\tilde{\mathbf{\Gamma}}_{\tau,S_P}\right) = 1, \tag{2.40}$$

and therefore it follows from Lemma 2.4.1 that

$$\operatorname{rank}\left(\tilde{\mathbf{\Gamma}}_{S_P}\right) \geq \max\left(\operatorname{rank}\left(\tilde{\mathbf{\Gamma}}_{b,S_P}\right), \operatorname{rank}\left(\mathbf{I}_{S_P}\mathbf{\Gamma}_\tau\right)\right), \tag{2.41}$$

$$k\text{-rank}\left(\tilde{\mathbf{\Gamma}}_{S_P}\right) \geq k\text{-rank}\left(\tilde{\mathbf{\Gamma}}_{b,S_P}\right). \tag{2.42}$$

We are now ready to state a *sufficient* condition that results in strictly larger number of independent measurements from the PID output than the FID. We say that a collection of subspaces $\mathcal{S} = \{S_i \in \mathbb{V} : i = 1, 2, \cdots, n\}$ of a vector space $\mathbb{V}$ forms a *virtually disjoint partition* if $\mathbb{V}$ is a *direct sum* of its subspaces $S_i, i = 1, 2, \cdots, n$, i.e., if $\oplus_{i=1}^n S_i = \mathbb{V}$ and $\cap_{i=1}^n S_i = \{\mathbf{0}\}$, where the operator $\oplus$ denotes the subspace sum [31].

Theorem 2.4.3. *If the number of grids N_b used for representing the Doppler parameter, and the augmented matrix $\tilde{\mathbf{\Gamma}}_{b,S_P}$ generated by the representative Doppler values forming*

the grid, satisfy:

$$N_b + N_\tau \geq M|S_P| + 1, \tag{2.43}$$

$$k\text{-rank}\left(\tilde{\mathbf{\Gamma}}_{b,S_P}\right) = \min\left(N_b, M|S_P|\right), \tag{2.44}$$

and the pilot locations in S_P are chosen such that

$$\text{rank}\left(\mathbf{I}_{S_P}\mathbf{J}^{(m)}\mathbf{I}_{S_P}^T\right) = |S_P|, m = 1, \ldots, M, \tag{2.45}$$

then:

$$|S_P| = \text{rank}\left(\sum_{m=1}^{M}\mathbf{A}_{S_P}^{(m)}\right) < \text{rank}\left(\tilde{\mathbf{A}}_{S_P}\right) = M|S_P|. \tag{2.46}$$

Proof. From (2.43) and (2.44), we get

$$\begin{aligned} M|S_P| &\geq \text{rank}\left(\tilde{\mathbf{\Gamma}}_{S_P}\right) \\ &\geq k\text{-rank}\left(\tilde{\mathbf{\Gamma}}_{S_P}\right) \\ &\geq \min\left(N_b + N_\tau - 1, M|S_P|\right) \\ &= M|S_P|, \end{aligned} \tag{2.47}$$

where the last inequality follows from Lemma 2.4.2, and hence

$$\text{rank}\left(\tilde{\mathbf{\Gamma}}_{S_P}\right) = M|S_P|. \tag{2.48}$$

Therefore, the row spaces of $\mathbf{I}_{S_P}\mathbf{\Gamma}^{(m)}, m = 1, \ldots, M$, form a virtually disjoint partition of the $M|S_P|$-dimensional row space of $\tilde{\mathbf{\Gamma}}_{S_P}$. Due to equation (2.26) and the condition in (2.45), the row space of $\mathbf{A}_{S_P}^{(m)}$ is equal to that of $\mathbf{I}_{S_P}\mathbf{\Gamma}^{(m)}$ for $m = 1, \ldots, M$. Hence, the row spaces of $\mathbf{A}_{S_P}^{(m)}, m = 1, \ldots, M$, also form a virtually disjoint partition of the $M|S_P|$-dimensional row space of $\tilde{\mathbf{\Gamma}}_{S_P}$. The result in (2.46) follows. □

Discussion

The result in Theorem 2.4.3 indicates that the pilot only measurements from the PID outputs can potentially lead to better channel estimates compared to that from the FID. The conditions (2.43) and (2.44) are not necessary; we find in our simulation studies that far fewer number of grid points N_b in the Doppler parameter leads to (2.46) being satisfied. To illustrate this point, Figures 2.4 and 2.5 show the distribution of singular values of the stacked up dictionary matrix $\tilde{\mathbf{A}}_{S_P}$ corresponding to the PID output for pilot subcarriers when the Doppler spreads are $b_{\max} = 5 \times 10^{-4}$ and $b_{\max} = 10^{-3}$, respectively, and when pilot carriers are chosen as in the numerical case study in Section 2.5. Also shown in this figure is a plot of the singular values of the dictionary matrix $\mathbf{A}_{S_P}$ corresponding to FID observation of pilot subcarriers. It is clear that the numerical rank of the stacked up dictionaries of the PID is greater than that of the FID, especially, when the dictionaries are designed for high Doppler spread. Therefore, using the sequence of observations from PIDs, which is tantamount to oversampling the OFDM receiver output, helps estimate the channel better.

We have shown that the sparse channel estimation from the PID output provides a good initial estimate of the channel matrix. Next, we justify that the proposed two stage algorithm that iterates between the sparse channel estimation and data detection steps in each stage can only improve the channel estimation and data detection accuracy with every iteration.

2.4.2 Convergence

Recall that our channel estimation is based on the sparse vector recovery framework expressed by (2.15) and (2.23) for stage 1 and stage 2, respectively. We recapitulate the channel estimation framework in the following form:

$$\mathbf{z} = \mathbf{A}(\mathbf{s})\mathbf{x} + \mathbf{v}, \tag{2.49}$$

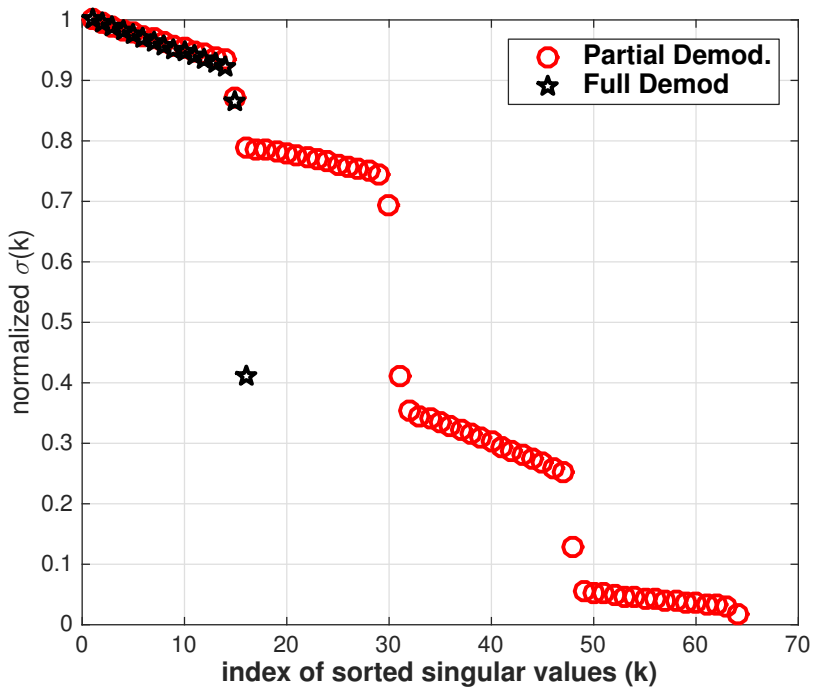

Figure 2.4: Singular values of the dictionary matrices corresponding to PID and FID outputs. Doppler spread $b_{\max} = 0.5 \times 10^{-3}$.

where $\mathbf{A}(\mathbf{s})$ indicates the dependence of dictionary matrix on the data symbols $\mathbf{s}$. Similarly, the data detection problem in the stage 1 and stage 2 is given by

$$\mathbf{z} = \mathbf{H}(\mathbf{x})\mathbf{s} + \mathbf{v}, \tag{2.50}$$

where the dependence of the channel matrix on the vector $\mathbf{x}$ is indicated via $\mathbf{H}(\mathbf{x})$. Note that $\mathbf{A}(\mathbf{s})\mathbf{x} = \mathbf{H}(\mathbf{x})\mathbf{s}$.

Ideally, for estimating the sparse channel, we would like to minimize $\|\mathbf{x}\|_0$ subject to $\|\mathbf{z} - \mathbf{H}(\mathbf{x})\mathbf{s}\|_2 \leq \eta$. This problem is NP-hard, and, therefore, we consider its convex relaxation:

$$C(\mathbf{x}, \mathbf{s}) = \|\mathbf{x}\|_1 + \lambda \|\mathbf{z} - \mathbf{H}(\mathbf{x})\mathbf{s}\|_2^2, \tag{2.51}$$

over $\mathbf{x}, \mathbf{s} \in \mathbb{C}$.

Let $\mathbf{x}^{(\nu)}$ denote the sparse channel vector estimated in the ν^{th} iteration. For a given

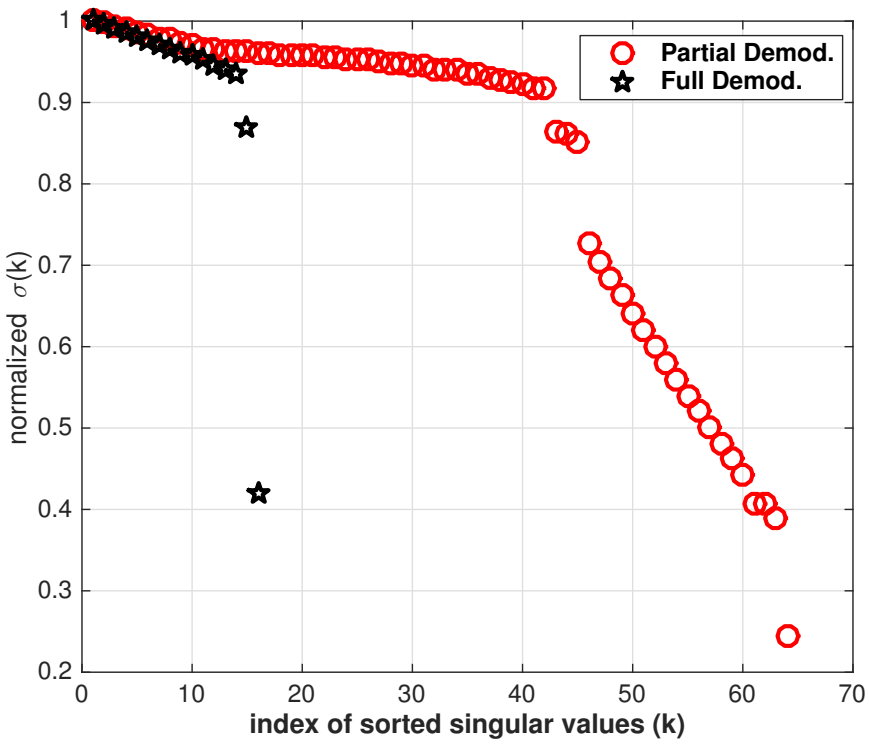

Figure 2.5: Singular values of the dictionary matrices corresponding to PID and FID outputs. Doppler spread $b_{\max} = 10^{-3}$.

$\mathbf{x}^{(\nu)}$, choosing

$$\mathbf{s}^{(\nu+1)} = \arg\min_{\mathbf{s}\in\mathbb{C}} \|\mathbf{z} - \mathbf{H}(\mathbf{x}^{(\nu)})\mathbf{s}\|_2, \tag{2.52}$$

ensures that $C(\mathbf{x}^{(\nu)}, \mathbf{s}^{(\nu+1)}) \leq C(\mathbf{x}^{(\nu)}, \mathbf{s}^{(\nu)})$. For a given $\mathbf{s}^{(\nu+1)}$, choosing

$$\mathbf{x}^{(\nu+1)} = \arg\min_{\mathbf{x}\in\mathbb{C}} C(\mathbf{x}, \mathbf{s}^{(\nu+1)}), \tag{2.53}$$

ensures that $C(\mathbf{x}^{(\nu+1)}, \mathbf{s}^{(\nu+1)}) \leq C(\mathbf{x}^{(\nu)}, \mathbf{s}^{(\nu)})$. Therefore, the cost $C(\mathbf{x}, \mathbf{s})$ reduces with every iteration and is bounded below by 0. Hence, the iterations in stage 1 and stage 2 converge to a local minimum of the ℓ_1 regularized joint cost function. We can show that, by associating a Laplacian prior to the channel vector $\mathbf{x}$, the solution $(\mathbf{x}, \mathbf{s})$ which minimizes $C(\mathbf{x}, \mathbf{s})$ is also a solution to joint channel estimation and maximum *a posteriori* probability (MAP) data detection problem. Note that the above recipe of iterating between channel estimation and data detection is unlike joint receivers that provide a low complexity

approximation to MAP detection [100], [59].

2.4.3 Lower Bound on the MSE

We obtain a lower bound on the MSE in the estimate of the channel matrix (see remark below) for the two classes of *unbiased* estimators: one that makes use of the observations at the output of the PID, and the other that uses only the observations from the FID. We have the following theorem.

Theorem 2.4.4. *For the PID measurement model in* (2.13)*, the MSE in the channel matrix* $\mathbf{H}$*, which is a function of the channel vector* $\mathbf{x}$*, can be lower bounded as*

$$\mathbb{E}\{\|\mathbf{H}-\hat{\mathbf{H}}\|_F^2\} \geq \ tr\left(\mathbf{F}_{\mathcal{S},\mathcal{S}}^{-1}\frac{\partial \mathbf{h}}{\partial \mathbf{x}_{\mathcal{S}}}^{H}\frac{\partial \mathbf{h}}{\partial \mathbf{x}_{\mathcal{S}}}\right), \tag{2.54}$$

$\mathcal{S}$ *is the support of the channel vector* $\mathbf{x}$*,* $\mathbf{F}_{\mathcal{S},\mathcal{S}} \in \mathbb{C}^{|\mathcal{S}|\times|\mathcal{S}|}$ *is the submatrix of the Fisher Information Matrix (FIM)* $\mathbf{F} \in \mathbb{C}^{N\times N}$*, corresponding to the rows and columns indexed by* $\mathcal{S}$*, for the observation model in* (2.13)*, given by*

$$\mathbf{F} = \sum_{m=1}^{M} \mathbf{A}^{(m)H}\mathbf{C}_m^{\dagger}\mathbf{A}^{(m)}, \tag{2.55}$$

$\mathbf{C}_m$ *is the covariance of the noise at the output of the PID, whose entries are given by* (2.8)*,* $\mathbf{h}(\mathbf{x}) \triangleq vec\,(\mathbf{H}) \in \mathbb{C}^{K^2\times 1}$*, the columns of the matrix* $\frac{\partial \mathbf{h}}{\partial \mathbf{x}} \in \mathbb{C}^{K^2\times N}$ *are given by*

$$\frac{\partial \mathbf{h}(\mathbf{x})}{\partial \mathbf{x}_k} = \begin{cases} vec\left(\sum_{m=1}^{M}\mathbf{J}^{(m)}\mathbf{\Gamma}_k^{(m)}\right), & k \in \mathcal{S}, \\ \mathbf{0}_{K^2}, & otherwise, \end{cases} \tag{2.56}$$

and $\frac{\partial \mathbf{h}}{\partial \mathbf{x}_{\mathcal{S}}}$ *is the submatrix of* $\frac{\partial \mathbf{h}}{\partial \mathbf{x}}$ *consisting of only the columns indexed by* $\mathcal{S}$*.*

Proof. First, we note that the channel matrix $\mathbf{H}$ can be related to the entries of the channel vector $\mathbf{x}$, defined in (2.12), by making use of (2.9). This allows us to express the channel matrix $\mathbf{H}$ as a function of the channel vector $\mathbf{x}$. The MSE of any unbiased estimator of $\mathbf{H}$ that makes use of the output from the PID, given by (2.13), cannot be better than

the Cramér Rao bound (CRB) [96] of the subclass of unbiased estimators which know the true dictionary matrices $\mathbf{A}^{(m)}, m = 1, 2, \ldots, M$, i.e., where a genie provides the estimator with the knowledge of the data symbols. The CRB, given the true dictionary matrices in (2.13), is the same as the MSE of an oracle estimator that knows the support $\mathcal{S}$ of the channel vector $\mathbf{x}$ [10]. The result follows. □

Theorem 2.4.5. *A lower bound on the MSE of the unbiased estimators of the channel matrix* $\mathbf{H}$*, that uses the observations from the FID measurement model in* (2.23)*, is given by*

$$\mathbb{E}\{\|\mathbf{H} - \hat{\mathbf{H}}\|_F^2\} \geq \ tr\left(\mathbf{G}_{\mathcal{S},\mathcal{S}}^{-1} \frac{\partial \mathbf{h}}{\partial \mathbf{x}_{\mathcal{S}}}^{H} \frac{\partial \mathbf{h}}{\partial \mathbf{x}_{\mathcal{S}}}\right), \tag{2.57}$$

where $\mathcal{S}$ *is the support of the channel vector* $\mathbf{x}$*,* $\mathbf{G} \in \mathbb{C}^{N \times N}$ *is the FIM for the FID observation model in* (2.23)*, given by:*

$$\mathbf{G} = \frac{1}{N_0} \mathbf{A}^H \mathbf{A}, \tag{2.58}$$

$\mathbf{h}(\mathbf{x}) \triangleq vec\,(\mathbf{H}) \in \mathbb{C}^{K^2 \times 1}$*, and the columns of the matrix* $\frac{\partial \mathbf{h}}{\partial \mathbf{x}} \in \mathbb{C}^{K^2 \times N}$ *are given as in Theorem 2.4.4.*

Proof. Similar to Theorem 2.4.4. □

Remarks

1. It is tempting to consider the MSE in the estimate of the sparse channel vector $\mathbf{x}$, in (2.12), defined on the delay-Doppler grid. While the MSE in the channel vector $\mathbf{x}$ relates to the MSE in the channel matrix $\mathbf{H}$, we assert that the latter is more meaningful for our problem. This is because, a small mismatch in support estimation (i.e., when the recovered support returns indices near the true support) can lead to a large MSE in the sparse vector $\mathbf{x}$, but need not translate to a large MSE in the channel. However, the data detection performance primarily depends on the fidelity in the estimation of $\mathbf{H}$, and not as much on $\mathbf{x}$. Hence, we consider the MSE in the channel matrix $\mathbf{H}$ as the performance metric in this work.

2. Theorems 2.4.4 and 2.4.5 allow us to compare the bounds on the MSE of unbiased estimators that use the PID outputs and those that use the FID outputs. Numerical evaluation shows that the bound on the MSE for the estimators that make use of PID outputs is indeed better. Also, our proposed two-stage data detection and channel estimation algorithm, that makes use of the PID outputs in stage 1 and the FID outputs in stage 2, approaches the lower bound at high SNR. See Section 2.5 for details.

2.5 Numerical Simulations

We simulate the performance of the proposed algorithm for the CP-OFDM system whose parameters are listed in Table 2.3. The specifications of the system matches with the settings used in the SPACE'08 experiment and is widely used for simulation studies in several past works, for example, [14, 34], and [106]. Pilot symbols are spaced uniformly. Half the null carriers are placed at the band edges and the remaining are inserted between the data as specified in [14, 34].

We consider two simulation models for the underwater acoustic communication channel. In model I, adopted from [14, 34], we generate sparse channels with a few discrete paths whose inter-arrival times are exponentially distributed with a mean of 1 ms. The path amplitudes are Rayleigh distributed with the average power decreasing exponentially with delay, where the difference between the beginning and the end of the guard time is 20 dB. The residual Doppler rate for each path is uniformly distributed in $[-b_{\max}, b_{\max}]$, where channels with $b_{\max} = 5 \times 10^{-4}$ and 1×10^{-3} are considered to be severely Doppler distorted in the underwater communication literature [110]. In model II, we simulate the time-varying stochastic channel response according to the model proposed in [72]. Model II incorporates the effect of frequency dependent attenuation, the surface/bottom scattering and other random fluctuations in the medium and source-receiver position. The authors report a good match of their theoretical model with the experimental data collected from four different deployment sites of varying degrees of mobility. We use model II to demonstrate the relatively strong performance of the proposed algorithm to

Table 2.3: CP-OFDM parameters used in the simulation.

Carrier frequency (f_c)	13 kHz
Bandwidth (B)	9.77kHz
No. of subcarriers (K)	1024
No. of pilots ($\|S_P\|$)	256
No. of nulls ($\|S_N\|$)	96
Symbol duration (T)	104.86 ms
Subcarrier spacing (Δf)	9.54 Hz
Guard interval (T_g)	24.6 ms

mismatches in the model assumptions.

We finally show the performance of our proposed algorithm on the measured time varying channel impulse response data available in WATERMARK [97]. We consider two channel measurements corresponding to a low Doppler spread channel and a high Doppler spread channel. These measured responses in WATERMARK include the effect of system hardware and the real world acoustic propagation as well.

We define the signal to noise ratio (SNR) as $\text{SNR} = \frac{E\{\|\mathbf{Hs}\|_2^2\}}{E\{\|\mathbf{v}\|_2^2\}}$, and the normalized MSE in channel estimation as $\text{NMSE} = \frac{E\{\|\mathbf{H}-\hat{\mathbf{H}}\|_F^2\}}{E\{\|\mathbf{H}\|_F^2\}}$, where $\mathbf{H} \in \mathbb{C}^{K\times K}$ and $\hat{\mathbf{H}} \in \mathbb{C}^{K\times K}$ are the true and the estimated channels, respectively.

2.5.1 Simulations using Model I

We first consider coded 16-QAM transmissions, and channels generated according to model I with $N_p = 15$ discrete paths and $b_{\max} = 10^{-3}$. The turbo code uses two rate-1/2 convolutional encoders with feedback and an interleaver of length 232 bits [69]. The bit error rate (BER) and normalized MSE are averaged over 1000 independent instantiations. For constructing the dictionary matrix, grids are formed using $N_b = 15$ points for the Doppler rate and $N_\tau = 480$ points for the delay resolution corresponding to an oversampling factor of $\lambda = 2$ over the guard interval. The PID and FID dictionary matrices

are, therefore, of size 1024×7200.

For the sparse channel recovery, we experiment with OMP [23] and MVR. For OMP, we set the number of nonzero entries to be recovered to $\hat{N}_p = 25$. The number of propagation paths need not be known precisely; as long as $\hat{N}_p > N_p$, simulation studies show good channel recovery. The MVR algorithm is iterated only once. We compare our proposed dual stage algorithm that uses PID outputs in stage 1 against the algorithms in [14,34], the least squares based channel estimation and data detection, and genie-aided data detection which uses the channel state information. For simulating the algorithm in [34], we use the ICI-aware receiver with an ICI depth parameter of $D = 6$.

In Figure 2.6, we show the normalized MSE in the channel matrix estimate for the different algorithms. For the proposed dual-stage algorithm, we iterate for $N_{\text{iter}} = 3$ through both stage 1 and stage 2. We use $M = 4$ PIDs in our simulations.[6] For the value of M used here, from equation (2.8), the noise at the output of the PID is uncorrelated among the pilot-only observations. The MVR algorithm leads to a lower MSE in the channel matrix estimate compared to OMP. The normalized MSE performance of the algorithms in [14, 34], that use the FID output for pilot-only measurements, is shown in Figure 2.6. The algorithm in [34] is similar to [14] but iterates to improve the data symbol detection; we use $N_{\text{iter}} = 6$ in the simulations of the iterative algorithm in [14]. Also included in Figure 2.6 are the normalized MSE performances of two least square channel estimation algorithms labeled `LS CDD (FID)` and `LS CDD (PID, Optm. Wt.)` in the plot. LS CDD (FID) estimates the channel using pilot measurements at FID output. LS CDD (PID, Optm. Wt.) estimates the channel using pilot measurements at optimally combined PID output. Only the combiner weights, for LS CDD (PID, Optm. Wt.), are computed using the true channel matrix (genie aided). Note that the performance of [106], in which combiner weights are estimated through an adaptive algorithm, cannot be better than LS CDD (PID, Optm. Wt.). Stage 1 recovers the channel better than the existing FID and PID based algorithms and hence provides a good estimate of unknown data

[6]Increasing M will in general improve the performance due to additional measurements being made available, but will also increase the computational complexity. Also, increasing M beyond a certain point will not yield significantly more effective measurements.

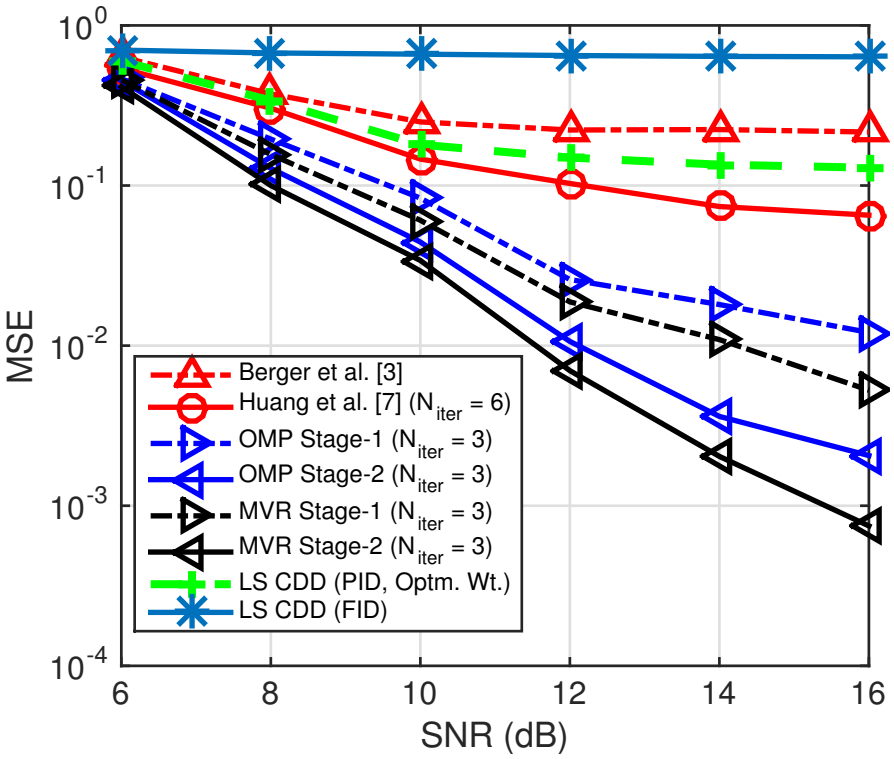

Figure 2.6: MSE in the channel matrix estimate of various sparse signal recovery algorithms. Doppler spread $b_{\max} = 10^{-3}$.

symbols to initialize stage 2. The MSE in the channel matrix further reduces at the end of stage 2, especially at high SNR, which leads to better symbol detection performance. Figure 2.7 shows the reduction in MSE for the iterative algorithms compared above, as the number of iterations is increased to $N_{\text{iter}} = 10$ at an SNR of 16 dB. It is seen that the proposed dual stage algorithm, at the end of stage 2, has settled in about 3 iterations.

Figure 2.8 compares the bit error rate (BER) versus SNR curves of the proposed dual stage algorithm with the least squares based channel estimation and coherent data detection algorithms LS CDD (FID) and LS CDD (PID, Optm. Wt.), the sparse channel recovery based algorithms reported in [14, 34] and the genie-aided data detection as a baseline. Note that LS CDD (FID) and LS CDD (PID, Optm. Wt.) perform coherent data detection at the FID and optimally combined PID outputs, respectively. The dual stage iterative algorithm proposed in this chapter clearly outperforms the existing sparse

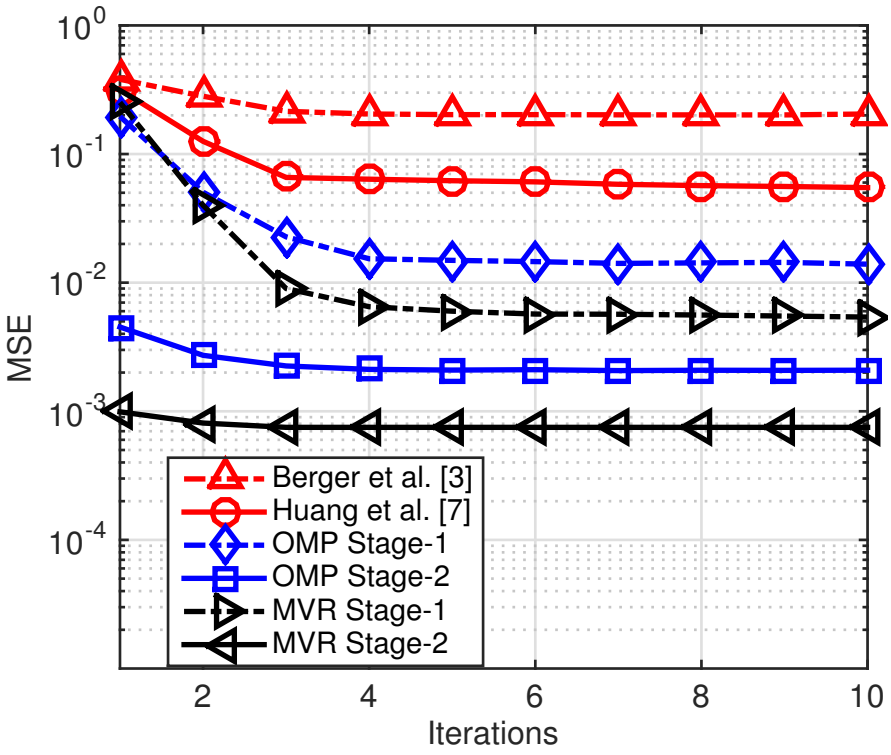

Figure 2.7: MSE versus number of iterations N_{iter} for various sparse channel recovery algorithms at SNR = 16 dB. Doppler spread $b_{\max} = 10^{-3}$.

channel recovery based algorithms and the least squares channel estimation based data detection algorithms, at all SNRs. Also, compared to the OMP based sparse channel recovery algorithm, the BER curve of the MVR based sparse channel recovery is closer to that of the genie aided data detection at the end of the stage 2.

Figure 2.9 shows the CRBs corresponding to the PID and the FID output, computed using (2.54) and (2.57), respectively. The CRB on the MSE of estimators that use only the FID output is higher than those that makes use of the output from the PID. Moreover, among the two sparse channel recovery algorithms, MVR based channel estimation achieves the CRB corresponding to PID observation at an SNR of about 30 dB, at the end of stage 2.

Figure 2.10 shows the BER performance when the Doppler scale is varied. While all the schemes perform nearly identical at zero Doppler spread, the performance gap of between the proposed scheme and other schemes widens as the Doppler scale increases,

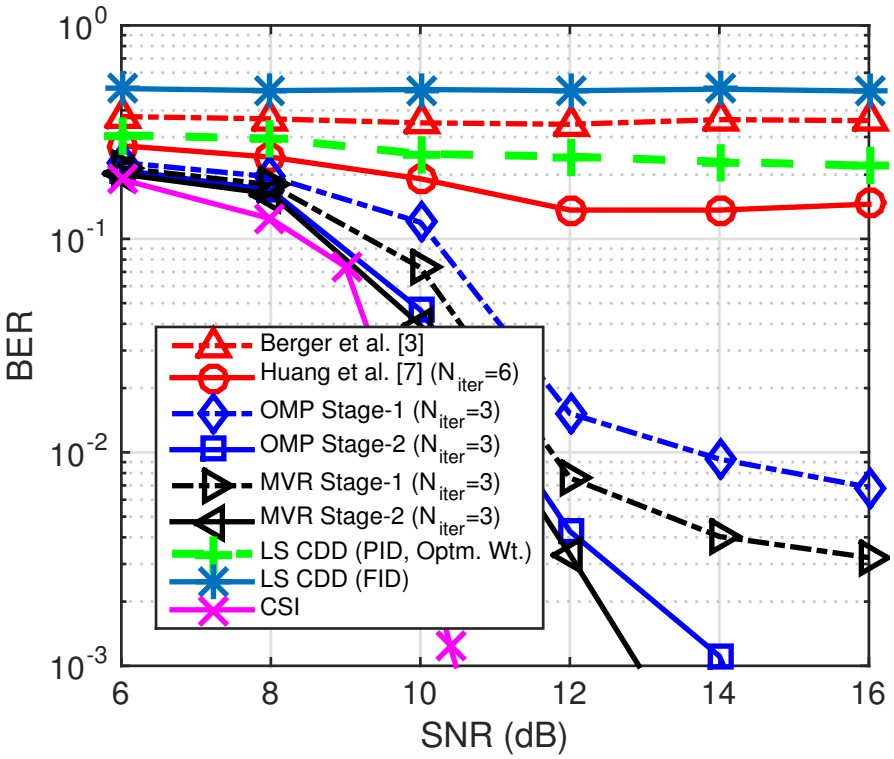

Figure 2.8: BER of various sparse channel recovery based algorithms and the genie-aided perfect CSI lower bound. Doppler spread $b_{\max} = 10^{-3}$.

highlighting the significance of PID based channel estimation in high Doppler spread scenarios.

Next, we examine the effect of pilot density on the BER performance [12, 13]. Figure 2.11 depicts the BER performance as the number of pilots used is varied while keeping the SNR constant at 12 dB and $b_{\max} = 10^{-3}$. We consider a pilot arrangement of sub-arrays of pilots, where each sub-array consists of 32 pilots at a regular spacing of 4. Also, the sub-arrays are spaced uniformly. For example, when $|S_P| = 96$, we form 3 sub-arrays each comprising of 32 pilots, and the spacing between the first elements of two consecutive sub-arrays is 128 subcarriers. We see that the gap between the proposed and existing algorithms increases dramatically with pilot density, implying that the proposed algorithm can achieve a given performance at a significantly lower pilot density.

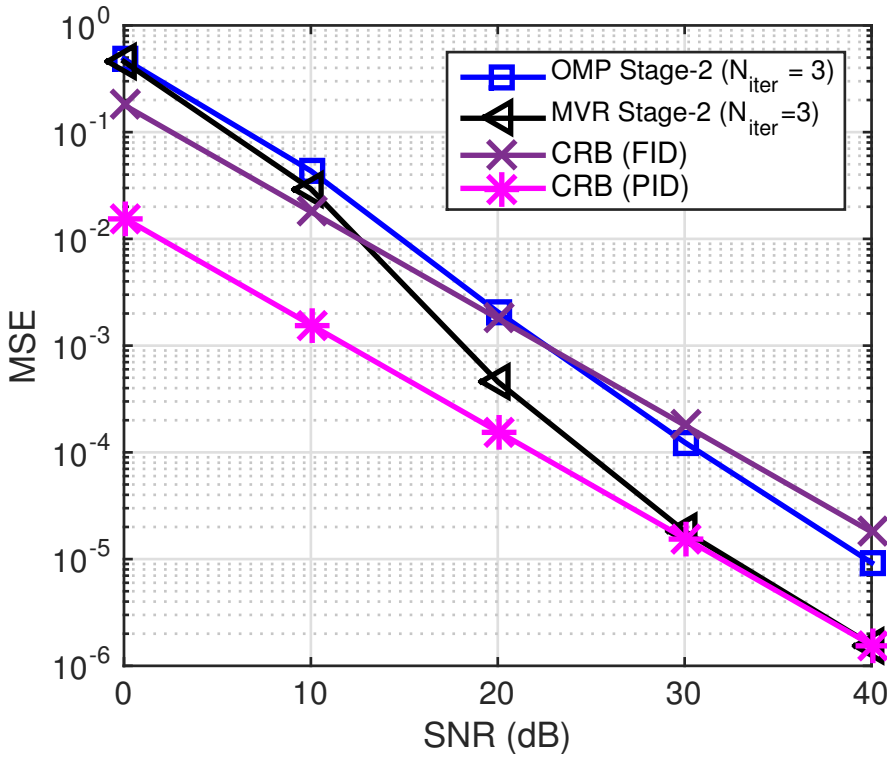

Figure 2.9: Comparison of the MSE in the channel matrix estimation of various sparse channel recovery based algorithms with the lower bound on the MSE for the FID and the PID observation models. Doppler spread $b_{\max} = 10^{-3}$.

2.5.2 Simulations using Model II

Now we examine the performance when the channel is simulated according to the model proposed in [72]. The time varying frequency response of the channel is modeled as

$$\tilde{H}(f,t) = \bar{H}_0(f) \sum_{p=1}^{N_p} h_p \tilde{\gamma}_p(f,t) e^{-j2\pi f \tau_p}, \tag{2.59}$$

where $\bar{H}_0(f)$ is the nominal frequency response of the direct path between the source and receiver that results in a frequency dependent propagation loss, h_p is the nominal channel coefficient of the p^{th} path that arrives at a nominal delay of τ_p, and the stochastic term $\tilde{\gamma}_p(f,t) = \gamma_p(f,t)e^{2\pi a_p(t) f t}$ is composed of the small-scale fading $\gamma_p(f,t)$ and the Doppler scale factor $a_p(t)$ corresponding to the p^{th} propagation path. The small-scale fading $\gamma_p(f,t)$ of the p^{th} path, arises from scattering at the rough sea surface and bottom that

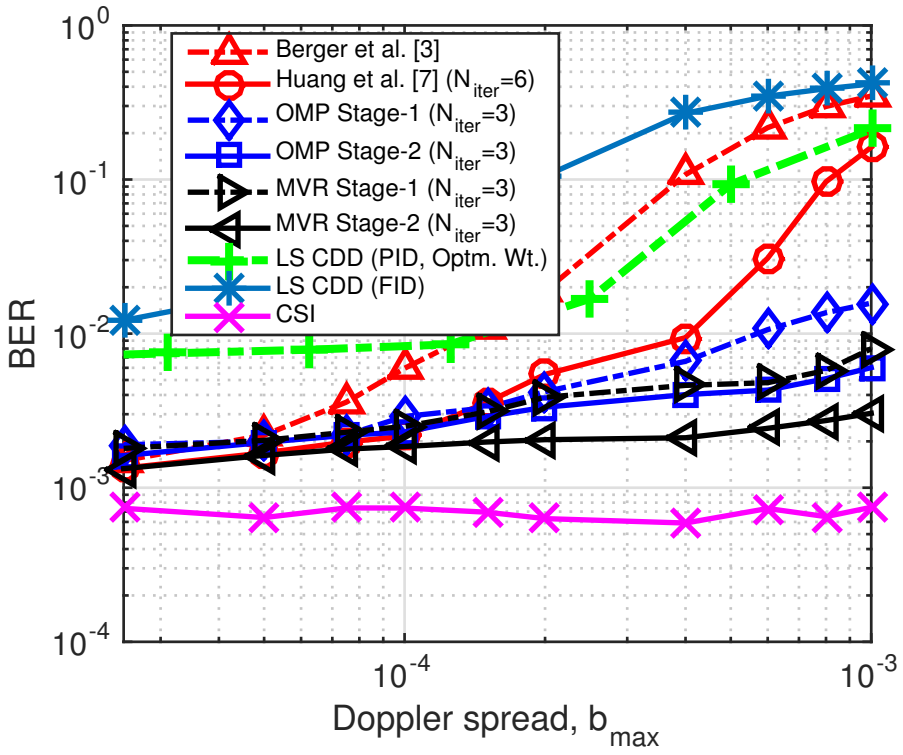

Figure 2.10: BER comparison of various channel estimation and data detection algorithms for different Doppler spreads and at SNR = 12 dB.

leads to a bunch of micro-paths whose amplitudes and delays are randomly distributed around that of the nominal ray path. The Doppler scale factor $a_p(t)$ is a composite effect of the vehicular motion, surface wave perturbations, and relative source-receiver drifts. The received signal for this channel is given by

$$\tilde{y}(t) = \int_0^T \tilde{c}(\tau, t)\tilde{x}(t-\tau)d\tau + \tilde{n}(t), \tag{2.60}$$

where $\tilde{c}(\tau, t) = \mathcal{F}_f^{-1}\{\tilde{H}(f, t)\}$ is the time-varying channel impulse response and $\mathcal{F}_f^{-1}$ is the inverse Fourier transform.

Note that the frequency dependence of the stochastic term $\tilde{\gamma}_p(f, t)$ distinguishes the channel model in (2.59) from the channel model implicit in (2.3). The model in (2.3) is widely used in the underwater communication literature for designing algorithms and benchmarking performance. In this work, additionally, we test the robustness of our

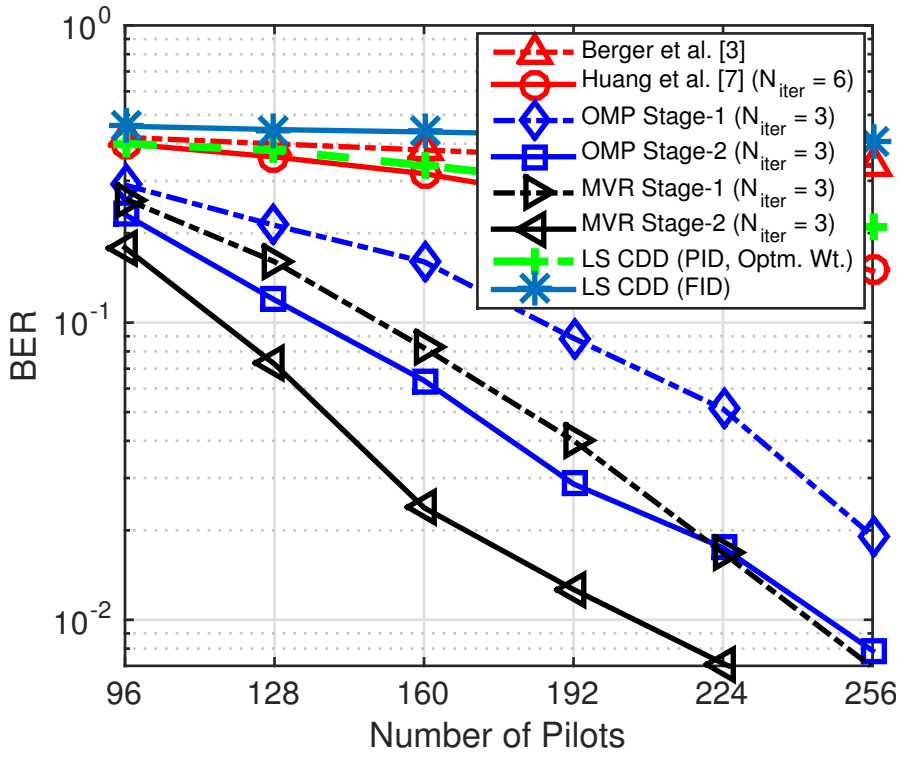

Figure 2.11: BER performance of system II with number of pilots used. SNR = 12 dB, Doppler spread $b_{\max} = 10^{-3}$.

proposed algorithm by evaluating its performance under the received signal given by (2.60) instead of (2.3).

Figure 2.12 shows a sample realization of the effective channel impulse response $\tilde{c}_r(\tau, t) = \tilde{c}(\tau, \frac{t}{1+\hat{a}})$ after resampling at the receiver. The channel is generated using the acoustic channel simulator code available in [87]. Table 2.4 shows the environmental parameters and source-receiver geometry used in this simulation. The transmitter and receiver are in a shallow water environment overlying a soft bottom. Small-scale surface variations, and relative drifts between the source and receiver, cause the channel taps to randomly fluctuate about their slowly varying mean. Specifically, the Doppler scales for this channel vary between $[-8.75 \times 10^{-4}, 10.0 \times 10^{-4}]$. Figure 2.13 shows the Doppler spectrum of the simulated channel averaged across the channel taps. A sample plot of an instantaneous channel response across frequency, obtained at subcarrier spacing, is shown in Figure 2.14. Significant variations are noticed between adjacent subcarriers for

a typical instance.

The channel *parameters* (path delays, Doppler scales, and amplitudes) vary smoothly between the successive OFDM symbols, for the acoustic channel simulator. For such channels, pilots need to be inserted only in the first OFDM block where the stage 1 runs in the pilot assisted mode followed by stage 2 that uses both pilot and data subcarrier measurements.[7] In the subsequent blocks, where no pilots are available, the algorithm switches to a decision directed mode where the pilots are now replaced with tentative estimates of data symbols. The tentative symbol estimates are formed using channel parameters found at the end of stage 2 in the previous block. An iteration of stage 1 and stage 2 tracks the channel and updates the symbols for the current block. More generally, the schemes in [35,101] exploit the channel coherence between the OFDM blocks to reduce the pilot overhead. They can be applied to improve the initial symbol estimates at the beginning of a new block in our algorithmic framework also. However, here we implement the simple approach just described.

Figure 2.15 shows the BER of the different algorithms for this channel. Pilots are employed only in the first OFDM block. While there are only about five significant ray paths in the channel impulse response, each ray path is in turn a bundle of several micro-paths. Therefore, we set the OMP based sparse channel estimator to recover a higher number of paths. We set the number of nonzero entries to be recovered to $\hat{N_p} = 46$ and use the same dictionary as before with $b_{\max} = 10^{-3}$. The proposed algorithm maintains a strong relative performance even in this difficult environment.

2.5.3 Performance on Watermark Data

WATERMARK is a recently proposed benchmark for comparing the performance of physical layer algorithms for underwater acoustic communications [70, 97, 98]. WATERMARK comes packaged with real world records of time-varying channel impulse response measurements for different environments and source-receiver geometries. The measured responses

[7] A pilot overhead of 30%, as in [14] and [34], is required for the previous channel model because the channel *parameters* were drawn independently in successive OFDM symbols.

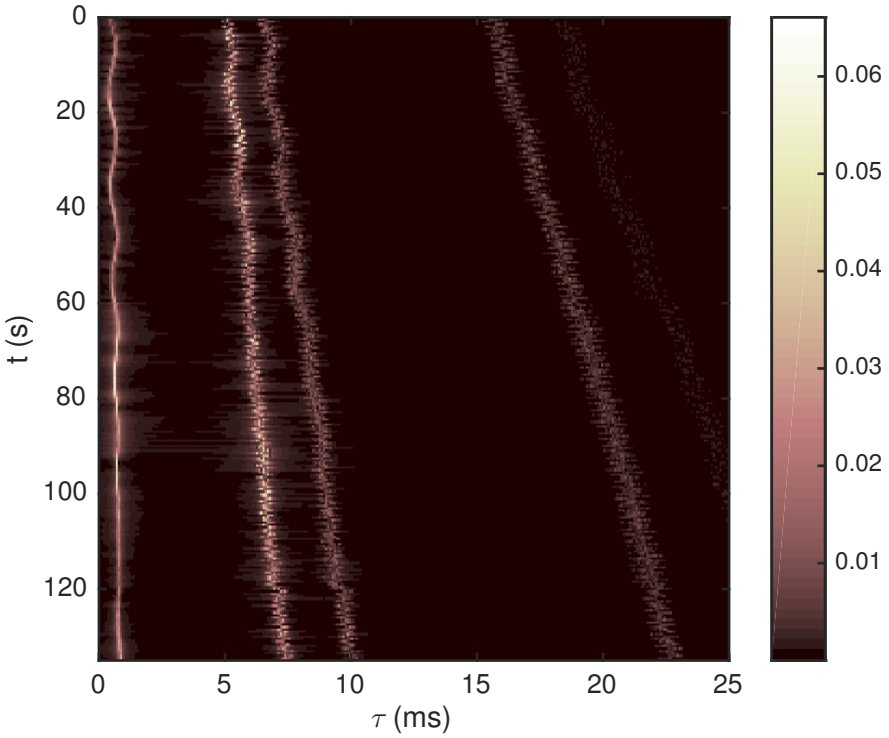

Figure 2.12: Acoustic channel impulse response based on model in [72].

include the acoustic propagation effects and the system hardware effects such as clock frequency offset. The replay facility allows for transmitting any communication waveform in the frequency band of measured responses. These features make WATERMARK a realistic and reproducible performance assessment tool.

We show the performance on two datasets, NOF1 and NCS1, corresponding to a low Doppler spread and high Doppler spread channel in the Norwegian shallow water and continental shelf, respectively (Table 2.1, [97]). The frequency band of both datasets is 10-18 kHz. Figure 2.16 shows an instantaneous channel response across frequency, obtained at subcarrier spacing, typical of the NOF1 and NCS1 channels. The Doppler spectrum of NOF1 has a sharp peak around zero frequency, with sidelobes less than -20 dB relative to the peak. On the other hand, the Doppler spectrum of NCS1 is significantly spread out within $[-15, 15]$ Hz (see Figure 3 in [98]). Doppler frequency spread of $\delta f = \pm 15$ Hz in NCS1 corresponds to a Doppler scale of $b_{\max} \approx \frac{|\delta f|}{f_c} = 1.1 \times 10^{-3}$, where $f_c = 14$ kHz is the band center frequency. While NOF1 is considered to be a benign channel, the NCS1

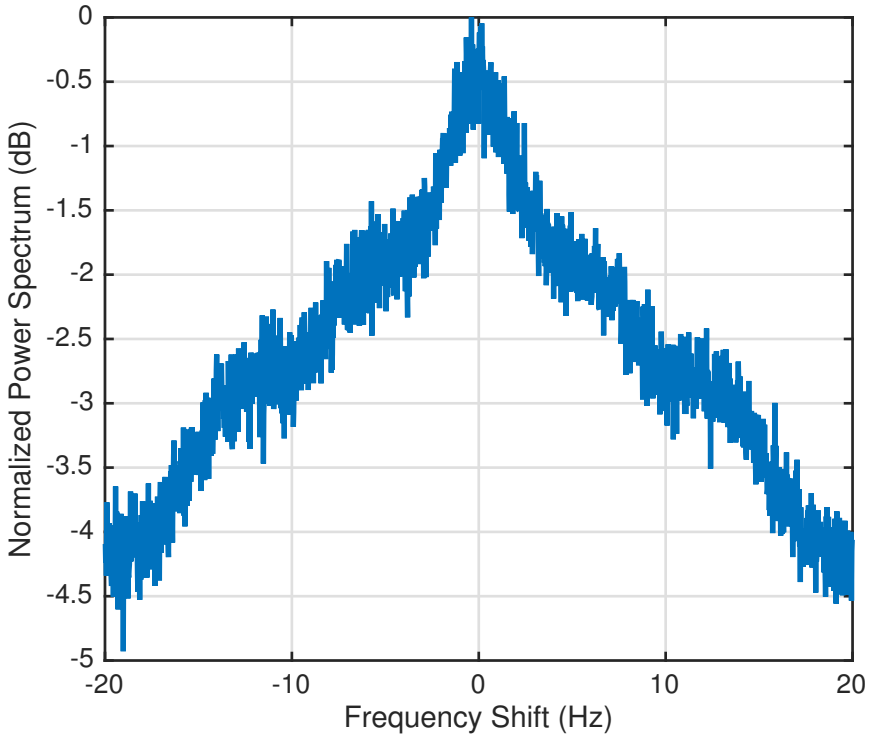

Figure 2.13: Doppler spectrum of the simulated acoustic channel.

channel is more challenging due to its smaller coherence time.

The CP-OFDM system parameters used in this study are as follows. Center frequency and bandwidth are 14 kHz and 8 kHz, respectively, to match the frequency band of measured channel responses in NOF1 and NCS1. A guard interval of 32 ms is used, considering the power delay profiles for NOF1 and NCS1, beyond which the channel response is attenuated significantly. The symbol interval for the 1024 subcarrier system is 128 ms and the subcarrier spacing is 7.8125 Hz. As with the acoustic channel simulation model, pilots are used only in the first OFDM block for training and the algorithm switches to a decision directed mode thereafter. Symbols are drawn from the QPSK constellation to enable a performance comparison with the algorithm in [7].

Figure 2.17 shows the BER performance on NOF1 channel. The algorithm `DCDD (PID)` performs differentially coherent data detection, as in [7], after combining the PID outputs. The combining weights are computed using channel estimate obtained through sparse channel recovery. The algorithms in [14], [34] and the proposed algorithm perform almost

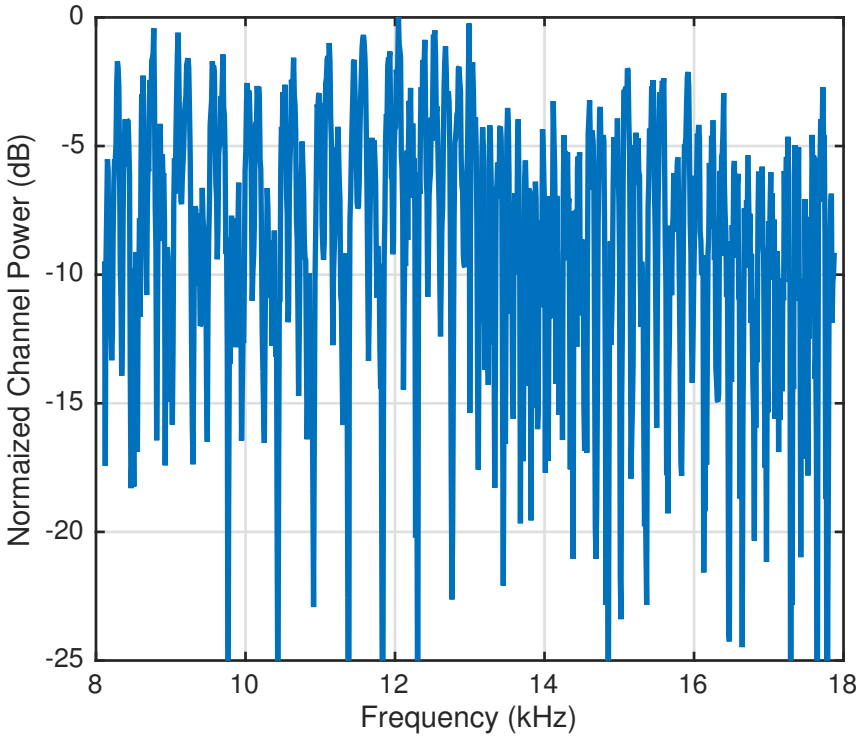

Figure 2.14: Instantaneous frequency response of the simulated channel.

equally well on this low Doppler spread channel. Figure 2.18 shows the BER performance on NCS1 channel. In this high Doppler spread channel, the proposed algorithm clearly outperforms the other algorithms.

2.6 Conclusions

In this chapter, we considered sparse channel estimation and data detection in a time-varying underwater acoustic channel for a CP-OFDM system. We used the measurements from the PID to track the time-variations within the OFDM symbol duration. We proposed a two-stage algorithm, where, in stage 1, we use the pilot-only measurements to estimate the channel and also detect the unknown data symbols. The MSE in the channel matrix estimation is reduced by iterating between the channel estimation and data detection for a fixed number of times. Thereafter, in stage 2, we use all the observations including data subcarriers to enhance the performance. We proposed a sparse channel recovery algorithm based on the minimum variance principle that bootstraps from the

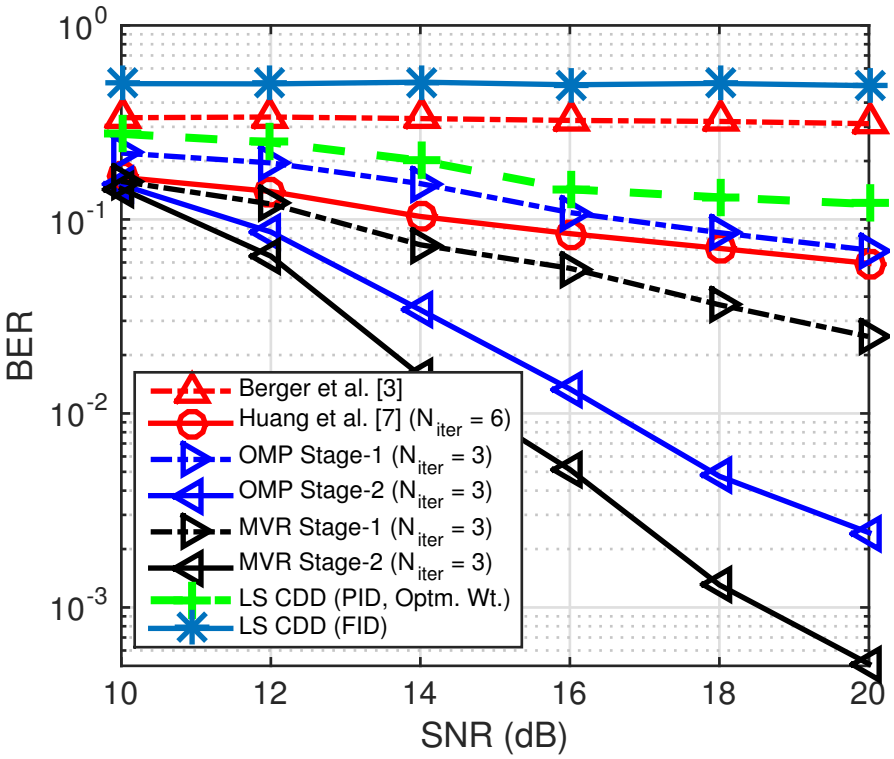

Figure 2.15: BER of various channel estimation and data detection algorithms on simulated acoustic channel.

initial estimate provided by the OMP and refines this estimate.

We showed that using the output from the PID in the stage 1 indeed provides a good initial estimate of the channel matrix in a high Doppler spread scenario and is therefore key to the improved data detection performance of the proposed algorithm. We showed that the PID provides a larger number of effective measurements than the FID, and, hence, a lower MSE in the channel matrix estimate is achievable when using measurements from the PID. Our simulation results confirmed that the proposed two-stage algorithm significantly reduces the BER in time-varying channels. For sparse signal recovery, we considered the OMP and MVR algorithm. MVR provided better estimates of the channel than OMP. MVR exhibits a performance similar to SBL in just one pass through the algorithm, while the latter takes several iterations to converge. Results for the experimental channel data in WATERMARK reaffirm the strong performance of the proposed scheme in harsh channel conditions. In this work, we considered a grid based recovery of the Doppler and delay

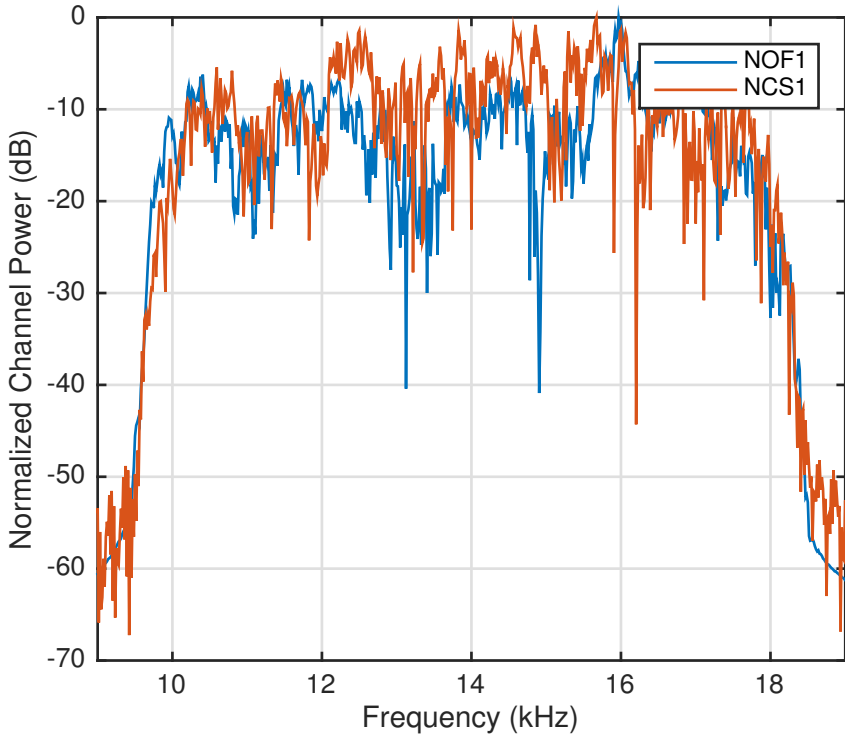

Figure 2.16: Instantaneous frequency response typical of the WATERMARK channels NOF1 and NCS1.

parameters; future work can consider gridless compressed sensing recovery methods and their performance. Extending the proposed approach to the case where the receiver is equipped with an array of hydrophones is also an interesting direction for future work.

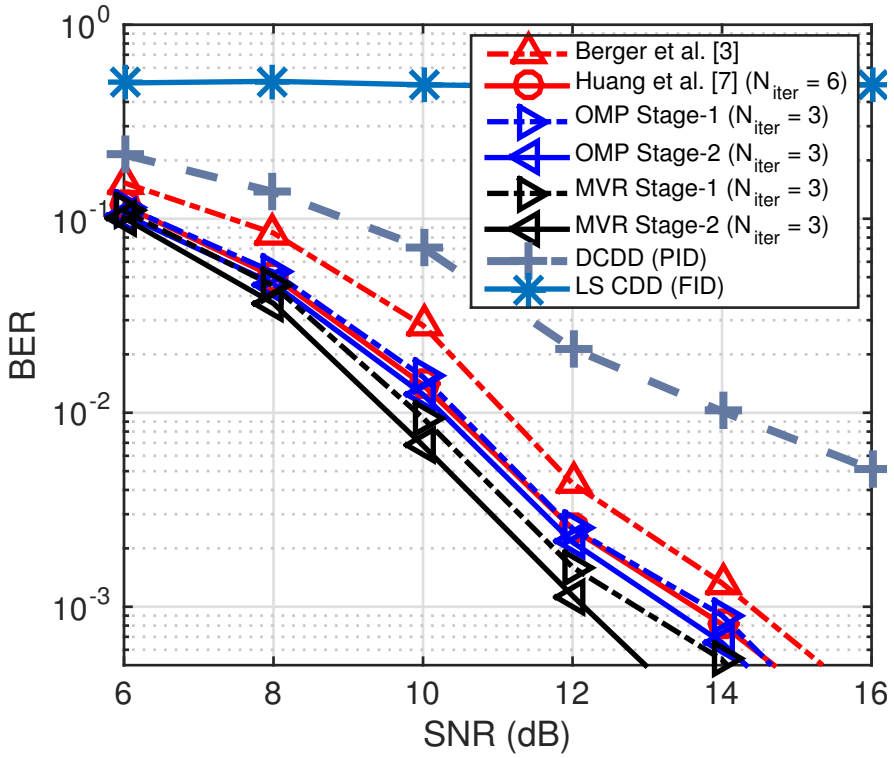

Figure 2.17: BER comparison of various channel estimation and data detection algorithms in the low Doppler spread WATERMARK channel NOF1.

Table 2.4: Underwater Channel Simulation Parameters.

Ocean depth (m)	100
Transmitter depth (m)	90
Receiver depth (m)	50
Channel distance (m)	1000
Spreading factor	1.7
Sound speed in water, c_w (m/s)	1500
Sound speed in bottom, c_b (m/s)	1200
Surface variance, σ_s^2 (m^2)	1.125
Bottom variance, σ_b^2 (m^2)	0.5
3 dB width of the PSD of intra-path delays, $B_{\delta,p}$ (Hz)	0.05
Number of intra-paths, S_p	20
Mean of intra-path amplitudes, μ_p	0.3
Variance of intra-path amplitudes, ν_p	10^{-4}
Transmitter drifting speed, v_{td} (m/s)	0.3
Transmitter drifting angle, θ_{td} (rad)	$\mathcal{U}(0, 2\pi)$
Receiver drifting speed, v_{rd} (m/s)	0.1
Receiver drifting angle, θ_{rd} (rad)	$\mathcal{U}(0, 2\pi)$
Transmitter vehicular speed, v_{tv} (m/s)	$\mathcal{N}(0, 1)$
Transmitter vehicular angle, θ_{tv} (rad)	$\mathcal{U}(0, 2\pi)$
Receiver vehicular speed, v_{rv} (m/s)	-3
Receiver vehicular angle, θ_{rv} (rad)	$\mathcal{U}(0, 2\pi)$
Surface variation amplitude, A_w (m)	0.9
Surface variation frequency, f_w (mHz)	0.6

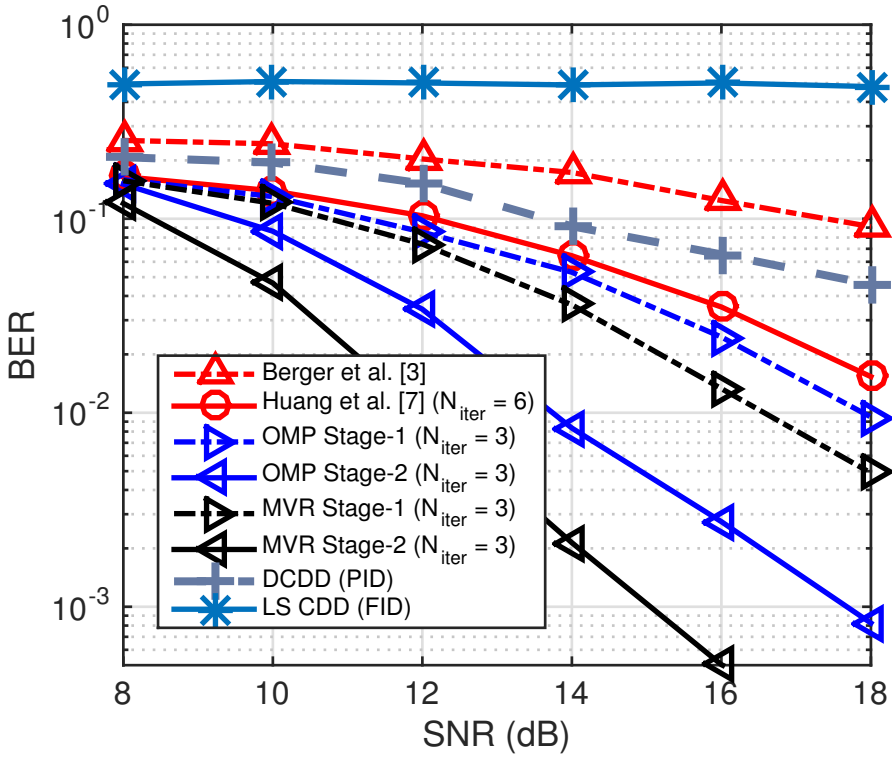

Figure 2.18: BER comparison of various channel estimation and data detection algorithms in the high Doppler spread ($b_{\max} \approx 10^{-3}$) WATERMARK channel NCS1.

Chapter 3

Variational Data Detection in Sweep Spread Carrier Communications

Sweep spread carrier (S2C) based underwater acoustic (UWA) communications is a practically attractive but less explored modulation scheme in the published literature. In this chapter, we present a rigorous treatment of the S2C communication receiver design and propose a data detection scheme that can handle challenging UWA channels. State-of-the-art S2C receivers based on the gradient heterodyne processing are only effective when the path delay and Doppler spread are moderate. We develop a new variational soft symbol decoding (VSSD) algorithm based on the principle of variational Bayes' inference for a general linear channel model. In channels with moderate delay and Doppler spreads, we show that the VSSD algorithm is equivalent to the existing gradient heterodyne receivers for S2C communications. We apply the VSSD algorithm to the i.i.d. Gaussian multiple-input multiple-output channel and show, through numerical simulations, that it far outperforms the minimum mean squared error (MMSE) data detection. We illustrate the dramatic improvement in the performance of the VSSD based S2C receiver in two different models of simulated UWA channels and two contrasting measured UWA environments publicly available in the WATERMARK channel dataset. The proposed VSSD algorithm recovers data symbols at a signal-to-noise ratio (SNR) which is at least 10 dB (8 dB) lower than the MMSE decoder for uncoded (rate 2/3 LDPC coded) communications

over UWA channels where the existing receivers either fail completely or must compromise on the data rate to maintain the bit error rate (BER) performance.

3.1 Introduction

Undersea exploration and monitoring presents vast opportunities and challenges alike – but a major hurdle to such missions arises from the difficulties in communicating underwater over long distances. Severe attenuation in the marine medium limits the range of electromagnetic, optical and magnetic induction based communications to just a few meters, leaving acoustic communications as the *de facto* means for wireless data transfer across tens of kilometers [17, 54, 55]. All the same, underwater acoustic (UWA) channels are by far the most difficult media for communication. They present a serious bottleneck in marine data networks due to limited data rate and large power demand. In particular, the data rates are limited by large delay spreads and path-dependent Doppler shifts. Multipath propagation of sound results in a delay spread in the order of tens of milliseconds [90] and time variations cause path-dependent Doppler shifts that are non-uniform over the bandwidth of the acoustic signal. Also, the communication nodes in an underwater sensor network are usually battery operated, and are therefore highly constrained on the amount of transmission power. High performance receivers, that recover data symbols at a low signal-to-noise ratio, are highly desirable in these applications.

Sweep spread carrier (S2C) communications [44] is inspired by the chirp, whistle and song type signaling used by dolphins and whales to communicate over long distances [1]. It uses linear frequency modulated (LFM) waveforms as carriers of digital data. The S2C transmission waveform, modulated by unimodular signal constellations such as quadrature phase shift keying (QPSK), has an ideal peak-to-average power ratio (PAPR). The technique is therefore battery friendly and implemented in a wide range of full-duplex commercial acoustic modems that are used in underwater sensor networks comprising autonomous underwater vehicles (AUVs), autonomous surface vehicles (ASVs), and moored underwater sensor nodes [2, 18, 79, 85]. Secure, reliable and covert communications, with a low probability of intercept, is rendered possible due to use of high bandwidth coded chirp

carriers whose exact pattern is known only to the transmitter and designated receiver. The details of the S2C transmitter and receiver side processing, performance analysis, and experimental results can be found in [45–49]. Despite its practical merits, success with real world deployment, and commercialization, relatively few published works such as [60] have explored and developed S2C communication further. In this chapter, we present a rigorous treatment of the S2C design principles, and propose an improved S2C receiver that can handle challenging UWA channels.

The S2C receiver in [44] extracts only the copy of a symbol arriving along the direct path. As a consequence, the part of the transmitted symbol energy arriving along paths other than the direct path is ignored. In [60], the authors use a maximum ratio combiner (MRC), which improves the performance of an S2C receiver by leveraging multipath diversity. The receiver in [60] performs well only when: (a) the ratio of the maximum delay spread to minimum differential delay among path arrivals is below a certain value, and (b) the Doppler spread is small. If either condition is violated, the intersymbol interference (ISI) cancellation becomes imperfect and MRC becomes suboptimal and ineffective.

The authors in [44] and [60] did not consider the effect of Doppler. Doppler due to relative motion between the source and receiver manifests as dilation/compression of the transmitted waveform. The effect of Doppler in underwater acoustic communications cannot be modeled as a frequency shift unless the waveform has a small time-bandwidth product. For large time-bandwidth product waveforms, typical of S2C communications, even for small relative speeds (comparable to $c/2\gamma$, where c is the speed of sound in water and γ is the time-bandwidth product of the transmitted signal), the underwater channel is best modeled as a wideband delay-scale channel [25, 38, 39]. In this chapter, we consider an S2C communication system similar to [44] and [60] but for the more general underwater channel model that includes the time-scaling effect of Doppler on the transmitted waveform.

Previous studies on UWA communications have considered the MMSE equalizer for (hard) data symbol detection or joint channel estimation and data detection in orthogonal frequency division multiplex (OFDM) and code division multiple access (CDMA)

based communications [14,34,88,102,110]. However, in coded communications, it is more important to estimate the soft symbols rather than perform hard symbol decision [26]. The variational Bayes' (VB) inference is a promising approach to obtain soft symbol estimates because, by design, it directly infers the posterior distributions of the transmitted data symbols. However, to the best of our knowledge, other than our initial work in the area [5, 94, 95], VB based soft symbol estimation has not been explored in the literature.

In this chapter, we present a new mathematical framework for S2C communications. Based on this, we develop a new decoder that uses the principle of variational Bayes' inference to determine the soft symbol estimates in harsh UWA channel environments. Our specific contributions are:

1. We present a mathematical framework for S2C data detection in doubly-spread UWA channels.

2. We show that the S2C receivers in [44] and [60] closely approximate the minimum mean squared error (MMSE) decoder for the AWGN channel and moderately delay spread UWA channels with well resolved path delays.

3. Previous works considered benign channels, but in practice the channel is rarely benign. We theoretically analyze the limitations of the existing S2C receivers in highly spread UWA channels and elicit the need to consider better receivers such as the MMSE receiver designed for the system model in this chapter.

4. In coded communications, it is required to obtain good soft-symbol estimates, which the previous S2C receivers do not consider. Using the VB inference approach, we derive a new iterative log-likelihood ratio (LLR) based soft symbol decoding receiver.

5. We show that the fixed point iterations for LLR based soft symbol decoding converge to a local optimum in the general case, and to a global optimum for orthogonal channel matrices whose important special cases are the AWGN and Rayleigh channels. Specifically, in AWGN and Rayleigh channels, we show that the proposed variational soft symbol decoder (VSSD) is a maximum-likelihood (ML) decoder and converges in a single iteration.

6. Through extensive numerical studies, we demonstrate the strong performance of the VSSD in harsh simulated channels where existing S2C receivers fail completely. For the WATERMARK channel dataset, we develop a suitable baseband measurement model for the S2C system and present the superior performance of the proposed decoder in two contrasting real world channels.

3.2 System Model

Consider an S2C system as in [44] and [60]. At the transmitter side, the carrier waveform is a succession of linear frequency modulated chirp pulses, each swept from a lower frequency limit f_L to an upper frequency limit f_H over a sweep duration T_{sw}, given by:

$$c(t) = e^{j\phi(t)},\ 0 \le t \le T_c, \tag{3.1}$$

where

$$\phi(t) \triangleq 2\pi \left(f_L t_r(t) + m_c t_r^2(t) \right) \tag{3.2}$$

is the time varying phase of the carrier waveform, with $t_r(t) = t - \left\lfloor \frac{t}{T_{\text{sw}}} \right\rfloor T_{\text{sw}}$ being the periodic ramp function having period T_{sw}, $2m_c = \frac{f_H - f_L}{T_{\text{sw}}}$ is the chirp rate, $T_c = N_c T_{\text{sw}}$ is the total carrier duration, and N_c is the number of chirp pulses comprising the carrier waveform.

The message signal containing pilot and data symbols is:

$$s(t) = \sum_{k=0}^{N-1} s_k g(t - kT), \tag{3.3}$$

where $s_k, k = 0, \ldots, N-1$, are a sequence of symbols drawn from a constant-modulus constellation such as quadrature phase shift keying (QPSK), T is the symbol duration, $N = \frac{T_c}{T}$ is the number of symbols in the data packet and $g(t)$ is a pulse shaping function, for example, a root-raised-cosine pulse with roll-off factor α. We denote the symbol bandwidth by B, which is given by $B \approx \frac{1+\alpha}{T}$. For a symbol interval T ($< T_{\text{sw}}$), we can

mount up to $M = \lfloor T_{\rm sw}/T \rfloor$ symbols within a chirp pulse. Note that there are $N = MN_c$ symbols in a data packet. For simplicity, we assume that $T_{\rm sw}/T$ is an integer.

The modulated transmit signal is given by

$$x(t) = \mathrm{Re}\left[s(t)c(t)\right], \tag{3.4}$$

which is prefixed with a preamble pulse and appended with a post-amble pulse to form a transmission frame. The preamble and post-amble are used for timing and synchronization, and for estimating the channel. A guard interval of T_g is used after (before) the preamble (post-amble) pulse to facilitate channel estimation. Using $N_c > 1$ helps in amortizing the overhead due to the guard interval over the total carrier duration of T_c.

The time-varying impulse response of the UWA channel is modeled as [51]:

$$h(t,\tau) = \sum_{p=0}^{N_{\rm P}-1} h_p(t)\delta\left(\tau - \tau_p(t)\right), \tag{3.5}$$

where $h_p(t)$ and $\tau_p(t)$ are the time-varying amplitude and delay, respectively, of the pth path, and $N_{\rm P}$ is the number of significant paths in the channel. The delay-scale model in (3.5) capture the effects of multipath propagation (i.e., reflection, scattering, and refraction) and the time variation of the propagation delays due to source-receiver motion, scattering by fluctuating ocean surfaces, and internal gravity waves such as interfacial waves and solitons within the fluid medium. As in [14, 34, 88, 110], we assume that the path amplitudes are constant within a data packet, that is, $h_p(t) = h_p$, and that the time variation of the path delays due to Doppler rate a_p can be approximated as

$$\tau_p(t) = \tau_p - a_p t. \tag{3.6}$$

After coarse Doppler scale compensation and synchronization, the received signal is given by

$$y(t) = \sum_{p=0}^{N_{\rm P}-1} y_p(t) + w(t), \tag{3.7}$$

where $w(t)$ is the additive white Gaussian noise (AWGN), $y_p(t) = h_p \mathrm{Re}\{s(\tilde{t} - \tau_p(\tilde{t}))c(\tilde{t} - \tau_p(\tilde{t}))\}$ is the Doppler compensated and timing adjusted version of the S2C signal reaching via the pth path, $\tilde{t} = \frac{t+\hat{\tau}}{1+\hat{a}}$ is the rescaled and shifted time-axis, $\hat{a}$ is the coarse Doppler scale estimated using the preamble and post-amble as in [51], and $\hat{\tau}$ is the starting time instance of the first (data) chirp pulse estimated from the preamble/post-amble as in [44] but after resampling. Using (3.6), we can write,

$$y_p(t) = h_p \sum_{k=0}^{N-1} \left(s_{k,\mathrm{Re}} \cos \phi_p(t) - s_{k,\mathrm{Im}} \sin \phi_p(t) \right) g_{p,k}(t), \tag{3.8}$$

where $g_{p,k}(t) \triangleq g\left(\overline{1+b_p}t - \tilde{\tau}_p - kT\right)$, with $b_p = \frac{a_p - \hat{a}}{1+\hat{a}}$ and $\tilde{\tau}_p = \tau_p - (1+b_p)\hat{\tau}$ being the residual Doppler scale and delay of the pth path after compensation, respectively, $s_{k,\mathrm{Re}}$ ($s_{k,\mathrm{Im}}$) is the real (imaginary) part of the symbol s_k, and $\phi_p(t) = \phi(\overline{1+b_p}t - \tilde{\tau}_p)$ is the time-scaled and delayed version of the carrier phase in (3.2).

Upon sampling at a rate F_s ($= 1/T_s$, where T_s is the sampling period), we may re-express the received signal in (3.7) in a vector form relevant to data detection, as:

$$\mathbf{y} = \mathbf{H}\mathbf{s} + \mathbf{w}, \tag{3.9}$$

where

$$\begin{aligned}
\mathbf{H} &= [\mathbf{C}_0\mathbf{h}, -\mathbf{S}_0\mathbf{h}, \ldots, \mathbf{C}_{N-1}\mathbf{h}, -\mathbf{S}_{N-1}\mathbf{h}] \in \mathbb{R}^{NL \times 2N}, \\
\mathbf{h} &= [h_0, h_1, \ldots, h_{N_\mathrm{P}-1}]^T \in \mathbb{R}^{N_\mathrm{P} \times 1}, \\
\mathbf{s} &= [s_{0,\mathrm{Re}}, s_{0,\mathrm{Im}}, \ldots, s_{N-1,\mathrm{Re}}, s_{N-1,\mathrm{Im}}]^T \in \mathbb{R}^{2N \times 1}, \\
\mathbf{w} &\sim \mathcal{N}\left(\mathbf{0}, \sigma^2 \mathbf{I}_{2N}\right),
\end{aligned}$$

$L = \lfloor F_s T \rfloor$ is the number of samples in the symbol duration, $\mathbf{C}_k \in \mathbb{R}^{NL \times N_\mathrm{P}}$ and $\mathbf{S}_k \in \mathbb{R}^{NL \times N_\mathrm{P}}$ are matrices whose entries are given by $C_k(l,p) = \cos \phi_p(lT_s)\, g_{p,k}(lT_s)$ and $S_k(l,p) = \sin \phi_p(lT_s)\, g_{p,k}(lT_s)$, respectively, for $0 \le k \le N-1$, $0 \le l \le NL-1$ and $0 \le p \le N_\mathrm{P} - 1$, and $\mathbf{I}_{2N}$ denotes the $2N \times 2N$ identity matrix. Since $g(t) = 0, t \notin [0,T]$, entries of $\mathbf{C}_k(:,p) \in \mathbb{R}^{NL \times 1}$ and $\mathbf{S}_k(:,p) \in \mathbb{R}^{NL \times 1}$ are zeros except for

$l \in \left\{ \left\lceil \frac{\tilde{\tau}_p + kT}{1+b_p T_s} \right\rceil, \ldots, \left\lfloor \frac{\tilde{\tau}_p + \overline{k+1}T}{1+b_p T_s} \right\rfloor \right\}$.

We now address the problem of data detection for the S2C communication model. First, we examine the two existing S2C receivers in the literature – the gradient heterodyne (GradH) receiver, pioneered in [44], and the path-based gradient heterodyne (pGradH) receiver proposed in [60].

3.3 Existing S2C Receivers: GradH and pGradH

We show that the GradH and pGradH based S2C receivers are minimum mean square error (MMSE) symbol detectors for the AWGN channel and a delay spread channel with well resolved path delays, respectively. We then introduce the reduced data measurement model, at the output of the GradH and pGradH preprocessors, that will be used in this work.

3.3.1 Optimality of GradH Receiver

Consider the received signal for the AWGN channel ($N_{\mathrm{P}} = 1, \tilde{\tau}_0 = 0, b_0 = 0, h_0 = 1$), given by

$$y(t) = \sum_{k=0}^{N-1} (s_{k,\mathrm{Re}} \cos\phi(t) - s_{k,\mathrm{Im}} \sin\phi(t)) g\left(t - kT\right) + w(t).$$

Upon sampling, the received signal is as in (3.7) with the channel matrix taking the block-diagonal form $\mathbf{H} = \mathbf{Q} = \mathrm{diag}\{\mathbf{Q}_0, \mathbf{Q}_1, \ldots, \mathbf{Q}_{N-1}\} \in \mathbb{R}^{NL \times 2N}$, where,

$$\mathbf{Q}_k = \mathrm{diag}\left(\mathbf{g}\right) \begin{bmatrix} \cos\phi^{(k)}[0] & \sin\phi^{(k)}[0] \\ \cos\phi^{(k)}[1] & \sin\phi^{(k)}[1] \\ \vdots & \vdots \\ \cos\phi^{(k)}[L-1] & \sin\phi^{(k)}[L-1] \end{bmatrix} \in \mathbb{R}^{L \times 2},$$

$\mathbf{g} = \left[g(0), g(T_s), \ldots, g\left(\overline{L-1}T_s\right)\right]^T \in \mathbb{R}^L$, and $\phi^{(k)}[l] = \phi\left((\tilde{k}-1)T + lT_s\right)$, $\tilde{k} = k - \lfloor \frac{k}{M} \rfloor M$, $l = 0, \ldots, L-1$, $k = 0, 1, \ldots, N-1$. In this case, there is no inter-symbol

interference (ISI), and the measurement corresponding to the kth symbol is given by

$$\mathbf{y}_k = \mathbf{Q}_k \mathbf{s}_k + \mathbf{w}_k, \tag{3.10}$$

where, for $k = 0, \ldots, N-1$,

$$\begin{aligned}
\mathbf{y}_k &= [\, y[(k-1)L], y[(k-1)L+1], \ldots, y[kL-1] \,]^T, \\
\mathbf{s}_k &= \left[s_{k,\mathrm{Re}}, s_{k,\mathrm{Im}} \right]^T \in \left\{ \left[\pm 1/\sqrt{2}, \pm 1/\sqrt{2} \right]^T \right\}, \\
\mathbf{w}_k &= \left[w_k[0], \ldots, w_k[L-1] \right]^T \sim \mathcal{N}\left(\mathbf{0}, \sigma^2 \mathbf{I}_L \right).
\end{aligned}$$

For equiprobable symbols $\mathbf{s}_k$, the MAP solution to (3.10) is the same as the ML estimator, and is given by

$$\hat{\mathbf{s}}_k^{(\mathrm{ML})} = \underset{\mathbf{s}_k \in \left\{ \left[\pm 1/\sqrt{2}, \pm 1/\sqrt{2} \right]^T \right\}}{\arg\min} \| \mathbf{y}_k - Q_k \mathbf{s}_k \|_2, \tag{3.11}$$

and the MMSE solution to (3.10) is given by

$$\hat{\mathbf{s}}_k^{(\mathrm{MMSE})} = \mathcal{S} \left[\left(\mathbf{Q}_k^T \mathbf{Q}_k + \sigma^2 \mathbf{I}_2 \right)^{-1} \mathbf{Q}_k^T \mathbf{y}_k \right], \tag{3.12}$$

where $\mathcal{S}[\cdot]$ is the slicing operation that quantizes each entry of its argument vector to the nearest symbol in the QPSK constellation.

Suppose the symbol time T (and hence L) is sufficiently large and the pulse shaping function, $g(t)$, is smooth, so that the following holds for all $0 \le k \le N-1$:

$$\sum_{l=0}^{L-1} g^2(lT_s) \cos^2\left(\phi^{(k)}[l] \right) \approx \sum_{l=0}^{L-1} g^2(lT_s) \sin^2\left(\phi^{(k)}[l] \right) \approx \beta,$$

and

$$\frac{1}{\beta} \sum_{l=0}^{L-1} g^2(lT_s) \cos\left(\phi^{(k)}[l] \right) \sin\left(\phi^{(k)}[l] \right) \approx 0,$$

where $\beta \triangleq \frac{1}{2} \sum_{l=0}^{L-1} g^2(lT_s)$. Then, we have $\mathbf{Q}_k^T \mathbf{Q}_k \approx \beta \mathbf{I}_2$. To observe the goodness of this

approximation, consider the S2C system in Table I, $L = 50$ raw samples per symbol, and a root-raised cosine pulse shaping function $g(t)$ with a roll-off $\alpha = 0.25$ and truncated to the symbol span. The diagonal entries of $\mathbf{Q}_k^T\mathbf{Q}_k$ differ by at most 0.09 dB, since

$$\max_k \frac{1}{\beta}\left|\sum_{l=0}^{L-1} g^2(lT_s)\cos\left(2\phi^{(k)}[l]\right)\right| < 0.02,$$

and the off-diagonal entries are at least -20 dB down compared to diagonal entires, since

$$\max_k \frac{1}{\beta}\left|\sum_{l=0}^{L-1} g^2(lT_s)\cos\left(\phi^{(k)}[l]\right)\sin\left(\phi^{(k)}[l]\right)\right| < 0.01.$$

Under these conditions, the MMSE receiver in (3.12) simplifies to the symbol-by-symbol decoder:

$$\hat{\mathbf{s}}_k^{(\text{GradH})} = \mathcal{S}\left[\mathbf{z}_k\right], \tag{3.13}$$

where $\mathbf{z}_k = \mathbf{Q}_k^T\mathbf{y}_k$. Note that $\mathbf{Q}_k$ can be viewed as a lowpass filter, and there is a decimation by a factor of L in going from $\mathbf{y}_k$ to $\mathbf{z}_k$. From (3.10), we see that $\mathbf{z}_k \approx \beta\mathbf{s}_k + \mathbf{v}_k$, where $\mathbf{v}_k = \mathbf{Q}_k^T\mathbf{w}_k \sim \mathcal{N}(\mathbf{0}, \beta\sigma^2\mathbf{I}_2)$, is affected only by the kth symbol. Also, $\mathbf{z}_k$ is a sub-vector of $\mathbf{z} = \mathbf{Q}^T\mathbf{y} \in \mathbb{R}^{2N\times 1}$, whose entries are precisely the sampled versions of the lowpass filtered in-phase and quadrature outputs of gradient heterodyne operation, as in [44], on the received signal. Therefore, the GradH receiver in [44] realizes a near MMSE decoder for S2C communication over an AWGN channel.

While the GradH receiver in (3.13) is an MMSE symbol detector for the AWGN channel, the receiver works reasonably well even for ISI channels with *moderate* delay spreads, as elaborated in [44]. It is shown in [60] that the GradH receiver recovers the symbol arriving along the *direct path* when

$$\frac{\mathcal{M}}{\mathcal{M}-1}\delta\tau_{\max} \le T_{sw} \le \mathcal{M}\delta\tau_{\min}, \tag{3.14}$$

where $\delta\tau_{\min} = \min_{0\le i<j\le N_\text{P}-1}|\tau_i - \tau_j|$ and $\delta\tau_{\max} = \max_{0\le i,j\le N_\text{P}-1}|\tau_i - \tau_j|$ are the smallest and largest separation between any two path arrival times τ_i and τ_j, and $\mathcal{M} \triangleq \frac{f_H - f_L}{B}$ is

called the spreading factor.

3.3.2 Optimality of pGradH Receiver

The pGradH receiver in [60] combines the symbol arriving along paths other than the direct path to leverage multipath diversity in addition to the gradient heterodyne and lowpass filtering operation. Here, we show that pGradH is a near MMSE decoder when the path delays are well resolved and condition (3.14) holds.

For a given channel $\mathbf{H}$, the MMSE receiver is given by

$$\hat{\mathbf{s}}^{(\mathrm{MMSE})} = \mathcal{S}\left[\left(\mathbf{H}^T\mathbf{H} + \sigma^2\mathbf{I}_{2N}\right)^{-1}\mathbf{H}^T\mathbf{y}\right]. \tag{3.15}$$

When condition (3.14) holds, $\mathbf{C}_i^T\mathbf{C}_j \approx \kappa_C\mathbf{I}_{N_\mathrm{P}}\delta_{i,j}$, where $\kappa_C = \mathbf{C}_i(:,p)^T\mathbf{C}_i(:,p)$ is nearly the same for all $0 \le i \le N-1$ and $0 \le p \le N_\mathrm{P}-1$, and $\delta_{i,j}$ is the Kronecker delta function. Similarly, $\mathbf{S}_i^T\mathbf{S}_j \approx \kappa_S\mathbf{I}_{N_\mathrm{P}}\delta_{i,j}$, where $\kappa_S = \mathbf{S}_i(:,p)^T\mathbf{S}_i(:,p)$, and $\mathbf{C}_i^T\mathbf{S}_j \approx 0$. Under these approximations, the MMSE receiver in (3.15) simplifies to the pGradH receiver in [60],

$$\hat{\mathbf{s}}_k^{(\mathrm{pGradH})} = \mathcal{S}\left[\sum_{p=0}^{N_\mathrm{P}-1}\frac{h_p}{|h_p|^2}\mathbf{z}_k^{(p)}\right], \tag{3.16}$$

where

$$\mathbf{z}_k^{(p)} = \mathbf{Q}_k^{(p)T}\mathbf{y}_k, \tag{3.17}$$

$$\mathbf{Q}_k^{(p)} = \mathrm{diag}\left(\mathbf{g}^{(p)}\right)\begin{bmatrix}\cos\phi_p^{(k)}[0] & \sin\phi_p^{(k)}[0]\\ \cos\phi_p^{(k)}[1] & \sin\phi_p^{(k)}[1]\\ \vdots & \vdots\\ \cos\phi_p^{(k)}[L-1] & \sin\phi_p^{(k)}[L-1]\end{bmatrix},$$

$\mathbf{g}^{(p)} \in \mathbb{R}^L$ has entries that are samples of the compressed/dilated and delayed pulse shaping function, $g_l^{(p)} = g\left(\overline{1+b_p}lT_s - \tilde{\tau}_p\right)$, $\phi_p^{(k)}[l] = \phi_p\left((\tilde{k}-1)T + lT_s\right)$, $\tilde{k} = k - \lfloor\frac{k}{M}\rfloor M$, $l = 0,\ldots,L-1$, $p = 0,\ldots,N_\mathrm{P}-1$, and $k = 0,1,\ldots,N-1$. Stacking up $\mathbf{z}_k^{(p)}, k =$

$0, 1, \ldots, N-1$, into a vector, we get

$$\mathbf{z}^{(p)} = \mathbf{Q}^{(p)T}\mathbf{y} \in \mathbb{R}^{2N\times 1}, \tag{3.18}$$

where $\mathbf{Q}^{(p)} = \text{diag}\{\mathbf{Q}_0^{(p)}, \mathbf{Q}_1^{(p)}, \ldots, \mathbf{Q}_{N-1}^{(p)}\} \in \mathbb{R}^{NL\times 2N}$. The entries of $\mathbf{z}^{(p)}$ are sampled versions of the lowpass filtered in-phase and quadrature outputs of *path-matched* gradient heterodyne operation, as in [60], on the received signal.

3.3.3 Reduced Data Measurement Model

We now present the data model for measurements, at *symbol rate*, at the output of the GradH and pGradH preprocessors. Henceforth, we use this reduced data measurement model instead of the raw signal samples at receiver front-end sampling rate, F_s, in (3.9).

The measurements at the output of GradH preprocessing, i.e., gradient heterodyne operation and lowpass filtering, can be written in the form

$$\mathbf{z} = \mathbf{G}\mathbf{s} + \mathbf{v}, \tag{3.19}$$

where $\mathbf{G} = \mathbf{Q}^T\mathbf{H} \in \mathbb{R}^{2N\times 2N}$ is the channel matrix at the output of the GradH preprocessor and lowpass filter, and $\mathbf{v} = \mathbf{Q}^T\mathbf{w} \sim \mathcal{N}(\mathbf{0}, \sigma^2\mathbf{Q}^T\mathbf{Q})$. In the special case of an AWGN channel (i.e., $\mathbf{H} = \mathbf{Q}$), with a large enough symbol duration T and smoothly varying pulse shaping function $g(t)$, the channel matrix $\mathbf{G} = \mathbf{Q}^T\mathbf{Q} \approx \beta\mathbf{I}_{2N}$ is nearly diagonal and $\mathbf{v} \sim \mathcal{N}(\mathbf{0}, \beta\sigma^2\mathbf{I}_{2N})$, as shown in Sec. 3.3.1.

The measurement model at the output of pGradH preprocessing assumes the same form as in (3.19), where $\mathbf{z} \in \mathbb{R}^{2N}$ is the output of the MRC processor given by $\mathbf{z} = \sum_{p=0}^{N_\text{P}-1} \frac{h_p}{|h_p|^2}\mathbf{z}^{(p)}$, $\mathbf{G} = \sum_{p=0}^{N_\text{P}-1} \frac{h_p}{|h_p|^2}\mathbf{G}^{(p)} \in \mathbb{R}^{2N\times 2N}$ is the effective channel matrix at the output of the MRC processor, $\mathbf{G}^{(p)} = \mathbf{Q}^{(p)T}\mathbf{H} \in \mathbb{R}^{2N\times 2N}$ is the channel matrix at the output of the pth branch of the pGradH preprocessor, $\mathbf{v} = \sum_{p=0}^{N_\text{P}-1} \frac{h_p}{|h_p|^2}\mathbf{v}^{(p)} \in \mathbb{R}^{2N}$ and $\mathbf{v}^{(p)} = \mathbf{Q}^{(p)T}\mathbf{w} \sim \mathcal{N}(\mathbf{0}, \sigma^2\mathbf{Q}^{(p)T}\mathbf{Q}^{(p)})$. For a moderately delay spread channel with well resolved path delays and large symbol duration, $\mathbf{Q}^{(p)T}\mathbf{Q}^{(q)} \approx \beta\delta_{p,q}I_{2N}, 0 \le p, q \le N_\text{P}-1$ due to (3.14). In this case, $\mathbf{G}^{(p)} \approx \beta h_p\mathbf{I}_{2N}$, $\mathbf{v}^{(p)} \sim \mathcal{N}(\mathbf{0}, \beta\sigma^2\mathbf{I}_{2N})$, and therefore $\mathbf{G}$, the

channel matrix at the output of the GradH and pGradH preprocessors, is nearly diagonal.

In the next section, we bring out the need to consider alternate S2C receiver processing in large delay spread channels.

3.4 Limitations of GradH and pGradH Receivers

For both GradH and pGradH receivers, the condition in (3.14) is needed to ensure that the ISI is negligible after gradient heterodyne operation and lowpass filtering. The condition (3.14) places a *lower limit* on the minimum differential path delay, $\delta\tau_{\min}$, of the multipath arrivals to avoid ISI ensuing from the mixing of adjacent symbols at the GradH and pGradH preprocessor outputs [60]. The condition (3.14) also places an *upper limit* on the channel delay spread, $\delta\tau_{\max}$, to avoid interference between the symbols on the corresponding frequency sweep slots of different chirp pulses. Together, these limits require the symbol rate, $R = 1/T$, of the existing S2C receivers to satisfy

$$R \leq \left(\frac{f_H - f_L}{1+\alpha}\right) \frac{\min\{\delta\tau_{\min}, T_{\rm sw} - \delta\tau_{\max}\}}{T_{\rm sw}}. \tag{3.20}$$

The upper limit on the achievable rate, in (3.20), is maximized when $T_{\rm sw} = \delta\tau_{\max} + \delta\tau_{\min}$, and the maximum rate achievable by the existing S2C receivers is given by

$$R_{\max} = \left(\frac{f_H - f_L}{1+\alpha}\right) \frac{\delta\tau_{\min}}{\delta\tau_{\max} + \delta\tau_{\min}}. \tag{3.21}$$

Note that the rate limiting condition $R \leq R_{\max}$ to avoid ISI at the preprocessor output of the existing S2C receivers, is equivalent to imposing a lower bound on the spreading factor: $\mathcal{M} \geq \frac{\delta\tau_{\max}}{\delta\tau_{\min}} + 1$. When the system is operated at a symbol rate $R = R_{\max}$, the spreading factor $\mathcal{M} = \frac{\delta\tau_{\max}}{\delta\tau_{\min}} + 1$.

Existing S2C receivers entail ISI when operating at a symbol rate greater than $R_{\max}$. Consider, for example, the S2C system in Table 3.1 operating in a UWA channel simulated in Sec. 3.6.2.1. There are 20 QPSK symbols (i.e., 40 bits) in one chirp pulse (S2C block) of duration $T_{\rm sw} = 10$ ms. Figure 3.1 shows a transmitted S2C frame, where the symbols

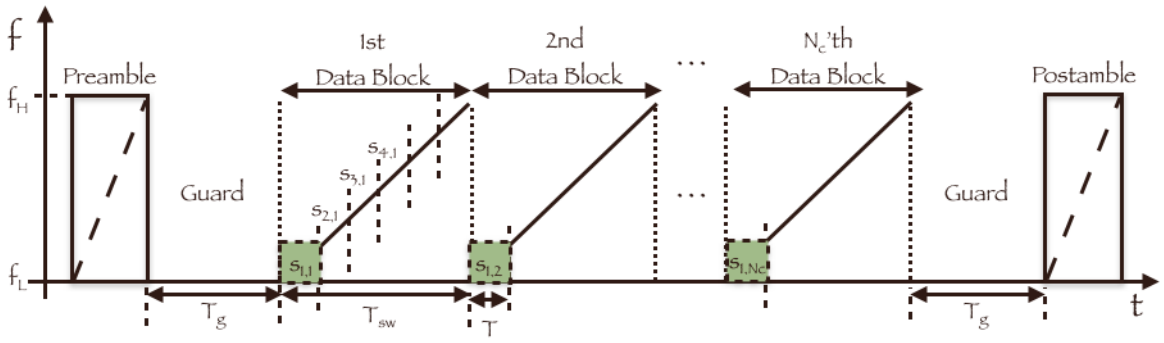

Figure 3.1: An S2C frame consisting of preamble, N_c chirp pulses (data blocks), and postamble. Although $T \geq \frac{1}{\sqrt{2m_c}}$ avoids ISI among adjacent symbols, inter-block interference (IBI) among the symbols mounted on the same frequency sweep slots (green slots) can happen if T_{sw} is smaller than the channel delay spread.

$s_{i,j}$ and $s_{i,j+1}$ can potentially interfere with the detection of $s_{i,j+2}, j = 1, 2, 3$. Figures 3.2 and 3.3 display the images of the raw channel matrix $\mathbf{H}$, in (3.9), and the corresponding effective channel $\mathbf{G}$, in (3.19), respectively. Yellow pixels show the large magnitude entries in the visual images of $|\mathbf{H}|$ and $|\mathbf{G}|$. Large magnitude off-diagonal entries lead to ISI. Compared to the raw channel matrix $\mathbf{H}$, the effective channel $\mathbf{G}$ after gradient heterodyne and lowpass filtering exhibit reduced ISI. This is shown by the relatively weaker (blue) off-diagonal entries of $|\mathbf{G}|$. The gradient heterodyne and lowpass filtering operation has reduced the strength of the off-diagonal entries in $\mathbf{G}$ that contribute to ISI among symbols within a chirp pulse (intra-block interference). But, strong residual inter-block interference remains at the GradH/pGradH preprocessor output as shown by the large magnitude (yellow) pixels around $G_{i,i-40}, 40 < i \leq 2N$, in Figure 3.3. In turn, this adversely affects the performance of the existing S2C receivers in a severely delay spread UWA channel. In such channels, existing S2C receivers must compromise on the data rate in order to restore the symbol recovery performance.

In the following section, we consider alternate receivers for S2C communications that can handle channel delay spreads greater than the chirp pulse duration and work well for symbol rates higher than the upper limit on the data rate, $R_{\max}$.

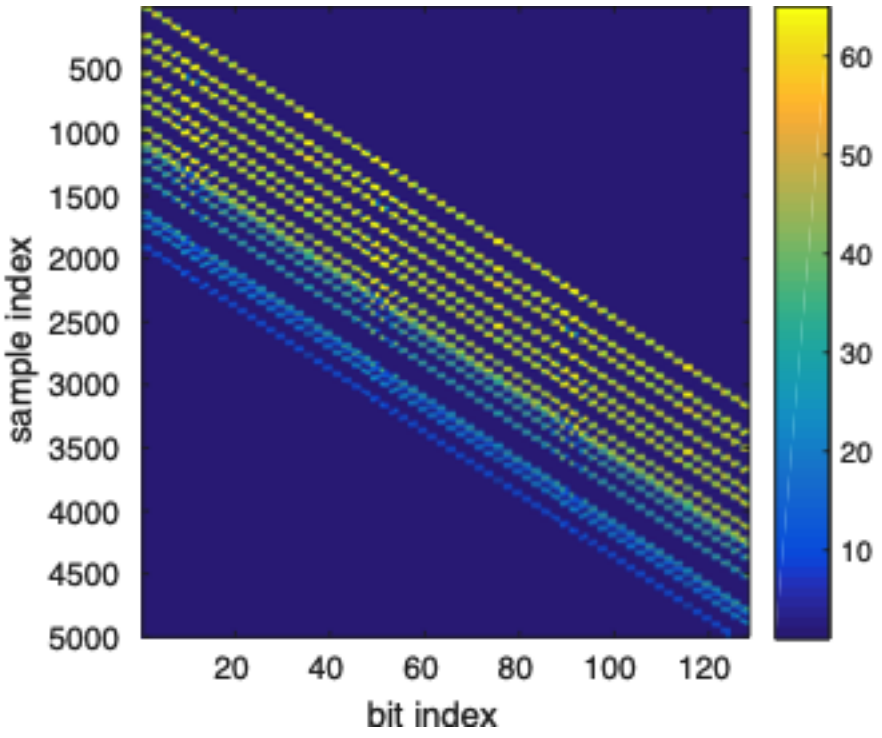

Figure 3.2: Channel matrix image, $|\mathbf{H}| \in \mathbb{R}^{NL\times 2N}$, before GradH processing. Pixel intensities are in linear units and only the portion corresponding to first 128 bits is shown. For the purpose of visualization, $|\mathbf{H}|$ is scaled such that the median of the entires of its scaled version assumes a value of $\frac{1}{6}$ on the color bar shown.

3.5 Variational Soft Symbol Decoder (VSSD)

We now develop a symbol detector based on the variational Bayes' inference that approximates the optimum MAP decoder and offers significantly improved performance over the MMSE receiver. The development of the VSSD is the main contribution of this work.

The optimum (MAP) decoder outputs the symbol vector $\mathbf{s} \in \mathcal{P} = \{-\frac{1}{\sqrt{2}}, +\frac{1}{\sqrt{2}}\}^{2N}$ that maximizes the posterior $p(\mathbf{s}|\mathbf{G},\mathbf{z}) = p(\mathbf{z}|\mathbf{G},\mathbf{s})p(\mathbf{s})/p(\mathbf{z}|\mathbf{G})$. Direct maximization of the posterior requires a computationally intensive search over 2^{2N} lattice points in $\mathcal{P}$. Computing the posterior symbol probabilities, which in turn yield the soft symbols to be input to the channel decoder, is also hard since the marginalization over $\mathbf{s}$ in $p(\mathbf{z}|\mathbf{G}) = \sum_{\mathbf{s}\in\mathcal{P}} p(\mathbf{s},\mathbf{z}|\mathbf{G})$ is involved. We instead seek a good approximation to the

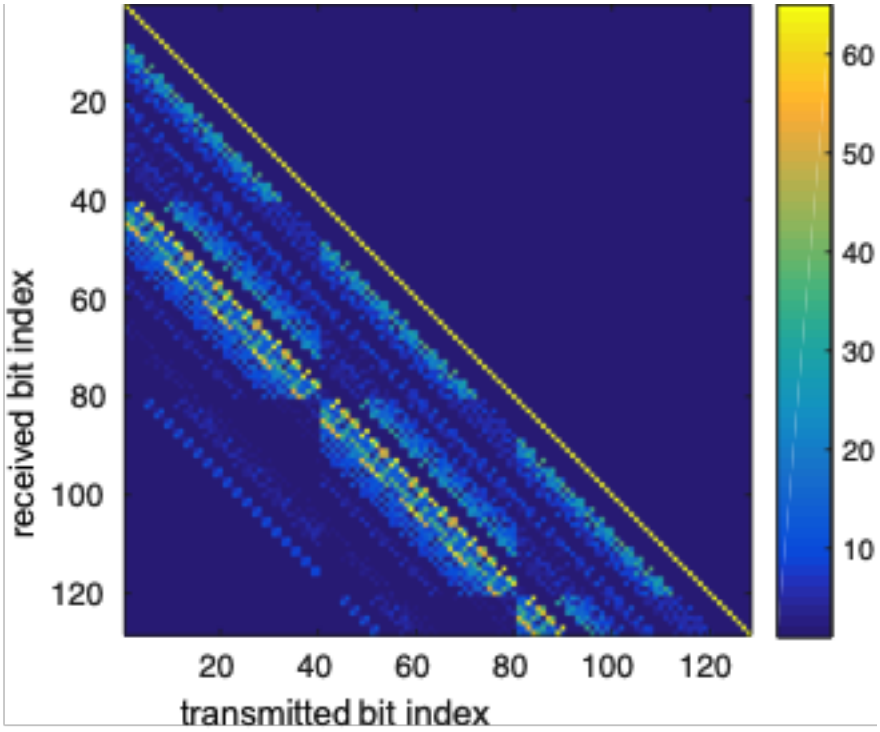

Figure 3.3: Channel matrix image, $|\mathbf{G}| \in \mathbb{R}^{2N \times 2N}$, after GradH processing. Pixel intensities are in linear units and only the portion corresponding to first 128 bits is shown. For the purpose of visualization, $|\mathbf{G}|$ is scaled such that the median of the entires of its scaled version assumes a value of $\frac{1}{6}$ on the color bar shown.

posterior, $q_\phi(\mathbf{s}|\mathbf{G}, \mathbf{z})$, called the variational decoder. Here, ϕ represents the model parameters whose values are estimated based on the variational inference principle, as explained below.

To make the problem tractable, we assume that the approximate posterior is fully factorizable:

$$q_\phi(\mathbf{s}|\mathbf{G}, \mathbf{z}) = \prod_{k=0}^{N-1} q_\phi(s_{k,\mathrm{Re}}|\mathbf{G}, \mathbf{z}) q_\phi(s_{k,\mathrm{Im}}|\mathbf{G}, \mathbf{z}). \tag{3.22}$$

Following Kingma et al. [50], the evidence lower bound (ELBO) on the log likelihood

of the observation is given by

$$\mathcal{L}(\theta, \phi, \mathbf{z}) = \mathbb{E}_{q_{\phi(\mathbf{s}|\mathbf{G},\mathbf{z})}} \log p_\theta(\mathbf{z}|\mathbf{G}, \mathbf{s}) - \mathbb{E}_{q_{\phi(\mathbf{s}|\mathbf{G},\mathbf{z})}} \left[\log \frac{q_\phi(\mathbf{s}|\mathbf{G}, \mathbf{z})}{p_\theta(\mathbf{s})} \right], \tag{3.23}$$

where $\log p_\theta(\mathbf{z}|\mathbf{G}, \mathbf{s})$ is the likelihood function and $p_\theta(\mathbf{s})$ is a prior on the symbol vector.

To bring $q_\phi(\mathbf{s}|\mathbf{G}, \mathbf{z})$ close to $p(\mathbf{s}|\mathbf{G}, \mathbf{z})$, we maximize the ELBO, $\mathcal{L}(\theta, \phi, \mathbf{z})$. The ELBO consists of the likelihood term

$$\mathbb{E}_{q_{\phi(\mathbf{s}|\mathbf{G},\mathbf{z})}} \log p_\theta(\mathbf{z}|\mathbf{G}, \mathbf{s}) = -N \log(2\pi\sigma^2) - \mathbb{E}_{q_{\phi(\mathbf{s}|\mathbf{G},\mathbf{z})}} \left[\frac{\|\mathbf{z} - \mathbf{G}\mathbf{s}\|^2}{2\sigma^2} \right], \tag{3.24}$$

and the regularizing term,

$$\mathbb{E}_{q_{\phi(\mathbf{s}|\mathbf{G},\mathbf{z})}} \left[\log \frac{q_\phi(\mathbf{s}|\mathbf{G}, \mathbf{z})}{p_\theta(\mathbf{s})} \right] = KL(q_\phi || p_\theta). \tag{3.25}$$

We assume a simple uniform prior $p_\theta(\mathbf{s}) = \frac{1}{2^{2N}}$. Therefore, when maximizing ELBO, the regularizing term acts to penalize the departure of the variational approximation q_ϕ from the uniform prior. On maximizing the ELBO, we get the following fixed point equations (see appendix for details):

$$\mathbf{q} = \varphi(\boldsymbol{\alpha}), \tag{3.26}$$

where

$$\begin{aligned} \alpha_j &= \frac{\sqrt{2}}{\sigma^2} \left(\mathbf{z}^T \mathbf{G}_{:,j} - \sum_{l=0}^{2N-1} G_{l,j} \left(\sum_i v_{l,i} - v_{l,j} \right) \right), \\ v_{l,j} &= \frac{1}{\sqrt{2}} G_{l,j} \left(2q_j - 1 \right), \\ \varphi(\alpha_j) &= \frac{1}{1 + e^{-\alpha_j}}, \end{aligned} \tag{3.27}$$

for $j = 1, \ldots, 2N - 1$.

Note that the fixed point iterations lead to *soft symbol* estimates in the form of the probability vector $\mathbf{q}$. We perform symbol detection by slicing the probability vector in

uncoded communications. In coded communications, the soft symbols are converted to LLRs and fed to the channel decoder.

The fixed point updates do not involve any matrix inversions and their computational complexity, $\mathcal{O}(N^2)$, is an order of magnitude smaller than the computational complexity, $\mathcal{O}(N^3)$, of the MMSE receiver.

Special Channels: It is insightful to specialize the fixed point iterations for some simple channel models. Consider the case when the channel matrix is orthogonal, i.e.,

$$\mathbf{G}_{:,i}^T \mathbf{G}_{:,j} = \| \mathbf{G}_{:,i} \|_2^2 \, \delta_{i,j}.$$

Note that the AWGN channel and Rayleigh fading channel are examples of orthogonal channels. In this case, the fixed point iterations in (3.26) reduce to the following one point update:

$$\mathbf{q} = \frac{1}{1 + e^{-\left(\frac{\sqrt{2}}{\sigma^2}\mathbf{G}^T\mathbf{z}\right)}}. \tag{3.28}$$

Therefore, deciding the hard symbols from the probability vector $\mathbf{q}$ is tantamount to slicing the matched filtered observation: $\tilde{\mathbf{z}} = \mathbf{G}^T\mathbf{z}$. Deciding $s_k = \pm\frac{1}{\sqrt{2}}$ based on $q_k \gtrless 0.5$ is equivalent to that based on $\tilde{z}_k \gtrless 0$. In other words, VSSD is an ML decoder for orthogonal channels.

Convergence: We show that every update of the fixed point iteration in (3.26) is along the gradient of the ELBO (ascent direction), and therefore cannot decrease the ELBO. To see this, consider the inner product of $\varphi(\boldsymbol{\alpha}) - \mathbf{q}$ and $\nabla\mathcal{L}$:

$$\left(\varphi(\boldsymbol{\alpha}) - \mathbf{q}\right)^T \nabla\mathcal{L} = \sum_{j=0}^{2N-1} \left(\varphi(\alpha_j) - q_j\right) \nabla\mathcal{L}_j. \tag{3.29}$$

We show in the appendix (see equation (3.66)) that $\nabla\mathcal{L}_j = \alpha_j - \log q_j + \log(1 - q_j)$. Each term in (3.29) is nonnegative since $\varphi(\alpha_j) - q_j \gtrless 0 \Leftrightarrow \alpha_j - \log q_j + \log(1 - q_j) \gtrless 0$. Thus, the inner product is nonnegative and hence the update $\mathbf{q} \to \varphi(\boldsymbol{\alpha}(\mathbf{q}))$ cannot decrease ELBO. Further, for any channel matrix, the ELBO is upper bounded by the marginal log likelihood, $\log p_\theta(\mathbf{z})$. Therefore, the fixed point iterations always converge to a stationary

point of the ELBO.

Next, we characterize the stationary points of the ELBO and elicit sufficient conditions that make these points a *global maximum*, *local maximum* or a *saddle point*.

Global Maximum: The entries of the Hessian matrix of $\mathcal{L}$ with respect to $\mathbf{q}$, i.e., $\nabla^2_{\mathbf{q}}\mathcal{L} \in \mathbb{R}^{2N\times 2N}$, are given by

$$\frac{\partial^2 \mathcal{L}}{\partial q_j^2} = -\frac{1}{q_j(1-q_j)} < 0, \tag{3.30}$$

$$\frac{\partial^2 \mathcal{L}}{\partial q_i \partial q_j} = \frac{\partial^2 \mathcal{L}}{\partial q_j \partial q_i} = -\frac{2}{\sigma^2}\sum_l G_{l,i}G_{l,j}, i \neq j, \tag{3.31}$$

where $i, j \in \{0, 1, \ldots, 2N-1\}$. For orthogonal channel matrices, the matrix $\mathbf{G}$ satisfies $\sum_l G_{l,i}G_{l,j} = 0$, which makes the Hessian negative definite and therefore the stationary point $\mathbf{q}_\star$ a global maximizer of the ELBO.

A larger class of channel matrices for which global convergence is guaranteed can be found by requiring $-\nabla^2_{\mathbf{q}}\mathcal{L}$ to be diagonally dominant, i.e.,

$$\eta_j \triangleq \frac{2}{\sigma^2}\sum_{i\neq j}\left|\sum_l G_{l,i}G_{l,j}\right| < \frac{1}{q_j(1-q_j)}, \forall j, \tag{3.32}$$

which implies:

$$q_j^2 - q_j + 1/\eta_j > 0, \forall j. \tag{3.33}$$

Now, the condition in (3.33) holds for every $0 \leq q_j \leq 1$ if and only if $0 \leq \eta_j < 4$. Note that $-\nabla^2_{\mathbf{q}}\mathcal{L}$ is symmetric and all its diagonal entries are positive. Since diagonal dominance of $-\nabla^2_{\mathbf{q}}\mathcal{L}$ implies its positive definiteness (p.d.), $-\nabla^2_{\mathbf{q}}\mathcal{L}$ is p.d. for the class of channel matrices $\mathcal{G} = \{\mathbf{G} \in \mathbb{R}^{2N\times 2N} : \sum_{i\neq j} |\sum_l G_{l,i}G_{l,j}| < 2\sigma^2, \forall j\}$ and therefore global convergence is guaranteed whenever $\mathbf{G} \in \mathcal{G}$.

Local Maximum: If $\mathbf{G} \in \mathcal{G}$, the limit point $\mathbf{q}_\star$ is a global maximizer. Or else, if $\mathbf{G} \notin \mathcal{G}$ and $q_{j,\star} \notin (\kappa_j^{(1)}, \kappa_j^{(2)}) \subset [0,1], \forall j$, where $\kappa_j^{(1,2)}$ are the roots of the equation $q_j^2 - q_j + 1/\eta_j = 0$ ($\eta_j > 4$) given by

$$\kappa_j^{(1,2)} = \frac{1 \pm \sqrt{1 - 4/\eta_j}}{2}, \forall j, \tag{3.34}$$

then the limit point $\mathbf{q}_\star$ is a local maximum.

Either Local Maximum or Saddle Point: If $\mathbf{G} \notin \mathcal{G}$ and $q_{j,\star} \in (\kappa_j^{(1)}, \kappa_j^{(2)})$, for some j, then the limit point $\mathbf{q}_\star$ is either a local maximum or a saddle point.

Consider, for example, a channel matrix with i.i.d. $\mathcal{N}(0,1)$ entries. The length of the interval $(\kappa_j^{(1)}, \kappa_j^{(2)})$ is given by

$$l_{N,j} = \kappa_j^{(2)} - \kappa_j^{(1)} = \sqrt{1 - 4/\eta_j}. \tag{3.35}$$

From the definition of η_j in (3.32), triangle inequality, and the i.i.d. property of the entries of G, we have:

$$\mathbb{E}[\eta_j] \leq \frac{2}{\sigma^2} \sum_{i \neq j} \sum_{l} \mathbb{E}\left[|G_{l,i}|\right] \mathbb{E}\left[|G_{l,j}|\right] = \frac{8N(2N-1)}{\pi\sigma^2}, \tag{3.36}$$

and therefore,

$$\mathbb{E}[l_{N,j}^2] = 1 - 4\mathbb{E}[1/\eta_j] \leq 1 - 4/\mathbb{E}[\eta_j] = 1 - \frac{\pi\sigma^2}{2N(2N-1)}, \tag{3.37}$$

where we used the fact that $\mathbb{E}[1/\eta_j] \leq 1/\mathbb{E}[\eta_j]$ which follows from Jensen's inequality and the convexity of $f(\eta) = 1/\eta, \eta > 0$. Since $\mathbb{P}\{\eta_j > 4\} \to 1$, as $N \to \infty$, for i.i.d. Gaussian channel matrices, the fixed point is in $(\kappa_j^{(1)}, \kappa_j^{(2)})$ with high probability. Furthermore, since for every $\delta > 0$, $\mathbb{P}\{l_{N,j}^2 > 1 - \delta\} \to 1$ as $N \to \infty$, we have $l_{N,j} \xrightarrow{p} 1$.

Since, in this case, $\mathbf{q}_\star$ could be a saddle point, we perturb $\mathbf{q}_\star$ so as to move out of the saddle region in an attempt to further increase the ELBO. If the ELBO is found to increase for a few attempts of random perturbation, we continue the iterations from the point yielding the highest ELBO.

Acceleration: Finally, we propose to accelerate the fixed point updates to achieve faster convergence. Specifically, we choose γ_n at the nth iterate so that the update,

$$\mathbf{q}_n = \mathbf{q}_{n-1} + \gamma_n \left[\varphi(\boldsymbol{\alpha}_{n-1}) - \mathbf{q}_{n-1}\right], \tag{3.38}$$

results in maximal increase of ELBO. The optimum value of γ_n can be found through a

1-D search over a bounded interval in $\mathbb{R}$. Specifically, the optimum value of γ_n in (3.38), that best increases ELBO, lies within $[\gamma_{\min}, \gamma_{\max}] \in \mathbb{R}$, with

$$\gamma_{\min} = \max\Big\{ \max_{\varphi(\alpha_j)>q_j} \tfrac{-q_j}{\varphi(\alpha_j)-q_j}, \max_{\varphi(\alpha_j)<q_j} \tfrac{1-q_j}{\varphi(\alpha_j)-q_j} \Big\},$$
$$\gamma_{\max} = \min\Big\{ \min_{\varphi(\alpha_j)<q_j} \tfrac{-q_j}{\varphi(\alpha_j)-q_j}, \min_{\varphi(\alpha_j)>q_j} \tfrac{1-q_j}{\varphi(\alpha_j)-q_j} \Big\}.$$

3.6 Numerical Simulations

We demonstrate the performance of VSSD in three different settings: the benchmark i.i.d. Gaussian multiple-input multiple-output (MIMO) channel, UWA channels simulated according to two different models in the literature, and real-world measured UWA channels. We define the signal to noise ratio (SNR) at the receiver as

$$\text{SNR} = \frac{E\{\|\mathbf{Gs}\|_2^2\}}{E\{\|\mathbf{v}\|_2^2\}}. \tag{3.39}$$

3.6.1 IID Gaussian MIMO Channel

We generate the channel matrix $\mathbf{G}$, with entries $G_{i,j} \overset{i.i.d.}{\sim} \mathcal{N}(0,1)$. First, we evaluate the BER of the VSSD receivers for $N = 10, 100$ symbols, for the uncoded QPSK signaling, and with perfect channel knowledge. We terminate the VSSD iterations at the nth iteration if $\|\mathbf{q}_n - \mathbf{q}_{n-1}\|_2 < 10^{-3}$. Figure 3.4 shows the BER plots for different SNR values. For $N = 10$ symbols, we show the BER of the ML decoder obtained by using the soft sphere decoder (SSD) in [91, 92] and whose implementation is available in [63]. The VSSD receiver, initialized with the soft symbol estimate of SSD, retains the SSD's optimum (ML) performance, as expected. When initialized with the MMSE estimate of the symbol vector, VSSD outperforms the MMSE receiver by a margin of about 8-9 dB at a BER of 10^{-3} for $N = 10$. Note that, while SSD outperforms VSSD for $N = 10$, sphere decoding

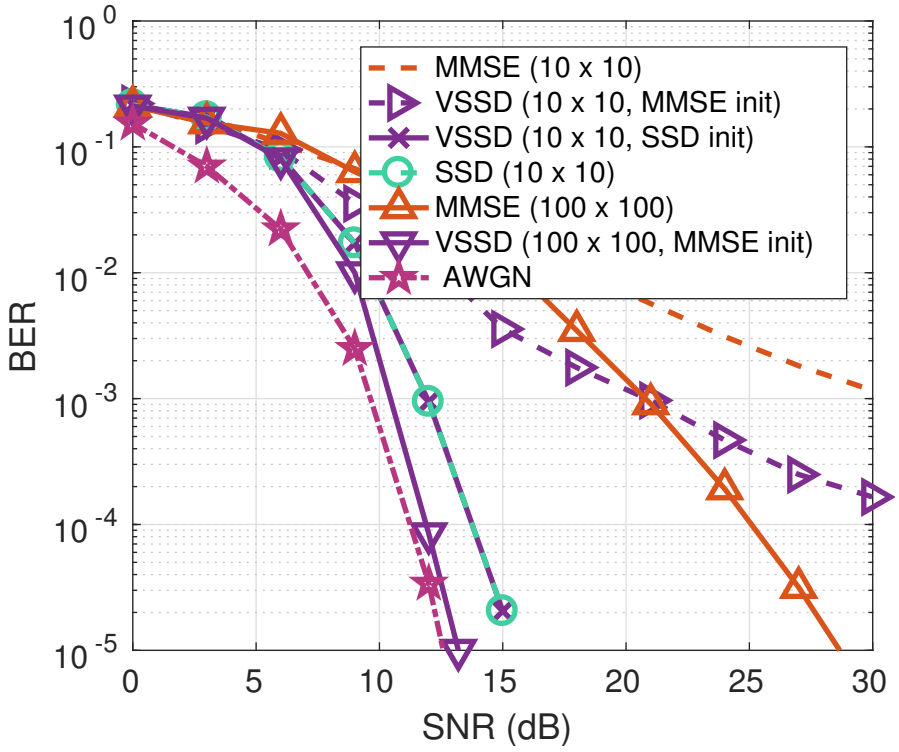

Figure 3.4: BER of VSSD, SSD and MMSE receivers for i.i.d. Gaussian channel matrix ($N = 10, 100$) and AWGN channel.

is not practical at large values of N due to its high computational complexity.[1] Moreover, for $N = 100$, the performance of the VSSD receiver on the i.i.d. Gaussian MIMO channel is close to that on an AWGN channel. On the AWGN channel, all receivers perform equally well, as expected.

In Figure 3.5, we compare the BER of the receivers for $N = 288$ symbols, for uncoded and coded QPSK communications, assuming perfect channel knowledge. For coded communication, we use a rate 1/2 and rate 2/3 LDPC code from [33]. In uncoded communication, the VSSD receiver achieves a BER of 10^{-3} at about 10 dB lower SNR than the MMSE receiver. In the rate 2/3 (1/2) coded communication, for a BER of 10^{-3}, VSSD outperforms MMSE receiver by an SNR margin of 8 dB (2 dB). For the same BER (10^{-3}), the VSSD receiver with a rate 2/3 code works at about 1 dB lower SNR than the MMSE

[1] On a 2.4 GHz Intel Xeon(R) processor, SSD takes 4.5 s on average to decode $N = 20$ symbols at SNR = 10 dB. For $N = 30$ symbols and at the same SNR, decoding does not finish within 5 minutes.

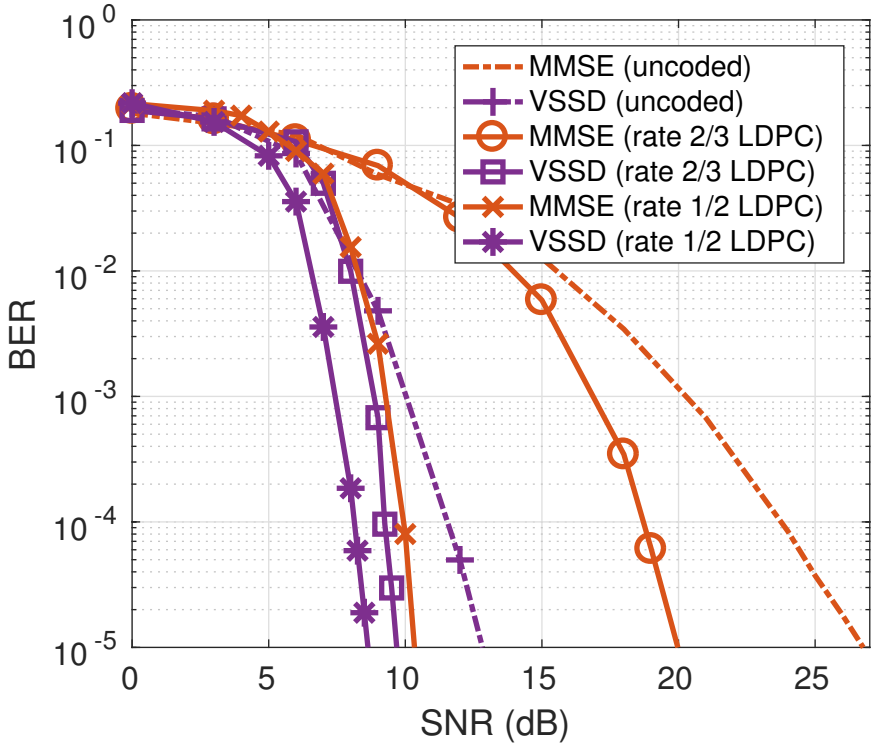

Figure 3.5: BER of VSSD and MMSE receivers for i.i.d. Gaussian channel matrix.

receiver with a rate 1/2 code. Therefore, VSSD receiver offers 33% higher data rate than the MMSE receiver, while achieving the same BER.

Next, we consider the effect of imperfect channel knowledge due to channel estimation error on the BER. To do so, we perturb the entries of the i.i.d. Gaussian channel matrix with i.i.d. Gaussian noise, i.e. $G_{i,j} = G_{i,j} + \epsilon_{i,j}$, where $\epsilon_{i,j} \sim \mathcal{N}(0, \Delta), 1 \leq i, j, \leq 2N$. Figure 3.6 shows the BER of VSSD and MMSE decoders for $\Delta = 1/4, 1/5$ and coded communications using a rate 2/3 LDPC code. VSSD receiver retains its performance advantage over MMSE even with channel estimation errors.

3.6.2 Simulated UWA Channels

We now consider the performance of VSSD based receiver for the S2C communication system in Table 3.1 over a simulated UWA channel. Note that the symbol rate that is

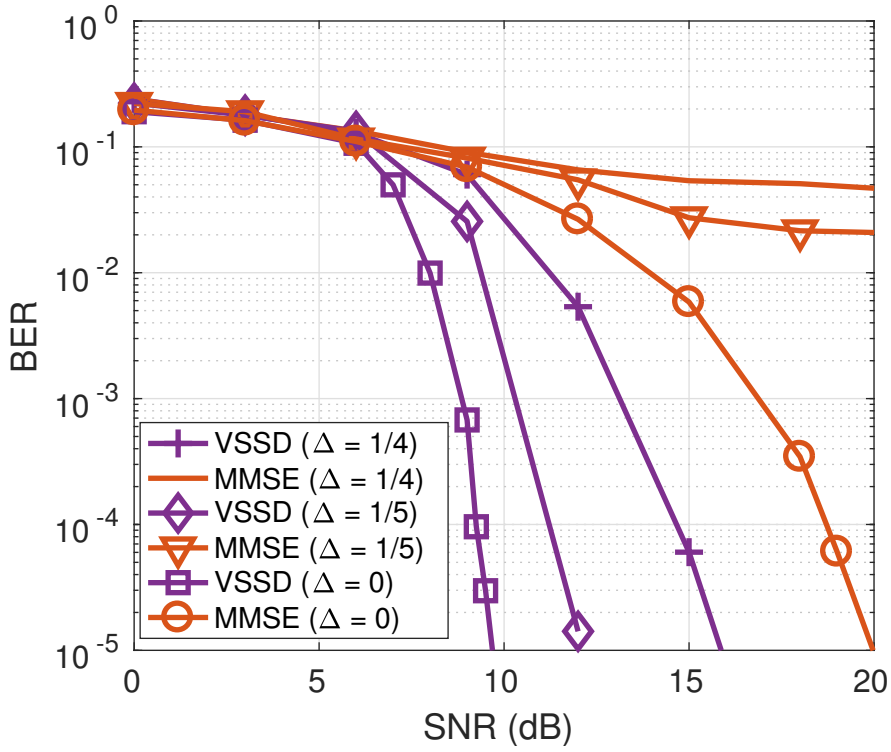

Figure 3.6: BER of VSSD and MMSE receivers, under channel estimation errors, for i.i.d. Gaussian channel matrix. Δ denotes the variance of the zero-mean additive Gaussian noise by which the channel matrix entries are perturbed to simulate channel estimation errors.

two times the upper limit, $R_* = \sqrt{2m_c} = 1$ kHz, on the existing S2C receivers.[2] A total of $N = 288$ QPSK symbols are mounted on a train of $N_c = 15$ chirp pulses. We investigate the performance for two models of UWA channels.

3.6.2.1 Model I

The first UWA channel model we consider is as in [14,34] and used by numerous researchers in the field. The channel is generated with $N_{\mathrm{P}} = 16$ discrete paths whose inter-arrival times, $\delta\tau$ are exponentially distributed with a mean of 1 ms. The guard interval, $T_g = 25$ ms, is chosen to well exceed the expected delay spread, $\mathbb{E}[\tau_{\max}] = N_p \mathbb{E}[\delta\tau] = 16$ ms.

[2] Adjacent symbol interference, within a chirp pulse, is avoided in existing S2C receivers only if $2m_cT \geq B \approx \frac{1+\alpha}{T} \Rightarrow R \leq \sqrt{\frac{2m_c}{1+\alpha}} \leq \sqrt{2m_c} \triangleq R_*$.

Table 3.1: S2C parameters used in the simulation.

Carrier frequency (f_c)	15 kHz
Bandwidth (W)	10 kHz
Chirp rate ($2m_c$)	1 MHz/s
Symbol duration (T)	0.5 ms
Sweep duration (T_{sw})	10 ms
Guard interval (T_g)	25 ms

The Doppler rates are uniformly distributed in $[-b_{\max}, b_{\max}]$, where $b_{\max} = 5 \times 10^{-4}$. The path amplitudes are Rayleigh distributed with the average power decreasing exponentially with delay, where the difference between the beginning and the end of the guard time is 20 dB. Notice that neither of the narrowband approximation conditions [38] $B/f_c \ll 1$ or $b_{\max} \ll 1/BT$ are met in this case. Therefore, it is pertinent to evaluate the symbol recovery schemes based on the system model (3.9) for S2C communications over such a wideband delay-scale channel.

Figure 3.7 shows the BER of the MRC [60], VSSD and MMSE based data detection assuming perfect channel knowledge. The MRC receiver has completely failed due to severe ISI at pGradH preprocessor output (see Figure 3.3). Again, from these plots, we notice a strong performance of the VSSD based symbol detection in an S2C receiver. The VSSD receiver attains a BER $= 10^{-3}$ at about 18 dB lower SNR than MMSE in uncoded communication. In coded communication, the SNR margin of VSSD over the MMSE receiver is 8 dB (3 dB) for rate 2/3 (1/2) LDPC code.

Figure 3.8 shows the number of VSSD iterations (averaged over at least 1000 trials) for different SNR. On an average, the number of iterations stay below 10 and the maximum number of iterations never crossed 15.

3.6.2.2 Model II

We consider the UWA channel model proposed in [72]. The acoustic channel simulator code, available at [87], is used for generating the time-varying channel. Table 3.2 lists

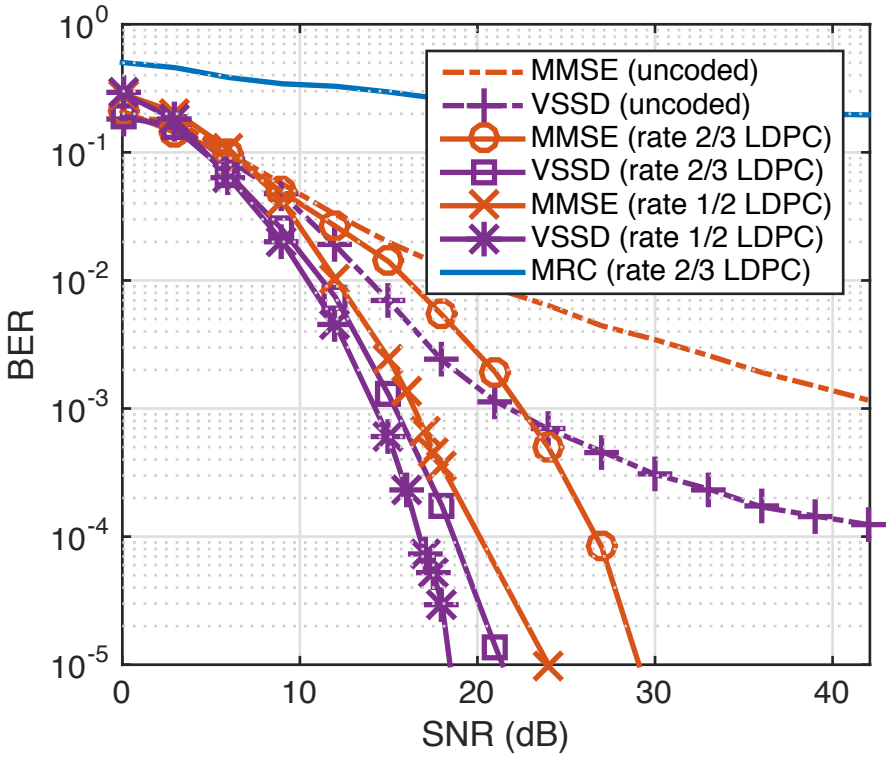

Figure 3.7: BER of VSSD and MMSE receivers over a UWA channel simulated according to the model in Berger et al. [14].

the parameters of the channel. A sample realization of the time-varying channel impulse response is shown in Figure 3.9. Note that the requirement, $T_g \geq \tau_{\max}$, is clearly met. Figure 3.10 shows an instance of the channel matrix ($\mathbf{G}$) at the output of S2C preprocessing during the UWA channel simulation run. The inter symbol interference for this UWA channel is milder than the channel simulated according to the model in [14] (see Figure 3.3). Figure 3.11 shows the BER plots of the VSSD and MMSE receivers with and without channel errors. VSSD maintains a significantly better performance than MMSE decoder, as before.

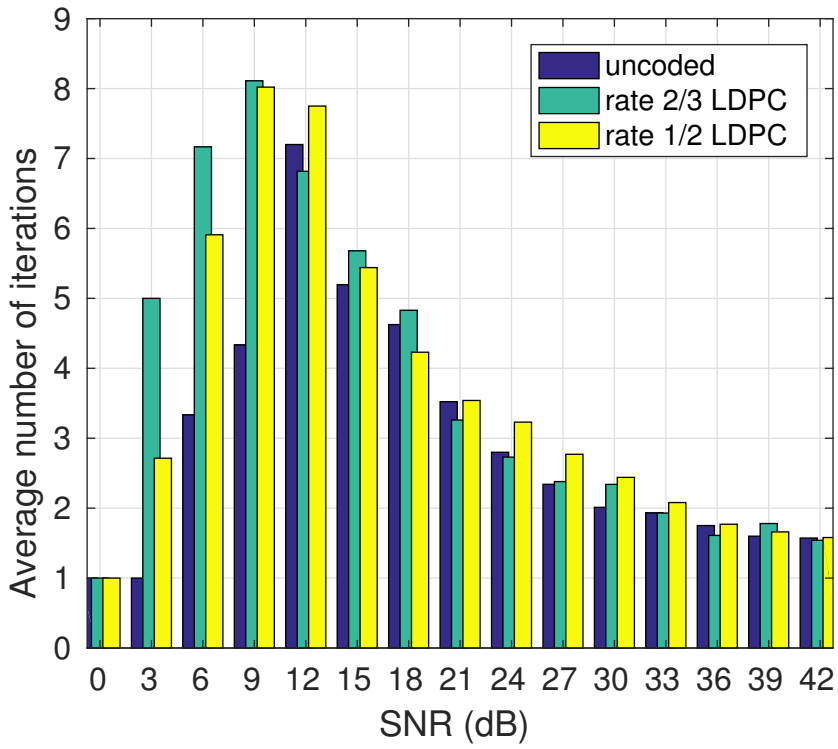

Figure 3.8: Number of VSSD iterations averaged over 1000 trials for each SNR.

3.6.3 Watermark Channels

The underWater AcousTic channEl Replay benchMARK (WATERMARK) is a publicly available realistic simulation tool that comes packaged with five measured UWA channels [70,98]. We use two of channel datasets, NOF1 and NCS1, that present two contrasting environments in the Norwegian seas [97]. The NOF1 channel is a Fjord in a shallow stretch of Oslofjorden, and the NCS1 channel is a continental shelf in the Norwegian sea. The measured time-varying channel impulse responses include the effects of system hardware impairments such as clock frequency offset, sampling jitter etc, apart from the acoustic propagation effects.

Channel Matrix Computation: We first relate the complex baseband form of the measured channel impulse response data in WATERMARK, denoted by $h_{\mathrm{B}}(t,\tau)$, and the channel matrix, $\mathbf{G}$, at the output of the gradient heterodyne and lowpass filtering operation.

Table 3.2: Underwater Channel Simulation Parameters.

Ocean depth (m)	100
Transmitter depth (m)	90
Receiver depth (m)	50
Channel distance (m)	1000
Spreading factor	1.7
Sound speed in water, c_w (m/s)	1500
Sound speed in bottom, c_b (m/s)	1200
Surface variance, σ_s^2 (m^2)	1.125
Bottom variance, σ_b^2 (m^2)	0.5
3 dB width of the PSD of intra-path delays, $B_{\delta,p}$ (Hz)	0.05
Number of intra-paths, S_p	20
Mean of intra-path amplitudes, μ_p	0.3
Variance of intra-path amplitudes, ν_p	10^{-4}
Transmitter drifting speed, v_{td} (m/s)	0.3
Transmitter drifting angle, θ_{td} (rad)	$\mathcal{U}(0, 2\pi)$
Receiver drifting speed, v_{rd} (m/s)	0.1
Receiver drifting angle, θ_{rd} (rad)	$\mathcal{U}(0, 2\pi)$
Transmitter vehicular speed, v_{tv} (m/s)	$\mathcal{N}(0, 1)$
Transmitter vehicular angle, θ_{tv} (rad)	$\mathcal{U}(0, 2\pi)$
Receiver vehicular speed, v_{rv} (m/s)	-3
Receiver vehicular angle, θ_{rv} (rad)	$\mathcal{U}(0, 2\pi)$
Surface variation amplitude, A_w (m)	0.9
Surface variation frequency, f_w (mHz)	0.6

Towards that end, we start with the baseband transmitted signal, given by

$$x_{\mathrm{B}}(t) = s(t)c(t)e^{-j2\pi f_c t}. \tag{3.40}$$

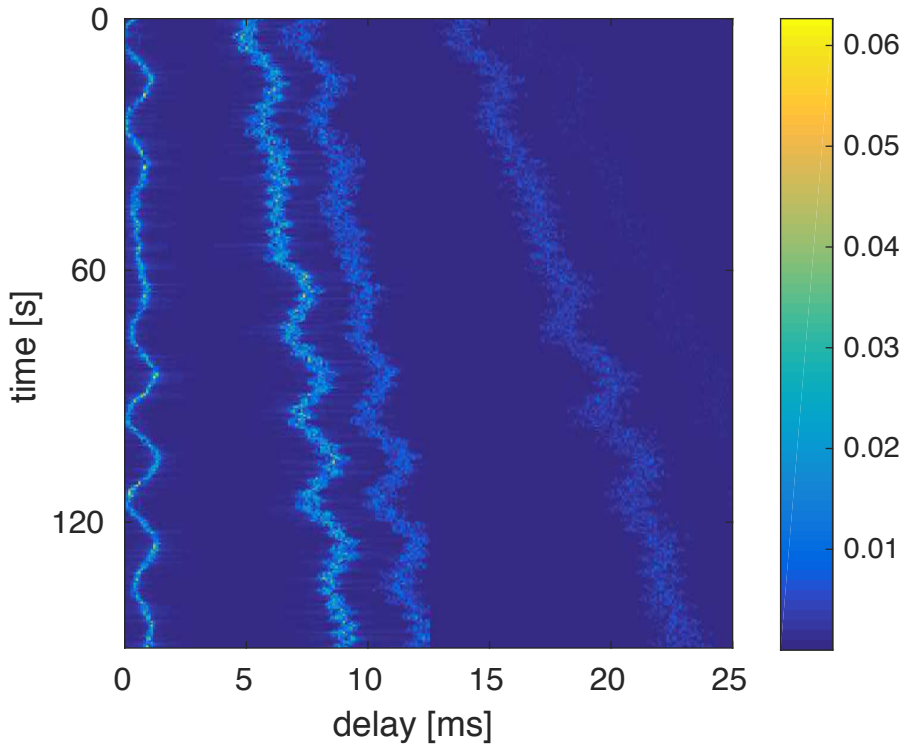

Figure 3.9: Acoustic channel impulse response based on model in [72]. The first, second and third arrivals from the left correspond to the direct, bottom-reflected, and surface-reflected paths, respectively. The last arrival corresponds to a multiply reflected surface-bottom arrival.

The received baseband signal is given by

$$y_{\mathrm{B}}(t) = \int_{\tau_{\min}(t)}^{\tau_{\max}(t)} h_{\mathrm{B}}(t, t-\tau) x_{\mathrm{B}}(\tau) d\tau + w_B(t), \tag{3.41}$$

where $\tau_{\min}(t) = \max\{0, t - T_d\}$, $\tau_{\max}(t) = \min\{t, T_c\}$, T_d denotes the maximum delay spread of the propagation channel and $w_B(t)$ is the complex valued noise in the baseband. Here, we made use of the fact that $h_{\mathrm{B}}(t, \tau) = 0$ for $\tau < 0$ (due to causality) and $\tau > T_d$, and $x_B(\tau) = 0$ for $\tau > T_c$, to arrive at the upper and lower limits of the integral in (3.41). Using (3.3), (3.40) and (3.41), the in-phase and quadrature components of the received

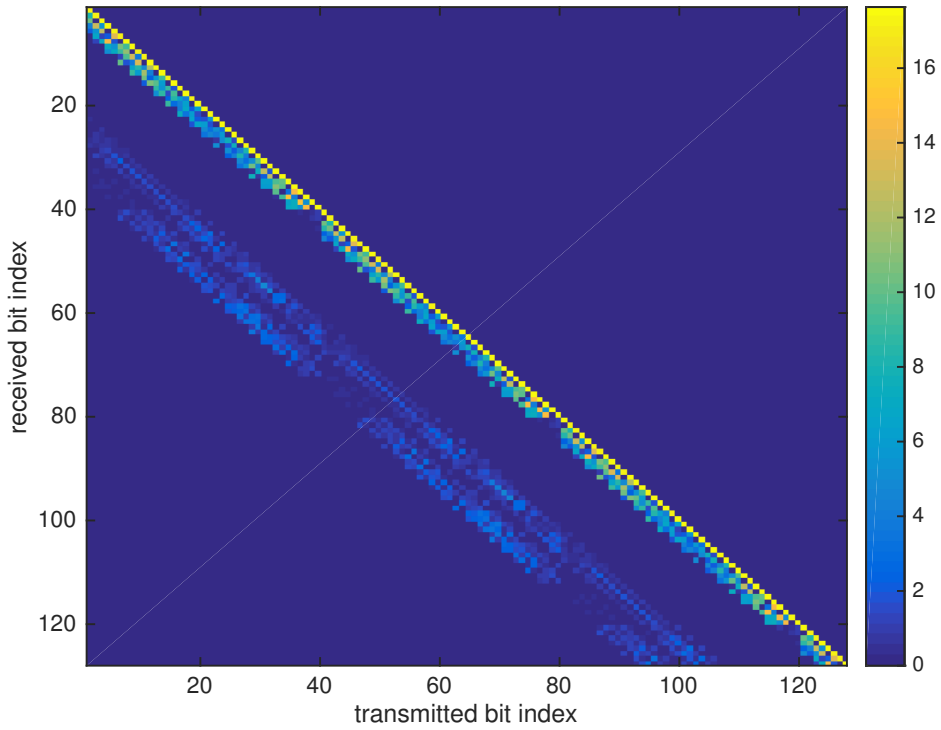

Figure 3.10: Channel matrix after GradH processing at an instance during the simulation run of the UWA channel model in [72].

signal can be expressed in the form:

$$y_{\mathrm{B,Re}}(t) = \sum_{k=0}^{N-1} H^{\mathrm{Re}}_{k,\mathrm{Re}}(t)s_{k,\mathrm{Re}} + H^{\mathrm{Im}}_{k,\mathrm{Re}}(t)s_{k,\mathrm{Im}} + w_{B,\mathrm{Re}}(t), \tag{3.42}$$

$$y_{\mathrm{B,Im}}(t) = \sum_{k=0}^{N-1} H^{\mathrm{Re}}_{k,\mathrm{Im}}(t)s_{k,\mathrm{Re}} + H^{\mathrm{Im}}_{k,\mathrm{Im}}(t)s_{k,\mathrm{Im}} + w_{B,\mathrm{Im}}(t), \tag{3.43}$$

where,

$$\begin{aligned} H^{\mathrm{Re}}_{k,\mathrm{Re}}(t) = &\int_{\tau^{(k)}_{\min}(t)}^{\tau^{(k)}_{\max}(t)} h_{\mathrm{B,Re}}(t, t-\tau)g(\tau - kT)\cos\phi_{\mathrm{B}}(\tau)d\tau \\ &- \int_{\tau^{(k)}_{\min}(t)}^{\tau^{(k)}_{\max}(t)} h_{\mathrm{B,Im}}(t, t-\tau)g(\tau - kT)\sin\phi_{\mathrm{B}}(\tau)d\tau, \end{aligned} \tag{3.44}$$

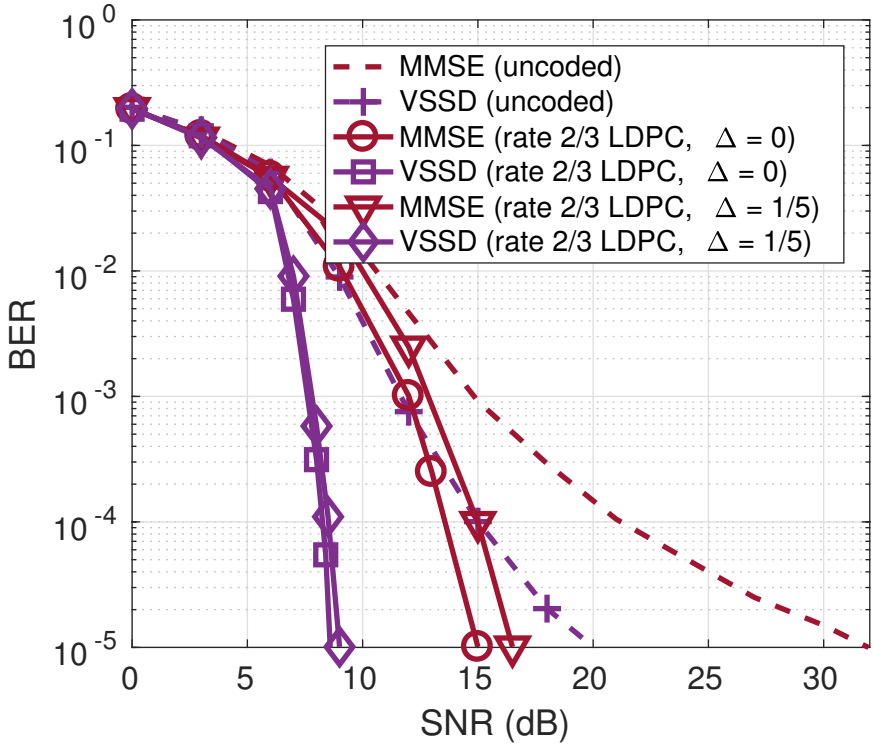

Figure 3.11: BER of VSSD and MMSE receivers for S2C communications over UWA channel simulated according to [72]. Δ denotes the variance of the i.i.d. zero-mean additive Gaussian noise by which the channel matrix entries are perturbed to simulate channel estimation errors.

$$H^{\mathrm{Im}}_{k,\mathrm{Re}}(t) = -\int_{\tau^{(k)}_{\min}(t)}^{\tau^{(k)}_{\max}(t)} h_{\mathrm{B,Re}}(t, t-\tau) g(\tau - kT) \sin\phi_{\mathrm{B}}(\tau) d\tau - \int_{\tau^{(k)}_{\min}(t)}^{\tau^{(k)}_{\max}(t)} h_{\mathrm{B,Im}}(t, t-\tau) g(\tau - kT) \cos\phi_{\mathrm{B}}(\tau) d\tau, \tag{3.45}$$

$$H^{\mathrm{Re}}_{k,\mathrm{Im}}(t) = \int_{\tau^{(k)}_{\min}(t)}^{\tau^{(k)}_{\max}(t)} h_{\mathrm{B,Re}}(t, t-\tau) g(\tau - kT) \sin\phi_{\mathrm{B}}(\tau) d\tau + \int_{\tau^{(k)}_{\min}(t)}^{\tau^{(k)}_{\max}(t)} h_{\mathrm{B,Im}}(t, t-\tau) g(\tau - kT) \cos\phi_{\mathrm{B}}(\tau) d\tau, \tag{3.46}$$

$$H^{\mathrm{Im}}_{k,\mathrm{Im}}(t) = \int_{\tau^{(k)}_{\min}(t)}^{\tau^{(k)}_{\max}(t)} h_{\mathrm{B,Re}}(t, t-\tau) g(\tau - kT) \cos\phi_{\mathrm{B}}(\tau) d\tau$$
$$- \int_{\tau^{(k)}_{\min}(t)}^{\tau^{(k)}_{\max}(t)} h_{\mathrm{B,Im}}(t, t-\tau) g(\tau - kT) \sin\phi_{\mathrm{B}}(\tau) d\tau, \tag{3.47}$$

$$\begin{aligned}
\phi_{\mathrm{B}}(t) &= 2\pi \left(f_L t_r(t) + m_c t_r^2(t) - f_c t \right), \\
\tau^{(k)}_{\min}(t) &= \max\{0, t - T_d, kT\}, \\
\tau^{(k)}_{\max}(t) &= \min\{t, T_c, (k+1)T\},
\end{aligned}$$

$w_{B,\mathrm{Re}}(t)$ and $w_{B,\mathrm{Im}}(t)$ are the real valued additive noises in the in-phase and quadrature channels. After sampling along t and τ axes, the received signal samples from (3.42)-(3.43) can be stacked and expressed in the form of (3.9). Entries of the channel matrix, $\mathbf{H} \in \mathbb{R}^{NL \times 2N}$, are found from discretized versions of (3.44)-(3.47). At time $t = nT_s$, the in-phase and quadrature measurement samples are given by

$$\mathbf{y}_B[n] = \sum_{k=0}^{N-1} \mathbf{H}_{n,k} \mathbf{s}_k + \mathbf{w}_B[n], \tag{3.48}$$

where $\mathbf{y}_B[n] = [y_{\mathrm{B,Re}}(nT_s), y_{\mathrm{B,Im}}(nT_s)]^T$, $\mathbf{H}_{n,k} \in \mathbb{R}^{2\times 2}$ is the block matrix,

$$\mathbf{H}_{n,k} = \begin{bmatrix} H^{\mathrm{Re}}_{k,\mathrm{Re}}(nT_s) & H^{\mathrm{Im}}_{k,\mathrm{Re}}(nT_s) \\ H^{\mathrm{Re}}_{k,\mathrm{Im}}(nT_s) & H^{\mathrm{Re}}_{k,\mathrm{Im}}(nT_s) \end{bmatrix} \in \mathbb{R}^{2\times 2}, \tag{3.49}$$

The channel matrix, $\mathbf{G}_{\mathrm{B}}$, after gradient heterodyne and lowpass filtering is given by

$$\mathbf{G}_{\mathrm{B}} = \mathbf{Q}_{\mathrm{B}}^T \mathbf{H} \in \mathbb{R}^{2N \times 2N}, \tag{3.50}$$

Table 3.3: S2C PARAMETERS USED IN SEC. 3.6.3

Frequency band ($f_L - f_H$)	10 - 18 kHz
Chirp rate ($2m_c$)	800 kHz/s
Symbol duration (T)	0.5 ms
Sweep duration (T_{sw})	10 ms
Guard interval (T_g)	25 ms

where $\mathbf{Q}_{\text{B}} = \text{diag}\{\mathbf{Q}_{\text{B},0}, \mathbf{Q}_{\text{B},1}, \ldots, \mathbf{Q}_{\text{B},N-1}\} \in \mathbb{R}^{2NL\times 2N}$,

$$\mathbf{Q}_{\text{B},k} = \text{diag}\left(\tilde{\mathbf{g}}\right) \begin{bmatrix} \mathbf{R}_{\phi_{\text{B}}^{(k)}[0]} + \mathbf{R}_{\phi_{\text{B}}^{(k)}[0]-\frac{\pi}{2}} \\ \mathbf{R}_{\phi_{\text{B}}^{(k)}[1]} + \mathbf{R}_{\phi_{\text{B}}^{(k)}[1]-\frac{\pi}{2}} \\ \vdots \\ \mathbf{R}_{\phi_{\text{B}}^{(k)}[L-1]} + \mathbf{R}_{\phi_{\text{B}}^{(k)}[L-1]-\frac{\pi}{2}} \end{bmatrix} \in \mathbb{R}^{2L\times 2},$$

$\mathbf{R}_\theta$ is the rotation matrix,

$$\mathbf{R}_\theta = \begin{bmatrix} \cos\theta & -\sin\theta \\ \sin\theta & \cos\theta \end{bmatrix} \in \mathbb{R}^{2\times 2},$$

$\tilde{\mathbf{g}} = [g[0], g[0], g[1], g[1], \ldots, g[L-1], g[L-1]]^T \in \mathbb{R}^{2L\times 1}$ and $\phi_{\text{B}}^{(k)}[l] = \phi_{\text{B}}\left((\tilde{k}-1)T + lT_s\right)$, $\tilde{k} = k - \lfloor \frac{k}{M} \rfloor M$, $l = 0, \ldots, L-1$.

Performance Evaluation: We now consider the performance of the proposed VSSD receiver over the WATERMARK channels for the S2C system in Table 3.3. The channel datasets NOF1 and NCS1 in WATERMARK have a delay (τ) coverage of $T_d = 128$ ms and $T_d = 32$ ms respectively. Therefore, the measured impulse response of NOF1 (NCS1) channel is available only at an interval of $\Delta t = 128$ ms ($\Delta t = 32$ ms) along the t-axis. To compute the entries of the channel matrix, $\mathbf{H}$ and hence $\mathbf{G}$, we require the channel impulse response at finer intervals corresponding to the baseband sampling frequency $F_s = 16$ kHz used in WATERMARK. We linearly interpolate the samples of measured baseband channel

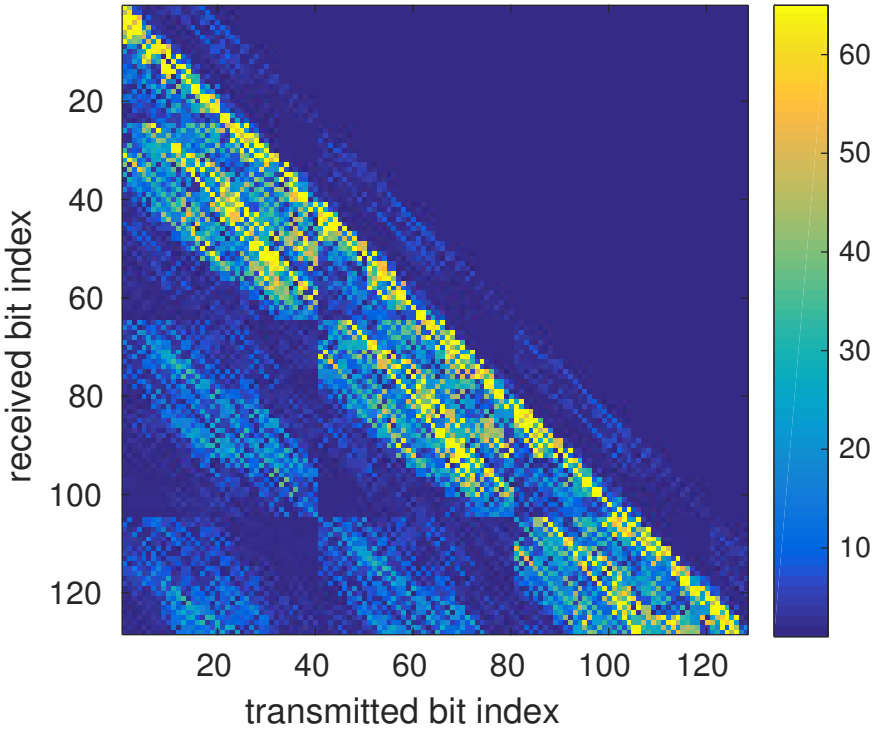

Figure 3.12: Channel matrix after GradH processing at an instance in the WATERMARK channel record NOF1.

impulse response to obtain the response at finer intervals.

For timing and synchronization, a chirp pulse of duration $T_p = 20$ ms in the frequency band 10-18 kHz, called preamble, is prefixed to the transmission waveform. A guard interval of $T_g = 25$ ms is inserted between the preamble and the start of modulated waveform to avoid interference. Note that, although the delay spread of NOF1 channel is $T_d = 128$ ms, the channel power delay profile falls by more than 20 dB beyond $T_g = 25$ ms. Matched filtering with the preamble waveform is used for detecting the start of the received waveform.

Figure 3.12 shows the computed channel matrix, $\mathbf{G}_{\mathrm{B}}$, for the first few bits in a received packet at one of the instances in the WATERMARK channel record NOF1. Significant ISI remains even after gradient hetrodyne and lowpass filtering, as indicated by the strong off-diagonal entries in matrix $\mathbf{G}_{\mathrm{B}}$.

Figure 3.13 shows the performance of VSSD and MMSE receivers on the WATERMARK channel NOF1. NOF1 is a stable channel with coherence time spanning over several

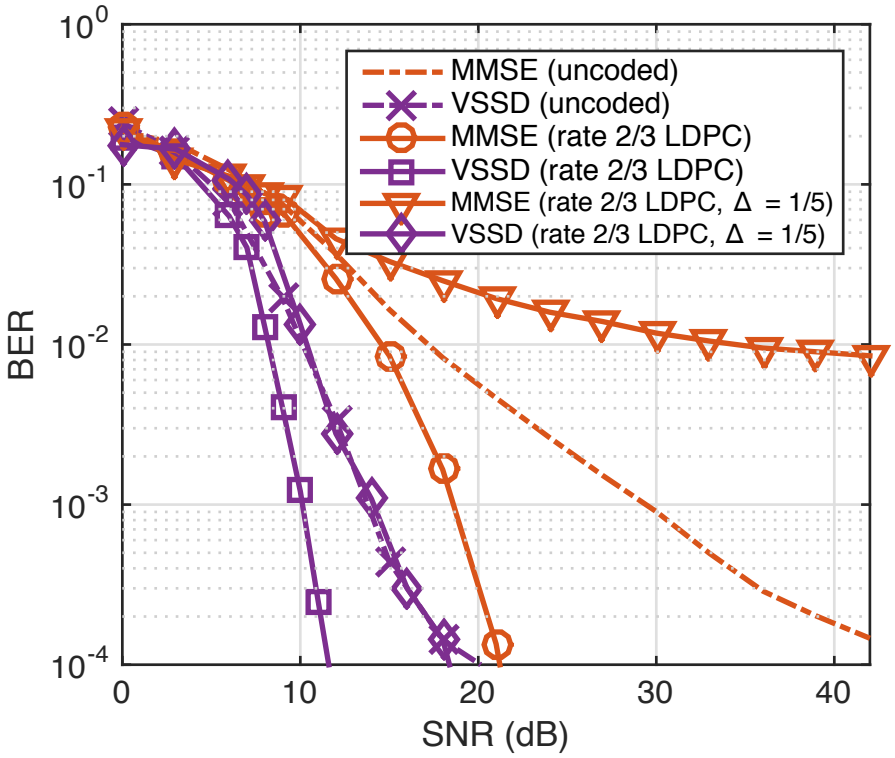

Figure 3.13: BER of VSSD and MMSE receivers for S2C communications over the NOF1 channel in WATERMARK. Δ denotes the variance of the i.i.d. zero-mean additive Gaussian noise by which the channel matrix entries are perturbed to simulate channel estimation errors.

seconds. VSSD outperforms MMSE receiver by a margin comparable to that in simulated UWA channels for both coded and uncoded communications in this real world channel also.

Figure 3.14 shows the BER of the proposed receiver on the NCS1 channel. NCS1 is characterized by a larger Doppler spread and therefore its impulse response varies significantly faster than NOF1. Both receivers require a higher SNR to achieve the same BER in NOF1 than NCS1. However, the strong relative performance of the VSSD receiver is maintained for both coded and uncoded communications even in this harsher UWA channel. While both NOF1 and NCS1 channels exhibit a comparable power delay profile, the coherence time of NCS1 is only about a tenth of a second that makes the channel

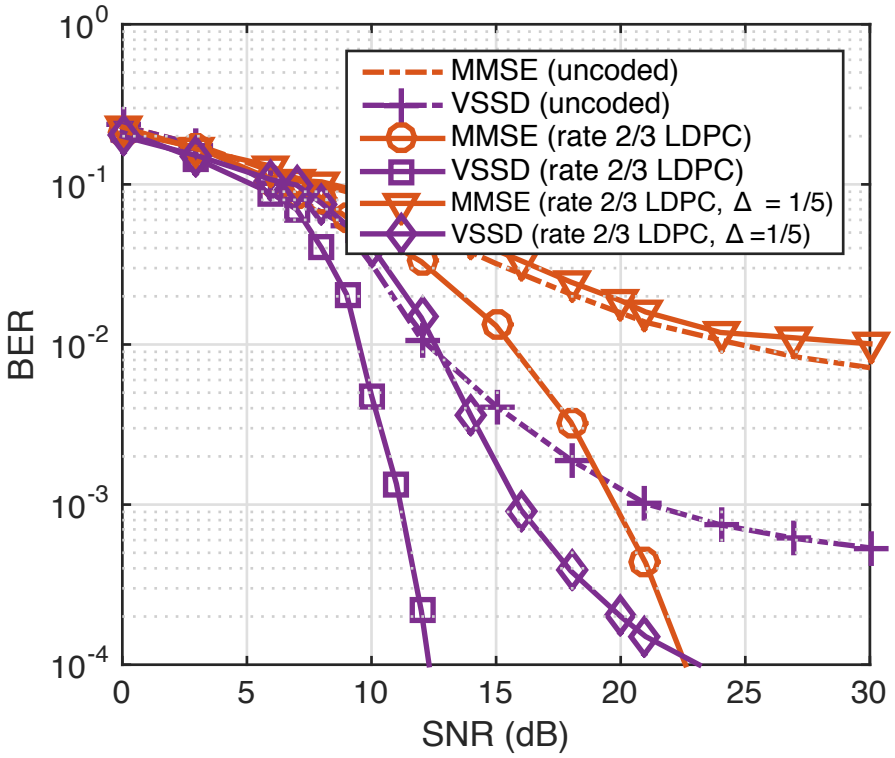

Figure 3.14: BER of VSSD and MMSE receivers for S2C communications over the NCS1 channel in WATERMARK. Δ denotes the variance of the i.i.d. zero-mean additive Gaussian noise by which the channel matrix entries are perturbed to simulate channel estimation errors.

prone to estimation errors. We see that, even in such challenging channel conditions as NCS1, VSSD is relatively resilient to channel estimation errors.

3.7 Conclusions

In this work, we considered data symbol detection in an S2C receiver for doubly spread UWA channels. We formulated the problem of data detection for S2C communications over a wideband delay-scale channel and showed that the two existing S2C receivers are near MMSE decoders in only certain benign UWA channels. In more severe channels, where the existing receivers either completely fail or must compromise on the data rate,

we developed a new soft symbol decoder based on variational Bayes' inference. The input to the new decoder is the reduced data measurements at the output of the gradient heterodyne preprocessor of the existing S2C receivers.

Our proposed VSSD decoder estimates a probability vector (soft symbols) whose KL-distance to the true posterior of the symbol vector is minimized by iterating through a fixed point equation. In benign UWA channels, the VSSD decoder reduces to the existing S2C receivers. We showed that the fixed point iterations converge to a stationary point of the evidence lower bound in variational inference. We presented a few sufficient conditions that help to characterize the stationary point as a global maximum, local maximum or saddle point. Simulation results showed that VSSD significantly outperforms the MMSE decoder and maintains a robust performance, even under channel estimation errors, in challenging UWA channels. We applied the VSSD decoder on two contrasting real world UWA channels in the publicly available WATERMARK datasets. The new decoder outperforms the MMSE decoder in these channels as well, by a margin comparable to that in simulated UWA channels.

The ideal PAPR and low probability of intercept properties of S2C communications make it a promising candidate for terrestrial radio-frequency (RF) communications as well. Also, the VSSD algorithm developed in this chapter is potentially applicable to other prevalent and emerging wireless communication systems.

3.8 Appendix: Evidence Lower Bound

We derive the ELBO for soft symbol estimation. The first term in (3.23) is given by

$$\mathbb{E}_{q_{\phi(\mathbf{s}|\mathbf{G},\mathbf{z})}} \log p_\theta(\mathbf{z}|\mathbf{G},\mathbf{s}) = -N\log(2\pi\sigma^2) - \mathbb{E}_{q_{\phi(\mathbf{s}|\mathbf{G},\mathbf{z})}}\left[\frac{\|\mathbf{z}-\mathbf{G}\mathbf{s}\|^2}{2\sigma^2}\right]. \tag{3.51}$$

Expanding the last term in (3.51), we get

$$\mathbb{E}_{q_{\phi(\mathbf{s}|\mathbf{G},\mathbf{z})}}\left[\|\mathbf{z}-\mathbf{G}\mathbf{s}\|^2\right] = \|\mathbf{z}\|^2 - 2\mathbf{z}^T\mathbf{G}\,\mathbb{E}_{q_{\phi(\mathbf{s}|\mathbf{G},\mathbf{z})}}[\mathbf{s}] + \mathbb{E}_{q_{\phi(\mathbf{s}|\mathbf{G},\mathbf{z})}}\left[\|\mathbf{G}\mathbf{s}\|^2\right]. \tag{3.52}$$

We define:

$$q_{k,\mathrm{Re}} \triangleq q_\phi \left(s_{k,\mathrm{Re}} = \frac{1}{\sqrt{2}} \middle| \mathbf{G}, \mathbf{z} \right) \in [0,1], \tag{3.53}$$

$$q_{k,\mathrm{Im}} \triangleq q_\phi \left(s_{k,\mathrm{Im}} = \frac{1}{\sqrt{2}} \middle| \mathbf{G}, \mathbf{z} \right) \in [0,1]. \tag{3.54}$$

Note that the approximate posterior is completely specified by the soft symbol vector $\mathbf{q} \in \mathbb{R}^{2N}$ formed by stacking up $\mathbf{q}_k = [q_{k^*,\mathrm{Re}}, q_{k^*,\mathrm{Im}}]^T \in \mathbb{R}^2, k = 0, 1, \ldots, N-1$. For our problem, we let the parameter $\phi \triangleq \mathbf{q}$.

The expectations in (3.52) can be evaluated as follows:

$$\mathbb{E}_{q_{\phi(\mathbf{s}|\mathbf{G},\mathbf{z})}} [s_{k,\mathrm{Re}}] = \frac{1}{\sqrt{2}} (2q_{k,\mathrm{Re}} - 1), \tag{3.55}$$

$$\mathbb{E}_{q_{\phi(\mathbf{s}|\mathbf{G},\mathbf{z})}} [s_{k,\mathrm{Im}}] = \frac{1}{\sqrt{2}} (2q_{k,\mathrm{Im}} - 1), \tag{3.56}$$

$$\mathbb{E}_{q_{\phi(\mathbf{s}|\mathbf{G},\mathbf{y})}} \left[\|\mathbf{Gs}\|^2 \right] = \sum_{l=0}^{2N-1} \mathbb{E}_{q_{\phi(\mathbf{s}|\mathbf{G},\mathbf{z})}} [\mathbf{Gs}]_l^2, \tag{3.57}$$

$$\mathbb{E}_{q_{\phi(\mathbf{s}|\mathbf{G},\mathbf{z})}} [\mathbf{Gs}]_l^2 = \sum_{k=0}^{N-1} \left(\eta_{l,k} + \nu_{l,k} \sum_{m \neq k} \nu_{l,m} \right), \tag{3.58}$$

where

$$\eta_{l,k} = \frac{1}{2} G_{l,k,\mathrm{Re}}^2 + \frac{1}{2} G_{l,k,\mathrm{Im}}^2 + G_{l,k,\mathrm{Re}} G_{l,k,\mathrm{Im}} (2q_{k,\mathrm{Re}} - 1)(2q_{k,\mathrm{Im}} - 1), \tag{3.59}$$

$$\nu_{l,m} = \frac{1}{\sqrt{2}} G_{l,m,\mathrm{Re}} (2q_{m,\mathrm{Re}} - 1) + \frac{1}{\sqrt{2}} G_{l,m,\mathrm{Im}} (2q_{m,\mathrm{Im}} - 1). \tag{3.60}$$

The ELBO regularizing term in (3.23) is

$$\mathbb{E}_{q_{\phi(\mathbf{s}|\mathbf{G},\mathbf{z})}} \left[\log \frac{q_\phi(\mathbf{s}|G, \mathbf{z})}{p_\theta(\mathbf{s})} \right] = KL(q_\phi || p_\theta). \tag{3.61}$$

We assume a uniform prior $p_\theta(\mathbf{s}) = \frac{1}{2^{2N}}$. We have:

$$\mathbb{E}_{q_{\phi(\mathbf{s}|G,\mathbf{z})}} \left[\log \frac{q_\phi(\mathbf{s}|G, \mathbf{z})}{p_\theta(\mathbf{s})} \right] = \log 2^{2N} - \sum_{k=0}^{N-1} \left[\mathcal{H}(q_{k,\mathrm{Re}}) + \mathcal{H}(q_{k,\mathrm{Im}}) \right], \tag{3.62}$$

where $\mathcal{H}$ is the binary entropy function given by

$$\mathcal{H}(q) = -q\log q - (1-q)\log(1-q). \tag{3.63}$$

On combining the likelihood and regularization terms, we find the overall ELBO to be

$$\begin{aligned}\mathcal{L}(\theta, \mathbf{q}, \mathbf{z}) = -N\log(2\pi\sigma^2) - \frac{\|\mathbf{z}\|^2}{2\sigma^2} + \frac{1}{\sqrt{2}\sigma^2}\mathbf{z}^T G(2\mathbf{q}-1) - \frac{1}{2\sigma^2}\sum_{l=0}^{2N-1}\sum_{k=0}^{N-1}\left(\eta_{l,k} + \nu_{l,k}\sum_{m\neq k}\nu_{l,m}\right) \\ - \log 2^{2N} + \sum_{k=0}^{N-1} -q_{k,\mathrm{Re}}\log q_{k,\mathrm{Re}} - (1-q_{k,\mathrm{Re}})\log(1-q_{k,\mathrm{Re}}) \\ + \sum_{k=0}^{N-1} -q_{k,\mathrm{Im}}\log q_{k,\mathrm{Im}} - (1-q_{k,\mathrm{Im}})\log(1-q_{k,\mathrm{Im}}).\end{aligned} \tag{3.64}$$

Known Noise Variance: In this case, we take θ to be the empty set. The derivative of the overall cost function with respect to $q_{k^*,\mathrm{Re}}$ is given by

$$\begin{aligned}\frac{\partial\mathcal{L}}{\partial q_{k^*,\mathrm{Re}}} = \frac{\sqrt{2}}{\sigma^2}\mathbf{z}^T\mathbf{G}_{:,k^*,\mathrm{Re}} - \frac{1}{2\sigma^2}\sum_{l=0}^{2N-1}\left(\frac{\partial\eta_{l,k^*}}{\partial q_{k^*,\mathrm{Re}}} + 2\frac{\partial\nu_{l,k^*}}{\partial q_{k^*,\mathrm{Re}}}\sum_{m\neq k^*}\nu_{l,m}\right) \\ - \log q_{k,\mathrm{Re}} + \log(1-q_{k,\mathrm{Re}}).\end{aligned} \tag{3.65}$$

We have $\frac{\partial\eta_{l,k}}{\partial q_{k,\mathrm{Re}}} = 2G_{l,k,\mathrm{Re}}G_{l,k,\mathrm{Im}}(2q_{k,\mathrm{Im}}-1)$ and $\frac{\partial\nu_{l,k}}{\partial q_{k,\mathrm{Re}}} = \sqrt{2}G_{l,k,\mathrm{Re}}$. The above can be simplified to

$$\frac{\partial\mathcal{L}}{\partial q_{k^*,\mathrm{Re}}} = \alpha_{k^*,\mathrm{Re}} - \log q_{k,\mathrm{Re}} + \log(1-q_{k,\mathrm{Re}}), \tag{3.66}$$

where

$$\alpha_{k^*,\mathrm{Re}} = \frac{\sqrt{2}}{\sigma^2}\mathbf{z}^T\mathbf{G}_{:,k^*,\mathrm{Re}} - \frac{1}{\sigma^2}\sum_{l=0}^{2N-1}G_{l,k^*,\mathrm{Re}}G_{l,k^*,\mathrm{Im}}(2q_{k^*,\mathrm{Im}}-1) - \frac{\sqrt{2}}{\sigma^2}\sum_{l=0}^{2N-1}G_{l,k^*,\mathrm{Re}}\sum_{m\neq k^*}\nu_{l,m}. \tag{3.67}$$

Setting $\frac{\partial\mathcal{L}}{\partial q_{k^*,\mathrm{Re}}} = 0$, we get $q_{k^*,\mathrm{Re}} = \varphi(\alpha_{k^*,\mathrm{Re}})$, where $\varphi(x) = \frac{1}{1+e^{-x}}$. Similarly, setting

$\frac{\partial \mathcal{L}}{\partial q_{k^*,\mathrm{Im}}} = 0$, we get $q_{k^*,\mathrm{Im}} = \varphi(\alpha_{k^*,\mathrm{Im}})$ where

$$\alpha_{k^*,\mathrm{Im}} = \frac{\sqrt{2}}{\sigma^2}\mathbf{z}^T\mathbf{G}_{:,k^*,\mathrm{Im}} - \frac{1}{\sigma^2}\sum_{l=0}^{2N-1} G_{l,k^*,\mathrm{Im}}G_{l,k^*,\mathrm{Re}}(2q_{k^*,\mathrm{Re}} - 1) - \frac{\sqrt{2}}{\sigma^2}\sum_{l=0}^{2N-1} G_{l,k^*,\mathrm{Im}}\sum_{m\neq k^*}\nu_{l,m}. \tag{3.68}$$

Stacking up $\mathbf{q}_k = [q_{k^*,\mathrm{Re}}, q_{k^*,\mathrm{Im}}]^T \in \mathbb{R}^2$ into a vector, we get the following fixed point equations:

$$\mathbf{q} = \varphi(\boldsymbol{\alpha}), \tag{3.69}$$

where the vector $\boldsymbol{\alpha} \in \mathbb{R}^{2N}$ is formed by stacking $\boldsymbol{\alpha}_k = [\alpha_{k^*,\mathrm{Re}}, \alpha_{k^*,\mathrm{Im}}]^T \in \mathbb{R}^2, k = 0, 1, \ldots, N-1$.

Unknown Noise Variance: In this case, we take $\theta = \{\sigma^2\}$. Differentiating the ELBO in (3.64) with respect to σ^2, we get

$$\frac{\partial \mathcal{L}}{\partial \sigma^2} = -\frac{N}{\sigma^2} + \frac{\|\mathbf{z}\|^2}{2\sigma^4} - \frac{1}{\sqrt{2}\sigma^4}\mathbf{z}^T\mathbf{G}(2\mathbf{q}-1) + \frac{1}{2\sigma^4}\sum_{l=0}^{2N-1}\sum_{k=0}^{N-1}\left(\eta_{l,k} + \nu_{l,k}\sum_{m\neq k}\nu_{l,m}\right). \tag{3.70}$$

Setting $\frac{\partial \mathcal{L}}{\partial \sigma^2} = 0$ and solving for σ^2, we find

$$\hat{\sigma}^2 = \frac{\|\mathbf{z}\|^2}{2N} - \frac{1}{\sqrt{2}N}\mathbf{z}^T\mathbf{G}(2\mathbf{q}-1) + \frac{1}{2N}\sum_{l=0}^{2N-1}\sum_{k=0}^{N-1}\left(\eta_{l,k} + \nu_{l,k}\sum_{m\neq k}\nu_{l,m}\right). \tag{3.71}$$

Unknown Channel and Noise Variance: In this case, we take $\theta = \{\sigma^2, \mathbf{G}\}$. To differentiate the ELBO with respect to $\mathbf{G}$, we notice that the terms in (3.64) that depend on $\mathbf{G}$ come from the left hand side of (3.52), i.e.,

$$\mathcal{L}_G = \mathbb{E}_{q_{\phi(\mathbf{s}|\mathbf{G},\mathbf{z})}}\left[(\mathbf{z}-\mathbf{G}\mathbf{s})^T(\mathbf{z}-\mathbf{G}\mathbf{s})\right]. \tag{3.72}$$

On differentiating $\mathcal{L}_G$ with respect to $G_{i,j}$ and setting to zero we get the following system of equations:

$$\mathbf{G}\overline{\mathbf{s}} = \mathbf{z}, \tag{3.73}$$

where $\overline{\mathbf{s}} \triangleq \mathbb{E}_{q_{\phi(\mathbf{s}|\mathbf{G},\mathbf{z})}}[\mathbf{s}]$. The jth entry of $\overline{\mathbf{s}}$ is given by $\overline{s}_j = \frac{1}{\sqrt{2}}(2q_j - 1)$, if a data symbol is mounted at jth symbol location. At locations where the pilot symbols are mounted (to facilitate channel estimation), we have $\overline{s}_j = p_j$, where p_j is a known pilot symbol mounted at jth location. The channel matrix estimate can be refined using (3.73) once an initial estimate of the soft symbol vector is obtained through the fixed point update in (3.69). Note that $\mathbf{G}$ has $4N^2$ entries that need to be estimated from $2N$ equations in (3.73). One way to accomplish this is to exploit channel sparsity as in [14]. To see that, we make use of the relation $\mathbf{G} = \mathbf{Q}^T\mathbf{H}$ and rewrite (3.73) in the form:

$$\mathbf{A}\mathbf{h} = \mathbf{z}, \tag{3.74}$$

where $\mathbf{A} = \sum_{i=0}^{N-1}\left(\overline{s}_{2i}\mathbf{Q}^T\mathbf{C}_i - \overline{s}_{2i+1}\mathbf{Q}^T\mathbf{S}_i\right) \in \mathbb{R}^{2N\times N_{\mathrm{P}}}$. Now, following the approach in [14], equation (3.74) can be readily turned into a form suitable for estimating the channel parameters $\{h_p, \tilde{\tau}_p, b_p : p = 0, 1, \ldots, N_{\mathrm{P}} - 1\}$. The expression for the noise variance is the same as in (3.71), and is evaluated during the iterations once the soft symbol vector and the channel estimates are obtained using the fixed point update and (3.73), respectively.

Chapter 4

Orthogonal Delay Scale Space Modulation

Orthogonal Time Frequency Space (OTFS) modulation is a recently proposed scheme for time-varying narrowband channels in terrestrial radio-frequency communications. Underwater acoustic (UWA) and ultra-wideband (UWB) communication systems, on the other hand, confront wideband time-varying channels. Unlike narrowband channels, for which time contractions or dilations due to Doppler effect can be approximated by frequency-shifts, the Doppler effect in wideband channels results in frequency-dependent non-uniform shift of signal frequencies across the band. In this paper, we develop an OTFS-like modulation scheme – Orthogonal Delay Scale Space (ODSS) modulation – for handling wideband time-varying channels. We derive the ODSS transmission and reception schemes from first principles. In the process, we introduce the notion of ω-*convolution* in the *delay-scale space* that parallels the *twisted convolution* used in the *time-frequency space*. The preprocessing 2D transformation from the Fourier-Mellin domain to the delay-scale space in ODSS, which plays the role of inverse symplectic Fourier transform (ISFFT) in OTFS, improves the bit error rate performance compared to OTFS and Orthogonal Frequency Division Multiplexing (OFDM) in wideband time-varying channels. Furthermore, since the channel matrix is rendered near-diagonal, ODSS retains the advantage of OFDM in terms of its low-complexity receiver structure.

4.1 Introduction

Orthogonal frequency division multiplexing (OFDM) is a spectrally efficient scheme for communication over frequency-selective channels. The scheme is particularly attractive in practice because a low complexity receiver side processing based on a subcarrier-by-subcarrier equalization recovers the data symbols in a delay spread channel. Receivers based on subcarrier-by-subcarrier equalizer, however, fail in a time-varying channel, resulting in severe degradation of communication performance. Orthogonal Time Frequency Space (OTFS) modulation is a recently proposed technique for use in frequency-selective and Doppler spread narrowband channels [27–30, 66, 77]. OFDM and OTFS techniques do not perform well in doubly-spread wideband channels where the effect of Doppler is to cause a time-scaling in the received waveform.

In high mobility *narrowband* channels, characterized by both delay spread (due to multipath) and Doppler spread (due to time variations and/or mobility), the OTFS scheme achieves a near constant gain channel for each subcarrier. The scheme employs special transformations at the transmitter to mount the information symbols on the carrier waveform, and corresponding inverse transformations to recover those symbols at the receiver. In wideband channels where the Doppler manifests as a time-scaling of the received waveform, however, the channel is no longer flat-fading across the OTFS subcarriers. The extent of detriment caused by a seemingly small time-scale factor, such as $\alpha = 1.001$, in wideband channels, if not handled well, is akin to the consequences narrated in [67]. Simply increasing the transmission power does not help in recovering the data from a waveform affected by Doppler. In [67], the navigation experts had to alter the descent trajectory of Huygens (transmitting probe) such that its descent to Titan (Saturn's moon) is almost perpendicular to the line joining Cassini (receiver). This contains the radial component of probe's velocity, thereby mitigating the stretching of the communication waveform due to Doppler. Avoiding Doppler is not possible in all practical situations. Our goal in this work is to develop a modulation scheme, suitable for *wideband* time-varying channels, with a demodulation counterpart that can be implemented as a low complexity receiver.

Wideband and ultra-wideband channel models abound in the literature on wireless

communications [8,21,25,42,58,61,64,65,78,82,105,108]. High mobility wireless channels are of topical interest in broadband high speed radio-frequency communications [4,24,32, 103]. Wideband time-varying channel models are commonly used in underwater acoustic communications also [19, 39, 40, 57, 72, 74, 80, 86, 90]. Several studies have considered the problem of communicating data over wideband doubly-spread channels [3, 14, 20, 22, 34, 36, 51, 52, 62, 81, 89, 106]. Two approaches have been explored in the literature. One approach is to estimate and compensate for the effect of Doppler in the received signal, equalize the effect of delay spread, and decode the data symbols [41, 51, 52, 62]. Despite such compensation, residual Doppler in the processed signal affects the communication performance in a multipath environment, since different paths are associated with different amounts of Doppler. The residual Doppler causes inter carrier interference (ICI) in multi-carrier communication systems. The second approach uses computationally expensive receivers that account for the ICI in data detection [14, 34, 36, 81, 106]. The recently proposed OTFS scheme is specifically developed to handle doubly-spread narrowband channels, and offer high performance, but at the cost of a more sophisticated message-passing based receiver architecture. To the best of our knowledge, no such scheme has been proposed in the literature for the case of wideband doubly-spread channels.

In this chapter, we systematically develop the processing blocks of a new modulation scheme – Orthogonal Delay Scale Space (ODSS) modulation. Specifically, inspired by the development of OTFS in [27, 28] for narrowband time-varying channels, we parallel its development by identifying the transformations necessary to handle the time-scaling effect of a wideband time-varying channel. Our contributions in this work are:

1. We derive the ODSS transmission and reception schemes from first principles. We identify the modulation and demodulation operations that are required for handling the time-scaling effect of wideband time-varying channels. In particular, we introduce a preprocessing 2D transformation from the Fourier-Mellin domain to the delay-scale space in ODSS. This transform plays the role of inverse symplectic Fourier transform (ISFFT) in OTFS. In contrast to the constant spectral width of the OFDM and OTFS subcarriers, the subcarriers of ODSS have a spectral width

that is proportional to the subcarrier frequency, which makes ODSS suitable for time-scale spread channels.

2. We introduce the notions of *ω-convolution* and *robust bi-orthogonality* in the *delay-scale space*. These parallel the notions of twisted convolution and robust bi-orthogonality, respectively, in the *time-frequency space* in the OTFS scheme.

3. We analytically derive conditions on the parameter values of the ODSS scheme that results in an ICI-free symbol reception at the receiver. As a consequence, the ODSS receiver is a low complexity processor that uses a subcarrier-by-subcarrier equalizer as in the case of OFDM over a time-invariant inter symbol interference channel.

4. We compare the performance of the ODSS scheme with OFDM and OTFS that uses a low complexity receiver based on subcarrier-by-subcarrier equalization. The ODSS receiver registers more than 100 fold reduction in the bit error rate (BER) compared to the OFDM and OTFS receivers employing subcarrier-by-subcarrier equalizers at an SNR of 24 dB.

Wideband doubly-spread (also known as multi-scale multi-lag) channels are found in underwater acoustic (UWA) and ultra wideband (UWB) radio communications. Low complexity subcarrier-by-subcarrier equalizers of standard OFDM and OTFS receivers suffer from performance impairment whose severity increases with Doppler spread. The ODSS scheme using subcarrier-by-subcarrier equalizer based receiver, developed in this paper, is therefore promising in such channels, particularly in applications that require a low complexity receiver.

We briefly describe the narrowband and wideband time-varying channel models in Section 4.2. In Section 4.3, we review the OTFS scheme devised for narrowband time-varying channels. We present the Mellin transformation and its properties in Section 4.4, which forms a part of the preprocessing transformation in the ODSS scheme. In Section 4.5, we develop the ODSS modulation and demodulation schemes and derive conditions on its parameters to make its output ICI-free. Section 4.6 discusses practical aspects of choosing transmit and receive filters that result in nearly ICI-free ODSS outputs. Finally,

through numerical simulations, we investigate the performance of ODSS in Section 4.7 and conclude in Section 4.8.

4.2 Doubly Spread Channel Models

A transmitted signal undergoes three changes when passing through a delay-scale propagation channel: (a) amplitude change due to path loss and fading, (b) delay, τ, corresponding to the length of the path traversed, and (c) time-scaling by a factor, $\alpha = \frac{c-v}{c+v}$, due to Doppler effect, where v is the velocity of a scatterer and c is the speed of the wave in the propagation medium. Multiple propagation paths can result in a continuum of delay and scale parameters, i.e., $\tau \in [\tau_l, \tau_h]$ and $\alpha \in [\alpha_l, \alpha_h]$. Such a *doubly-spread* propagation channel is characterized by the wideband spreading function, $h(\tau, \alpha)$, that corresponds to the amplitude gain of the time-scaled and delayed copy of the transmitted signal reaching the receiver along a reflected path. The received signal is a superposition of the amplitude-scaled, time-scaled, and delayed versions of the transmitted signal, $s(t)$, given by [25]

$$r_s(t) = \iint h(\tau, \alpha)\sqrt{\alpha} s\left(\alpha(t-\tau)\right) d\tau d\alpha, \tag{4.1}$$

where we have omitted the limits of integration, which we do throughout this paper, for notational brevity. Note that the scaling by $\sqrt{\alpha}$ in the integrand above preserves the energy of the time-scaled copy of the transmitted signal, since $\int \left|\sqrt{\alpha} s(\alpha t)\right|^2 dt = \int |s(t)|^2 dt$.

The delay-scale channel representation used in (4.1) is called the *wideband channel model*. Modeling the Doppler effect by approximating the time-scale by a frequency shift, i.e., using $\nu \approx (\alpha - 1) f_c$, where f_c is the center frequency of the signal band, leads to the narrowband model. The narrowband approximation holds if two conditions are met [39]:

(A-1) Signal has a small fractional bandwidth: $B/f_c \ll 1$, where B is the signal bandwidth, and

(A-2) The receiver moves slowly relative to the transmitter, such that its position does

not change significantly compared to the positional resolution of the signal: $v \ll \frac{c}{2BT}$, where T is the signal duration.[1]

Under the assumptions above, the signal reflected by a scatterer moving with velocity v and arriving along a path of delay, $\tau \in [\tau_l, \tau_h]$, is given by $s_{\tau,\nu} = s(t-\tau)e^{j2\pi\nu(t-\tau)}$, where $j = \sqrt{-1}$, and $\nu = (\alpha - 1)f_c \approx -\frac{2v}{c} f_c \in [\nu_l, \nu_h]$ is the frequency shift due to the Doppler effect [84]. Making the change of variables $\alpha \to \nu$: $\alpha = 1 + \nu/f_c$ in (4.1), noting that $\sqrt{\alpha}s\left(\alpha(t-\tau)\right) \approx s_{\tau,\nu} = s(t-\tau)e^{j2\pi\nu(t-\tau)}$ under narrowband assumptions, and defining the narrowband channel spreading function to be $h_{\tau,\nu}(\tau,\nu) \triangleq \frac{1}{f_c} h(\tau, \alpha = 1+\nu/fc)$, we get the following expression for the received signal at the output of a narrowband channel [25,28]:

$$r_s(t) = \iint h(\tau,\nu) s\left(t-\tau\right) e^{j2\pi\nu(t-\tau)} d\tau d\nu, \tag{4.2}$$

where we drop the subscripts in $h(\tau,\nu)$ for notational brevity.

Remark 1: Violation of either (A-1) or (A-2) would require one to model the channel as wideband. For example, UWA communications over a frequency band of 10-20 kHz has a fractional bandwidth of $B/f_c = 0.67$ ($B/f_c > 0.25$ is considered high [39]). The low speed of sound in water also results in a high v/c ratio ($10^{-3} - 10^{-1}$) that violates (A-2). Similarly, large time-bandwidth product ($10^5 - 10^6$) UWB radio-frequency communications may violate (A-2) [39, 61]. For example, a radio-frequency UWB communication with $BT = 10^6$, from a high-speed train traveling at $v = 270$ km/h, clearly violates (A-2).

Remark 2: The notion of *wideband channel* we use here is different from the definition of a *wideband system* used in the communications literature. A wideband system is one for which the signaling (messaging) bandwidth significantly exceeds the coherence bandwidth ($\propto \frac{1}{\tau_h - \tau_l}$) of the channel. The notion of wideband channel we use here is related to the frequency-dependent effect of the Doppler whereas the latter definition is related to the channel delay-spread.

In the next section, we review the development of OTFS communication for the narrowband channel model as prelude to the development of ODSS for wideband channels,

[1] In the case of OFDM, T is the duration of an OFDM symbol.

which is the main contribution of this paper.

4.3 Review of OTFS Communication

OTFS converts a narrowband time-varying delay-spread wireless channel into a time-independent channel represented by a complex gain [27–30]. OFDM communication, on the other hand, converts a static (i.e., Doppler-free) multipath channel into a single tap channel, thus completely eliminating inter symbol interference (ISI). It has been shown that OTFS reduces to asymmetric OFDM (A-OFDM) in static multipath channels [77]. In narrowband time-varying delay-spread channels that arise in high mobility scenarios, OTFS receivers using turbo, message passing or MMSE equalizers outperform OFDM receivers using a sphere decoder or MMSE equalizer [28, 30, 77]. We briefly describe the transmitter and receiver of an OTFS communication system and the propagation of the OTFS signal over narrowband time-varying delay-spread channels in the following subsections, primarily, to setup some notations in the paper.

4.3.1 OTFS Transmitter

OTFS transmitter, shown in Fig. 4.1, comprises the OTFS transform followed by the Heisenberg transform. The data (information bits) to be communicated, after bit-to-symbol mapping, are multiplexed onto a discrete 2D delay-Doppler domain grid of size $N \times M$. The OTFS transform maps the information symbols (e.g., QAM symbols), $x[k,l]$, in the discrete delay-Doppler space to the 2D sequence, $X[n,m]$, in the time-frequency domain by means of an inverse symplectic Fourier transform (ISFFT) as follows:

$$X[n,m] = \frac{1}{NM} \sum_{l=0}^{M-1} \sum_{k=0}^{N-1} x[k,l] e^{j2\pi\left(\frac{nl}{N} - \frac{mk}{M}\right)}, \tag{4.3}$$

where $m \in \{0,1,\ldots,M-1\}, n \in \{0,1,\ldots,N-1\}$. The (N,M) periodized version of the input (respectively, output) 2D sequence, $x_p[k,l]$ (resp. $X_p[n,m]$), of the ISFFT reside on the lattice (reciprocal lattice), $\Lambda^{\perp} \triangleq \{(k\Delta\tau, l\Delta\nu) : k,l \in \mathbb{Z}\}$ (respectively, $\Lambda \triangleq$

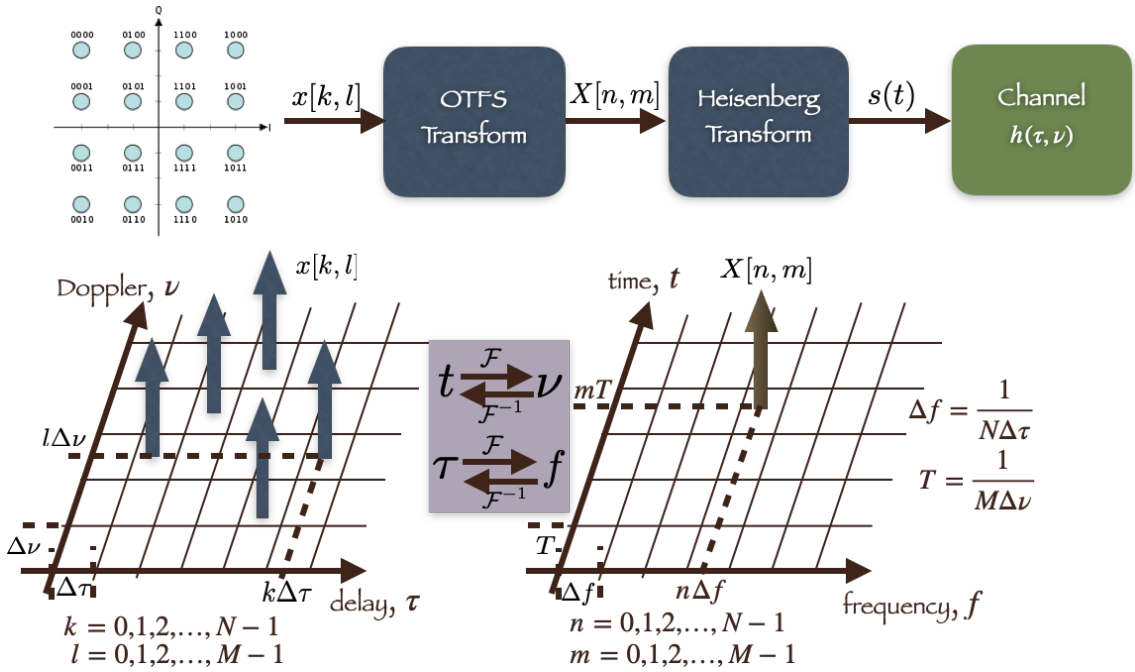

Figure 4.1: OTFS transmission scheme

$\{(mT, n\Delta f) : m, n \in \mathbb{Z}\}$), where T and Δf are the spacings on time and frequency axes, and

$$\Delta\tau = \frac{1}{N\Delta f}, \ \Delta\nu = \frac{1}{MT}, \tag{4.4}$$

are the spacings on the delay and Doppler domain respectively. The Heisenberg transform converts the 2D time-frequency data, $X[n, m]$, to a 1D continuous time-series, $s(t)$, given by

$$s(t) = \sum_{m=0}^{M-1} \sum_{n=0}^{N-1} X[n, m] e^{j2\pi n\Delta f(t-mT)} g_{\text{tx}}(t - mT), \tag{4.5}$$

where $g_{\text{tx}}(t)$ is the transmit pulse shaping function. We assume that the transmitted signal, $s(t)$, satisfies the narrowband assumption (A-1).

The Heisenberg transform can be viewed as a map parametrized by the 2D time-frequency sequence, $X[n, m]$, and producing $s(t)$ when fed with g_{tx}, i.e., $s(t) = \Pi_X(g_{\text{tx}}(t))$:

$$s(t) = \int_\nu \int_\tau X(\tau, \nu) e^{j2\pi\nu(t-\tau)} g_{\text{tx}}(t - \tau) d\tau d\nu, \tag{4.6}$$

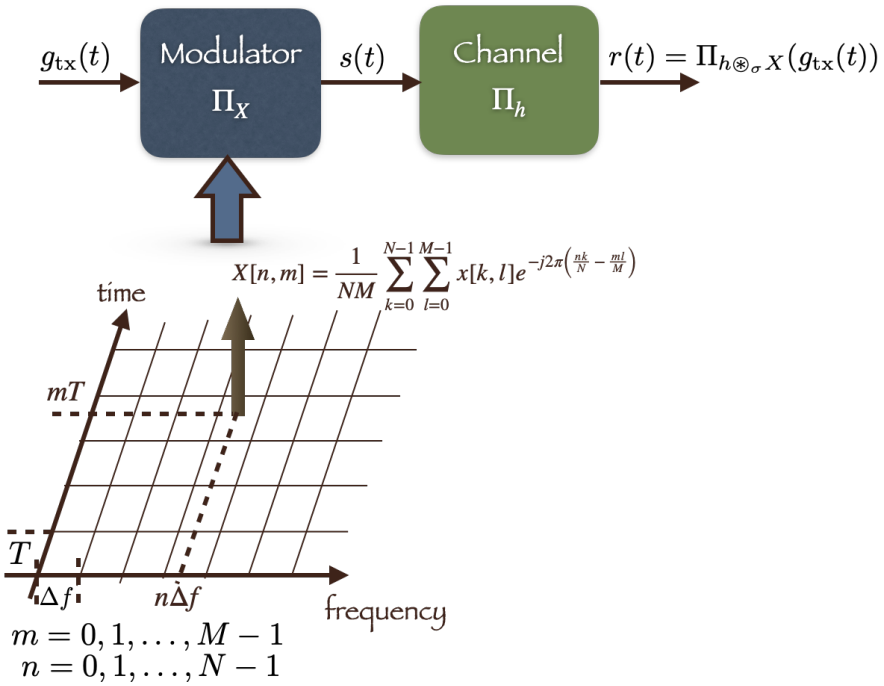

Figure 4.2: Cascade of OTFS modulator and propagation channel

where

$$X(\tau, \nu) = \sum_{m=0}^{M-1} \sum_{n=0}^{N-1} X[n,m] \delta(\tau - mT, \nu - n\Delta f), \tag{4.7}$$

with $\delta(\cdot)$ denoting the Dirac delta function. The above interpretation of the Heisenberg transform is helpful in relating the input and output of the OTFS system in the next subsection.

4.3.2 OTFS Signal Propagation

The signal, at the OTFS receiver, after propagating through a narrowband channel is given by $r(t) = r_s(t) + w(t)$, where $r_s(t)$ is the output of a narrowband channel as in (4.2) and $w(t)$ is the additive noise. As shown in [28], the received signal, $r_s(t)$, can be expressed as

$$r_s(t) = \Pi_f(g_{\text{tx}}(t)) = \int_\nu \int_\tau f(\tau, \nu) e^{j2\pi\nu(t-\tau)} g_{\text{tx}}(t-\tau) d\tau d\nu, \tag{4.8}$$

where f is the *twisted convolution* of h and X, denoted by $h \circledast_\sigma X$, defined as follows:

$$f(\tau,\nu) = \int_{\nu'}\int_{\tau'} h(\tau',\nu')X(\tau-\tau',\nu-\nu')e^{j2\pi\nu'(\tau-\tau')}d\tau' d\nu', \tag{4.9}$$

which, due to (4.7), can be written as a finite sum:

$$f(\tau,\nu) = \sum_{n=0}^{N-1}\sum_{m=0}^{M-1} h(\tau-mT,\nu-n\Delta f)X[n,m]e^{j2\pi(\nu-n\Delta f)mT}. \tag{4.10}$$

The received signal is, therefore, a result of passing the transmit pulse shaping function through an equivalent channel parameterized by the twisted convolution of the physical channel and the data dependent 2D time-frequency signal. Fig. 4.2 depicts this interpretation. The signal received by the OTFS receiver, including the additive noise $w(t)$, is given by

$$r(t) = r_s(t) + w(t) = \Pi_{h\circledast_\sigma X}(g_{\text{tx}}(t)) + w(t). \tag{4.11}$$

4.3.3 OTFS Receiver

The receiver performs OTFS demodulation followed by equalization and symbol decoding. OTFS demodulation is a two step process: discrete Wigner transform followed by symplectic Fourier transform (SFFT). The discrete Wigner transform (inverse of the discrete Heisenberg transform) is obtained by sampling the cross-ambiguity function between the received signal, $r(t)$, and a receive pulse shaping function, $g_{\text{rx}}(t)$. The demodulated time-frequency signal is given by

$$\hat{Y}[n,m] = A_{g_{\text{rx}},r}(\tau,\nu)|_{\tau=mT,\nu=n\Delta f}, \tag{4.12}$$

where

$$A_{g_{\text{rx}},r}(\tau,\nu) \triangleq \int_t e^{-j2\pi\nu(t-\tau)} g^*_{\text{rx}}(t-\tau)r(t)dt = A_{g_{\text{rx}},r_s}(\tau,\nu) + A_{g_{\text{rx}},w}(\tau,\nu). \tag{4.13}$$

It can be shown that

$$A_{g_{\rm rx},r_s}(\tau,\nu) = f(\tau,\nu) \circledast_\sigma A_{g_{\rm rx},g_{\rm tx}}(\tau,\nu) = \sum_{n=0}^{N-1}\sum_{m=0}^{M-1} X[n,m] H_{n,m}(\tau,\nu), \tag{4.14}$$

where

$$H_{n,m}(\tau,\nu) \triangleq \int_{\nu''}\int_{\tau''} h(\tau'',\nu'') e^{j2\pi\nu'' mT} A_{g_{\rm rx},g_{\rm tx}}(\tau-\tau''-mT, \nu-\nu''-n\Delta f) \times e^{j2\pi(\nu''+n\Delta f)(\tau-\tau''-mT)} d\tau'' d\nu''. \tag{4.15}$$

At this point, it is assumed that

1. the channel response, $h(\tau,\nu)$, has a finite support bounded by $(\tau_{\max},\nu_{\max})$, and
2. *bi-orthogonality* of transmit and receive pulses holds in a robust manner [28], i.e., the cross-ambiguity function vanishes in a neighborhood around the *non-zero* lattice points, $(mT, n\Delta f)$: $A_{g_{\rm rx},g_{\rm tx}}(\tau,\nu) = 0$, for $\tau \in (mT-\tau_{\max}, mT+\tau_{\max})$ and $\nu \in (n\Delta f - \nu_{\max}, n\Delta f + \nu_{\max})$ except around the lattice point corresponding to $m = 0, n = 0$.

Due to the above assumptions, upon sampling at $\tau = m_0 T$ and $\nu = n_0\Delta f$, we find $H_{n,m}[n_0,m_0] = 0$ whenever $n \neq n_0$ or $m \neq m_0$, so that (4.14) simplifies to

$$A_{g_{\rm rx},r_s}[n_0,m_0] = H_{n_0,m_0}[n_0,m_0] X[n_0,m_0], \tag{4.16}$$

where[2]

$$H_{n_0,m_0}[n_0,m_0] = \int_\nu\int_\tau e^{-j2\pi\nu\tau} h(\tau,\nu) A_{g_{\rm rx},g_{\rm tx}}(\tau,\nu) e^{j2\pi(\nu m_0 T - n_0\Delta f\tau)} d\tau d\nu. \tag{4.17}$$

Note that we choose $T \geq 2\tau_{\max}$ and $\Delta f \geq 2\nu_{\max}$ to avoid ISI and ICI, respectively, and

[2]Many papers on OTFS, either explicitly or implicitly, assume $A_{g_{\rm rx},g_{\rm tx}}(\tau,\nu) = 1$ in a neighborhood of $(\tau = 0, \nu = 0)$ contained in the support of $h(\tau,\nu)$. It is unclear if there are practical transmit and receive pulse shaping functions that satisfy this assumption, so we retain the term $A_{g_{\rm rx},g_{\rm tx}}(\tau,\nu)$ in the integrand in (4.17).

hence ensure the validity of (4.16). This means that, for a given N and M (and hence the number of symbols NM), the duration and bandwidth of the transmitted OTFS signal, $s(t)$, must be at least $2M\tau_{\max}$ and $2N\nu_{\max}$, respectively. The spectral efficiency of the OTFS scheme can, therefore, be at most $\frac{1}{4\tau_{\max}\nu_{\max}}$ symbols/s/Hz in a channel with a delay spread $\tau_{\max}$ and Doppler spread $\nu_{\max}$. These choices, according to (4.4), result in $\Delta\tau \leq \frac{1}{2N\nu_{\max}}$ and $\Delta\nu \leq \frac{1}{2M\tau_{\max}}$ in the delay-Doppler plane. Consider an OTFS transmit signal of bandwidth, $N\Delta f = 2N\nu_{\max}$, which is the minimum required bandwidth to avoid ICI. As the narrowband assumption requires the signal bandwidth to satisfy $N\Delta f < \kappa f_c$, where $\kappa \ll 1$, we must choose $N < \kappa\frac{f_c}{2\nu_{\max}}$. Clearly, barring implementation aspects, there is no such upper limit on the choice of M.

The output of the discrete Wigner transform is, therefore, given by

$$\hat{Y}[n,m] = H_{n,m}[n,m]X[n,m] + W[n,m], \tag{4.18}$$

where $W[n,m] = A_{g_{\text{rx}},w}(\tau,\nu)|_{\tau=mT,\nu=n\Delta f}$ is the additive noise in the discrete time-frequency space. The OTFS demodulator output is obtained by taking SFFT of the discrete Wigner transform output:

$$\begin{aligned} \hat{y}[k,l] &= \sum_{m=0}^{M-1}\sum_{n=0}^{N-1} \hat{Y}[n,m]e^{-j2\pi\left(\frac{nl}{N}-\frac{mk}{M}\right)}, & (4.19)\\ &= \sum_{m=0}^{M-1}\sum_{n=0}^{N-1} x[n,m]h_v\left(\frac{k-m}{MT},\frac{l-n}{N\Delta f}\right) + w[k,l], & (4.20) \end{aligned}$$

where $h_v(.,.)$ is obtained by sampling $\left(\nu = \frac{k-m}{MT}, \tau = \frac{l-n}{N\Delta f}\right)$ the function

$$\begin{aligned} h_v(\nu,\tau) &= \sum_{n=0}^{N-1}\sum_{m=0}^{M-1} H_{n,m}[n,m]e^{j2\pi(\tau n\Delta f-\nu mT)}\\ &= \iint e^{-j2\pi\nu'\tau'}h(\tau',\nu')A_{g_{\text{rx}},g_{\text{tx}}}(\tau',\nu')v(\nu-\nu',\tau-\tau')d\tau' d\nu', \end{aligned} \tag{4.21}$$

where $v(\nu,\tau) = \sum_{m=0}^{M-1}\sum_{n=0}^{N-1} e^{j2\pi(\tau n\Delta f-\nu mT)}$ is a periodic function on the $\tau-\nu$ plane with

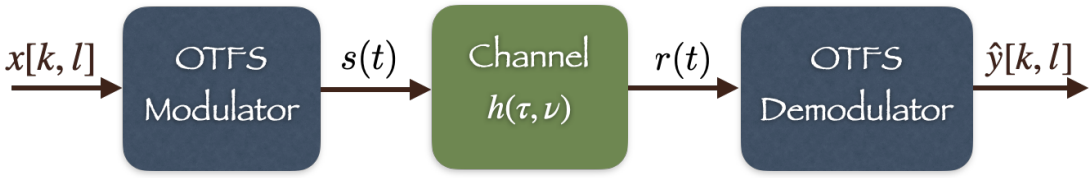

Figure 4.3: OTFS Block Diagram

periods $N\Delta\tau$ and $M\Delta\nu$ in delay and Doppler, respectively.

Equation (4.20) depicts the input-output relation in an OTFS system that can be written in the following vectorized form:

$$\mathbf{y} = \mathbf{H}\mathbf{x} + \mathbf{w}, \tag{4.22}$$

where $\mathbf{y} \in \mathbb{C}^{NM\times 1}$ is the output of the OTFS demodulator whose $(k + Nl)$-th entry is $y[k, l]$, $\mathbf{H} \in \mathbb{C}^{NM\times NM}$ is the effective channel matrix, $\mathbf{x} \in \mathbb{C}^{NM\times 1}$ is the symbol vector whose $(k + Nl)$-th entry is $x[k, l]$ and $\mathbf{w} \in \mathbb{C}^{NM\times 1}$ is the additive noise at the OTFS demodulator output. Fig. 4.3 summarizes various stages at a block level from the input to output of an OTFS system.

Equalization and symbol decoding is performed after OTFS demodulation to recover the transmitted information bits. In OTFS modulation, developed for the narrowband channel model in (4.2), the information symbols were mounted on the delay-Doppler grids. Fourier and inverse Fourier transforms were made use of to move between τ and f domains, and between t and ν domains, respectively. In the new ODSS modulation, to be developed for the wideband channel model in (4.1), we shall make use of the Mellin and inverse Mellin transforms to move between the scale (α) domain and Mellin (β) domain, respectively. We next present the Mellin transform and its discrete counterpart before we develop the ODSS modulation scheme for wideband delay-scale channels.

4.4 Mellin Transform and its Properties

The Mellin transform was developed in [15] as a solution to the problem of finding the transform that enjoys a *scale-invariance* property, i.e., the Mellin transform of the signal

$\sqrt{a}x(a\alpha), a > 0, \alpha > 0$, is same as that of the original signal, $x(\alpha)$, except for a phase shift. The Mellin transform of a signal $x(\alpha), \alpha > 0$, is defined by

$$\mathcal{M}_x(\beta) \triangleq \int_0^\infty \frac{1}{\sqrt{\alpha}} x(\alpha) e^{j2\pi\beta \log(\alpha)} d\alpha, \tag{4.23}$$

where $\beta \in \mathbb{R}$ is the Mellin variable. The Mellin transform exists for signals, $x(\alpha)$, in the Hilbert space $\mathcal{L}^2\left(\mathbb{R}^+, \frac{d\alpha}{\sqrt{\alpha}}\right)$ which is the set of square integrable functions ($\mathcal{L}^2$-functions) over $\mathbb{R}^+$, attached with a measure $\frac{d\alpha}{\sqrt{\alpha}}$ instead of $d\alpha$. We may interpret Mellin transform as the Fourier transform of the function $\sqrt{e^t}x(e^t), t \in \mathbb{R}$ [83].

We state a few important properties that make Mellin transform attractive for working with time-scaling effect of Doppler in wideband channels [15, 39].

1. The scale-invariance property of the Mellin transform follows from the definition in (4.23): the Mellin transform of the scaled version $\sqrt{a}x(a\alpha), a > 0$, of $x(\alpha)$ is given by $a^{-j2\pi\beta}\mathcal{M}_x(\beta)$ which is the same as the Mellin transform of the original signal except for a phase shift. Note that this scale-invariance property parallels the shift-invariance property of the Fourier transform: the Fourier transform of $x(t-\tau)$ is $e^{-j2\pi f\tau}X(f)$ where $X(f)$ is the Fourier transform of $x(t)$ [68].

2. The Mellin transform of the dilation-invariant product of two functions $x_1(\alpha)$ and $x_2(\alpha)$, defined by $(x_1 \circ x_2)(\alpha) = \sqrt{\alpha}x_1(\alpha)x_2(\alpha)$, is given by the linear convolution of the Mellin transforms of the two functions: $\mathcal{M}_{x_1 \circ x_2}(\beta) = \mathcal{M}_{x_1}(\beta) \circledast \mathcal{M}_{x_2}(\beta)$.

3. The geometrical Dirac comb, $\Delta_A(\alpha) = \sum_{n=-\infty}^{\infty} A^{n/2}\delta(\alpha - A^n)$, in the scale-space, $\mathbb{R}^+$, transforms to an arithmetical comb in the Mellin space, $\mathcal{M}_{\Delta_A}(\beta) = \frac{1}{\ln A}\sum_{n=-\infty}^{\infty}\delta(\beta - \frac{n}{\ln A})$.

4. Parseval's theorem: $\int_{-\infty}^{\infty}\mathcal{M}_{x_1}(\beta)\mathcal{M}^*_{x_2}(\beta)d\beta = \int_0^\infty x_1(\alpha)x_2^*(\alpha)d\alpha$.

5. The Mellin transform of the multiplicative convolution of two functions $x_1(\alpha)$ and $x_2(\alpha)$, defined by $(x_1 \vee x_2)(\alpha) = \int_0^\infty \sqrt{\alpha}x_1(\alpha')x_2(\frac{\alpha}{\alpha'})\frac{d\alpha'}{\alpha'}$, is given by the product of the Mellin transforms of the two functions: $\mathcal{M}_{x_1 \vee x_2}(\beta) = \mathcal{M}_{x_1}(\beta)\mathcal{M}_{x_2}(\beta)$.

6. The inverse Mellin transform is given by

$$x(\alpha) \triangleq \frac{1}{\sqrt{\alpha}} \int_{-\infty}^{\infty} \mathcal{M}_x(\beta) e^{-j2\pi\beta \log(\alpha)} d\beta, \alpha > 0, \tag{4.24}$$

which follows immediately upon noting the relation between the Mellin and Fourier transforms.

We now consider the effect of discretization on Mellin transform relations [15,16]. First, consider geometric sampling in the scale domain (α-domain) with ratio q. The Mellin transform of the sampled version of $x(\alpha)$, i.e., $x_s(\alpha) \triangleq (x \circ \Delta_q)(\alpha) = \sum_{n=-\infty}^{\infty} q^{n/2} x(q^n)\delta(\alpha - q^n)$, is given by

$$\begin{aligned} \mathcal{M}_{x_s}(\beta) &= \mathcal{M}_{x\circ\Delta_q}(\beta) \\ &\overset{(a)}{=} \mathcal{M}_x(\beta) \circledast \mathcal{M}_{\Delta_q}(\beta) \\ &\overset{(b)}{=} \frac{1}{\ln q} \sum_{n=-\infty}^{\infty} \mathcal{M}_x\left(\beta - \frac{n}{\ln q}\right) \qquad (4.25) \\ &\triangleq \mathcal{M}_x^P(\beta), \qquad (4.26) \end{aligned}$$

where the step (a) follows from the fact that Mellin transform of a dilation-invariant product in the scale domain corresponds to the convolution of Mellin transforms in the Mellin domain, and step (b) follows upon an evaluation of the convolution in step (a). Therefore, geometric sampling in the scale domain leads to periodization in the Mellin domain. Aliasing due to scale domain geometric sampling is avoided if:

1. the Mellin spectrum is β-limited, i.e., $\mathcal{M}_x(\beta)$ is nonzero only in a finite interval $[\beta_1, \beta_2]$, and

2. the geometric sampling ratio, q, satisfies

$$\frac{1}{\ln q} \geq \beta_2 - \beta_1. \tag{4.27}$$

Next, consider sampling the Mellin domain function, $\mathcal{M}_x(\beta)$. Sampling in the Mellin

space results in

$$M_s(\beta) \triangleq \frac{1}{\ln Q} \sum_{n=-\infty}^{\infty} \mathcal{M}_x\left(\frac{n}{\ln Q}\right) \delta\left(\beta - \frac{n}{\ln Q}\right) \tag{4.28}$$

$$\stackrel{(c)}{=} \mathcal{M}_x(\beta)\mathcal{M}_{\Delta_Q}(\beta)$$

$$\stackrel{(d)}{=} \mathcal{M}_{x \vee \Delta_Q}(\beta), \tag{4.29}$$

where equality (c) follows from the formula for the Mellin transform of a geometric impulse train in the scale domain, and (d) follows from the fact that multiplicative convolution in scale domain corresponds to the product of the Mellin transforms. We see that the sampled version of the Mellin transform of $x(\alpha)$, i.e., $M_s(\beta)$, is the inverse Mellin transform of the *dilatocycled* version of $x(\alpha)$ given by

$$x_d(\alpha) \triangleq (x \vee \Delta_Q)(\alpha) = \sum_{n=-\infty}^{\infty} Q^{n/2} x(Q^n \alpha). \tag{4.30}$$

Thus, sampling in the Mellin domain leads to dilatocycling in the scale domain. Aliasing due to Mellin domain sampling is avoided if:

1. the signal in the scale domain has a finite support, $[\alpha_1, \alpha_2]$, and
2. the dilatocycling ratio, Q, satisfies: $Q \geq \frac{\alpha_2}{\alpha_1}$.

In the absence of aliasing, $x_d(\alpha)$ equals $x(\alpha)$ for $\alpha \in [\alpha_1, \alpha_2]$.

Finally, the discrete Mellin transformation is obtained by geometric sampling of the finitely supported and dilatocycled signal $x_d(\alpha), \alpha \in [\alpha_1, \alpha_2]$, in the scale domain. The sampled version of $x_d(\alpha)$ is given by

$$x_{ds}(\alpha) \triangleq (x_d \circ \Delta_q)(\alpha) = \sum_{n=-\infty}^{\infty} q^{n/2} x_d(q^n) \delta(\alpha - q^n). \tag{4.31}$$

It is clear from the discussions above that the Mellin transform of $x_{ds}(\alpha)$ is the periodized version of $M_s(\beta)$:

$$\mathcal{M}_{x_{ds}}(\beta) = M_s^P(\beta) \triangleq \frac{1}{\ln q} \sum_{n=-\infty}^{\infty} M_s\left(\beta - \frac{n}{\ln q}\right), \tag{4.32}$$

where we require $\frac{1}{\ln q} \geq \beta_2 - \beta_1$ to avoid aliasing. Substituting $M_s(\beta)$ from (4.28) in (4.32) and restricting $Q = q^N$, where N is a positive integer, we get:

$$M_s^P(\beta) = \frac{1}{\ln q \ln Q} \sum_{m=-\infty}^{\infty} \sum_{n=-\infty}^{\infty} \mathcal{M}_x\left(\frac{m}{N \ln q}\right) \delta\left(\beta - \frac{nN+m}{\ln q}\right). \tag{4.33}$$

Changing $m \to k = m + nN$ and using the definition of periodized version, we get

$$M_s^P(\beta) = \frac{1}{\ln Q} \sum_{k=-\infty}^{\infty} \mathcal{M}_x^P\left(\frac{k}{N \ln q}\right) \delta\left(\beta - \frac{k}{\ln q}\right). \tag{4.34}$$

It is now straightforward to show that the discrete Mellin transform relationship is given by

$$\mathcal{M}_x^P\left(\frac{k}{\ln Q}\right) = \sum_{n=J}^{J+N-1} q^{n/2} x_d(q^n) e^{j2\pi nk/N}, \tag{4.35}$$

where J is the integer part of $\ln \alpha_1 / \ln q$. The transform length $N = \frac{\ln Q}{\ln q}$ must satisfy the condition

$$N \geq (\beta_2 - \beta_1) \ln\left(\frac{\alpha_2}{\alpha_1}\right), \tag{4.36}$$

to avoid aliasing and allow reconstruction of the scale and Mellin domain functions from their samples.

Similarly, the discrete inverse Mellin transform is given by

$$x_d(q^n) = \frac{q^{-n/2}}{N} \sum_{k=K_i}^{K_i+N-1} \mathcal{M}_x^P\left(\frac{k}{\ln Q}\right) e^{-j2\pi kn/N}, \tag{4.37}$$

where K_i is the integer part of $\beta_1 \ln Q$.

4.5 ODSS Communication For Wideband Channels

We now turn to developing the ODSS modulation. The goal of ODSS modulation is to convert a wideband, time-varying, delay-scale spread channel into a time-independent channel represented by a complex gain. To this end, we introduce the 2D *ODSS transform* (and its inverse) which is a combination of discrete Fourier transform on one axis (the delay axis) and inverse Mellin transform on the other (the scale axis.) The development of ODSS parallels the development of OTFS in Section 4.3. In the process, we appropriately modify the two key properties – twisted convolution property and robust biorthogonality – that were used in the development of OTFS. We develop the transmitter and receiver of an ODSS communication system and the propagation of the signal over wideband time-varying channels in the following subsections, which is the main contribution of this work. While we develop ODSS in a manner similar to the development of OTFS, we note that the two modulation schemes are distinct and do not generalize or reduce to each other.

4.5.1 ODSS Transmitter

The information bits, after bit-to-symbol mapping, are multiplexed onto the discrete 2D Mellin-Fourier domain of size, $M_{\text{tot}} = \sum_{n=0}^{N-1} M(n)$, where $M(n) = \lfloor q^n \rfloor$. The ODSS transform maps the data symbols (e.g., QAM symbols), $\{x[k,l] : k = 0, 1, \ldots, N-1, l = 0, 1, \ldots, M(k)\}$, in the discrete Mellin-Fourier space to the 2D sequence, $X[n,m]$, in the scale-delay domain by taking an inverse discrete Mellin transform along the scale axis (see (4.37)) and a discrete Fourier transform along the delay axis, as follows:

$$X[n,m] = \frac{q^{-n/2}}{N} \sum_{k=0}^{N-1} \frac{\sum_{l=0}^{M(k)-1} x[k,l] e^{j2\pi\left(\frac{ml}{M(k)} - \frac{nk}{N}\right)}}{M(k)}, \tag{4.38}$$

where $m \in \{0, 1, \ldots, M(n)-1\}, n \in \{0, 1, \ldots, N-1\}$. The periodized version of the input (respectively, output) 2D sequence, $x_p[k,l]$ (resp. $X_p[n,m]$), reside on the lattice (reciprocal lattice), $\Lambda^{\perp} = \{(k\Delta\beta, l\Delta f) : k, l \in \mathbb{Z}\}$ (resp. $\Lambda = \{(m\Delta\tau, q^n) : m, n \in \mathbb{Z}\}$), where $\Delta\beta = \frac{1}{N \ln q}$, Δf, $\Delta\tau$ are the spacings on the Mellin, Fourier and delay axes,

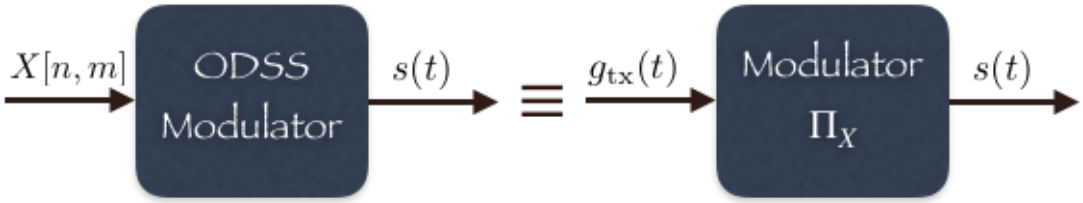

Figure 4.4: ODSS Modulator Representation

respectively; $\Delta\tau = \frac{1}{W}$, $W \triangleq M\Delta f$, and q is the geometric sampling ratio on the scale axis. The sampling ratio, q, and discrete Mellin transform length, N, are chosen to satisfy the conditions in (4.27) and (4.36). We may express (4.38) in the vectorized form:

$$\mathbf{X} = \mathcal{T}_{\text{iMF}}\mathbf{x}, \tag{4.39}$$

where $\mathbf{x} \in \mathbb{C}^{M_{\text{tot}}\times 1}$ is the symbol vector obtained by stacking $x[k,l]$ into a vector, $\mathbf{X} \in \mathbb{C}^{M_{\text{tot}}\times 1}$ is the vector obtained by stacking $X[n,m]$, and $\mathcal{T}_{\text{iMF}} \in \mathbb{C}^{M_{\text{tot}}\times M_{\text{tot}}}$ is the matrix representing the 2D ODSS transform in (4.38).

The ODSS modulator converts the 2D time-frequency data, $X[n,m]$, to a 1D continuous time-series, $s(t)$, given by

$$s(t) = \sum_{n=0}^{N-1}\sum_{m=0}^{M(n)-1} X[n,m]q^{n/2}g_{\text{tx}}\left(q^n\left(t - \frac{m}{q^nW}\right)\right), \tag{4.40}$$

where $g_{\text{tx}}(t)$ is the transmit pulse shaping function of duration $T = 1/W$. The ODSS modulation can be viewed as a map parametrized by the 2D Mellin-Fourier sequence, $X[n,m]$, and producing $s(t)$ when fed with g_{tx}, i.e., $s(t) = \Pi_X(g_{\text{tx}}(t))$:

$$s(t) = \iint X(\tau,\alpha)\sqrt{\alpha}g_{\text{tx}}(\alpha(t-\tau))d\tau d\alpha, \tag{4.41}$$

where

$$X(\tau,\alpha) = \sum_{n=0}^{N-1}\sum_{m=0}^{M(n)-1} X[n,m]\delta(\tau - \frac{m}{q^nW}, \alpha - q^n). \tag{4.42}$$

The above interpretation of the ODSS transform, depicted in Fig. 4.4, is helpful in relating the input and output of an ODSS communication system in the next subsection.

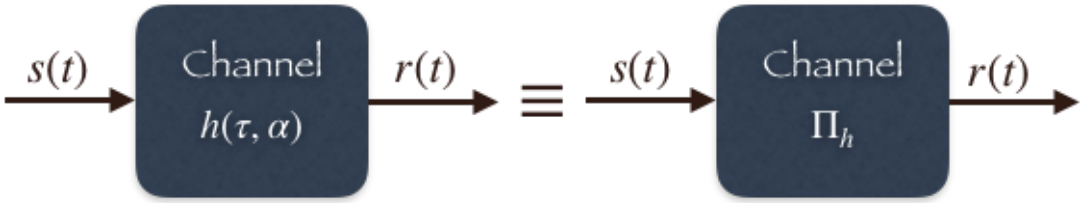

Figure 4.5: Wideband Channel Representation

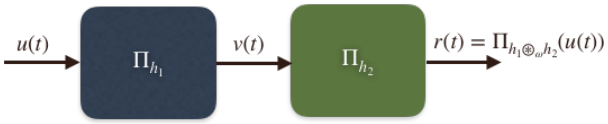

Figure 4.6: ω-convolution

4.5.2 ODSS Signal Propagation

The signal, at the ODSS receiver, after propagating through a wideband delay-scale channel is given by $r(t) = r_s(t) + w(t)$, where $r_s(t)$ is as in (4.1), and $w(t)$ is the additive noise.

We may, equivalently, view the propagation channel as performing the map $\Pi_h(s) : s(t) \to r_s(t)$ as shown in Fig. 4.5. Next, we introduce the notion of ω-convolution to describe the equivalent of the cascade of the ODSS modulator and the propagation channel.

The cascade of two delay-scale channels, as shown in Fig. 4.6, is equivalent to a single channel, i.e., $\Pi_{h_2}(\Pi_{h_1}(s)) = \Pi_h(s)$, where $h(\tau, \alpha) = h_2(\tau, \alpha) \circledast_\omega h_1(\tau, \alpha)$ and the symbol $\circledast_\omega$ denotes the ω-convolution defined by

$$h(\tau, \alpha) = \iint h_2(\tau', \alpha') h_1\left(\alpha'(\tau - \tau'), \frac{\alpha}{\alpha'}\right) d\tau' d\alpha'. \tag{4.43}$$

The derivation of the above is provided in the supplementary material in Sec. 4.9.1.

In light of the above result, we may write the signal after propagation through the channel, $r_s(t)$, as

$$r_s(t) = \Pi_{h \circledast_\omega X}(g_{\text{tx}}) = \iint f(\tau, \alpha) \sqrt{\alpha} g_{\text{tx}}(\alpha(t - \tau)) d\tau d\alpha$$

where $f(\tau, \alpha)$ is given by (see Sec. 4.9.2 in the supplementary material):

$$f(\tau, \alpha) = \sum_n \sum_m X[n, m] h\left(\tau - \frac{m}{\alpha W}, \frac{\alpha}{q^n}\right) q^{-n}.$$

The received signal is, therefore, a result of passing the transmit pulse shaping function through an equivalent channel parameterized by the ω-convolution of the physical channel and the data dependent 2D delay-scale signal. Fig. 4.7 depicts this interpretation. The signal received by the ODSS receiver, including the additive noise $w(t)$, is given by

$$r(t) = r_s(t) + w(t) = \Pi_{h \circledast_\omega X}(g_{\text{tx}}(t)) + w(t). \tag{4.44}$$

4.5.3 ODSS Receiver

The ODSS receiver performs ODSS demodulation followed by equalization and symbol decoding. ODSS demodulation is a two step process: extracting the transmitted scale-delay signal followed by an inverse ODSS transform. We describe the two steps in the following two subsections.

4.5.3.1 Scale-delay signal extraction

The scale-delay signal is extracted by sampling the cross-ambiguity function between the received signal and the pulse shaping function at the receiver side. The demodulated scale-delay signal is given by

$$\hat{Y}[n, m] = A_{g_{\text{rx}}, r}(\tau, \alpha)|_{\tau = \frac{m}{q^n W}, \alpha = q^n}, \tag{4.45}$$

where

$$\begin{aligned} A_{g_{\text{rx}}, r}(\tau, \alpha) &\triangleq \int g_{\text{rx}}^*(\alpha(t - \tau)) \sqrt{\alpha} r(t) dt \\ &= A_{g_{\text{rx}}, r_s}(\tau, \alpha) + A_{g_{\text{rx}}, w}(\tau, \alpha). \end{aligned} \tag{4.46}$$

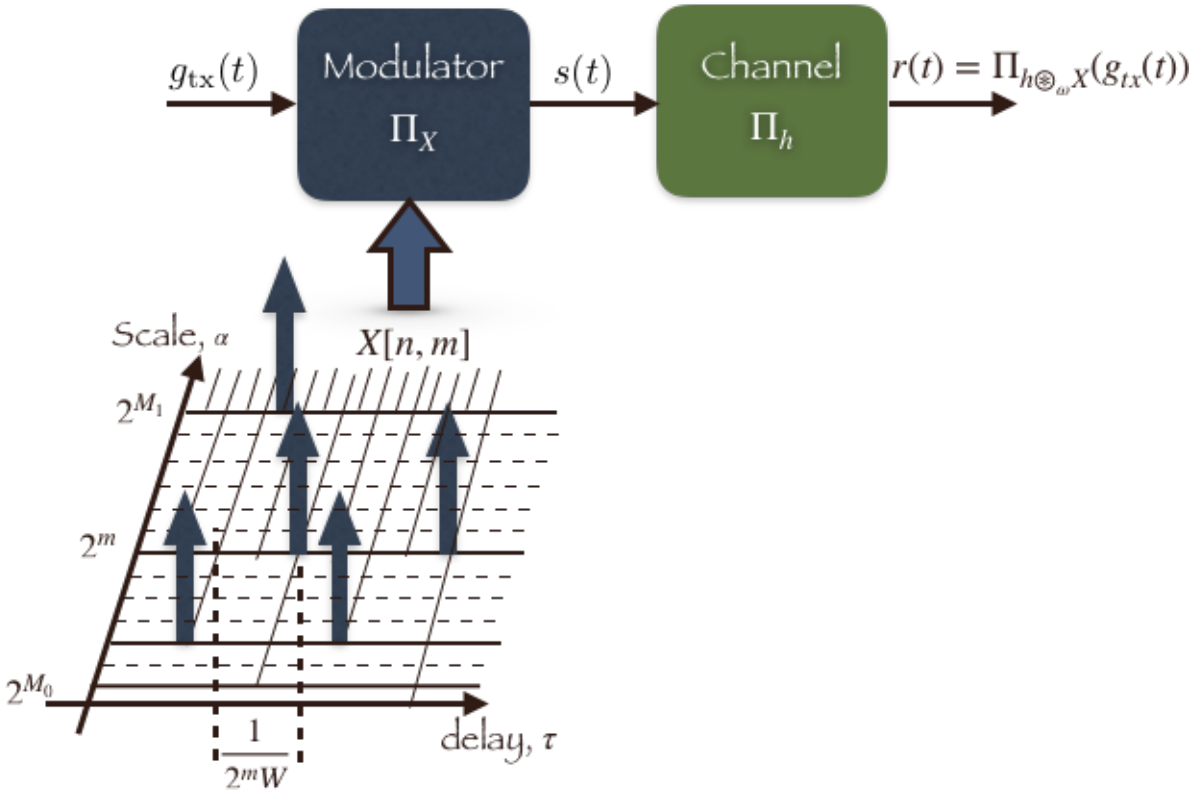

Figure 4.7: Received ODSS signal

It is shown in the supplementary material, Sec. 4.9.3, that

$$A_{g_{\text{rx}},r_s}(\tau,\alpha) = \sum_n \sum_m X[n,m] H_{n,m}(\tau,\alpha), \tag{4.47}$$

where

$$H_{n,m}(\tau,\alpha) = \iint h(\tau'',\alpha'') A_{g_{\text{rx}},g_{\text{tx}}}\left(\alpha'' q^n \left(\tau - \frac{m}{\alpha'' q^n W} - \tau''\right), \frac{\alpha}{\alpha'' q^n}\right) d\tau'' d\alpha''.$$

We assume that

1. the channel response has a finite support, i.e., $h(\tau,\alpha)$ is non-zero only for $-\tau_{\max} \leq \tau \leq \tau_{\max}$ and $\frac{1}{\alpha_{\max}} \leq \alpha \leq \alpha_{\max}$, where $\alpha_{\max} \geq 1$, and

2. *robust bi-orthogonality* holds between the transmit and receive pulses in the following manner. The cross-ambiguity function vanishes in the neighborhood of all lattice points $(\frac{m}{q^n W}, q^n)$ *except* $(0,1)$ corresponding to $m = 0$ and $n = 0$. That is,

$A_{g_{\rm rx},g_{\rm tx}}(\tau,\alpha)=0$ for $\tau\in(\frac{m}{q^nW}-\tau_{\max},\frac{m}{q^nW}+\tau_{\max})$ and $\alpha\in(q^n/\alpha_{\max},q^n\alpha_{\max})$ except when $m=0$ and $n=0$.[3]

Then, on sampling at $\tau=\frac{m_0}{q^{n_0}W}$ and $\alpha=q^{n_0}$, we find that $H_{n,m}[n_0,m_0]=0$ whenever $n\neq n_0$ or $m\neq m_0$, and

$$H_{n_0,m_0}[n_0,m_0]=\iint h(\tau',\alpha')A_{g_{\rm rx},g_{\rm tx}}\left(q^{n_0}\left(\frac{m_0}{q^{n_0}W}(\alpha'-1)-\alpha'\tau'\right),\frac{1}{\alpha'}\right)d\tau' d\alpha'. \quad (4.48)$$

so that the noise free part of the extracted scale-delay signal is given by

$$A_{g_{\rm rx},r_s}[n_0,m_0] \;=\; H_{n_0,m_0}[n_0,m_0]X[n_0,m_0]. \quad (4.49)$$

Consider, for example, a channel without delay and Doppler spread: $h(\tau,\alpha)=h_0\delta(\tau,\alpha-1)$. In this case, we find: $H_{n,m}(\tau,\alpha)=A_{g_{\rm rx},g_{\rm tx}}\left(\tau-\frac{m}{q^nW},\frac{\alpha}{q^n}\right)$. Upon sampling at $\tau=\frac{m_0}{q^{n_0}W}$ and $\alpha=q^{n_0}$, due to robust bi-orthogonality, $H_{n,m}[n_0,m_0]=0$ whenever $n\neq n_0$ or $m\neq m_0$, and

$$H_{n_0,m_0}[n_0,m_0]=h_0A_{g_{\rm rx},g_{\rm tx}}(0,1)=h_0,$$

so that, in this special case, the noise free part of the extracted scale-delay signal is given by

$$A_{g_{\rm rx},r_s}[n_0,m_0]=h_0X[n_0,m_0]. \quad (4.50)$$

Therefore, for an ideal channel without delay and Doppler spread, the ODSS scheme produces a constant gain for all signal components in the extracted delay-scale domain.

In general, we find from (4.49) that the ODSS scheme leads to an ISI free, time-independent, scalar complex channel gain for each *delay-scale* domain output at the receiver. The extracted delay-scale signal at the ODSS receiver is, therefore, given by

$$\hat{Y}[n,m]=H_{n,m}[n,m]X[n,m]+W[n,m], \quad (4.51)$$

[3]Bi-orthogonality cannot be satisfied exactly; our choice of waveforms for ODSS implementation is discussed in Section 4.6

where $W[n,m] = A_{g_{\rm rx},w}(\tau,\alpha)|_{\tau=\frac{m}{q^n W},\alpha=q^n}$ is the additive noise in the discrete delay-scale space.

To avoid ICI, and hence obtain (4.49), we need to

1. choose q such that:
$$\frac{q^{n'}}{\alpha'' q^n} \notin \left(\alpha_{\max}^{-1}, \alpha_{\max}\right), \tag{4.52}$$
$\forall \alpha'' \in (\alpha_{\max}^{-1}, \alpha_{\max})$, whenever $n' \neq n$, and

2. choose q and W such that:
$$\alpha'' q^n \left(\frac{m'}{W} - \frac{m}{\alpha'' q^n W} - \tau''\right) \notin (-\tau_{\max}, \tau_{\max}), \tag{4.53}$$
$\forall \tau'' \in (-\tau_{\max}, \tau_{\max})$ and $\alpha'' \in (\alpha_{\max}^{-1}, \alpha_{\max})$, whenever $m' \neq m$.

We first choose the geometric sampling ratio, q, to meet the condition in (4.52). If $n' > n$, we want $q^{n'-n} \geq \alpha_{\max}\alpha''$, which is satisfied if: $\forall n' > n, q^{n'-n} \geq \alpha_{\max}^2$, i.e., if $q \geq \alpha_{\max}^2$. Similarly, if $n' < n$, we require $q^{n'-n} \leq \alpha''\alpha_{\max}^{-1}$ which is met if: $\forall n' < n, q^{n'-n} \leq \alpha_{\max}^{-2}$, i.e., if $q \geq \alpha_{\max}^2$. Therefore, we may choose

$$q = \alpha_{\max}^2. \tag{4.54}$$

Clearly, since $\alpha_{\max} \geq 1$, we have $q \geq 1$. Aside, we also note that the choice of q in (4.54) together with the robust bi-orthogonality property renders $A_{g_{\rm rx},g_{\rm tx}}(\tau,\alpha) = 0$, $\alpha \notin (\alpha_{\max}^{-1}, \alpha_{\max})$.

Next, with q as in (4.54), we choose W to satisfy the condition in (4.53). The condition in (4.53) is equivalent to

$$\inf_{(\tau'',\alpha'')\in S} \left|\alpha''\alpha_{\max}^{2n} m' - m - \alpha''\alpha_{\max}^{2n}\tau'' W\right| \geq W\tau_{\max}, \tag{4.55}$$

whenever $m' \neq m$, where $S \triangleq \{(\tau'',\alpha'') : \tau'' \in (-\tau_{\max}, \tau_{\max}), \alpha'' \in (\alpha_{\max}^{-1}, \alpha_{\max})\}$. The condition in (4.55) places an upper bound on W, as we shall soon see.

First, consider a channel without Doppler, i.e., $\alpha_{\max} = 1$, in which case the condition

in (4.55) specializes to

$$\inf_{(\tau'',1)\in S} |m' - m - \tau'' W| \geq W\tau_{\max}, \tag{4.56}$$

whenever $m' \neq m$. The condition in (4.56), for a Doppler-free channel, is satisfied if we choose

$$W \leq \frac{1}{2\tau_{\max}}. \tag{4.57}$$

This implies that the duration of the transmitted signal, $s(t)$, must be larger than $2M\tau_{\max}$ in a Doppler-free channel having a delay spread of $2\tau_{\max}$. The choices $W = \frac{1}{2\tau_{\max}}$ and $q = 1$ for a Doppler-free channel, and the robust bi-orthogonality property, render the cross ambiguity $A_{g_{\rm rx},g_{\rm tx}}(\tau, 1) = 0$, $\tau \notin (-\tau_{\max}, \tau_{\max})$. Notice that, for a Doppler-free channel, with the choice of $q = 1$ we must use $N = 1$ and the ODSS modulation scheme defaults to asymmetric OFDM (A-OFDM), which is a scheme that converts delay-spread channels into a single tap complex channel in the Fourier domain. This behavior is very similar to the OTFS modulation scheme [77].

Finally, we discuss the choice of W in ODSS modulation for a doubly-spread delay-scale channel that is both delay-spread and Doppler-distorted. Let $m' > m$. Now, if the condition in (4.55) is satisfied by $m' = m + 1$, then it will be satisfied by every $m' > m$. The expression $|\alpha''\alpha_{\max}^{2n} m' - m - \alpha''\alpha_{\max}^{2n}\tau'' W|$, in (4.55), is minimized by $\alpha'' = \alpha_{\max}^{-1}$ and $\tau'' = \tau_{\max}$, when W is such that $W\tau_{\max} < 1$, and hence $\alpha''\alpha_{\max}^{2n} m' - m - \alpha''\alpha_{\max}^{2n}\tau'' W > 0$. For these settings, with $m' = m + 1$, we find that $|\alpha''\alpha_{\max}^{2n} m' - m - \alpha''\alpha_{\max}^{2n}\tau'' W| \geq W\tau_{\max} \implies \alpha_{\max}^{2n-1} + (\alpha_{\max}^{2n-1} - 1)m - \alpha_{\max}^{2n-1}\tau_{\max} W \geq W\tau_{\max}$ and hence

$$W \leq \frac{\alpha_{\max}^{2n-1} + (\alpha_{\max}^{2n-1} - 1)m}{(1 + \alpha_{\max}^{2n-1})\,\tau_{\max}}. \tag{4.58}$$

Therefore, if

$$W \leq \frac{1}{(1 + \alpha_{\max})\,\tau_{\max}} \triangleq W_{m'>m}, \tag{4.59}$$

the condition in (4.55) is satisfied for $m' > m$. A similar argument, for $m' < m$, leads us

to the following bound on W for satisfying the condition in (4.55):

$$W \leq \frac{1}{(1+\alpha_{\max}^{2N-3})\,\tau_{\max}} \triangleq W_{m'<m}. \tag{4.60}$$

To satisfy both (4.59) and (4.60), for every $m' \neq m$, we choose

$$W = \min\left(W_{m'>m}, W_{m'<m}.\right) \tag{4.61}$$

Equations (4.54) and (4.61) provide the choices of the parameters q and W, respectively, for the ODSS modulation. For the Doppler-free channel ($\alpha_{\max} = 1$), we observe that the choice of W reduces to $W = \frac{1}{2\tau_{\max}}$, which agrees with (4.57). In a Doppler-distorted channel, we see that the choice of W according to (4.61) entails a longer transmit signal duration compared to a Doppler-free channel.

4.5.3.2 The ODSS input-output relation

The ODSS demodulator output is obtained by taking the discrete Mellin-Fourier transform of the delay-scale signal in (4.51):

$$\begin{aligned}\hat{y}[k,l] &= \sum_{n=0}^{N-1}\sum_{m=0}^{M(n)-1} q^{n/2}\hat{Y}[n,m]e^{j2\pi\left(\frac{nk}{N}-\frac{ml}{M(n)}\right)}, \\ &= \sum_{n=0}^{N-1}\sum_{m=0}^{M(n)-1} h_w[l-m,k-n]\,x[n,m] + w[k,l], \end{aligned}\tag{4.62}$$

where $h_w[l,k]$ is obtained by sampling the frequency $\left(f = \frac{lW}{M}\right)$ and Mellin variable $\left(\beta = \frac{k}{N\ln q}\right)$ arguments of the function

$$h_w(f,\beta) = \sum_{n=0}^{N-1}\sum_{m=0}^{M(n)-1} H_{n,m}[n,m]e^{j2\pi\left(\beta n\ln q - \frac{m}{W}f\right)}$$

$$= \iint h(\tau', \alpha') \sum_{m=0}^{M-1} \sum_{n=0}^{N-1} e^{j2\pi\left(\beta n \ln q - f\frac{m}{W}\right)} A_{g_{\text{rx}}, g_{\text{tx}}} \left(q^n \left(\frac{m}{W} (\alpha' - 1) - \alpha' \tau' \right), \frac{1}{\alpha'} \right) d\tau' d\alpha'. \tag{4.63}$$

An Example: Consider the channel response due to a collection of discrete reflectors associated with path delays and Doppler scales $(\tau_i, \alpha_i), i = 1, 2, \ldots, P$:

$$h(\tau, \alpha) = \sum_{i=1}^{P} h_i \delta(\tau - \tau_i) \delta(\alpha - \alpha_i). \tag{4.64}$$

For the above channel response model, we find that $H_{n,m}[n, m]$ in (4.48) evaluates to

$$H_{n,m}[n, m] = \sum_{i=1}^{P} h_i A_{g_{\text{rx}}, g_{\text{tx}}} \left(q^n \left(\frac{m}{W} (\alpha_i - 1) - \alpha_i \tau_i \right), \frac{1}{\alpha_i} \right), \tag{4.65}$$

and hence

$$h_w[l, k] = \sum_{i=1}^{P} h_i \sum_{n'=0}^{N-1} \sum_{m'=0}^{M(n')-1} e^{j2\pi\left(\frac{n'k}{N} - \frac{m'l}{M(n')}\right)} A_{g_{\text{rx}}, g_{\text{tx}}} \left(q^{n'} \left(\frac{m' (\alpha_i - 1)}{W} - \alpha_i \tau_i \right), \frac{1}{\alpha_i} \right). \tag{4.66}$$

The input-output relation in an ODSS system, given by (4.62), can be depicted in the following vectorized form:

$$\mathbf{y} = \mathbf{H}\mathbf{x} + \mathbf{w}, \tag{4.67}$$

where $\mathbf{y} \in \mathbb{C}^{M_{\text{tot}} \times 1}$ is the output of the ODSS demodulator obtained by stacking $y[k, l]$ into a vector, $\mathbf{H} \in \mathbb{C}^{M_{\text{tot}} \times M_{\text{tot}}}$ is the effective channel matrix, $\mathbf{x} \in \mathbb{C}^{M_{\text{tot}} \times 1}$ is the symbol vector obtained by stacking $x[k, l]$ into a vector, and $\mathbf{w} \in \mathbb{C}^{M_{\text{tot}} \times 1}$ is the additive noise at the ODSS demodulator output.

4.5.3.3 Data Decoding

Using (4.67), we can use either an MMSE decoder or a message passing based decoder to recover the transmitted data symbols. This involves equalizing a channel matrix of size $M_{\text{tot}} \times M_{\text{tot}}$ which is not close to diagonal. As a consequence, it is computationally

expensive to perform channel equalization in the Mellin-Fourier domain signal represented by (4.67).

Motivated by the above, we now present an alternative, simple, decoder that uses a subcarrier-by-subcarrier MMSE equalizer in the delay-scale domain instead of the Mellin-Fourier domain. We first express (4.51) in a matrix-vector form as follows:

$$\hat{\mathbf{Y}} = \mathbf{D}\mathbf{X} + \mathbf{W}, \tag{4.68}$$

where $\hat{\mathbf{Y}} \in \mathbb{C}^{M_{\text{tot}} \times 1}$ is a vector obtained by stacking the outputs $Y[n, m]$, $\mathbf{D} \in \mathbb{C}^{M_{\text{tot}} \times M_{\text{tot}}}$ is a diagonal matrix formed by stacking $H_{n,m}[n, m]$ along its diagonal, $\mathbf{X} \in \mathbb{C}^{M_{\text{tot}} \times 1}$ contains the data symbols obtained by stacking $X[n, m]$, and $\mathbf{W} \in \mathbb{C}^{M_{\text{tot}} \times 1}$ is the additive noise.

Data decoding proceeds after an MMSE equalizer on $\hat{\mathbf{Y}}$:

$$\hat{\mathbf{Z}} = \mathbf{D}^H \left(\mathbf{D}\mathbf{D}^H + \sigma_W^2 I\right)^{-1} \hat{\mathbf{Y}}, \tag{4.69}$$

where σ_W^2 is the noise variance in the delay-scale domain.

The data symbol vector is then obtained as follows:

$$\hat{\mathbf{x}} = \mathcal{S}\left(\mathcal{T}_{\text{iMF}}^{-1} \hat{\mathbf{Z}}\right), \tag{4.70}$$

where the operator $\mathcal{S}(.)$ slices each entry in the input vector to the nearest symbol in the transmitted constellation.

Remarks: If the robust bi-orthogonality condition is not satisfied exactly, as in the case of OTFS, expression (4.47) will not reduce to (4.49) and hence the measurement model (4.51) in the delay-scale domain will not ensue. In that case, $\mathbf{D}$ will not be exactly diagonal. The matrix $\mathbf{D}$ will be *nearly* diagonal if the robust bi-orthogonality is approximately satisfied (see Fig. 4.16 in the supplementary material, Sec. 4.9.7), so that it is reasonable to consider a diagonal approximation to $\mathbf{D}$ for equalization purposes. Such an approximation cannot be made in the Mellin-Fourier domain because, even if $\mathbf{D}$ is near-diagonal, $\mathbf{H}$ is not close to diagonal (see Fig. 4.17 in the supplementary material,

Sec. 4.9.7).

4.5.3.4 Computational Complexity

The ODSS transmitter implements transformation from Mellin-Fourier domain to the delay-scale domain at the transmitter followed by the modulator that generates the waveform to transmit. The $M_{\text{tot}} \times M_{\text{tot}}$ transform matrix is a fixed precoder matrix that can be precomputed and stored in the memory. The computational complexity of the transmitter is, therefore, $\mathcal{O}(M_{\text{tot}}^2)$. The ODSS receiver performs matched filtering, subcarrier-by-subcarrier equalization and inverse Mellin-Fourier transformation. Assuming that matched filtering is performed in the receiver front-end and that the inverse transform matrix is precomputed, the computational complexity of the receiver is also $\mathcal{O}(M_{\text{tot}}^2)$, excluding channel estimation overheads. For the same symbol rate, OFDM and OTFS have a lower complexity of $\mathcal{O}(M_{\text{tot}} \log M_{\text{tot}})$ due to efficient computations based on the Fast Fourier Transform (FFT) algorithm. The relation between Mellin and the Wavelet/Fourier transforms can be exploited to speed up the transform computations in ODSS also [83]. Development of a computationally efficient architecture for ODSS is beyond the scope of this thesis.

4.6 Transmit and Receive Filters

The transmit and receive filters (pulse shaping functions), $g_{\text{tx}}(t)$ and $g_{\text{rx}}(t)$, are required to be bi-orthogonal in a robust manner, as described in sections 4.3 and 4.5, for both OTFS and ODSS modulations. However, this is not possible (see Sec. 4.9.4 and Sec. 4.9.5 of the supplementary material): we cannot find transmit and receive filters that exactly satisfy robust bi-orthogonality. Consequently, in most implementations of OTFS, pulse shaping functions such as rectangular, raised cosine and Dolph-Chebyshev windows are employed both at the transmitter and receiver [75]. We adopt a similar approach in ODSS and show its effectiveness through numerical simulations; in particular, our choice of ODSS

subcarriers results in the channel matrix D represented in (4.68) becoming nearly diagonal in the delay-scale domain.

In this work, to form the transmit pulse-shaping filter, we employ a basic chirplet generated by linearly sweeping frequency from $f_1 = \frac{1}{\sqrt{q}}$ to $f_2 = \sqrt{q}$ in T seconds:

$$g_0(t) = e^{j2\pi\left(f_1 t + \frac{1}{2}\kappa t^2\right)}, 0 \le t \le T, \tag{4.71}$$

where $\kappa = \frac{f_2 - f_1}{T}$ is the chirp sweep rate. The basic chirplet duration T is also the ODSS symbol duration.

To reduce the spectral sidelobes, we apply a PHYDYAS filter based window [9] to obtain the transmit pulse-shaping filter $g_{\text{tx}}(t) = g_{\text{w}}(t)g_0(t)$, where $g_{\text{w}}(t)$ is the window function given by

$$g_{\text{w}}(t) = 1 + 2\sum_{k=1}^{K-1}(-1)^k A[k]\cos\left(\frac{2\pi kt}{KT}\right), \tag{4.72}$$

with $A[k], k = 1, 2, \ldots, K-1$, being the PHYDYAS reference filter coefficients. In simulations, we use an overlap factor of $K = 3$, for which the PHYDYAS filter coefficient values are: $A[1] = 0.91143783$ and $A[2] = 0.41143783$ [9].

From the above linearly modulated pulse, or *chirplet*, the ODSS subcarrier waveforms are generated by q-adic compression and shifting (see (4.40)):

$$s_{m,n}(t) = q^{n/2} g_{\text{tx}}\left(q^n\left(t - \frac{m}{q^n W}\right)\right), \tag{4.73}$$

where $m = 0, 1, \ldots, M(n) - 1$, $M(n) = \lfloor q^n \rfloor$, and $n = 0, 1, \ldots, N-1$. We will see that these subcarriers, when used over a delay-scale spread channel, result in a sparse and nearly diagonal channel matrix in the delay-scale domain, enabling the use of low complexity receivers in that domain.

4.7 Numerical Results

In this section, we investigate the bit error rate (BER) performance of the ODSS modulation scheme. To that end, we first design the subcarriers of ODSS modulation respecting the criteria developed in Sec. 4.5 to avoid ICI. Although robust bi-orthogonality cannot be satisfied in an exact manner (the same as in the case of OTFS) due to the reasons mentioned in Sec. 4.6, we use transmit and receive pulses that lead to a low complexity receiver. In subsection 4.7.1, we discuss these aspects. In the subsection 4.7.2, we present BER performance results for the ODSS modulation scheme designed in subsection 4.7.1.

4.7.1 ODSS Waveform

Recall our discussions in Sec. 4.5.3 leading to the choice of geometric sampling ratio, q, and the transmit filter bandwidth, $W(q)$, for avoiding ICI in ODSS modulation. From the discussion preceding (4.54), we choose q such that $\sqrt{q} > \alpha_{\max} \geq 1$.

Let B denote the system bandwidth and N be the number of q-adic scales (compressions) on the scale axis. The bandwidth occupied by the transmit pulse shaping filter and all its time-compressed copies is $\sum_{n=0}^{N-1} q^n W(q)$. Clearly, for the transmit signals to fit within the system bandwidth, we need:

$$\sum_{n=0}^{N-1} q^n W(q) < B. \tag{4.74}$$

The maximum allowable transmit filter bandwidth is given by (see (4.61))

$$W_{\max}(q,N) \triangleq \begin{cases} \frac{1}{(1+\alpha_{\max})\tau_{\max}}, & N = 1, \\ \frac{1}{\left(1+\alpha_{\max}^{2N-3}\right)\tau_{\max}}, & \text{otherwise.} \end{cases} \tag{4.75}$$

Considering (4.74), the upper limit (in (4.75)) on the transmit filter bandwidth is satisfied if:

$$W(q) < \frac{B}{\sum_{n=0}^{N-1} q^n} = \frac{B(q-1)}{q^N - 1} < W_{\max}(q,N). \tag{4.76}$$

We choose the number of q-adic scales, to be the smallest integer N, say, $N(q)$, that satisfies (4.76). We choose the transmit filter bandwidth, $W(q)$, to be

$$W(q) = \frac{B(q-1)}{q^{N(q)}-1}. \tag{4.77}$$

Then, the number of symbols that can be mounted is $M_{\text{tot}}(q) = \sum_{n=0}^{N(q)-1} \lfloor q^n \rfloor$.

Let the duration of the ODSS symbol block be $T(q) = \frac{\gamma}{W(q)}$, where $\gamma > 1$ a factor that accounts for the increase in length of the filter above the minimum duration of $\frac{1}{W(q)}$. Note that the choice of $N = N(q)$ results in the smallest ODSS symbol duration that can be used. Then, the spectral efficiency of the ODSS modulation scheme (in symbols/s/Hz) is given by

$$\eta(q) = \frac{M_{\text{tot}}(q)}{BT(q)} = \frac{M_{\text{tot}}(q)W(q)}{\gamma B} = \frac{M_{\text{tot}}(q)(q-1)}{\gamma(q^{N(q)}-1)}. \tag{4.78}$$

In Sec. 4.9.6 of the supplementary material, through a numerical example, we demonstrate that ODSS can operate with a spectral efficiency close to one symbol per second per Hertz.

Consider the ODSS subcarrier waveforms, constructed as discussed in Sec. 4.6, on a dyadic ($q = 2$) tiling in the delay-scale space for a symbol block duration of $T = 1.9$ seconds and time-scale indices $n = 0, 1, \ldots, 6$. Fig. 4.8 shows the ODSS subcarrier spectra. From these figures, we notice that the subcarrier bandwidth doubles for every scale increment and so does the number of time-compressed and shifted subcarriers at each scale. The ODSS waveforms, thus constructed, are nearly orthogonal (see Sec. 4.9.6 of the supplementary material for more details).

4.7.2 BER Performance

We turn to investigate the communication performance of the ODSS scheme. We simulate the transmitter and receiver of three schemes – OFDM, OTFS and ODSS – operating in a doubly-spread (i.e., time scale and delay spread) channel. We evaluate the bit error rate (BER) performance as the signal to noise ratio (SNR) at the receiver is varied.

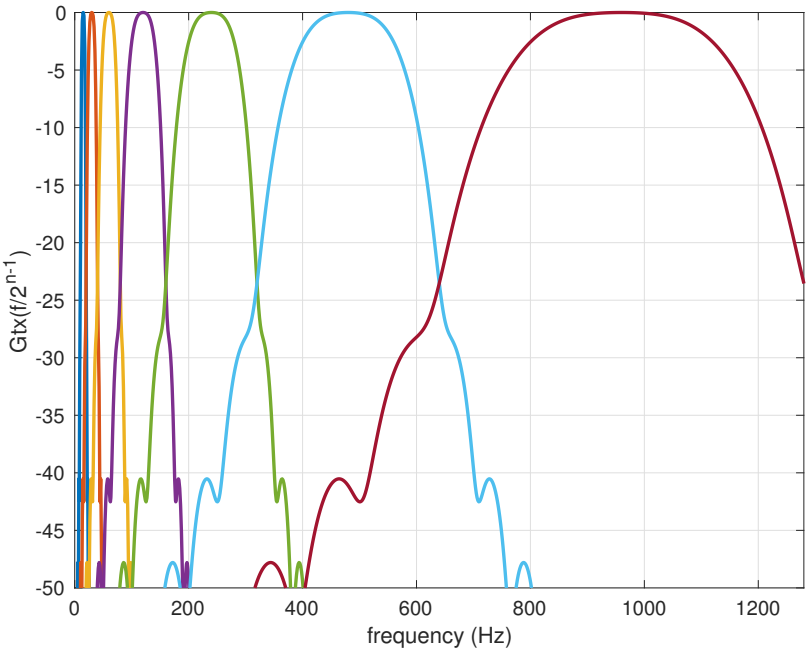

Figure 4.8: ODSS subcarrier spectra. Note that the seven subcarriers, for $n = 0, 1, \ldots, 6$, span a frequency band of $0 - 1280$ Hz.

For fair comparison, we evaluate all three schemes with a low-complexity subcarrier-by-subcarrier MMSE equalizer at the receiver. In the case of OFDM, channel equalization is performed in the frequency domain where the symbols are mounted. Subcarrier-by-subcarrier MMSE channel equalizer is implemented in the time-frequency (resp. delay-Doppler) domain outputs for OTFS (resp. ODSS). The evaluation of the performance with more computationally expensive message passing based equalizers is relegated to future work.

We define the SNR as the ratio of the signal and noise powers at the receiver front-end. The transmitted ODSS signal waveform, given in (4.40), can be expressed as

$$\mathbf{s} = \mathbf{G}\mathbf{X}, \tag{4.79}$$

where the columns of the matrix $\mathbf{G}$ are the basis waveforms (compressed and shifted versions of chirplets), $\mathbf{X} = \mathcal{T}_{\text{iMF}}\mathbf{x}$, $\mathbf{x}$ being the vectorized version of the symbols on the 2D-Mellin-Fourier domain grid. The signal at the receiver, after the transmitted ODSS

waveform propagates through a doubly-spread channel in (4.64), is given by: $r_s(t) = \sum_{p=1}^{P} h_p s\left(\alpha_p(t-\tau_p)\right)$.

To compute the SNR at the receiver side, we ignore the effect of time scale ($0.999 < \alpha_p < 1.001$) since we need only the power of the signal component in the receiver waveform. The received signal power is given by

$$P_s = \mathbb{E}(|r_s(t)|^2) = \mathbb{E}(\sum_{i=1}^{P}\sum_{j=1}^{P} h_i^* h_j s^*(t-\tau_i)s(t-\tau_j)). \tag{4.80}$$

Next, assuming that the channel coefficients $\{h_p \sim \mathcal{CN}(0,1) : p = 1, 2, \ldots, P\}$ are mutually independent and independent of the transmitted signal, we find

$$P_s = \sum_{i=1}^{P} \mathbb{E}(|h_i|^2)\mathbb{E}|s(t-\tau_i)|^2 = P\mathbb{E}|s(t)|^2, \tag{4.81}$$

where we made use of the fact that power of the signal is not affected by delay. Therefore, making use of (4.79), we have

$$P_s = \mathbb{E}\{\mathbf{X}^H\mathbf{G}^H\mathbf{G}\mathbf{X}\} = \frac{1}{F_sT}\mathrm{Tr}\{\mathbf{G}\mathbb{E}\left[\mathbf{X}\mathbf{X}^H\right]\mathbf{G}^H\}, \tag{4.82}$$

where F_s is the sampling rate. Since the ODSS transform preserves energy, $\mathbb{E}\left[\mathbf{X}\mathbf{X}^H\right] = \mathbb{E}\left[\mathbf{x}\mathbf{x}^H\right] = \mathbf{I}$ and therefore

$$P_s = \frac{1}{F_sT}\mathrm{Tr}\{\mathbf{G}\mathbf{G}^H\}. \tag{4.83}$$

We compare the three schemes when they operate at the same spectral efficiency. For BER performance evaluation, we consider acoustic communications in the frequency band, $[f_c - B/2, f_c + B/2]$, where $f_c = 12.8$ kHz and $B = 1.28$ kHz. Both OFDM and OTFS use $N_{\mathrm{FFT}} = 2560$ point FFT and they mount every twentieth subcarrier with a binary phase shift keying (BPSK) symbol. The receivers first down-convert the received signal to the frequency band from DC to 1280 Hz. Then, they use a waveform sampling rate of $F_s = 1280$ Hz and a PHYDYAS filter (with an overlap factor $K = 3$) for pulse shaping. The spectral width of the subcarriers has increased by three-fold, from $W = 0.5$

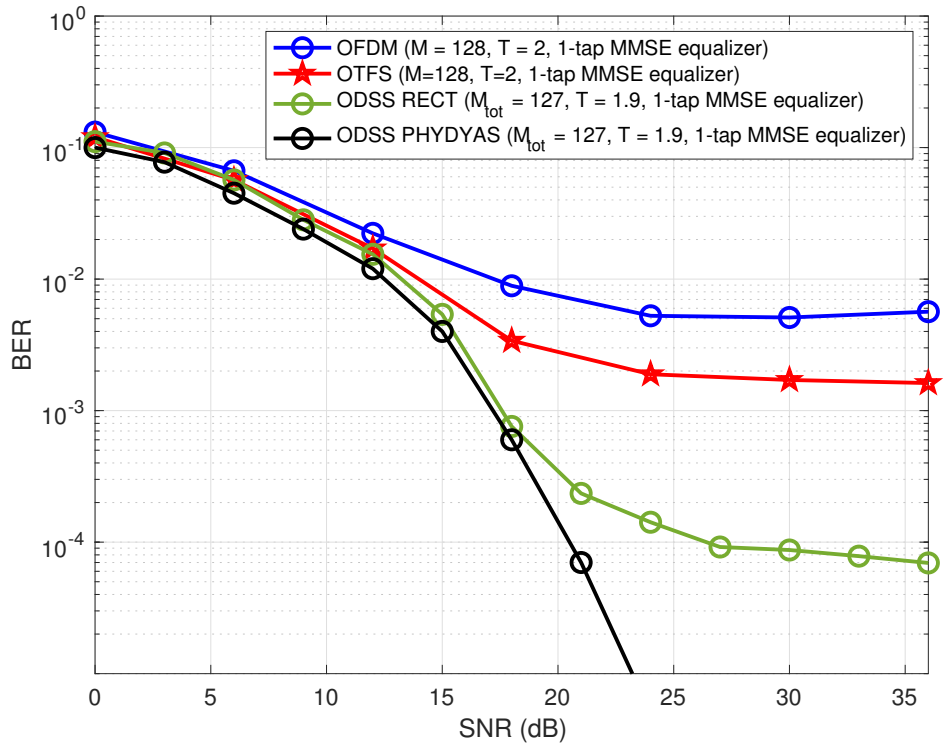

Figure 4.9: BER performance of OFDM, OTFS and ODSS schemes using one-tap MMSE channel equalizers in a wideband delay-scale spread channel with $\tau_{\max} = 10$ ms, $\alpha_{\max} = 1.001$ and $P = 20$ paths.

Hz to $W = 1.5$ Hz, due to pulse shaping by PHYDYAS filter. The utilized subcarriers of the OFDM are spaced well apart, by $\Delta F = 10$ Hz, with significant guard band and without overlap (see Sec. 4.9.7, Fig. 4.18 in the supplementary material).

Figure 4.9 shows the performance of the three modulation schemes as a function of the SNR, in a doubly-spread channel with a delay spread of $\tau_{\max} = 10$ ms, maximum Doppler scale $\alpha_{\max} = 1.001$ and number of paths $P = 20$. The path amplitudes are Rayleigh distributed, $h_p \overset{i.i.d.}{\sim} \mathcal{CN}(0,1) : p = 1, 2, \ldots, P$. The path delays, τ_p, and time-scales, α_p, are drawn uniformly from $(0, \tau_{\max})$ and $(1/\alpha_{\max}, \alpha_{\max})$, respectively. Notice that the delays, τ_p, and time-scales, α_p, are drawn from continuous distributions and do not necessarily lie on the sampling grid. We oversample the transmitted signal by a factor of 8, round-off the channel delay taps to this higher-rate sampled time grid, perform resampling by a rational approximation of the resampling rates α_p (to within an error of $\epsilon = 10^{-5}$),

obtain the received signal after propagating through the delay-scale channel, and finally downsample to obtain the received signal at the original sampling rate. All the receivers use a low-complexity subcarrier-by-subcarrier MMSE equalizer based symbol decoder. We notice the superior performance of the proposed ODSS scheme, while OFDM performs the worst. This is mainly due to the larger ICI among the high frequency subcarriers of OFDM and OTFS when compared to ODSS (see Sec. 4.9.8). In a time-scale channel, the frequency shift is non-uniform and increases with frequency. The ODSS subcarriers have a bandwidth that also increases with frequency, and are therefore relatively unaffected by the Doppler due to time scaling. Fig. 4.9 also shows the performance of ODSS with both the rectangular and PHYDYAS pulse shaping filter. We see that the PHYDYAS filter reduces ICI and thereby eliminates the error floor within the range of SNR considered.

Figure 4.10 shows the performance of the three schemes at an SNR of 18 dB in a doubly-spread channel with a delay spread of $\tau_{\max} = 10$ ms and maximum Doppler scale $\alpha_{\max} = 1.001$, as the number of paths P is varied. The performance advantage of the ODSS scheme increases with the number of paths. In a doubly-spread wideband channel, ODSS whose performance is not limited by a BER floor, unlike the other two schemes, benefits due to diversity gain as the number of paths increases.

Finally, we vary the maximum Doppler scale spread, $\alpha_{\max}$, from $\alpha_{\max} = 1.0$ (zero Doppler channel) to $\alpha_{\max} = 1.001$ keeping all other parameters fixed ($\tau_{\max} = 10$ ms, $P = 20$ and SNR $= 20$ dB.). Figure 4.11 shows the BER performance of the three schemes. The ODSS modulation, designed to handle a maximum Doppler scale spread of $\alpha_{\max} = 1.001$, has a nearly constant BER for $1.0 \leq \alpha_{\max} \leq 1.001$. OFDM and OTFS schemes suffer due to ICI from Doppler distortion, for $\alpha_{\max} > 1$, that gets severe as the Doppler spread increases.

4.8 Conclusions

We developed a new low complexity modulation scheme for a delay and Doppler time-scale spread wideband channel, which we called Orthogonal Delay Scale Space (ODSS) modulation. We examined the performance of OFDM, OTFS and ODSS modulation schemes

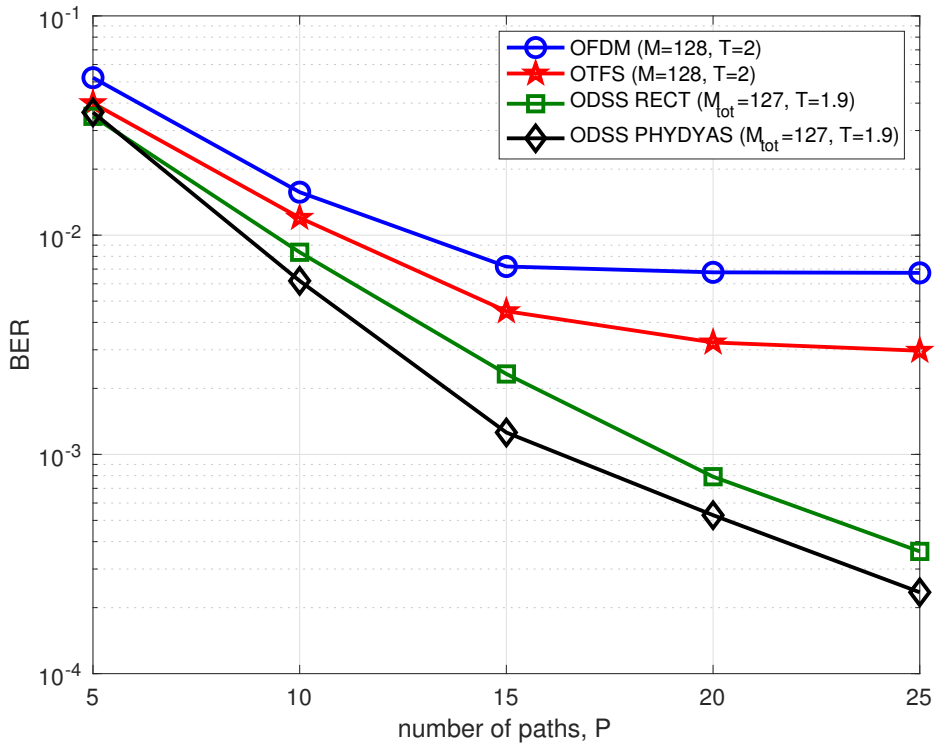

Figure 4.10: BER performance of OFDM, OTFS and ODSS using one-tap MMSE channel equalizer as the number of paths, P, is varied in a doubly-spread wideband channel with $\tau_{\max} = 10$ ms, $\alpha_{\max} = 1.001$ and at SNR= 18 dB.

through numerical simulations when the receiver employs a low complexity channel equalizer. In doubly distorted wideband channels, the ODSS receiver using a subcarrier-by-subcarrier equalizer showed a clear performance advantage over the OFDM and OTFS receivers. Also, as the number of multipaths increased, ODSS showed even better performance, taking advantage of the increased multipath diversity, whereas the other two schemes suffered due to their inability to handle ICI.

The ODSS scheme was developed by systematically identifying the transmitter and receiver side modulation and demodulation functions suited for *wideband* time-varying channels. In the process, we introduced the 2D ODSS transform composed of the inverse Fourier and Mellin transforms from the Fourier-Mellin domain (symbol space) to the delay-scale domain (waveform space). We recognized the ω-convolution property that helped in developing the input-output model for the ODSS scheme. We showed that the

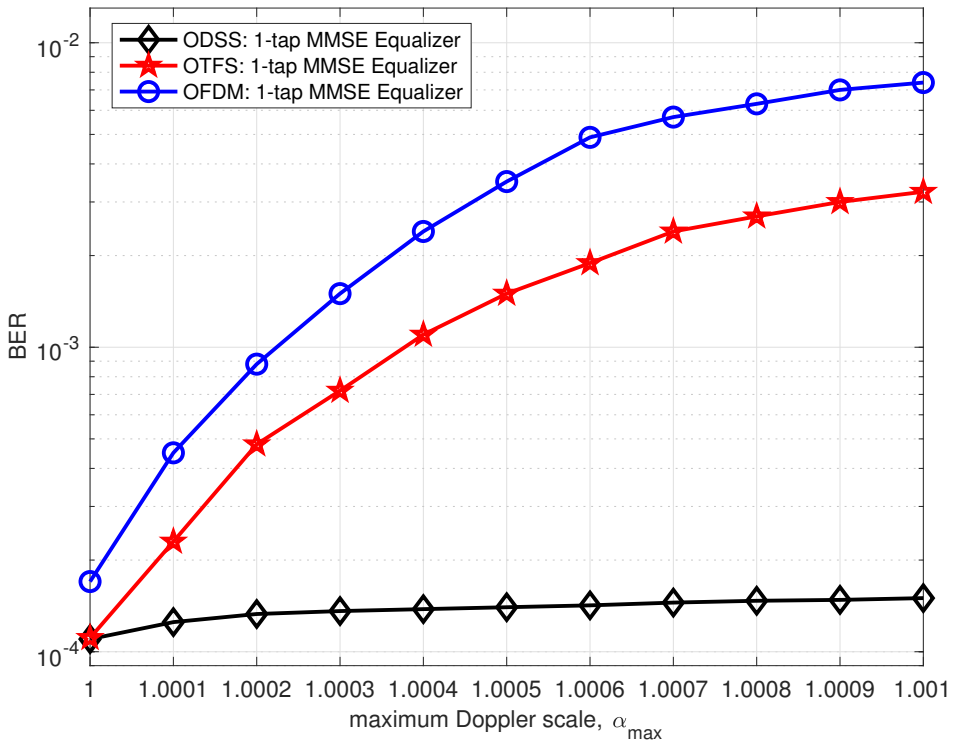

Figure 4.11: BER performance of OFDM, OTFS and ODSS as the Doppler scale spread parameter, $\alpha_{\max}$, is varied in a wideband channel with $P = 20$, $\tau_{\max} = 10$ ms and at SNR= 20 dB.

proposed scheme can operate with a spectral efficiency close to one symbol per second per Hertz. With our choice of filtered wideband chirplet, as the basic ODSS waveform, we obtained a channel matrix which was nearly diagonal thus allowing the use of a subcarrier-by-subcarrier equalizer in the delay-scale domain.

While this work introduced the ODSS modulation scheme, there are several directions that can be explored. These include developing better-performing message-passing based receivers, analyzing the peak-to-average power ratio and energy efficiency, extension to multiple antennas at the transceivers, analyzing the diversity-multiplexing gain trade-offs, developing channel estimation schemes, analyzing performance under imperfect channel state information, designing good transmit and receive pulse shaping functions, and so on.

4.9 Supplementary Material

4.9.1 Proof of (4.43)

We show that a cascade of two delay-scale channels, as shown in Figure 4.6, is equivalent to a single channel, i.e., $\Pi_{h_2}(\Pi_{h_1}(s)) = \Pi_h(s)$, where $h(\tau,\alpha) = h_2(\tau,\alpha) \circledast_\omega h_1(\tau,\alpha)$ and the symbol $\circledast_\omega$ denotes the ω-convolution defined by

$$h(\tau,\alpha) = \iint h_2(\tau',\alpha') h_1\left(\alpha'(\tau-\tau'), \frac{\alpha}{\alpha'}\right) d\tau' d\alpha'. \tag{4.84}$$

To show this, we substitute

$$v(t) = \iint h_1(\tau'',\alpha'')\sqrt{\alpha''} u\left(\alpha''(t-\tau'')\right) d\tau'' d\alpha'',$$

into the relation

$$r(t) = \iint h_2(\tau',\alpha')\sqrt{\alpha'} v\left(\alpha'(t-\tau'),\right) d\tau' d\alpha',$$

and make the change of variables, $\tau'' \to \alpha'(\tau-\tau')$ and $\alpha'' \to \alpha/\alpha'$, to obtain

$$\begin{aligned} r(t) &= \iint\iint h_2(\tau',\alpha') h_1\left(\alpha'(\tau-\tau'), \frac{\alpha}{\alpha'}\right) d\tau' d\alpha' \sqrt{\alpha} u(\alpha(t-\tau)) d\tau d\alpha \\ &= \int\int h(\tau,\alpha)\sqrt{\alpha} u(\alpha(t-\tau)) d\tau d\alpha, \end{aligned}$$

where $h(\tau,\alpha)$ is given by (4.84).

4.9.2 Derivation of (4.44)

Using (4.42) and the definition of ω-convolution in (4.43), we can express $f(\tau,\alpha) = h(\tau,\alpha) \circledast_\omega X(\tau,\alpha)$ as

$$\begin{aligned} f(\tau,\alpha) &= \iint h(\tau',\alpha') \sum_n \sum_m X[n,m] \delta\left(\alpha'(\tau-\tau') - \frac{m}{q^n W}, \frac{\alpha}{\alpha'} - q^n\right) d\tau' d\alpha' \\ &= \sum_n \sum_m X[n,m] \iint h(\tau',\alpha') \delta\left(\alpha'(\tau-\tau') - \frac{m}{q^n W}, \frac{\alpha - q^n\alpha'}{\alpha'}\right) d\tau' d\alpha' \end{aligned}$$

$$\stackrel{(e)}{=} \sum_n \sum_m X[n,m] h\left(\tau - \frac{m}{\alpha W}, \frac{\alpha}{q^n}\right) q^{-n}, \tag{4.85}$$

where the last equality (e) follows from the following properties of the Dirac delta function:

1. Generalized scaling property:

$$\delta(\mathbf{g}(\mathbf{x})) = \sum_{\{\mathbf{x}_0 : \mathbf{g}(\mathbf{x}_0)=\mathbf{0}\}} \frac{\delta(\mathbf{x}-\mathbf{x}_0)}{\left|\det \frac{\partial(g_1,\ldots,g_n)}{\partial(x_1,\ldots,x_n)}\right|_{\mathbf{x}=\mathbf{x}_0}},$$

   where $\mathbf{g} : \mathbb{R}^n \to \mathbb{R}^n$ is a bi-Lipschitz function and $\left|\det \frac{\partial(g_1,\ldots,g_n)}{\partial(x_1,\ldots,x_n)}\right| \neq 0$ for $\mathbf{x} \in \{\mathbf{x}_0 : \mathbf{g}(\mathbf{x}_0) = \mathbf{0}\}$.

2. Sifting property:

$$\int \mathbf{f}(\mathbf{x}) \delta(\mathbf{x}-\mathbf{x}_0) d\mathbf{x} = \mathbf{f}(\mathbf{x}_0).$$

4.9.3 Derivation of (4.47)

$$\begin{aligned}
A_{g_{\mathrm{rx}},r_s}(\tau,\alpha) &= \int g^*_{\mathrm{rx}}(\alpha(t-\tau))\sqrt{\alpha} r_s(t) dt \\
&= \int g^*_{\mathrm{rx}}(\alpha(t-\tau))\sqrt{\alpha} \iint f(\tau',\alpha')\sqrt{\alpha'} g_{\mathrm{tx}}(\alpha'(t-\tau'))\, d\tau' d\alpha' dt \\
&= \iint f(\tau',\alpha') \int g^*_{\mathrm{rx}}(\alpha(t-\tau))\sqrt{\alpha\alpha'} g_{\mathrm{tx}}(\alpha'(t-\tau'))\, dt d\tau' d\alpha' \\
&= \iint f(\tau',\alpha') \int g^*_{\mathrm{rx}}\left(\frac{\alpha}{\alpha'}(t' - \alpha'(\tau-\tau'))\right) \sqrt{\frac{\alpha}{\alpha'}} g_{\mathrm{tx}}(t') dt' d\tau' d\alpha' \\
&= \iint f(\tau',\alpha') A_{g_{\mathrm{rx}},g_{\mathrm{tx}}}\left(\alpha'(\tau-\tau'), \frac{\alpha}{\alpha'}\right) d\tau' d\alpha' \\
&= f(\tau,\alpha) \circledast_\omega A_{g_{\mathrm{rx}},g_{\mathrm{tx}}}(\tau,\alpha).
\end{aligned} \tag{4.86}$$

It is now straightforward to see that

$$A_{g_{\mathrm{rx}},r_s}(\tau,\alpha) = f(\tau,\alpha) \circledast_\omega A_{g_{\mathrm{rx}},g_{\mathrm{tx}}}(\tau,\alpha)$$

$$\begin{aligned} &\overset{(e)}{=} \iint \sum_n \sum_m X[n,m] h\left(\tau' - \frac{m}{\alpha' W}, \frac{\alpha'}{q^n}\right) q^{-n} A_{g_{\rm rx},g_{\rm tx}}\left(\alpha'(\tau-\tau'), \frac{\alpha}{\alpha'}\right) d\tau' d\alpha' \\ &\overset{(f)}{=} \sum_n \sum_m X[n,m] H_{n,m}(\tau,\alpha), \end{aligned} \tag{4.87}$$

where we used (4.44) at step (e), and the following definition at step (f):

$$H_{n,m}(\tau,\alpha) \triangleq \iint h\left(\tau' - \frac{m}{\alpha' W}, \frac{\alpha'}{q^n}\right) q^{-n} A_{g_{\rm rx},g_{\rm tx}}\left(\alpha'(\tau-\tau'), \frac{\alpha}{\alpha'}\right) d\tau' d\alpha'. \tag{4.88}$$

By a transformation of variables, $\tau'' = \tau' - \frac{m}{\alpha' W}$ and $\alpha'' = \frac{\alpha'}{q^n}$, and using the fact that the determinant of the Jacobian of this transformation is q^n, we can rewrite the double integral in (4.88) as

$$H_{n,m}(\tau,\alpha) \;=\; \iint h(\tau'',\alpha'') A_{g_{\rm rx},g_{\rm tx}}\left(\alpha'' q^n \left(\tau - \frac{m}{\alpha'' q^n W} - \tau''\right), \frac{\alpha}{\alpha'' q^n}\right) d\tau'' d\alpha''. \tag{4.89}$$

4.9.4 Pulse Shaping Functions for OTFS

The narrowband cross-ambiguity function, apropos of OTFS modulation, between the transmit and receive pulse shaping functions is defined by (see (4.13))

$$A_{g_{\rm rx},g_{\rm tx}}(\tau,\nu) \triangleq \int_t e^{-j2\pi\nu(t-\tau)} g^*_{\rm rx}(t-\tau) g_{\rm tx}(t) dt. \tag{4.90}$$

It is clear from (4.90) that, for a given τ, the functions $\Psi(\nu) = A_{g_{\rm rx},g_{\rm tx}}(\tau,\nu) e^{-j2\pi\nu\tau}$ and $\psi(t) = g^*_{\rm rx}(t-\tau) g_{\rm tx}(t)$ are Fourier pairs, and therefore

$$g^*_{\rm rx}(t-\tau) g_{\rm tx}(t) = \int_\nu A_{g_{\rm rx},g_{\rm tx}}(\tau,\nu) e^{j2\pi\nu(t-\tau)} d\nu. \tag{4.91}$$

Consider, for example, a narrowband cross-ambiguity function, $A_{g_{\rm rx},g_{\rm tx}}(\tau,\nu)$, which is non-zero only on $S = I_\tau \times I_\nu$, where $I_\tau = (-\tau_{\max}, \tau_{\max})$ and $I_\nu = (-\nu_{\max}, \nu_{\max})$, and

$A_{g_{\rm rx},g_{\rm tx}}(\tau,\nu)=1, \forall(\tau,\nu)\in S$. In this case, we see from (4.91) that

$$g^*_{\rm rx}(t-\tau)g_{\rm tx}(t)=\begin{cases}2\nu_{\max}\ \mathrm{sinc}\left(2\nu_{\max}(t-\tau)\right), & \tau\in I_\tau\\ 0, & \text{otherwise.}\end{cases} \tag{4.92}$$

This is clearly impossible: to have $g^*_{\rm rx}(t-\tau)g_{\rm tx}(t)$ and its Fourier transform ($t\rightarrow\nu$) $A_{g_{\rm rx},g_{\rm tx}}(\tau,\nu)$ to be both finitely supported. Hence, we cannot design transmit and receive filters that exactly satisfy robust bi-orthogonality. Also, more generally, even if $A_{g_{\rm rx},g_{\rm tx}}(\tau,\nu)$ is not identically unity $\forall(\tau,\nu)\in S$, due to Heisenberg's uncertainty principle, it is still impossible to find transmit and receive filters that are robustly bi-orthogonal [75].

4.9.5 Pulse Shaping Functions for ODSS

In ODSS, the wideband cross-ambiguity function between the transmit and receive pulse shaping functions is defined by (see (4.46))

$$A_{g_{\rm rx},g_{\rm tx}}(\tau,\alpha)\triangleq\int g^*_{\rm rx}\left(\alpha(t-\tau)\right)\sqrt{\alpha}g_{\rm tx}(t)dt. \tag{4.93}$$

Let $G_{\rm tx}(f)$ and $G_{\rm rx}(f)$ denote the Fourier transforms of the transmit and receive pulse shaping functions, $g_{\rm tx}(t)$ and $g_{\rm rx}(t)$, respectively. Then, by Parseval's theorem, we can express the integral in (4.93) as

$$A_{g_{\rm rx},g_{\rm tx}}(\tau,\alpha)=\frac{1}{\sqrt{\alpha}}\int G^*_{\rm rx}\left(\frac{f}{\alpha}\right)G_{\rm tx}(f)e^{j2\pi f\tau}df. \tag{4.94}$$

It is clear from (4.94) that, for a given α, the functions $\psi(\tau)=A_{g_{\rm rx},g_{\rm tx}}(\tau,\alpha)$ and $\Psi(f)=\frac{1}{\sqrt{\alpha}}G^*_{\rm rx}\left(\frac{f}{\alpha}\right)G_{\rm tx}(f)$ are Fourier pairs, and therefore

$$\frac{1}{\sqrt{\alpha}}G^*_{\rm rx}\left(\frac{f}{\alpha}\right)G_{\rm tx}(f)=\int A_{g_{\rm rx},g_{\rm tx}}(\tau,\alpha)e^{-j2\pi f\tau}d\tau. \tag{4.95}$$

Setting $f = \alpha$ in (4.95), we obtain

$$\frac{1}{\sqrt{\alpha}} G_{\text{rx}}^{*}(1) G_{\text{tx}}(\alpha) = \int A_{g_{\text{rx}},g_{\text{tx}}}(\tau, \alpha) e^{-j2\pi\alpha\tau} d\tau, \tag{4.96}$$

from where, by replacing α with f, we can determine $G_{\text{tx}}(f)$ up to a scale factor $1/G_{\text{rx}}^{*}(1)$, provided $G_{\text{rx}}^{*}(1) \neq 0$. On the other hand, setting $f = 1$ and replacing α with $1/\alpha$ in (4.95), leads to

$$\sqrt{\alpha} G_{\text{rx}}^{*}(\alpha) G_{\text{tx}}(1) = \int A_{g_{\text{rx}},g_{\text{tx}}}(\tau, 1/\alpha) e^{-j2\pi\tau} d\tau, \tag{4.97}$$

from where, by replacing α with f, we can find $G_{\text{rx}}(f)$ up to a scale factor $1/G_{\text{tx}}^{*}(1)$, provided $G_{\text{tx}}^{*}(1) \neq 0$. We determine the transmit and receive pulse shaping functions in the time domain by Fourier inversion of $G_{\text{tx}}(f)$ and $G_{\text{rx}}(f)$, respectively.

Consider, for example, a wideband cross-ambiguity function, $A_{g_{\text{rx}},g_{\text{tx}}}(\tau, \alpha)$, which is non-zero only for $S = \{(\tau, \alpha) : \tau \in (-\tau_{\max}, \tau_{\max}), \alpha \in (1/\alpha_{\max}, \alpha_{\max})\}$, where $\alpha_{\max} \geq 1$, and $A_{g_{\text{rx}},g_{\text{tx}}}(\tau, \alpha) = e^{j2\pi f_0 \tau}/\sqrt{\alpha}$, for $(\tau, \alpha) \in S$, where $f_0 = \frac{\alpha_{\max}^{-1} + \alpha_{\max}}{2}$. In this case, we find that the Fourier transform of the transmit pulse shaping function is given by

$$G_{\text{tx}}(f) = \begin{cases} \frac{2\tau_{\max}}{G_{\text{rx}}^{*}(1)} \text{sinc}\left((f - f_0)\tau_{\max}\right), & f \in \left(\frac{1}{\alpha_{\max}}, \alpha_{\max}\right), \\ 0, & \text{otherwise}, \end{cases} \tag{4.98}$$

and the receive pulse shaping function in the Fourier domain is given by

$$G_{\text{rx}}^{*}(f) = \begin{cases} \frac{2\tau_{\max}}{G_{\text{tx}}(1)} \text{sinc}\left((f_0 - 1)\tau_{\max}\right), & f \in \left(\frac{1}{\alpha_{\max}}, \alpha_{\max}\right), \\ 0, & \text{otherwise}. \end{cases} \tag{4.99}$$

We immediately recognize the impossibility of designing *finite* duration transmitter and receiver pulse shaping filters for ODSS modulation that satisfy the robust bi-orthogonality condition exactly. While the receiver pulse shaping filter, given by (4.99), is exactly rectangular (in frequency domain), the transmitter pulse shaping filter, given by (4.98), is nearly rectangular (in frequency domain) since for typical values of channel delay spread, $\tau_{\max}$, and Doppler scale, $\alpha_{\max}$, $\alpha_{\max} - 1/\alpha_{\max} \ll \frac{1}{\tau_{\max}}$ holds. Therefore, the

pulse shaping filters in the time domain cannot be finite duration waveforms. Conversely, finite duration pulse shaping filters cannot have spectra, as in (4.98) and (4.99), and hence do not satisfy the robust bi-orthogonality condition exactly. We are thus left to choose filters that are nearly bi-orthogonal in a robust manner.

4.9.6 ODSS: Spectral Efficiency and Orthogonality

Consider the choice of ODSS modulator parameters for an underwater communication system of bandwidth $B = 10$ kHz operated in a channel with a Doppler spread of $\alpha_{\max} = 1.001$ [109]. In Fig. 4.12, we plot the transmit filter bandwidth, in (4.77), and the maximum allowed bandwidth, given by (4.75), for different channel delay spreads as the sampling ratio q is varied. The spectral efficiency of the ODSS modulation with these parameters and $\gamma = 2$ is plotted as a function of q in Fig. 4.13.

Fig. 4.14 shows the ODSS subcarrier waveforms, constructed as discussed in Sec. 4.6, on a dyadic ($q = 2$) tiling in the delay-scale space for a symbol block duration of $T = 1.9$ seconds and time-scale indices $n = 0, 1, \ldots, 6$.

The pairwise correlations of the ODSS subcarrier waveforms are shown as an image in Fig. 4.15: the intensity of (m, n)th cell denotes the magnitude of the correlation between the mth and nth subcarrier waveforms. We see that the correlation matrix is nearly diagonal as the normalized cross-correlation between any two distinct ODSS subcarrier waveforms is less than -74 dB.

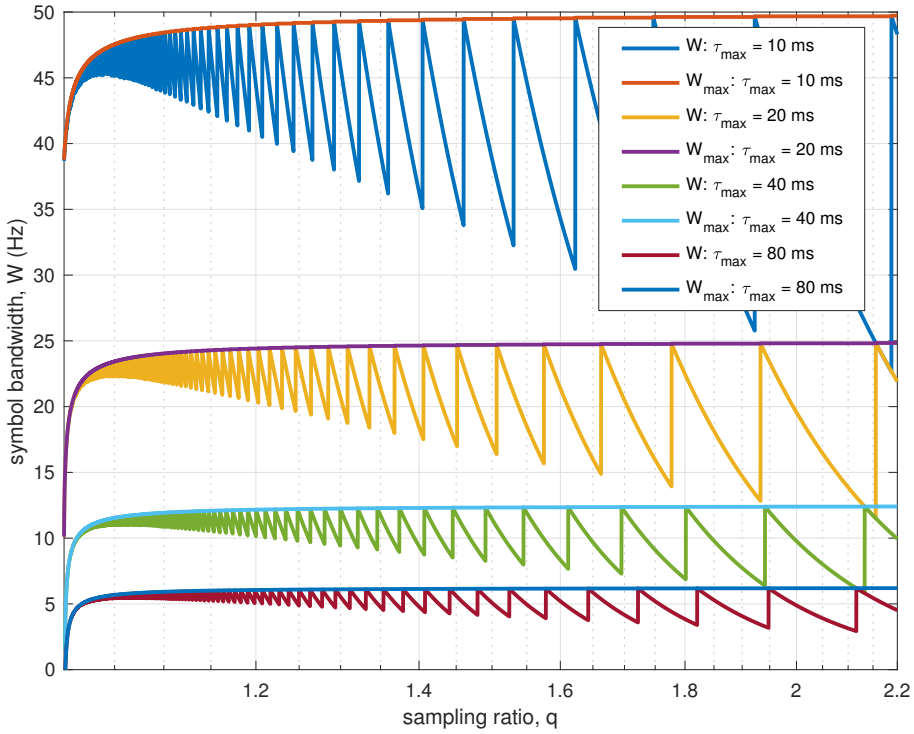

Figure 4.12: Plots of the transmit filter bandwidth, W in (4.77), and maximum allowed bandwidth, $W_{\max}$ in (4.75), as the sampling ratio, q, is varied for various channel delay spreads. Small values of the transmit filter bandwidth, and hence a long symbol duration, needs to be used in channels with large delay spread.

4.9.7 ODSS Channel Matrix

Figures 4.16 and 4.17 show the ODSS channel matrix in the delay-scale and Mellin-Fourier domains, respectively, for one of the simulated channel instances. The ODSS channel matrix in the delay-scale domain is nearly diagonal and, therefore, a single-tap channel equalizer can be implemented in this domain.

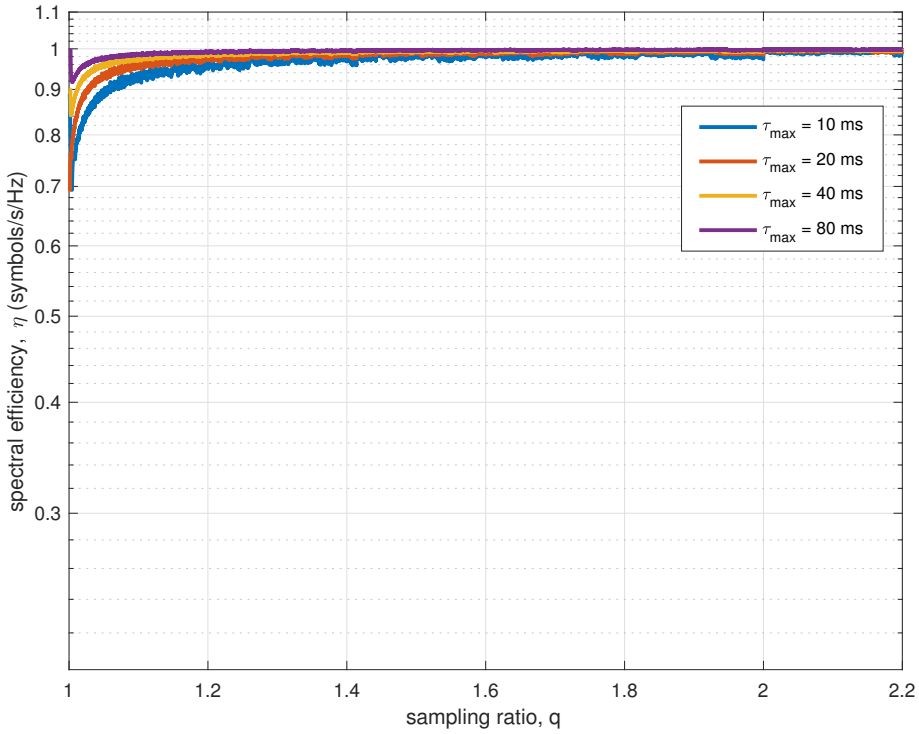

Figure 4.13: Plots of the spectral efficiency, η (in symbols/s/Hz), of the ICI-free ODSS scheme as the sampling ratio, q, is varied. The spectral efficiency of the ODSS is quite close to unity for $q > 1.2$.

4.9.8 Effect of Time-scaling: ODSS versus OFDM

To illustrate the effect of Doppler on OFDM and ODSS, we mount a symbol only on one of the subcarriers, say, the $n_{\text{sub}} = 64$. We then observe the processed subcarrier outputs, for 100 channel realizations, in the neighborhood of n_{sub}. In Figs. 4.19 and 4.20, we plot the OFDM and ODSS receiver outputs, respectively. Spurious pickup by subcarriers 63 and 65 in OFDM is due to Doppler. In contrast, the ICI due to time-scaling effect of the channel is negligible in ODSS, thus illustrating its suitability for such channels.

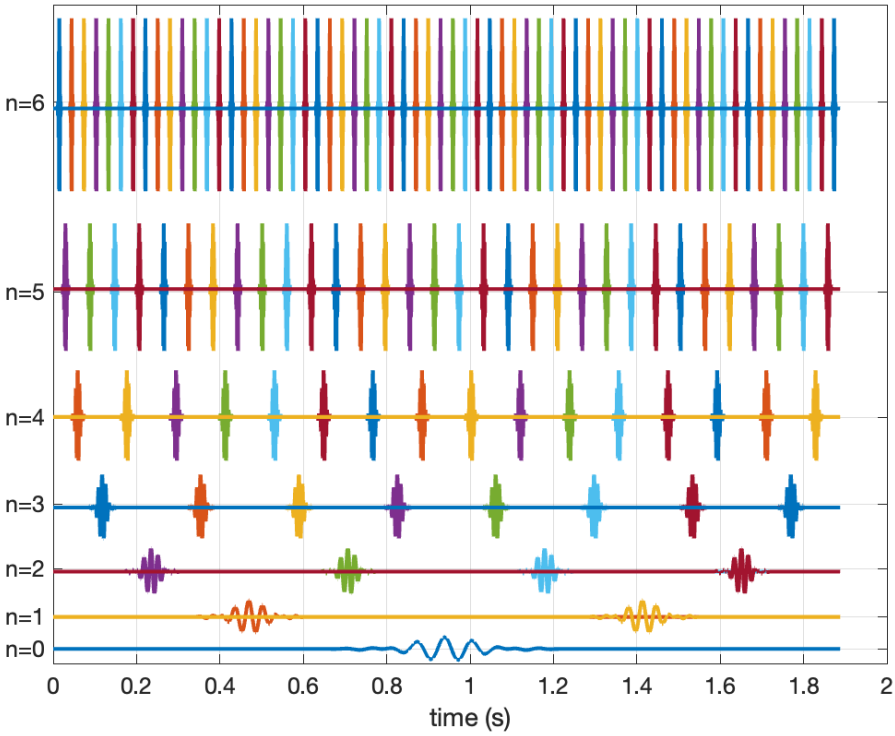

Figure 4.14: ODSS subcarriers, for $n = 0, 1, \ldots, 6$, on a dyadic ($q = 2$) tiling over an ODSS symbol duration of $T = 1.9$ seconds. Note that a total of $N_7 = 127$ subcarriers are tiled in the symbol duration.

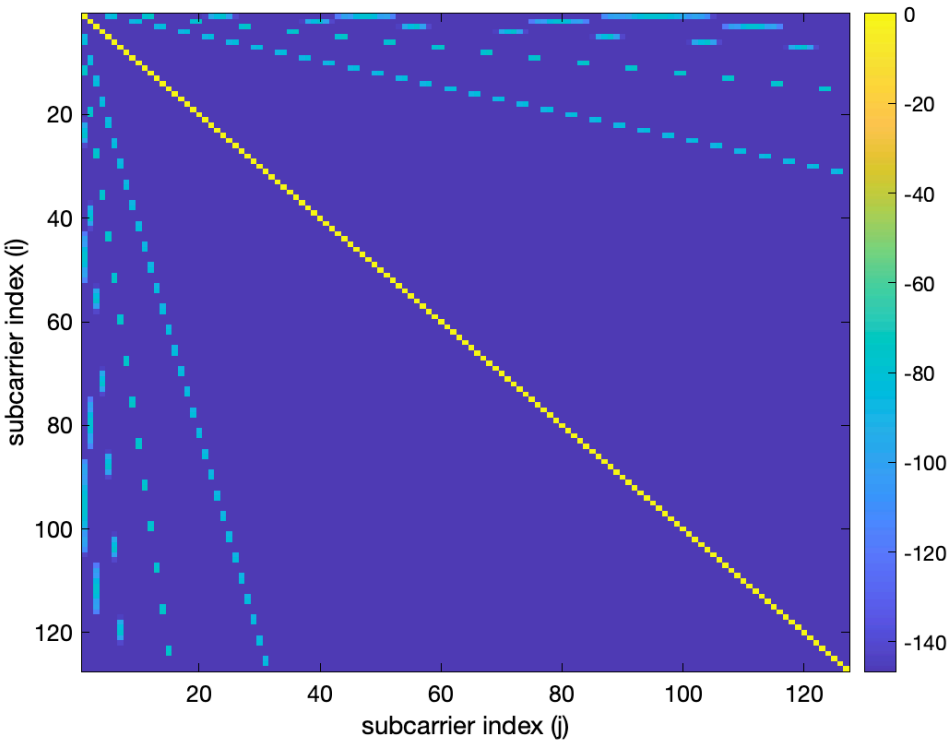

Figure 4.15: ODSS subcarrier waveform correlation matrix, for $n = 0, 1, \ldots, 6$. The normalized correlation (in dB) values are color coded and displayed. The peak intensity corresponds to 0 dB (yellow). The cross-correlation between any two distinct ODSS subcarrier waveforms is less than -74 dB.

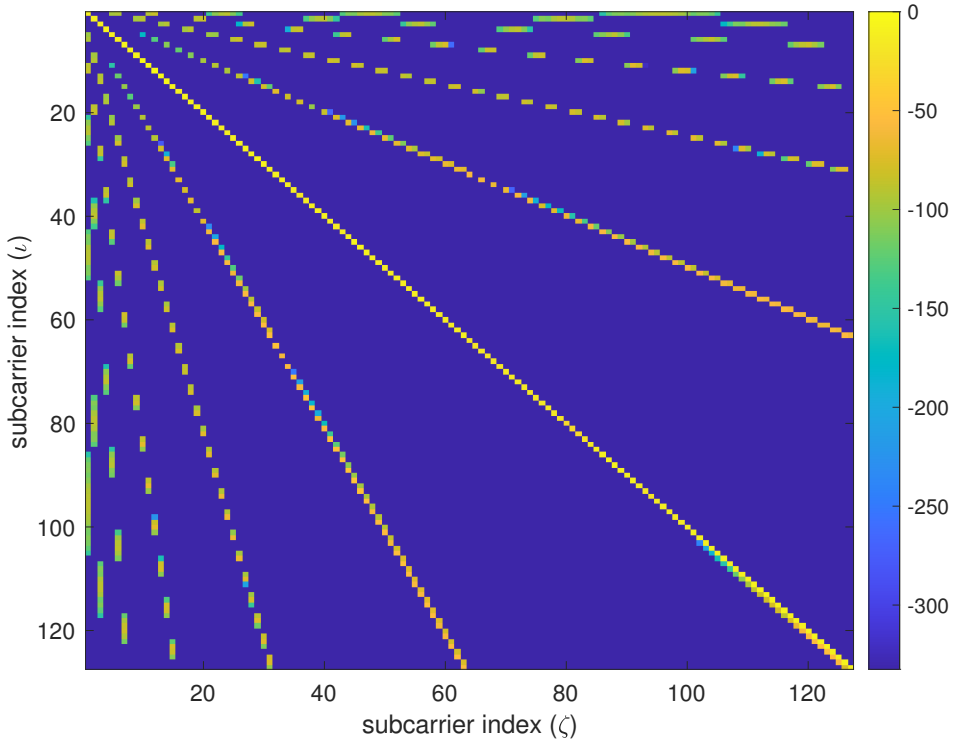

Figure 4.16: ODSS channel matrix (normalized magnitude, in dB) is nearly diagonal in the delay-scale domain with the maximum ICI level not exceeding −25 dB. Channel equalization can be implemented by multiplying each delay-scale domain measurement with a respective complex number.

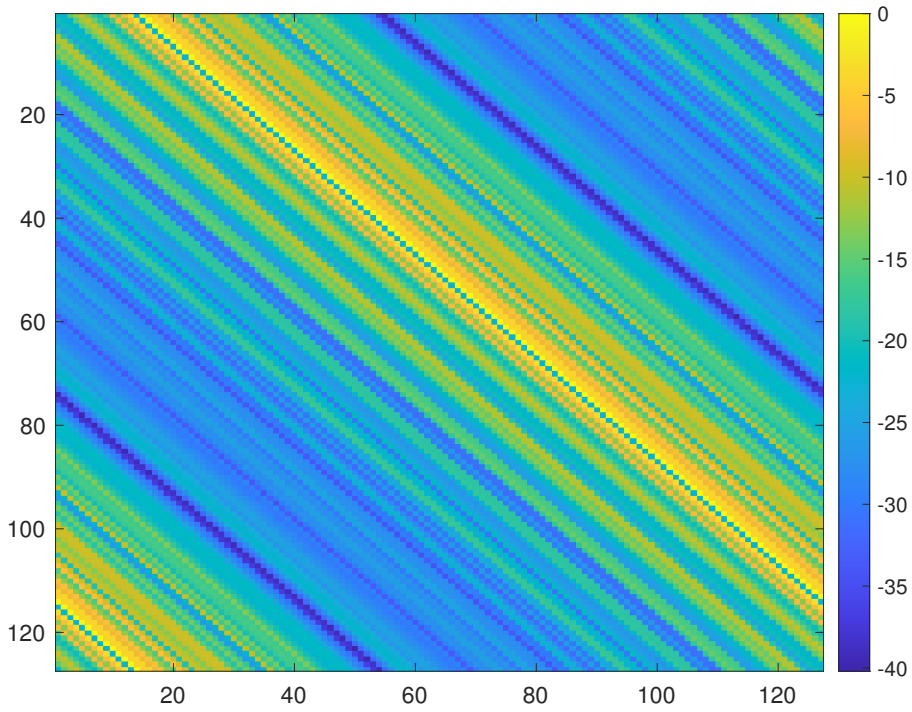

Figure 4.17: ODSS channel matrix (normalized magnitude, in dB) in the Mellin-Fourier domain. Channel equalizer complexity in the Mellin-Fourier domain is high due to the non-sparse nature of the associated channel matrix.

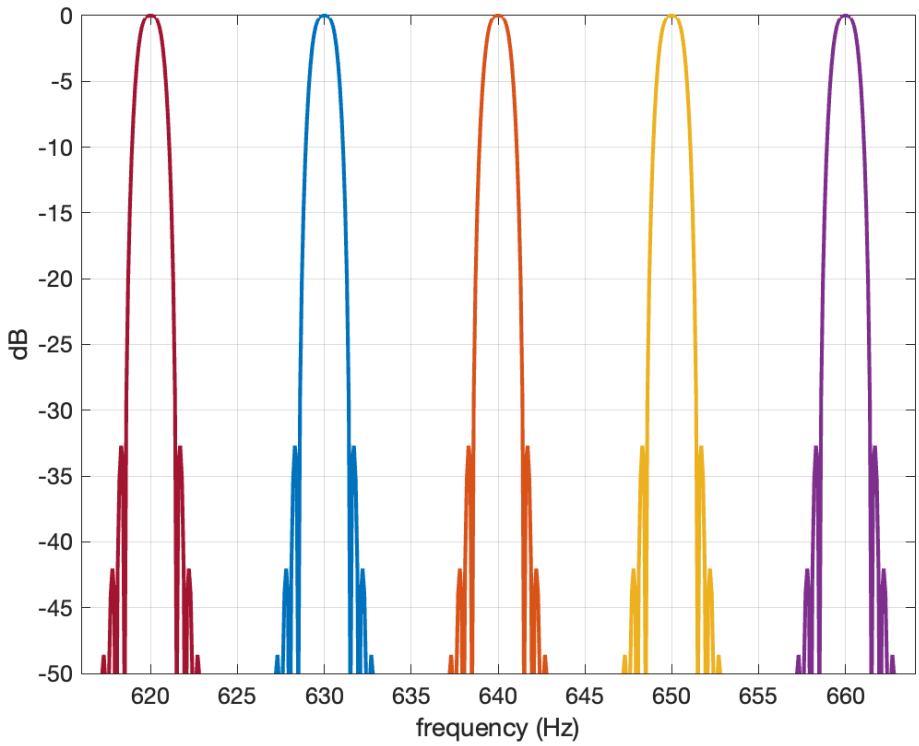

Figure 4.18: Spectrum of the pulse shaped OFDM subcarriers in the frequency band 615-665 Hz. The subcarriers are spaced at $\Delta F = 10$ Hz. The 3-dB spectral width of the subcarriers, after pulse shaping by PHYDYAS filter, is $W = 1.5$ Hz.

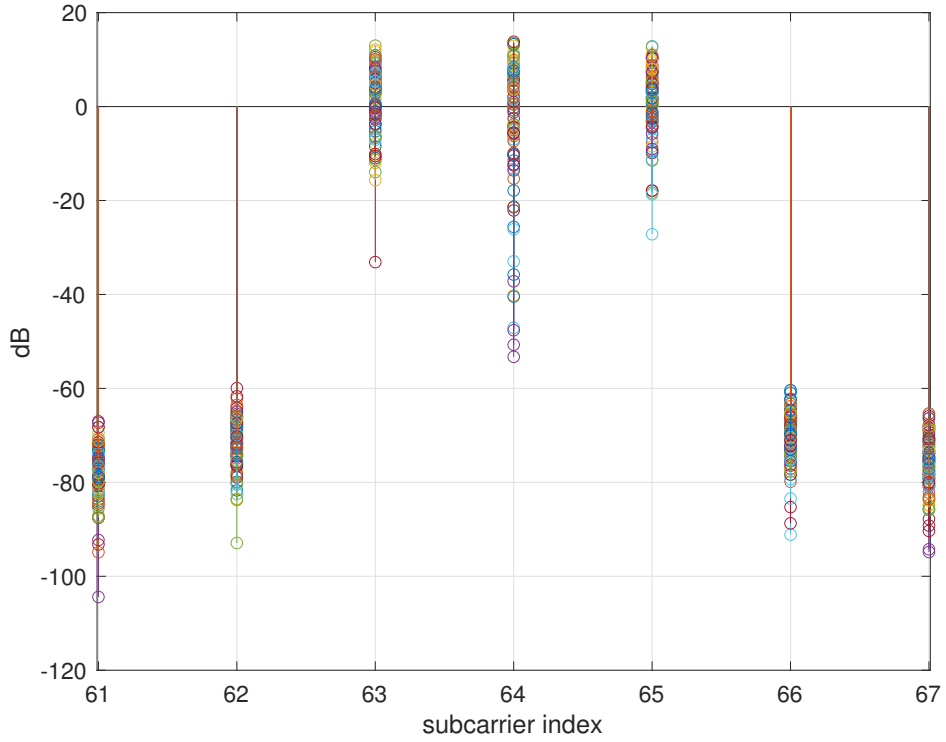

Figure 4.19: OFDM receiver processed subcarrier outputs. Only the 64th subcarrier is transmitted with a BPSK symbol across a channel with $\alpha_{\max} = 1.001$. A Doppler shift of $\delta f_c = (\alpha_{\max} - 1) f_c = 12.8$ Hz ($> \Delta F$) is experienced by the 64th subcarrier (corresponding to $f_c = 12.8$ kHz). Spurious pickups due to ICI can be observed on the 63rd and 65th subcarriers.

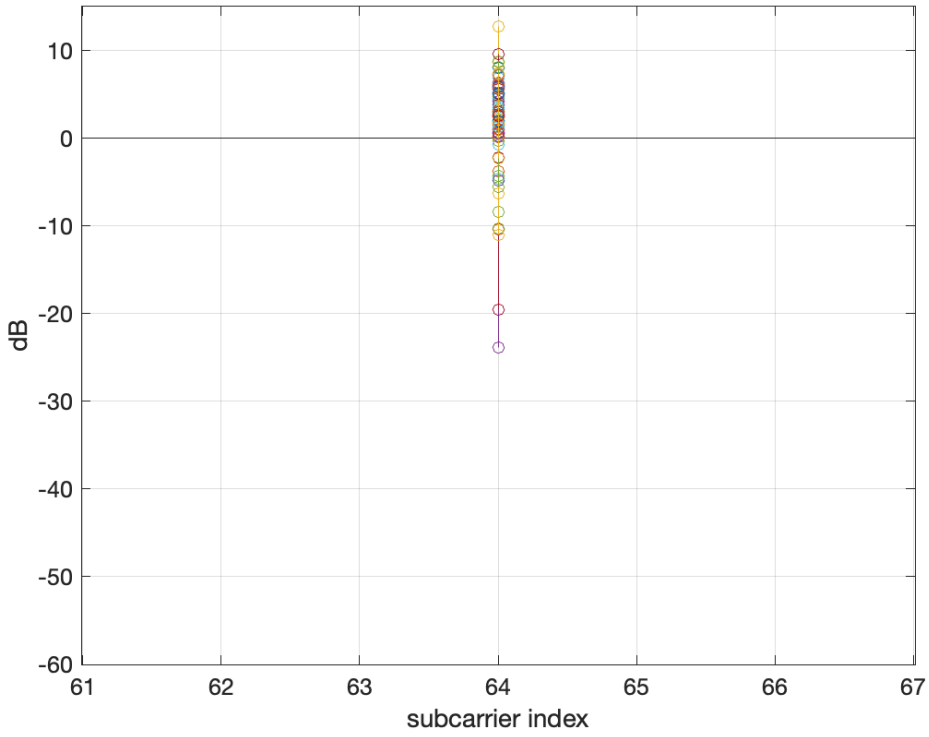

Figure 4.20: ODSS receiver processed subcarrier outputs in a delay-scale spread channel. Only the 64th subcarrier is transmitted with a BPSK symbol across a channel with $\alpha_{\max} = 1.001$. Unlike OFDM, ICI is avoided in ODSS.

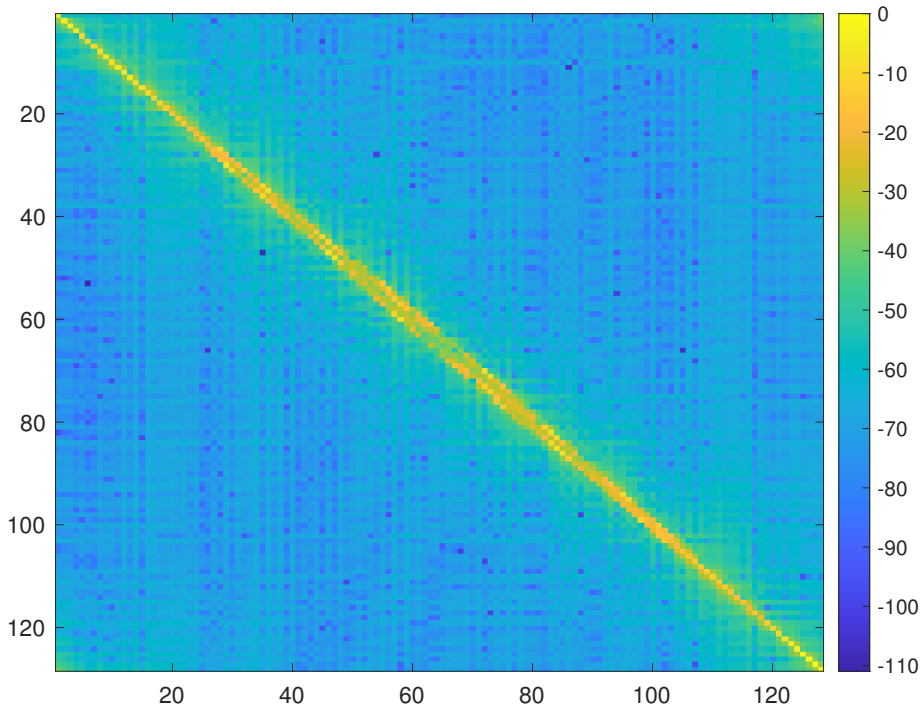

Figure 4.21: OTFS channel matrix (normalized magnitude, in dB) in the time-frequency domain for a simulated delay-scale channel realization. The channel matrix is non-diagonal with a severe ICI in excess of 0 dB relative to some diagonal entries.

Chapter 5

Variable Bandwidth Multicarrier Communications

In this chapter, we develop a new waveform for communicating over a delay and time-scale spread wideband channel. This waveform, named Variable Bandwidth Multicarrier (VBMC) waveform, comprises multiple subcarriers that are constructed from chirp pulses used in radars and sonars, and is a multicarrier analogue of the sweep spread carrier waveform that time multiplexes the digital symbols onto a single chirp pulse. We design the subcarrier chirps to occupy progressively increasing, frequency-dependent bandwidth from the lower to upper frequency edge of the communication band. Due to this, the subcarriers of the VBMC waveform maintain their near mutual orthogonality even after passing through a delay and scale spread channel, resulting in low inter-carrier interference, and thereby facilitating low complexity subcarrier-by-subcarrier decoding at the receiver. Numerical simulation of the bit error rate over delay-scale channels shows that the VBMC waveform outperforms the widely used Cyclic Prefix Orthogonal Frequency Division Multiplexing (CP-OFDM) and the recently developed Orthogonal Time-Frequency Space (OTFS) waveforms.

5.1 Introduction

Orthogonal frequency division multiplex (OFDM) communications employs multiple complex sinusoids as the carriers of digital information. The OFDM waveform, attached with a cyclic prefix (CP-OFDM) or zero padded (ZP-OFDM), eliminates the inter-carrier interference (ICI) in delay-spread multipath channels due to the orthogonality of its subcarriers. In channels that are also Doppler spread, the OFDM subcarriers lose their orthogonality due to multiple path-dependent Doppler shifts (time-scales) in a narrowband (wideband) channel. In such doubly-spread narrowband and wideband channels, OFDM receivers must employ sophisticated equalizers at the receiver side to tackle the resulting ICI.

Most radio frequency (RF) wireless communication channels are narrowband (or underspread): the effect of Doppler can be well approximated by a *uniform shift* of signal frequencies.[1] Orthogonal Time-Frequency Space (OTFS) waveform is a recently proposed modulation scheme for the delay and Doppler spread narrowband channels [27–30, 51]. In the channels commonly encountered in underwater acoustic (UWA) or ultra-wideband (UWB) RF communications, the effect of Doppler due to the motion of source, receiver, or scatterer, is to time-compress or dilate a *wideband* waveform [25]. Time-scaling on wideband signals manifests in a *non-uniform shift* of signal frequencies across the frequency band and is, therefore, unlike the effect of Doppler in a narrowband channel. The subcarriers of OFDM and OTFS are uniformly spaced in the frequency domain: in a wideband time-scale channel, they undergo frequency-dependent shifts which increase with frequency. Severe ICI ensues in such cases, leading to poor performance of low complexity single-tap equalizers.

In this chapter, we propose a new waveform, variable bandwidth multicarrier (VBMC) waveform, that performs well in multipath channels with path-dependent time-scales while using a simple, single-tap equalizer and subcarrier-by-subcarrier symbol decoding. VBMC is comprised of several subcarriers constructed by linearly sweeping the frequency in time

[1] Note that a narrowband *channel* is different from the conventional narrowband *waveform* (waveform bandwidth $<$ channel coherence bandwidth.)

across the band allotted to each subcarrier. We choose a variable and frequency-dependent subcarrier bandwidth that increases with frequency and a subcarrier duration that reduces with frequency. These aspects distinguish our VBMC from the traditional OFDM that uses multiple frequency continuous wave (CW) sinusoidal pulses of constant bandwidth and duration. These are also the features that make VBMC suitable for communication over delay-scale spread channels.

The delay and time-scale spread channel model has been used in several works [39, 51, 61]. In this work, we use the well known continuous time Shannon basis for representing the transmitted signal, which allows us to accurately generate delayed and scaled versions of bandlimited signals as they pass through the channel. We introduce and describe the construction of a modulation dictionary whose columns are the subcarriers of a multicarrier waveform. The framework we develop here allows us to systematically model the delay-scale channel as a linear transformation that can be used to design and evaluate various waveforms for communications on a level playing field. Finally, we present numerical studies using our delay-scale channel modeling framework, comparing the performance of VBMC with OFDM and OTFS.

5.2 Received Signal Model

In this section, we develop and present our delay-scale spread channel model. Consider a signal $s(t)$ transmitted over a medium that presents P scattering paths. The received signal, prior to noise being added, is a superposition of the signals due to each scatterer:

$$r_s(t) = \sum_{p=1}^{P} r_s(t; h_p, \tau_p, \alpha_p) = \sum_{p=1}^{P} h_p \sqrt{\alpha_p} s\left(\alpha_p(t-\tau_p)\right),$$

where the tuple (h_p, τ_p, α_p) contains the gain, delay and time-scale parameters associated with the pth scattering path.

We let $\alpha_{\max} \geq 1$ and $\tau_{\max} \geq 0$ denote the maximum scale and delay *spread* of the wideband channel, respectively, so that $\alpha_p \in [\alpha_{\max}^{-1}, \alpha_{\max}]$ and $\tau_p \in [0, \tau_{\max}]$. The above channel is known as a *delay-scale spread channel* due to multiple scatterers with possibly

different triples (h_p, τ_p, α_p).

The transmitted signal is of the form $s(t) = s_{\mathrm{BB}}(t)e^{j2\pi f_c t}$, where f_c is the center frequency and $s_{\mathrm{BB}}(t)$ is the complex baseband signal, band-limited to $-B/2 \leq f \leq B/2$. The Shannon-Nyquist sampling theorem admits the representation of such a signal in terms of its complex-valued discrete-time samples $s_{\mathrm{BB}}[m] = s_{\mathrm{BB}}\left(m/F_s\right)$, obtained at a rate $F_s \geq B$, as a linear combination of the Shannon basis vectors in $\mathcal{B}_\infty = \{\mathrm{sinc}\left(B(t - m/F_s)\right), t \in \mathbb{R}, m \in \mathbb{Z}\}$ [71]:

$$s_{\mathrm{BB}}(t) = \sum_{m=-\infty}^{\infty} s_{\mathrm{BB}}[m]\mathrm{sinc}\left(B(t - m/F_s)\right), \tag{5.1}$$

where $\mathrm{sinc}(x) \triangleq \frac{\sin \pi x}{\pi x}, x \neq 0$ and $\mathrm{sinc}(x) \triangleq 1, x = 0$.

In practice, we must use a waveform of finite duration, say, T, that is at best only *approximately* bandlimited. In this work, we consider a sampling rate $F_s > B$ such that the finite duration baseband signal, $s_{\mathrm{BB}}(t)$, has a negligible fraction of its total energy outside $-\frac{F_s}{2} \leq f \leq \frac{F_s}{2}$. Let $M = \lfloor F_s T \rfloor > BT$ be the number of samples of $s(t)$ over its finite time duration, $0 \leq t \leq T$. The orthogonal projection of $s(t)$ onto the finite dimensional space spanned by the basis vectors in $\mathcal{B}_M = \{\mathrm{sinc}\left(B(t - m/F_s)\right), 0 \leq t \leq T, m = 0, 1, \ldots, M-1\}$ is given by

$$\mathcal{P}s(t) \triangleq \sum_{m=0}^{M-1} s_{\mathrm{BB}}[m]\mathrm{sinc}\left(Bt - mB/F_s\right) e^{j2\pi f_c t}, \tag{5.2}$$

$0 \leq t \leq T$. We assume that $\epsilon = \|s(t) - \mathcal{P}s(t)\|_2$ is negligible and henceforth consider $s(t) \approx \mathcal{P}s(t)$.[2]

If the receiver is synchronized to the first arriving path, i.e., $\tau_1 = 0$, using the representation of $s(t)$ in (5.2), the delay-scale spread channel output (before adding noise) can be written as

$$r_s(t) = \sum_{p=1}^{P} h_p \sqrt{\alpha_p} \sum_{m=0}^{M-1} s_{\mathrm{BB}}[m]\mathrm{sinc}\left(\alpha_p B(t - \tau_p) - nB/F_s\right) e^{j2\pi f_c \alpha_p (t-\tau_p)}, \tag{5.3}$$

[2]The accuracy of the approximation can be improved by use of a large enough sampling rate and/or good pulse shaping transmit filters.

where $0 \leq t \leq T + \tau_{\max}$ due to the delay spread in the channel. The value of the residual time-scale spread, for example, in harsh UWA channels, is $\alpha_{\max} = 1.001$ after coarse resampling [14, 51]. The waveform in a UWA communication system operating over a frequency band from $f_L = 10$ kHz to $f_H = 20$ kHz will then experience a worst case bandwidth expansion of $\delta f = \alpha_{\max} f_H - \frac{1}{\alpha_{\max}} f_L = 30$ Hz due to time-scale spread. While a sampling rate of $B_{\max} = 10.03$ kHz is enough, we use a higher sampling rate to maintain good accuracy of approximation in (5.2), considering the finite duration of the waveform. Similarly, in UWA channels, a delay spread of tens of milliseconds is typical [90].

After complex demodulation using the center frequency, the received signal in the baseband is $r_{\mathrm{BB,s}}(t) = r_s(t)e^{-j2\pi f_c t}$. Using $r_s(t)$ in (5.3), the samples of the received signal in the baseband, $r_{\mathrm{BB,s}}[m'] = r_{\mathrm{BB,s}}(m'/F_s)$, can be expressed as

$$r_{\mathrm{BB,s}}[m'] = \sum_{m=0}^{M-1} s_{\mathrm{BB}}[m] \sum_{p=1}^{P} h_p \sqrt{\alpha_p} e^{-j2\pi f_c \alpha_p \tau_p} \times e^{j2\pi f_c (\alpha_p - 1) m'/F_s} \mathrm{sinc}\left(B(\alpha_p m' - m)/F_s - \alpha_p \tau_p B\right), \quad (5.4)$$

for $m' = 0, 1, \ldots, M' - 1$, where $M' = \lfloor F_s T + F_s \tau_{\max} \rfloor$ is the number of signal samples at the delay-scale channel output.

We may write (5.4) in the matrix-vector notation, including the additive receiver noise, as follows:

$$\mathbf{r} = \mathbf{H}\mathbf{s} + \mathbf{w}, \quad (5.5)$$

where $\mathbf{w} \in \mathbb{C}^{M'}$ is the vector containing the receiver noise samples $w[m]$,

$$\mathbf{s} = [s_{\mathrm{BB}}[0], s_{\mathrm{BB}}[1], \ldots, s_{\mathrm{BB}}[M-1]]^T \in \mathbb{C}^M, \quad (5.6)$$

$$\mathbf{r} = [r_{\mathrm{BB}}[0], r_{\mathrm{BB}}[1], \ldots, r_{\mathrm{BB}}[M'-1]]^T \in \mathbb{C}^{M'}, \quad (5.7)$$

$r_{m'} = r_{\mathrm{BB}}[m'] = r_{\mathrm{BB,s}}[m'] + w[m']$, and $\mathbf{H} \in \mathbb{C}^{M' \times M}$ is the delay-scale propagation channel

matrix whose $(m', m)^{\text{th}}$ entry is given by

$$H_{m',m} = \sum_{p=1}^{P} h_p \sqrt{\alpha_p} e^{-j2\pi f_c \alpha_p \tau_p} e^{j2\pi f_c (\alpha_p - 1) m'/F_s} \text{sinc}\left(B(\alpha_p m' - m)/F_s - \alpha_p \tau_p B\right). \quad (5.8)$$

We make a few quick observations. For $P = 1$, $h_1 = h \sim \mathcal{CN}(0, 1)$, $\tau_1 = 0$, $\alpha_1 = 1$, $w[m'] \sim \mathcal{CN}(0, \sigma^2)$, and if $s_m = s_{\text{BB}}[m], m = 0, 1, 2, \ldots, M-1$ are M transmit symbols from a constellation, the received signal $r_m = h\, s_m + w[m], m = 0, 1, 2, \ldots, M-1$ follows the familiar Rayleigh fading model with a single path corrupted by AWGN. Also, with P paths, $\alpha_p = 1$ (no Doppler), and with path delays $\tau_p = n_p/F_s$ that are *integer* multiples of the sampling interval, we can diagonalize the channel using the CP-OFDM waveform, where, the first L samples of the baseband waveform are used for the cyclic prefix and the remaining $N_s = M - L$ samples are used for information encoding (corresponding to a cyclic prefix of duration $T_{\text{CP}} = L/F_s$ and an OFDM symbol duration of $T_{\text{symb}} = N_s/F_s$, respectively.) If the bandwidth and hence the sampling rate are high, a delay-spread channel with path delays that are *non-integer* multiples of the sampling interval is still approximately diagonalized by the CP-OFDM waveform. Finally, when $\alpha_p \neq 1$, the channel is time-varying and CP-OFDM witnesses ICI at the output of DFT processing.

5.3 Modulation Dictionary and Waveforms

In this section, we present the notion of *modulation waveform dictionary*, and describe its construction for the different waveforms compared in this chapter. Expressing the system model in terms of a modulation dictionary allows us to systematically analyze any communication waveform.

Consider a stream of information bits $b_q, q = 1, 2, \ldots, N \log_2 Q$, that get mapped to N ($\leq N_s = M - L$) complex symbols, $x_n \in \mathbb{C}, n = 1, 2, \ldots, N$, from a Q-QAM constellation. Let $\mathbf{x} \in \mathbb{C}^N$ denote the complex symbol vector whose nth entry is x_n. Let $\mathbf{G} \in \mathbb{C}^{M \times N}$ represent a modulation waveform dictionary whose columns are the subcarriers of the information symbols $x_n \in \mathbb{C}, n = 1, 2, \ldots, N$. The samples of the baseband waveform are

given by

$$\mathbf{s} = \mathbf{G}\mathbf{x}. \tag{5.9}$$

We now present the construction of $\mathbf{G}$ for the OFDM, OTFS and the proposed VBMC waveforms.

5.3.1 OFDM and OTFS Waveforms

The modulation waveform dictionary for CP-OFDM communications is constructed from the N-point inverse DFT matrix. For a CP of length $L > F_s\tau_{\max}$, the modulation dictionary $\mathbf{G} \in \mathbb{C}^{M\times N}$, with $M = N_s + L$, is obtained by appending the last L rows of the $N_s \times N_s$ inverse DFT matrix on its top and retaining only N ($\leq N_s$) columns corresponding to the subcarriers of OFDM mounted with symbols. In the case of OTFS, the N information symbols mounted along the delay axis is first Fourier transformed to the frequency axis before mounting them on the OFDM subcarriers. A subsequent inverse DFT operation undoes the DFT operation of the inverse symplectic Fourier transform. Therefore, the modulation dictionary of OTFS is obtained by prefixing the rows of an $N_s \times N_s$ identity matrix with its last L rows and retaining only the N ($\leq N_s$) columns corresponding to the subcarriers mounted with symbols. Thus, we observe that, in the setting considered in this chapter, OTFS reduces to a single carrier (SC) communication scheme that simply time-multiplexes the symbols on a single carrier corresponding to the band center frequency. Note that this is not the case when multiple symbols are transmitted per frame, since OTFS uses a single CP for the entire frame.

5.3.2 Variable Bandwidth Multicarrier Waveform

Recall that time scaling results in a non-uniform shift of the signal frequencies. Specifically, if the time-scale factor is α, a spectral component at f shifts by $\delta f = (\alpha - 1)f$. This means that subcarriers of the OFDM and OTFS waveform, that are uniformly spaced on the frequency axis, shift by different amounts under time-scaling distortions. As a result, ICI ensues whose magnitude increases with subcarrier frequency, rendering a receiver

using low complexity single tap equalizer and symbol-by-symbol decoding ineffectual in these schemes. This key observation motivates us to consider a frequency dependent bandwidth for the subcarriers in a multicarrier communication scheme for wideband delay-scale channels.

We now describe the construction of the VBMC subcarriers. The communication band from f_L to f_H is divided into N frequency cells of varying widths, and a VBMC subcarrier is associated with each cell. The VBMC subcarriers are linear frequency modulated (LFM) chirp pulses that sweep a bandwidth depending on the subcarrier frequency cell. Let Δf be the width of the first subcarrier's frequency cell. We choose $\Delta f = \beta/T_{\text{symb}}$ where T_{symb} is the VBMC symbol duration and β is a factor to accommodate bandwidth expansion due to pulse shaping. Consider the frequencies $f_n, n = 0, 1, 2, \ldots, N$, with $f_0 = f_L$ and

$$f_{n+1} = f_n \left(1 + \Delta f / f_L\right) = f_L \left(1 + \Delta f / f_L\right)^n . \tag{5.10}$$

The number of VBMC subcarriers N, for a given Δf and frequency band f_L to f_H, is found from:

$$N = \left\lfloor \frac{\log\left(f_H / f_L\right)}{\log\left(1 + \Delta f / f_L\right)} \right\rfloor . \tag{5.11}$$

An nth VBMC subcarrier, located in the frequency cell $[f_{n-1}, f_n]$, $n = 1, 2, \ldots, N$, is an LFM pulse $c_n(t)$ of duration

$$T_n = \left(\frac{\alpha_{\max}^{-1} f_1 - \alpha_{\max} f_0}{\alpha_{\max}^{-1} f_n - \alpha_{\max} f_{n-1}} \right) T, \tag{5.12}$$

and chirp rate

$$k_n = \frac{\alpha_{\max}^{-1} f_n - \alpha_{\max} f_{n-1}}{T_n}, \tag{5.13}$$

given by

$$c_n(t) = \frac{1}{\sqrt{T_n}} e^{j2\pi\left(f_{c,n} t + \frac{1}{2} k_n t^2\right)}, -T_n/2 \le t \le T_n/2, \tag{5.14}$$

where

$$f_{c,n} = \frac{\alpha_{\max} f_{n-1} + \alpha_{\max}^{-1} f_n}{2}, \tag{5.15}$$

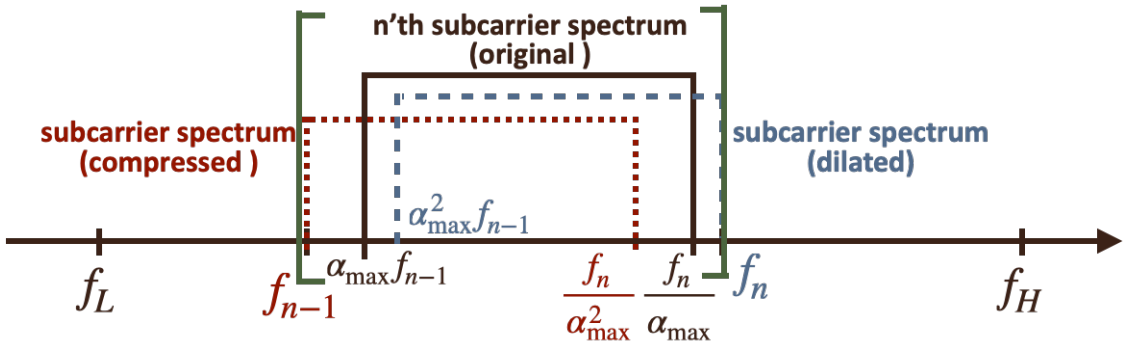

Figure 5.1: Effect of worst-case time compression and dilation on the nth VBMC subcarrier spectrum.

is the subcarrier center frequency. Note that the duration, chirp rate, and frequency sweep of the chirp subcarriers all vary with the subcarrier frequency.

The VBMC subcarriers designed above (with $\beta > 1$) to communicate N symbols over a channel with maximum delay and scale spreads of $\tau_{\max}$ and $\alpha_{\max}$, respectively, have a higher per symbol bandwidth, resulting in greater time-bandwidth product than the subcarriers of OFDM. This helps VMBC achieve a better symbol detection performance.

The modulation dictionary, $\mathbf{G} \in \mathbb{C}^{M \times N}$, for VBMC is constructed as follows. As in OFDM/OTFS, we choose $L \geq F_s \tau_{\max}$ and set $M = N_s + L$, where $N_s = F_s T_{\text{symb}}$. The rows of $\mathbf{G}$ contain the samples of the VBMC subcarrier waveforms. Let $M_n = \lfloor F_s T_n \rfloor$ and $m_n = \lfloor \frac{M - M_n}{2} \rfloor$. The nth column of $\mathbf{G}$ contains the M_n samples of the nth VBMC subcarrier, for $n = 0, 1, \ldots, N-1$:

$$G_{m,n} = \begin{cases} c_n \left(\frac{m - m_n}{F_s} - \frac{T_n}{2} \right), & m_n \leq m \leq m_n + M_n - 1 \\ 0, & \text{otherwise} \end{cases} \tag{5.16}$$

We now briefly discuss VBMC in relation with other similar waveforms in the literature.

1. The patented sweep spread carrier (S2C) waveform used in UWA communications, and implemented in a commercial modem, uses chirp pulse as a single carrier [44,45]. In S2C, symbols are time-multiplexed on a complex chirp carrier that sweeps the

entire communication band, every symbol occupying a duration of $T_{\text{symb}} = T/N$ and bandwidth of $\Delta f = \beta N/T$. VBMC is a multicarrier waveform with chirp subcarriers, with the nth symbol occupying a bandwidth $\Delta f_n = \alpha_{\max}^{-1} f_n - \alpha_{\max} f_{n-1}$ and duration $T_n = \beta/\Delta f_n$.

2. VBMC has a structure resembling Orthogonal Delay Scale Space (ODSS) waveform in that their subcarriers have a varying bandwidth and duration (See Chapter 4 and [6].) In fact, ODSS using basic chirplet $c_0(t)$ and a scaling ratio of $q = 1 + \Delta f/f_L$ *without* the precoding ODSS transform (i.e., inverse discrete Mellin-Fourier transform) reduces to VBMC. It is interesting to note that the condition $q = 1 + \Delta f/f_L = f_n/f_{n-1} > \alpha_{\max}^2$ must be met to design the VBMC subcarriers (since we need $\Delta f_n > 0$), which is the same as the condition for the ODSS waveform design to contain the ICI. To see how this condition helps in containing the ICI, consider the worst-case compression or dilation of the nth VBMC subcarrier waveform by the maximum time-scale factor, $\alpha_{\max}$. A compression (dilation) of the waveform results in dilation (compression) of its spectrum, as depicted in Figure 5.1. The condition, $q = f_n/f_{n-1} > \alpha_{\max}^2$, prevents the nth subcarrier spectrum from having a significant overlap with the adjacent subcarrier spectra even when it undergoes compression or dilation by the largest time-scale factor in a delay-scale spread channel.

3. A waveform with a similar time-frequency tiling structure was proposed in [104]. We highlight a few distinguishing features of VBMC compared to the Multi-Layer Block Transmission (MLBT) waveform in [104]:

   (a) In [104], the choice of compressive time-scale factor for the transmission waveform is only to ensure non-overlapping frequency bands for the inter-layer MLBT subcarriers. In our development of VBMC (and ODSS), we relate the choice of waveform time-scale, q, to the maximum channel scale spread, $\alpha_{\max}$, i.e., we require: $q > \alpha_{\max}^2$ to contain ICI.

   (b) We use chirp based subcarrier pulses, in lieu of the Shannon wavelets in [104],

that can potentially be designed for a larger duration and hence high time-bandwidth product leading to a better symbol detection performance.

(c) The use of chirp pulses and incorporation of the maximum channel scale spread into our waveform design results in a nearly orthogonal subcarrier waveforms even after the distortion caused by delay-scale channel. Consequently, VBMC receiver performs quite well (see Section 5.5) with the least complexity single-tap equalizers. In [104], equalization of N_l banded channel matrices (not purely diagonal) of size $(K'+1) \times K'$ is needed, where K' is the number of number of layers, N_l is the number of symbols mounted in each layer, and $N = KN_l$ is the total number of symbols in MLBT.[3]

(d) Modeling errors due discretization of scale and lag parameters is avoided in our system model development which also provides a general framework (through the notion of a *waveform dictionary*) for comparing different waveforms. A detailed discussion of the modeling error due to scale and lag discretization is found in the Appendix, in Section 5.8.

(e) Channel parameters, $\tau_{\max}$ and $\alpha_{\max}$, used for performance studies in [104] are not typical of UWA environments and communication systems. The channel delay spread, $\tau_{\max}$, is usually in tens of milliseconds. Also, the typical value of maximum channel time-scale spread is $\alpha_{\max} \sim 1.001$ after a coarse Doppler compensation of the received waveform.

In the next section, we present the end-to-end system model and the symbol decoding from the received front-end signal.

[3]If we consider only one symbol per layer ($N_l = 1$), as in this work, then $K' = N$.

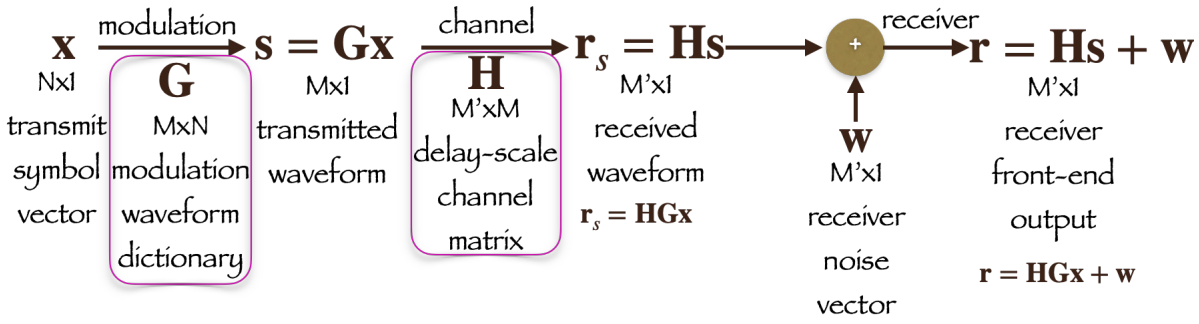

Figure 5.2: System model based on the waveform dictionary, $\mathbf{G}$.

5.4 Symbol Decoding

The receiver front-end signal samples are the noise corrupted output of the composite channel HG whose input is the transmitted symbol vector. Using (5.9) in (5.5), we have

$$\mathbf{r} = HG\mathbf{x} + \mathbf{w} \in \mathbb{C}^{M'}. \tag{5.17}$$

Figure 5.2 depicts the system model whose input is the transmitted data symbols and the output is the receiver front-end signal samples given by (5.17).

The transmitted data symbols can be decoded from the received signal samples. The minimum mean square error (MMSE) estimate of the symbol vector $\mathbf{x}$ is given by:

$$\mathbf{z} = \mathbf{W}_{\text{MMSE}}\mathbf{r} = \mathbf{W}_{\text{MMSE}}\mathbf{HGx} + \mathbf{u} \in \mathbb{C}^{N}, \tag{5.18}$$

where $\mathbf{W}_{\text{MMSE}} \triangleq \left(\mathbf{G}^H\mathbf{H}^H\mathbf{HG} + \sigma^2\mathbf{I}_N\right)^{-1}\mathbf{G}^H\mathbf{H}^H$ is the MMSE weight matrix and $\mathbf{u} = \mathbf{W}_{\text{MMSE}}\mathbf{w}$ is the noise at the MMSE equalizer output. Symbol decoding then proceeds by slicing the entries of $\mathbf{z}$ to the closest symbol in the Q-QAM constellation. Figure 5.3 shows the symbol decoding steps described above.

If the modulation dictionary $\mathbf{G}$ is such that the matrix $\mathbf{D} = \mathbf{G}^H\mathbf{H}^H\mathbf{HG}$ is diagonal, we may do a *subcarrier-by-subcarrier* equalization and decoding from the received symbol

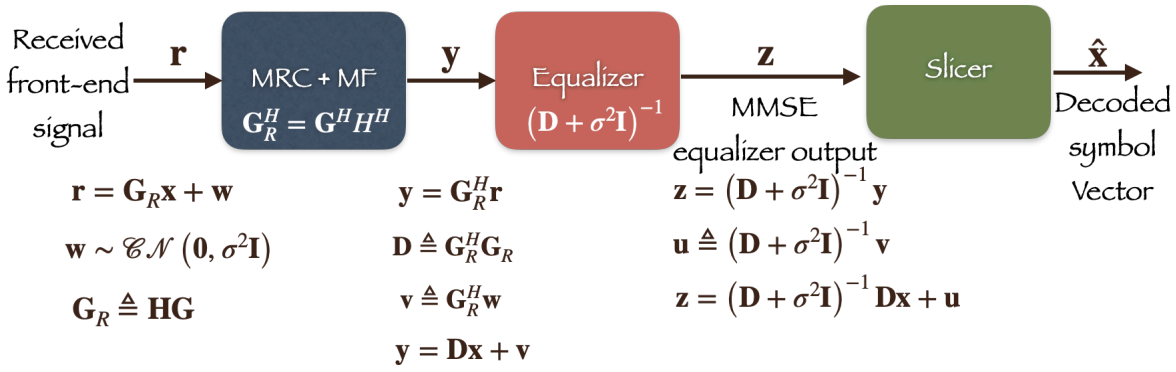

Figure 5.3: MMSE receiver and symbol detection.

vector. The MMSE equalizer output can be expressed in terms of $\mathbf{D}$ as follows:

$$\mathbf{z} = \left(\mathbf{D} + \sigma^2\mathbf{I}_N\right)^{-1}\mathbf{Dx} + \mathbf{u}. \tag{5.19}$$

Even if $\mathbf{D}$ is only close to diagonal, a subcarrier-by-subcarrier symbol equalization and decoding using the best diagonal approximation of $\mathbf{D}$ performs quite well in practice. Based on the entries of $\mathbf{D}$, we define the signal to interference plus noise ratio (SINR) for the nth symbol to be:

$$\text{SINR}_n = \frac{|D_{n,n}|^2}{\sum_{n' \neq n} |D_{n,n'}|^2 + \sigma_{v,n}^2}, \tag{5.20}$$

where $\sigma_{v,n}^2 = \sigma^2 D_{n,n}$ is the noise power contained in the nth symbol measurement, i.e., at the output of the maximum ratio combiner (MRC) (pre-multiplication by $\mathbf{H}$) followed by matched filtering (MF) (pre-multiplication by $\mathbf{G}$). Subcarrier by subcarrier decoding performs well when the symbol SINR values are high.

A full complexity MMSE equalizer involves the inversion of an $N \times N$ matrix with a computational complexity of $\mathcal{O}(N^3)$. For a one-tap MMSE equalizer, using the best diagonal approximation of $\mathbf{D}$, the computational complexity is only $\mathcal{O}(N)$.

5.5 Numerical Simulations

In this section, we present computer simulation results of UWA communications using OFDM, OTFS and VBMC waveforms over $f_L = 10$ kHz to $f_H = 20$ kHz band.[4] A symbol duration of $T_{\text{symb}} = 20$ ms is considered for waveform design in all schemes with a pulse shaping factor of $\beta = 2$. A sampling rate of $F_s = 21$ kHz, which is more than twice the communication bandwidth, is used in all systems to minimize the representation errors. With these settings, we have $\Delta f = \beta/T_{\text{symb}} = 100$ Hz and $N = 70$ (computed using (5.11)). The parameter $L = \lceil F_s \tau_{\max} \rceil$ is chosen based on the channel delay spread. Throughout, we use the VBMC waveform designed for $\alpha_{\max} = 1.001$ regardless of the actual value of channel scale spread. OFDM and OTFS employ an $N_{\text{FFT}} = F_s T_{\text{symb}} = 420$ point DFT of which only $N_{\text{FFT}}/2 = 210$ subcarriers are within the transmission frequency band due to oversampling. Of these $N_{\text{FFT}}/2 = 210$ subcarriers, every third subcarrier is mounted with an information symbol to maintain the same data rate across all waveforms; the rest are null subcarriers. We draw i.i.d. data symbols from a BPSK constellation in this study.

As in [6], we define SNR as the ratio of the received front-end signal power to noise power. We evaluate the bit error rate (BER) performance of CP-OFDM, CP-OTFS and VBMC waveforms of identical duration, $T = T_{\text{symb}} + \tau_{\max}$, as the SNR is varied from -9 dB to 21 dB. We simulate a delay-scale channel whose $h_p \overset{i.i.d.}{\sim} \mathcal{CN}(0,1)$, $\tau_p \overset{i.i.d.}{\sim} \mathcal{U}(0, \tau_{\max})$ and $\alpha_p \overset{i.i.d.}{\sim} \mathcal{U}(\alpha_{\max}^{-1}, \alpha_{\max})$, for $p = 1, 2, \ldots, P$. For this channel model and for the waveform types considered here, it can be shown that the received signal power $P_{\text{Rx, r}} \triangleq \mathbb{E}\{\mathbf{x}^H \mathbf{G}^H \mathbf{H}^H \mathbf{H} \mathbf{G} \mathbf{x}\} \approx P P_{\text{Tx, s}}$ where $P_{\text{Tx, s}} \triangleq \mathbb{E}\{\mathbf{s}^H \mathbf{G}^H \mathbf{G} \mathbf{s}\}$ is the transmitted signal power (see Appendix, Section 5.7). The average BER is computed in this work using $N_{\text{trial}} = 5000$ Monte Carlo trials where, in each trial, the symbols and the channel parameters are drawn from their respective distributions. We may speed up the simulations using semi-closed form expressions derived in the Appendix, Section 5.9, where we

[4] UWA channels are one of the harshest communication media with large delay and Doppler spreads. Also, a fractional bandwidth of $\frac{f_c}{B} = 0.67 > 0.25$ and relatively high v/c (v = scatterer velocity, c = sound speed) ratios in the range 10^{-3}–10^{-1} renders channel as wideband.

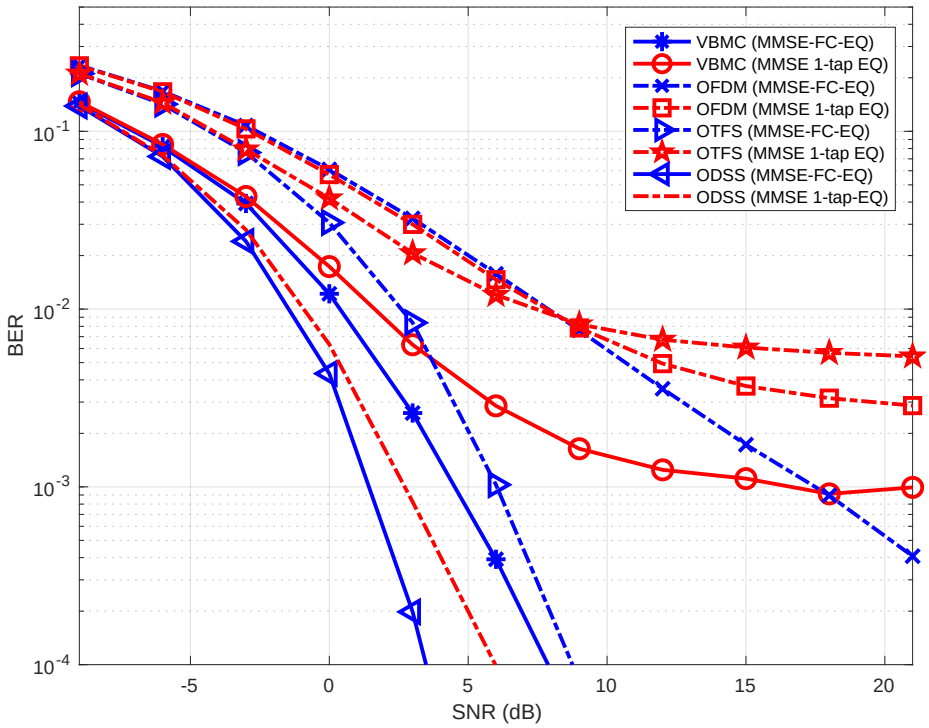

Figure 5.4: BER performance plots for $P = 20$, $\tau_{\max} = 10$ ms, $\alpha_{\max} = 1.001$.

only need to draw random instances of the channel in each trial.

Figure 5.4 shows the BER performance of the three schemes in a delay-scale channel with $P = 20$ paths, $\tau_{\max} = 10$ ms, and $\alpha_{\max} = 1.001$. Note that the channel spread, defined by $\eta_{\max} \triangleq \tau_{\max}\Delta f_{\max} = \tau_{\max}\left(\alpha_{\max} - 1\right) f_H$, where $\Delta f_{\max} = \left(\alpha_{\max} - 1\right) f_H$ is the maximum Doppler frequency spread, is $\eta_{\max} = 0.2 < 0.25$, making it an underspread channel [25, 39]. The total waveform duration is $T = 30$ ms leading to a spectral efficiency of 0.23 bits/s/Hz, which is reasonable for long-range UWA communication. We show the performance of both full complexity MMSE channel equalizer (MMSE-FC-EQ), as in (5.18), and the computationally simpler one-tap MMSE equalizer (MMSE-1-tap-EQ) obtained by replacing all non-diagonal entries of $\mathbf{D}$ with zero. VBMC using the MMSE receiver with a full complexity equalizer outperforms all other schemes. While all waveforms with a one-tap equalizer exhibit a BER floor beyond a certain SNR, VBMC using the one-tap MMSE equalizer has the lowest BER floor which is at least a third (fifth) of OFDM (OTFS) waveform at SNR = 15 dB. Figure 5.4 also shows the BER performance of the ODSS modulation implemented as an overlay on VBMC. The ODSS

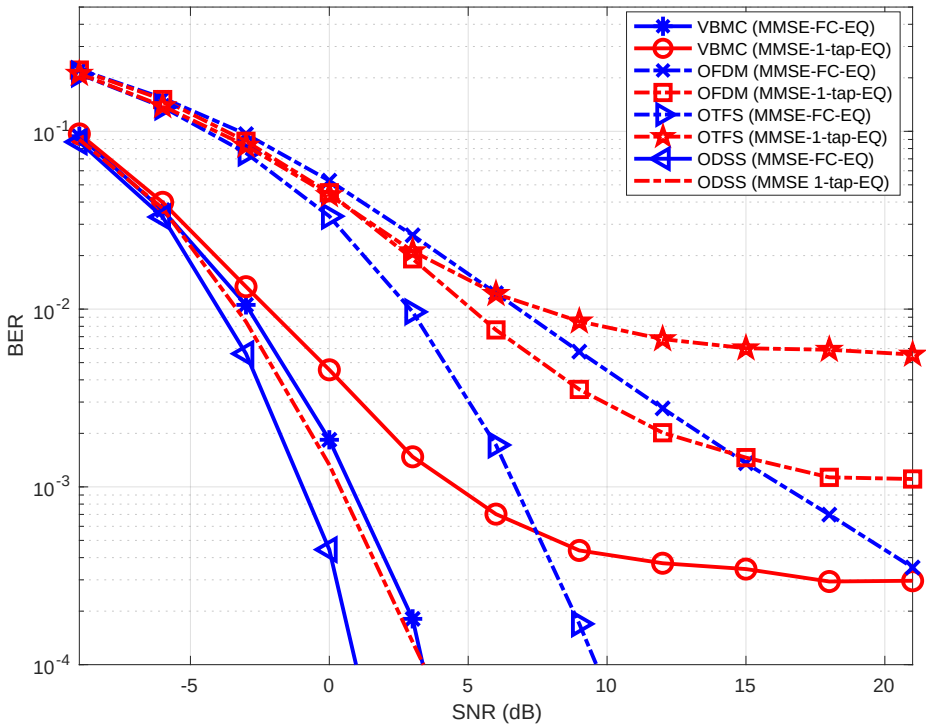

Figure 5.5: BER performance plots for $P = 20$, $\tau_{\max} = 20$ ms, $\alpha_{\max} = 1.002$.

chirplets are constructed using $q = 1+\Delta f/f_L = 1.01$. The data symbol vector, containing $N = 70$ BPSK symbols in the Mellin-Fourier domain, is subject to the ODSS transform before mounting on the ODSS chirplets. Both FC and 1-tap ODSS receivers outperform the VBMC receivers. The FC ODSS receiver achieves BER $= 10^{-3}$ at an SNR which is at least ΔSNR $= 3$ dB better than VBMC. The BER of the 1-tap ODSS receiver floors below BER $= 10^{-5}$ (not shown). We attribute the improvement in ODSS performance over VBMC to its better *effective diversity* [76]; a thorough analysis is beyond the scope of this thesis.

Figure 5.5 compares the BER of the three schemes in an overspread delay-scale channel with $P = 20$ paths, $\tau_{\max} = 20$ ms, and $\alpha_{\max} = 1.002$. In this case, the maximum Doppler frequency spread is quite high: $\eta_{\max} = 0.8 > 0.25$, making the channel overspread. The waveform duration is now $T = 40$ ms resulting in a reduced spectral efficiency of 0.175 bits/s/Hz. As the channel becomes more spread, VBMC performs even better compared to the other schemes.Among the receivers using a one-tap equalizer, the BER of VBMC is less than a third (twentieth) of OFDM (OTFS) at SNR $= 15$ dB. Compared to the

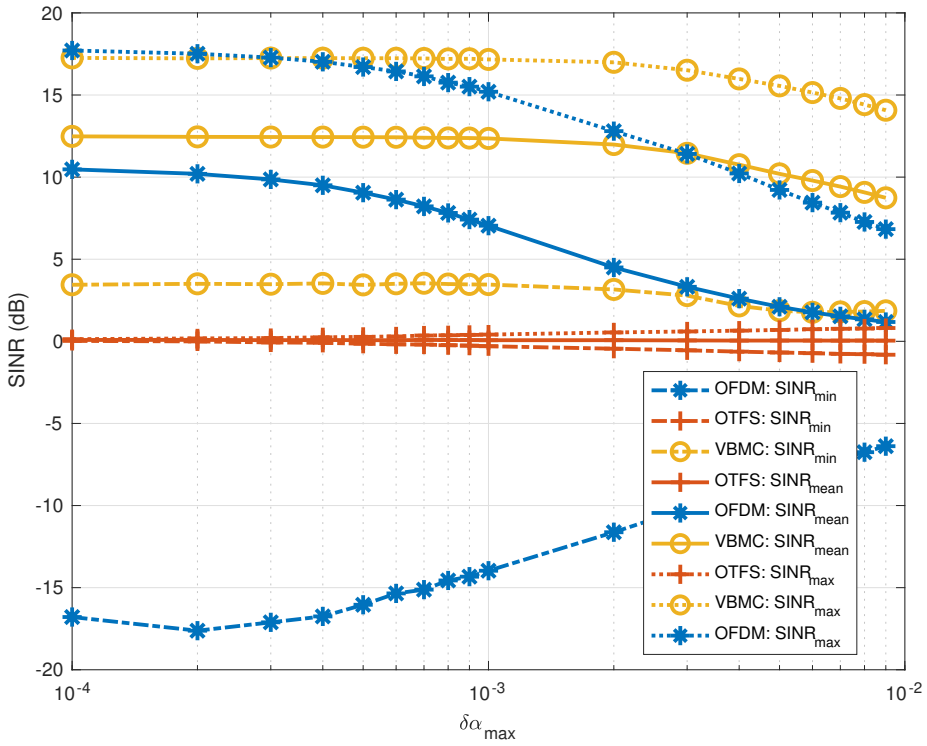

Figure 5.6: SINR plots for VBMC, OFDM and OTFS in a delay-scale spread channel with $P = 20, \tau_{\max} = 20$ ms and SNR $= 6$ dB.

underspread channel considered in Figure 5.4, the VBMC receiver's performance has improved: using the full complexity (one-tap) equalizer, it achieves BER $= 10^{-3}$ at an SNR which is lower by about ΔSNR $= 3$ dB (ΔSNR $= 10$ dB). Figure 5.5 also shows the performance of the ODSS waveform using full complexity and one-tap MMSE equalizers in the overspread channel. With worsening channel conditions (from being underspread to overspread), ODSS receivers perform even better and also maintain their relative edge over the VBMC waveform.

To elucidate where the performance improvement comes from, we compute the minimum, mean and maximum of the symbol SINR values given by (5.20), for SNR $= 6$ dB, in a channel with $P = 20$ paths and $\tau_{\max} = 20$ ms. Figure 5.6 shows these for the three schemes as a function of the Doppler scale spread. The SINR values vary the most in OFDM and the least in OTFS scheme. The SINR plots of the VBMC waveform designed

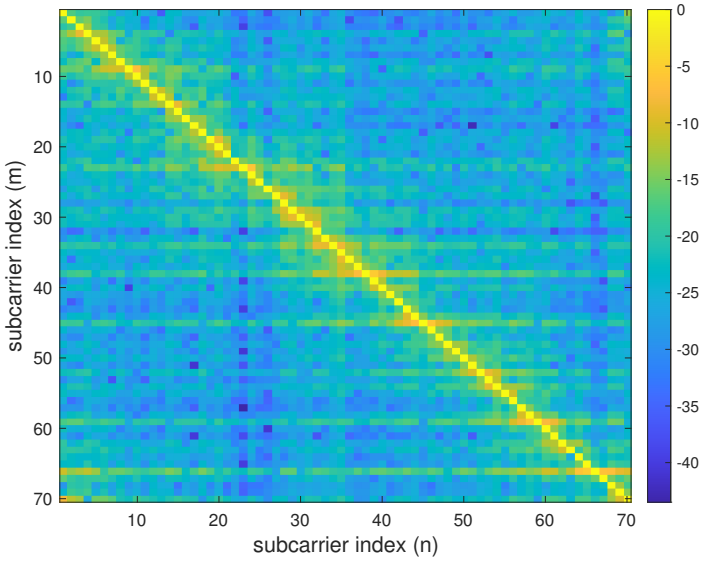

Figure 5.7: OFDM composite channel matrix: $20\log_{10}|\mathbf{D}|$.

for $\alpha_{\max} = 1.001$ has the highest mean SINR compared to the mean SINR for other waveforms over a wide range of maximum scale spread. This results in the lower BER floor of VBMC using a one-tap MMSE equalizer.

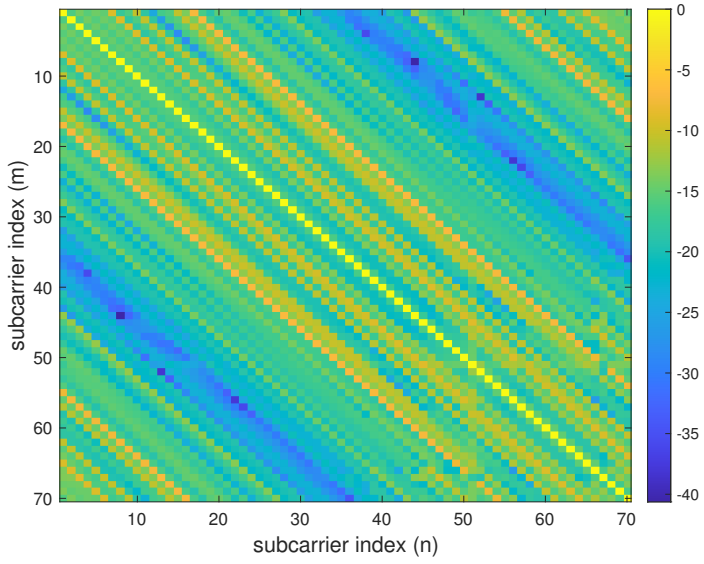

Figure 5.8: OTFS composite channel matrix: $20\log_{10}|\mathbf{D}|$.

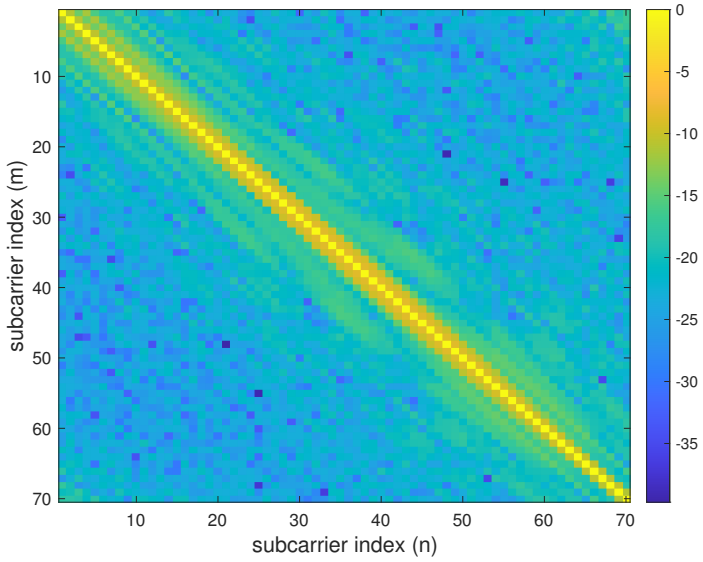

Figure 5.9: VBMC composite channel matrix: $20\log_{10}|\mathbf{D}|$.

Figures 5.7, 5.8, and 5.9 show a random realization of the entries of the composite channel matrix ($\mathbf{D} = \mathbf{G}^H\mathbf{H}^H\mathbf{H}\mathbf{G}$) during the simulation runs for OFDM, OTFS and VBMC, respectively, in a delay scale channel with $P = 20$ paths, $\tau_{\max} = 10$ ms, and $\alpha_{\max} = 1.001$. The diagonal entries are normalized to 0 dB and magnitudes (in dB) are color-coded with the highest magnitude represented by bright yellow and the lowest by dark blue color. The composite channel matrix, $\mathbf{D}$, of VBMC is nearly diagonal compared to OFDM and OTFS that exhibit significant off-diagonal entries. Also, we notice a relatively smaller variation in the magnitude of the diagonal entries of the VBMC channel matrix. To quantify the variation among the diagonal entries of the channel matrices of these waveforms more thoroughly, we examine their Jain's fairness index defined as follows:

$$\mathcal{J}_D = \frac{|\sum_n D_{n,n}|^2}{N\sum_n |D_{n,n}|^2}. \tag{5.21}$$

Figure 5.10 shows the plot of Jain's index of the diagonal entries of $\mathbf{D}$ for the three waveforms in a delay scale channel with $P = 20$ paths. The plot corroborates our observation about the diagonal entries of the VBMC channel matrix which has the highest fairness index of all and hence least variation among the diagonal entries. In particular, we note

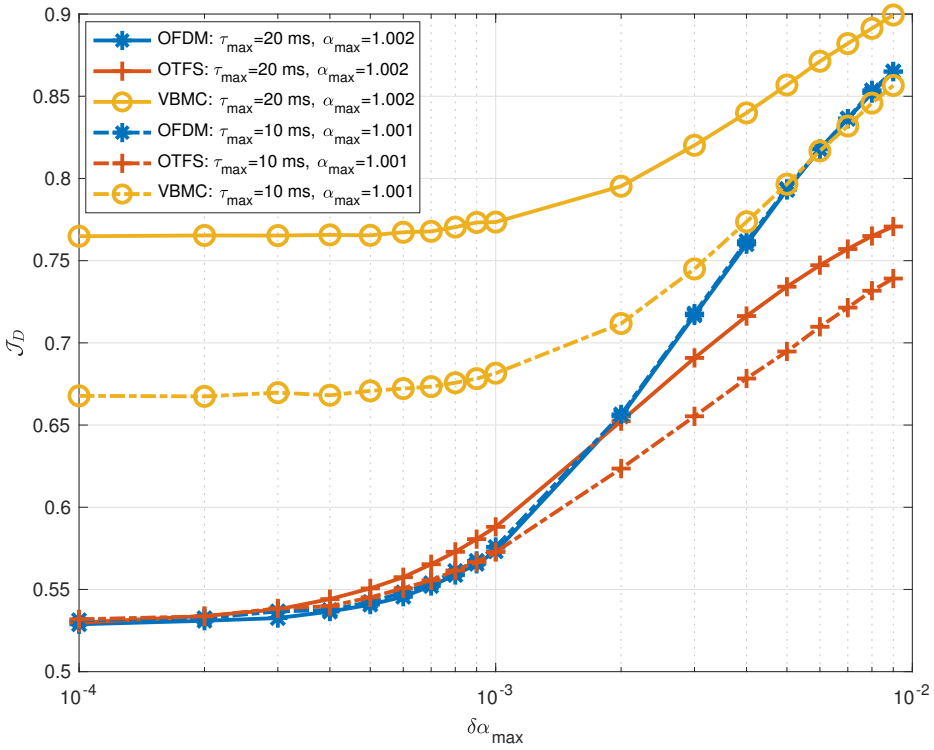

Figure 5.10: Jain's fairness index of the diagonal entries of OFDM, OTFS and VBMC composite channel matrix, D.

that the fairness index of VBMC improves when the channel is more spread.

5.6 Conclusions

In this work, we introduced the Variable Bandwidth Multicarrier (VBMC) waveform for digital communications over delay and scale spread wideband channels. Based on the well known representation theorem of bandlimited signals in terms of their discrete time samples, we presented an end-to-end system model that allows an accurate comparison of different modulation waveforms in a delay and scale spread channel. We briefly related our proposed waveform with other two similar waveforms in the literature. Finally, we investigated the BER performance through numerical simulations and showed that VBMC has a lower BER floor than the OFDM and OTFS receivers when using a one-tap equalizer.

We empirically showed that the VBMC waveform has the highest mean SINR in the received symbol vector among the three schemes, even in highly spread channel conditions, which explains its superior performance. In this work, we used perfect channel state information at the receiver (CSIR). Future work can consider channel estimation and equalization, evaluating the peak-to-average power ratio, diversity order, channel capacity, and developing computationally efficient architectures for modulation and demodulation for the VBMC waveform.

5.7 Appendix A: Transmitted and Received Signal Power

Transmitted power of the waveform, $\mathbf{s} = G\mathbf{x}$, is given by:

$$\begin{aligned} P_{\mathrm{Tx},s} &= \mathbb{E}\{\mathbf{x}^H\mathbf{G}^H\mathbf{G}\mathbf{x}\} \\ &= \mathbb{E}\{\mathrm{tr}\left(\mathbf{x}^H\mathbf{G}^H\mathbf{G}\mathbf{x}\right)\} \\ &= \mathbb{E}\{\mathrm{tr}\left(\mathbf{G}^H\mathbf{G}\mathbf{x}\mathbf{x}^H\right)\} \\ &= \mathrm{tr}\left(\mathbf{G}^H\mathbf{G}\right)\mathbb{E}\{\mathbf{x}\mathbf{x}^H\} \\ &= \sigma_{\mathrm{s}}^2\mathrm{tr}\left(\mathbf{G}^H\mathbf{G}\right) \end{aligned} \tag{5.22}$$

where we assume that symbols are i.i.d. with an average per symbol power, σ_{s}^2, so that we have: $\mathbb{E}\{\mathbf{x}\mathbf{x}^H\} = \sigma_{\mathrm{s}}^2\mathbf{I}$.

The signal component of the received waveform is given by

$$\mathbf{r}_s = \mathbf{G}_R\mathbf{x}, \tag{5.23}$$

where $\mathbf{G}_R = \mathbf{H}\mathbf{G}$ is the composite channel matrix whose nth column can be expressed as

$$\mathbf{G}_{R,n} = \sum_{p=1}^{P} h_p\sqrt{\alpha_p}\mathbf{G}_n\left(\tau_p, \alpha_p\right), \tag{5.24}$$

where $\mathbf{G}_n\left(\tau_p, \alpha_p\right)\mathbb{C}^{M'\times 1}$ is a column vector whose entries are the samples of the time-scaled and delayed version (by α_p and τ_p, respectively) of the nth subcarrier of the transmitted multicarrier waveform. For example, for the VBMC waveform, the samples of $c_n(\alpha_p(t-\tau_p)), -\frac{T_n}{2\alpha_p} + \tau_p \le t \le \frac{T_n}{2\alpha_p} + \tau_p$, taken at $t = l/F_s, l = L_1, \ldots, L_2$, where $L_1 = \left\lceil\left(-\frac{T_n}{2\alpha_p} + \tau_p\right)F_s\right\rceil$ and $L_2 = \left\lfloor\left(\frac{T_n}{2\alpha_p} + \tau_p\right)F_s\right\rfloor$, occupy the entries $G_{m,n}\left(\tau_p, \alpha_p\right), m = m_n + \lceil\tau_p F_s\rceil, \ldots, m_n + \lceil\tau_p F_s\rceil + L_2 - L_1$.

Assuming $h_p \overset{i.i.d.}{\sim} \mathcal{CN}\{0,1\}$, $\tau_p \overset{i.i.d.}{\sim} \mathcal{U}\{0, \tau_{\max}\}$, and $\alpha_p \overset{i.i.d.}{\sim} \mathcal{U}\{\alpha_{\max}^{-1}, \alpha_{\max}\}$, as in the

simulation studies, we have

$$\begin{aligned}\mathbb{E}\{\mathbf{G}_R^H\mathbf{G}_R\} &= \sum_{p=1}^{P}\mathbb{E}\{|h_p|^2\}\mathbb{E}\{\alpha_p\mathbf{G}_p^H\mathbf{G}_p\} \\ &= \sum_{p=1}^{P}\mathbb{E}\{\alpha_p\mathbf{G}_p^H\mathbf{G}_p\} \approx P\mathbb{E}\{\mathbf{G}^H\mathbf{G}\}\end{aligned}$$

since $\alpha_p \approx 1$, and delayed-and-scaled versions of the subcarrier waveforms approximately maintain their original power and cross-correlations. Therefore, the received waveform power is given by

$$\begin{aligned}P_{\mathrm{Rx},s} &= \sigma_{\mathrm{s}}^2\,\mathrm{tr}\left(\mathbb{E}\{\mathbf{G}_R^H\mathbf{G}_R\}\right) \\ &= \sigma_{\mathrm{s}}^2 M\,\mathrm{tr}\left(\mathbf{G}^H\mathbf{G}\right) = PP_{\mathrm{Tx},s}.\end{aligned} \tag{5.25}$$

5.8 Appendix B: Multi-Layer Block Transmission

In [104], authors propose a multi-layer block transmission (MLBT) waveform of the form:

$$s(t) = \sum_{k'=0}^{K'-1}\sum_{n=0}^{N_l-1} a^{k'/2}s_{k',n}p\left(a^{k'}t - nT_{\mathrm{symb}}\right)e^{j2\pi f_{c,0}a^{k'}t}, \tag{5.26}$$

where the pulse, $p(t)$, is a Shannon wavelet given by:

$$p(t) = \frac{1}{\sqrt{T_{\mathrm{symb}}}}\mathrm{sinc}\left(\frac{t}{T_{\mathrm{symb}}}\right), \tag{5.27}$$

K' denoting the number of *layers*, $f_{c,0}$ the carrier frequency of the first layer ($k' = 0$), N_l the number of symbols mounted per layer, and a being the *base scale* used by the transmitter. The layer k' is associated with a center frequency of $f_{c,k'} = a^{k'}f_{c,0}$ and a bandwidth of $W_{k'} = \frac{a^{k'}}{T_{\mathrm{symb}}}$. We immediately recognize that the MLBT employs a variable bandwidth design for its subcarriers. We, however, note the following distinctions in the design of VBMC subcarriers.

- The Shannon wavelet used in [104] has a bandwidth $W_0 = \frac{1}{T_{\mathrm{symb}}}$ which is fixed by

the symbol duration. In contrast, the VBMC chirp pulse duration can be chosen to be larger than $1/W_0$ and can therefore have higher time-bandwidth product.

- We limit, by design, the bandwidth of the VBMC chirp subcarriers to protect them from potential bandwidth expansion due to waveform compression by a factor of up to $\alpha_{\max}$.

The system model used in [104] is based on the approximation of the received signal in a continuous delay-scale channel given by

$$r_s(t) = \iint h(\tau,\alpha)\sqrt{\alpha}s\left(\alpha(t-\tau)\right)d\tau d\alpha, \tag{5.28}$$

by the following discrete scale-lag signal representation:

$$r_s^{\mathrm{SL}}(t) = \sum_{r=0}^{R}\sum_{k'=0}^{K'-1} e^{j2\pi f_c a^{k'+r}t}\sum_{l=0}^{L(k'+r)} \overline{h}_{r,l}^{k'} a^{r/2}\overline{s}_{k'}\left(a^r t - l\frac{T_{\mathrm{symb}}}{a^{k'}}\right), \tag{5.29}$$

where $R = \lceil \log \alpha_{\max}/\log a \rceil$ is the number of discrete scales, $L(r) = \lceil a^r \tau_{\max}/T_{\mathrm{symb}} \rceil$ is the number of discrete lags, $\overline{s}_{k'}(t) = \sum_{n=0}^{N_l} s_{k',n} p_{k'}(t - nT_{\mathrm{symb}}/a^{k'})$ and $p_{k'}(t) = a^{k'/2}p(a^{k'}t)$.

The receiver measurements for symbol decoding are obtained after baseband conversion and matched filtering of $r^{\mathrm{SL}}(t)$ with $p_k(t - mT_{\mathrm{symb}}/a^k), k = 0, 1, \ldots, K' + R, m = 0, 1, 2, \ldots, N_l$, and neglecting the cross-talk term. Note that, as mentioned in [104], cross-talk depends on the pulse properties; and the Shannon wavelet was shown to be a choice that resulted in negligible cross-talk. Authors also show numerically, by loading a single information symbol on $p(t)$, and hence working with one layer $K' = 1$, that the normalized mean squared-error between $r_s^{\mathrm{SL}}(t)$ and $r_s(t)$ is small for the discrete channel path model given by:

$$h(\tau,\alpha) = \sum_{p=1}^{N_p} h_p \delta(\tau - \tau_p)\delta(\alpha - \alpha_p). \tag{5.30}$$

For the discrete channel path model in (5.30), the received signal in (5.28) reduces to the

form given by (5.1). The NMSE is defined as follows [104]

$$\text{NMSE}_{\text{MSML}} = \frac{\sum_{r=0}^{R}\sum_{l=0}^{L(r)}\left|\int p_r\left(t - l\frac{T_{\text{symb}}}{a^r}\right)\left(r_s(t) - r_s^{\text{SL}}(t)\right)e^{-j2\pi f_c a^r t}dt\right|^2}{\sum_{r=0}^{R}\sum_{l=0}^{L(r)}\left|\int p_r\left(t - l\frac{T_{\text{symb}}}{a^r}\right)r_s(t)e^{-j2\pi f_c a^r t}dt\right|^2}. \tag{5.31}$$

Figure 5.11 shows the plot of $\text{NMSE}_{\text{MSML}}$ as $\alpha_{\max}$ is varied for the same parameter settings as used in the numerical results section of [104]. A sampling rate of $F_s = 128$ kHz is used for approximating the integral in (5.31) by a summation, and $N_{\text{trials}} = 100$ channel realizations are used for averaging $\text{NMSE}_{\text{MSML}}$. The plot closely matches the NMSE result for the Shannon wavelet in [104].

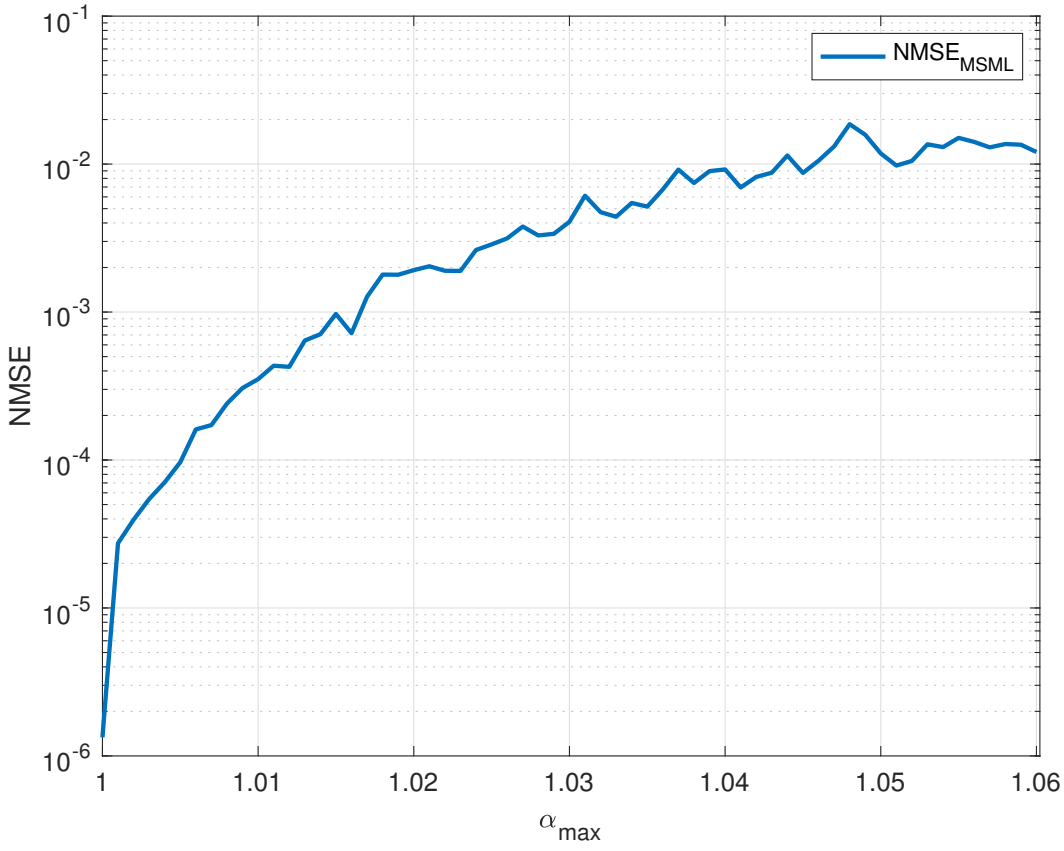

Figure 5.11: NMSE as in [104] for a single information symbol and $K' = 1$.

Note that the NMSE metric above captures only the difference in the projections of $r_s^{\text{SL}}(t)$ and $r_s(t)$ for the scales, $r = 0, 1, \ldots, R$, and lags, $l = 0, 1, \ldots, L(r)$. To evaluate the

error due to approximation in a multi-layer setup ($K' > 1$) and multiple symbols ($N_l > 1$), we denote $\mathbf{y}_{\text{SL}} \in \mathbb{C}^{(K'+R)N_l \times 1}$ and $\mathbf{y}_0 \in \mathbb{C}^{(K'+R)N_l \times 1}$ as the vector of measurements obtained after baseband conversion and matched filtering with $p_k(t - mT_{\text{symb}}/a^k), k = 0, 1, \ldots, K' + R, m = 0, 1, 2, \ldots, N_l$, from $r_{\text{SL}}(t)$ and $r_s(t)$, respectively. Similarly, we denote $\mathbf{y}_{\text{model}} \in \mathbb{C}^{(K'+R)N_l \times 1}$ as the vector of measurements obtained after baseband conversion, matched filtering from $r_{\text{SL}}(t)$ and ignoring the cross-talk as in [104]. We define the NMSE due to scale and lag parameter discretization for investigating it in the case of multiple layers ($K' > 1$) and/or symbols ($N_l > 1$) as follows:

$$\begin{aligned} \text{NMSE}_{\text{SL}}(K') &\triangleq \frac{\| \mathbf{y}_{\text{SL}} - \mathbf{y}_0 \|^2}{\| \mathbf{y}_0 \|^2} \\ &= \frac{\sum_{k=0}^{K'+R-1} \sum_{m=0}^{N_l-1} \left| \int p_k \left(t - m\frac{T_{\text{symb}}}{a^k} \right) \left(r_s(t) - r_s^{\text{SL}}(t) \right) e^{-j2\pi f_c a^k t} dt \right|^2}{\sum_{k=0}^{K'+R-1} \sum_{m=0}^{N_l-1} \left| \int p_k \left(t - m\frac{T_{\text{symb}}}{a^k} \right) r_s(t) e^{-j2\pi f_c a^k t} dt \right|^2}. \end{aligned} \tag{5.32}$$

Observe that $\text{NMSE}_{\text{SL}}(K')$ is different from $\text{NMSE}_{\text{MSML}}$ even for $K' = 1$. $\text{NMSE}_{\text{SL}}(K')$ represents the modeling error in the symbol measurements due to scale and lag parameter discretization – the inner summation runs across all symbol measurements, $m = 0, 1, \ldots, N_l - 1$, in each layer for evaluating $\text{NMSE}_{\text{SL}}(K')$ while it runs over all lags, $l = 0, 1, \ldots, L(r)$, due to delay spread for evaluating $\text{NMSE}_{\text{MSML}}$. We may define the normalized cross-talk level and the NMSE in the final symbol measurements due to both modeling error and cross-talk as follows:

$$\text{NMSE}_{\text{cross-talk}}(K') \triangleq \frac{\| \mathbf{y}_{\text{model}} - \mathbf{y}_{\text{SL}} \|^2}{\| \mathbf{y}_{\text{SL}} \|^2}. \tag{5.33}$$

$$\text{NMSE}_{\text{model}}(K') \triangleq \frac{\| \mathbf{y}_{\text{model}} - \mathbf{y}_0 \|^2}{\| \mathbf{y}_0 \|^2}. \tag{5.34}$$

We evaluate the NMSE at different stages (as defined above) for $K' = 1, 2, 3$, and $N_l = 1$ for the same parameter settings as in [104]. We observe that as the number of

layers increase beyond $K' = 1$, while the cross-talk is indeed small for Shannon wavelet, the NMSE in the measurement model, $\text{NMSE}_{\text{model}}(K')$, increases. When the cross-talk is negligible, the plots of $\text{NMSE}_{\text{SL}}(K')$ and $\text{NMSE}_{\text{model}}(K')$ nearly coincide as expected (for $K' = 2, 3$). The $\text{NMSE}_{\text{model}}(K')$ in the symbol measurements is, therefore, predominantly due to the approximation error in the received signal model arising from scale and lag discretization.

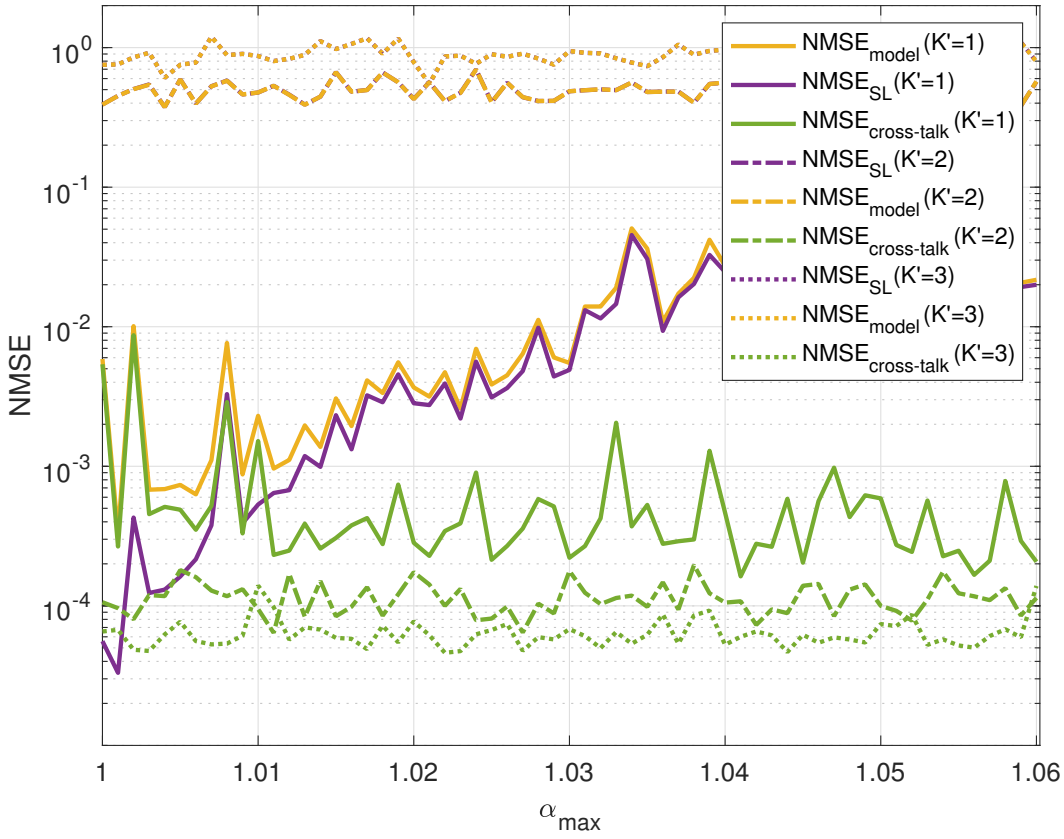

Figure 5.12: NMSE at different stages for $K' = 1, 2, 3$.

5.9 Appendix C: Bit Error Rate Performance

In this section, we investigate the bit error rate of the MMSE receiver for the generic system model, presented in this chapter, which applies to a large class of waveforms that

are expressible in the form given by (5.9): $\mathbf{s} = \mathbf{G}\mathbf{x}$, where $\mathbf{G}$ is the waveform dictionary and $\mathbf{x}$ is the symbol vector.

The MMSE equalizer output, given by (5.19), is reproduced below for convenience:

$$\mathbf{z} = \left(\mathbf{D} + \sigma^2 \mathbf{I}_N\right)^{-1} \mathbf{D}\mathbf{x} + \mathbf{u}, \tag{5.35}$$

where $\mathbf{u} = \left(\mathbf{D} + \sigma^2 \mathbf{I}\right)^{-1} \mathbf{G}_R^H \mathbf{w}$ is the symbol noise.

The symbol error vector is given by

$$\mathbf{e} = \mathbf{z} - \mathbf{x} = \mathbf{E}\mathbf{x} + \mathbf{u}, \tag{5.36}$$

where $\mathbf{E} \triangleq \left(\left(\mathbf{D} + \sigma^2 \mathbf{I}\right)^{-1} \mathbf{D} - \mathbf{I}\right)$.

The covariance, $\mathbf{C}_u$, of the symbol noise vector, $\mathbf{u}$, is given by

$$\begin{aligned} \mathbf{C}_u = \mathbb{E}\{\mathbf{u}\mathbf{u}^H\} &= \left(\mathbf{D} + \sigma^2 \mathbf{I}\right)^{-1} \mathbf{G}_R^H \mathbb{E}\{\mathbf{w}\mathbf{w}^H\} \mathbf{G}_R \left(\mathbf{D} + \sigma^2 \mathbf{I}\right)^{-1} \\ &= \sigma^2 \left(\mathbf{D} + \sigma^2 \mathbf{I}\right)^{-1} \mathbf{G}_R^H \mathbf{G}_R \left(\mathbf{D} + \sigma^2 \mathbf{I}\right)^{-1} \\ &= \sigma^2 \left(\mathbf{D} + \sigma^2 \mathbf{I}\right)^{-1} \mathbf{D} \left(\mathbf{D} + \sigma^2 \mathbf{I}\right)^{-1} \end{aligned} \tag{5.37}$$

Consider the singular value decomposition (SVD) of $\mathbf{D} = \mathbf{G}_R^H \mathbf{G}_R = \mathbf{G}^H \mathbf{H}^H \mathbf{H} \mathbf{G}$:

$$\mathbf{D} = \mathbf{U}\mathbf{\Sigma}\mathbf{U}^H, \tag{5.38}$$

where $\mathbf{\Sigma} = \mathrm{diag}\{\sigma_n^2 : n = 1, 2, \ldots, N\}$.

Replacing $\mathbf{D}$ with its SVD in (5.37), we get

$$\mathbf{C}_u = \sigma^2 \mathbf{U} \left(\mathbf{\Sigma} + \sigma^2 \mathbf{I}\right)^{-1} \mathbf{\Sigma} \left(\mathbf{\Sigma} + \sigma^2 \mathbf{I}\right)^{-1} \mathbf{U}^H. \tag{5.39}$$

For a given channel matrix $\mathbf{H}$, and hence $\mathbf{D}$ and $\mathbf{G}_R$, the symbol noise vector, $\mathbf{u} \sim \mathcal{CN}\left(\mathbf{0}, \mathbf{C}_u\right)$. Therefore, the variance of the mth symbol noise vector entry, $u_m \sim$

$\mathcal{CN}\left(0, \sigma_{u_m}^2\right)$, is given by

$$\sigma_{u_m}^2 = \mathbb{V}\text{ar}\{u_m\} = C_u[m,m] = \sigma^2 \sum_{n=1}^{N} |U_{mn}|^2 \frac{\sigma_n^2}{\left(\sigma_n^2 + \sigma^2\right)^2}. \tag{5.40}$$

In the next subsection, we derive a high SNR approximation for the symbol error probability.

5.9.1 Symbol Error Probability, P_e^{∞}: A High SNR Approximation

Consider i.i.d. BPSK symbols, $\{\pm 1\}$, placed in $\mathbf{x}$ with $\mathbb{P}(x_m = \pm 1) = \frac{1}{2}$. Since for BPSK symbols, $\mathbf{x}$ is a real vector, the slicing and comparison

$$\text{Re}\left(z_m\right) \underset{+1}{\overset{-1}{\lessgtr}} 0, \tag{5.41}$$

is a detector for the mth symbol x_m. The test statistic for symbol detection, in this case, therefore follows from (5.36)

$$\text{Re}\{\mathbf{z}\} = \mathbf{x} + \mathbf{E}^{(r)}\mathbf{x} + \mathbf{u}_r, \tag{5.42}$$

where $\mathbf{E}^{(r)} = \text{Re}\{\mathbf{E}\} = \text{Re}\{\left(\mathbf{D} + \sigma^2\mathbf{I}_N\right)^{-1}\mathbf{D}\} - \mathbf{I}$ and $\mathbf{u}_r = \text{Re}\{\mathbf{u}\}$. Let us denote $\mathbf{z}_r \triangleq \text{Re}\{\mathbf{z}\}$ and $\mathbf{e}_r = \text{Re}\{\mathbf{e}\} = \mathbf{E}^{(r)}\mathbf{x} + \mathbf{u}_r$. Using these notation in (5.42), we have

$$\mathbf{z}_r = \mathbf{x} + \mathbf{e}_r. \tag{5.43}$$

We may write $\mathbf{u} = \mathbf{W}_{\text{mmse}}\mathbf{w}$, where $\mathbf{W}_{\text{mmse}} = \left(\mathbf{D} + \sigma^2\mathbf{I}\right)^{-1}\mathbf{G}_R^H$ is the MMSE equalizer matrix. Therefore, we have

$$\mathbf{u}_r = \mathbf{W}_{\text{mmse},r}\mathbf{w}_r - \mathbf{W}_{\text{mmse},i}\mathbf{w}_i, \tag{5.44}$$

where $\mathbf{W}_{\text{mmse},r} = \text{Re}\{\mathbf{W}_{\text{mmse}}\}$, $\mathbf{W}_{\text{mmse},i} = \text{Im}\{\mathbf{W}_{\text{mmse}}\}$, $\mathbf{w}_r = \text{Re}\{\mathbf{w}\}$. and $\mathbf{w}_i = \text{Im}\{\mathbf{w}\}$.

The covariance of $\mathbf{u}_r$ is given by

$$\mathbf{C}_u^{(r)} = \mathbb{E}\{\mathbf{u}_r \mathbf{u}_r^H\} = \frac{\sigma^2}{2}\left(\mathbf{W}_{\text{mmse},r}\mathbf{W}_{\text{mmse},r}^H + \mathbf{W}_{\text{mmse},i}\mathbf{W}_{\text{mmse},i}^H\right). \tag{5.45}$$

Given $\mathbf{H}$, the probability that the mth symbol is decoded incorrectly is given by

$$P_{e|\mathbf{H}}(x_m) = \frac{1}{2}\mathbb{P}\left(\text{Re}\{e_m\} > 1 | x_m = -1, \mathbf{H}\right) + \frac{1}{2}\mathbb{P}\left(\text{Re}\{e_m\} < -1 | x_m = 1, \mathbf{H}\right). \tag{5.46}$$

Let Δx_m denote the mth entry of $\mathbf{Ex}$ so that

$$e_m = \Delta x_m + u_m = \Delta x_m + \sigma_{u_m}\tilde{u}_m, \tag{5.47}$$

where $\tilde{u}_m \sim \mathcal{CN}(0,1)$.

For high enough SNR, $\Delta x_m \approx 0$. Therefore, at high SNR:

$$\mathbb{P}\left(\text{Re}\{e_m\} > 1 | x_m = -1, \mathbf{H}\right) \approx \mathbb{P}\left(\text{Re}\{\tilde{u}_m\} > \frac{1}{\sigma_{u_m}^{(r)}(\mathbf{H})}\Big|\mathbf{H}\right) = \mathcal{Q}\left(\frac{1}{\sigma_{u_m}^{(r)}(\mathbf{H})}\right), \tag{5.48}$$

where $\sigma_{u_m}^{(r)}(\mathbf{H}) = \sqrt{C_u^{(r)}[m,m]}$ and we show the dependence of $\sigma_{u_m}^{(r)}$ on $\mathbf{H}$ via $\mathbf{C}_u^{(r)}$.

Also, as $\Delta x_m \approx 0$, we have

$$\mathbb{P}\left(\text{Re}\{e_m\} > 1 | x_m = -1, \mathbf{H}\right) \approx \mathbb{P}\left(\text{Re}\{e_m\} < -1 | x_m = 1, \mathbf{H}\right). \tag{5.49}$$

Using (5.49) in (5.46), we find

$$P_{e|H}^{\infty}(x_m) = \mathcal{Q}\left(\frac{1}{\sigma_{u_m}^{(r)}(\mathbf{H})}\right). \tag{5.50}$$

The symbol error probability (SEP) for the mth BPSK symbol is thus given by:

$$P_e^{\infty}(x_m) = \mathbb{E}_{\mathbf{H}}\{P_{e|\mathbf{H}}(x_m)\} = \mathbb{E}_{\mathbf{H}}\left\{\mathcal{Q}\left(\frac{1}{\sigma_{u_m}^{(r)}(\mathbf{H})}\right)\right\}. \tag{5.51}$$

A closed form expression for $P_e^{\infty}(x_m)$ in (5.51) appears to be difficult since it involves integrating over the joint PDF of the entries of $\mathbf{H}$. We may instead evaluate $P_e^{\infty}(x_m)$ through Monte Carlo simulations by drawing the triples, $h_p \overset{i.i.d.}{\sim} \mathcal{CN}(0,1)$, $\tau_p \overset{i.i.d.}{\sim} \mathcal{U}(0,\tau_{\max})$ and $\alpha_p \overset{i.i.d.}{\sim} \mathcal{U}(\alpha_{\max}^{-1},\alpha_{\max})$, for $p = 1,2,\ldots,P$, in a fairly large number of trials and averaging $\{P_{e|\mathbf{H}_i}^{\infty}(x_m) : i = 1,2,\ldots,N_{\text{trials}}\}$ to obtain $\hat{P}_e^{\infty}(x_m)$. An estimate of the average BER, for high SNR regime, is then given by

$$\hat{P}_e^{\infty} = \frac{1}{M}\sum_{m=1}^{M} \hat{P}_e^{\infty}(x_m). \tag{5.52}$$

The symbol error rate approximation can also be found for QPSK symbols as follows. Consider i.i.d. QPSK symbols, $\{\pm\frac{1}{\sqrt{2}} \pm j\frac{1}{\sqrt{2}}\}$, placed in $\mathbf{x}$ with $\mathbb{P}(x_m = \pm\frac{1}{\sqrt{2}} \pm j\frac{1}{\sqrt{2}}) = \frac{1}{4}$. The real and imaginary parts of the mth QPSK symbol, x_m, is found from the following slicing and comparison detection operation on the real and imaginary parts, respectively, of the mth entry of $\mathbf{z}$:

$$\mathrm{Re}\,(x_m) : \mathrm{Re}\,(z_m) \underset{+\frac{1}{\sqrt{2}}}{\overset{-\frac{1}{\sqrt{2}}}{\lessgtr}} 0, \tag{5.53}$$

$$\mathrm{Im}\,(x_m) : \mathrm{Im}\,(z_m) \underset{+\frac{1}{\sqrt{2}}}{\overset{-\frac{1}{\sqrt{2}}}{\lessgtr}} 0. \tag{5.54}$$

The BER for the mth QPSK symbol follows by recognizing that the SNR of the real and imaginary parts of the mth QPSK symbol measurements are both $SNR_m^{(r)} = \frac{1}{2\sigma_{u_m}^{2(r)}(\mathbf{H})}$ since $\sigma_{u_m}^{(r)}(\mathbf{H}) = \sigma_{u_m}^{(i)}(\mathbf{H})$, which in turn is a consequence of $C_u^{(i)} \triangleq \mathbb{E}\{\mathbf{u}_i\mathbf{u}_i^H\} = \mathbf{C}_u^{(r)}$, where $\mathbf{u}_i = \mathbf{W}_{\text{mmse},r}\mathbf{w}_i + \mathbf{W}_{\text{mmse},i}\mathbf{w}_r$. As a result, for the mth QPSK symbol, a high SNR approximation for the BER is

$$P_e^{\infty}(x_m) = \mathbb{E}_{\mathbf{H}}\{P_{e|\mathbf{H}}(x_m)\} = \mathbb{E}_{\mathbf{H}}\left\{\mathcal{Q}\left(\frac{1}{\sqrt{2}\sigma_{u_m}^{(r)}(\mathbf{H})}\right)\right\}. \tag{5.55}$$

5.9.2 Symbol Error Probability, $P_e^{(u)}$: An Upper Bound

Let Δx_m^* be the maximum value that $\mathrm{Re}\,(\Delta x_m)$ takes when $x_m = -1$. Then

$$\Delta x_m^* = \sum_{n \neq m} |\mathrm{Re}\,(E_{mn})\,| - \mathrm{Re}\,(E_{mm})\,. \tag{5.56}$$

We, therefore, find:

$$\begin{aligned} \mathbb{P}\,(\mathrm{Re}\{e_m\} > 1 | x_m = -1, \mathbf{H}) &\leq \mathbb{P}\left(\mathrm{Re}\{\tilde{u}_m\} > \frac{(1 - \Delta x_m^*)}{\sigma_{u_m}^{(r)}} \Big| \mathbf{H}\right) \\ \implies \mathbb{P}\,(\mathrm{Re}\{e_m\} > 1 | x_m = -1, \mathbf{H}) &\leq \mathcal{Q}\left(\frac{(1 - \Delta x_m^*(\mathbf{H}))}{\sigma_{u_m}^{(r)}(\mathbf{H})}\right) \end{aligned}$$

An upper bound on BER for the BPSK symbols is thus given by

$$P_e^{(u)} \leq \frac{1}{M} \sum_{m=1}^{M} \mathbb{E}_{\mathbf{H}} \left\{ \mathcal{Q}\left(\frac{(1 - \Delta x_m^*(\mathbf{H}))}{\sigma_{u_m}^{(r)}(\mathbf{H})}\right)\right\}. \tag{5.57}$$

An upper bound on the BER of QPSK symbols can be arrived by following an approach similar to that leading to (5.55). We can show that

$$P_e^{(u)} \leq \frac{1}{M} \sum_{m=1}^{M} \mathbb{E}_{\mathbf{H}} \left\{ \mathcal{Q}\left(\frac{(1 - \Delta x_m^*(\mathbf{H}))}{\sqrt{2}\sigma_{u_m}^{(r)}(\mathbf{H})}\right)\right\}. \tag{5.58}$$

5.9.3 Symbol Error Probability, $P_e^{(a)}$: An Approximation

An approximate expression for $P_{e|\mathbf{H}}(x_m)$, valid for all SNR, is obtained by considering (approximating) $\mathbf{E}^{(r)}\mathbf{x}$ to be a Gaussian random vector with zero mean and covariance $\mathbf{C}_e^{(r)} = \mathbb{E}\{\mathbf{E}^{(r)}\mathbf{x}\mathbf{x}^H\mathbf{E}^{(r)H}\} = \mathbf{E}^{(r)}\mathbb{E}\{\mathbf{x}\mathbf{x}^H\}\mathbf{E}^{(r)H} = \mathbf{E}^{(r)}\mathbf{E}^{(r)H}$. Since $\mathbf{x}$ is independent of $\mathbf{w}$ and hence $\mathbf{u} = \mathbf{W}_{\mathrm{mmse}}\mathbf{w}$, $\mathbf{e}_r = \mathbf{E}^{(r)}\mathbf{x} + \mathbf{u}_r$ is also Gaussian with zero mean and covariance $\mathbf{C}_e^{(r)} = \mathbf{E}^{(r)}\mathbf{E}^{(r)H} + \mathbf{C}_u^{(r)}$. An approximate expression for the mth BPSK SEP then follows:

$$P_e^{(a)} = \frac{1}{M} \sum_{m=1}^{M} \mathbb{E}_{\mathbf{H}} \left\{ \mathcal{Q}\left(\frac{1}{\sigma_{e_m}^{(r)}(\mathbf{H})}\right)\right\}, \tag{5.59}$$

where $\sigma_{e_m}^{(r)}(\mathbf{H}) = \sqrt{C_e^{(r)}[m,m]}$. Similarly, when using QPSK symbols, an approximate BER is given by

$$P_e^{(a)} = \frac{1}{M}\sum_{m=1}^{M}\mathbb{E}_{\mathbf{H}}\left\{\mathcal{Q}\left(\frac{1}{\sqrt{2}\sigma_{e_m}^{(r)}(\mathbf{H})}\right)\right\}, \tag{5.60}$$

5.9.4 Symbol Error Probability, P_e: An Accurate Evaluation

The inaccuracy in $P_e^{(a)}$ is not only due to non-Gaussian distribution of $\mathbf{E}_r\mathbf{x}$ but also due to the fact that $\mathbf{e}_r = \mathbf{E}_r\mathbf{x} + \mathbf{u}_r$ is *not* independent of $\mathbf{x}$. In this subsection, we present a better estimate for SEP using the knowledge of $\mathbf{x}$. Note that this is not restrictive in practical estimation of SEP much as we do make use of the true symbol vector $\mathbf{x}$ in most numerical simulations and computation of bit errors for investigating the communication performance. An advantage of the estimation approach we present here is that far fewer Monte Carlo trials suffice to yield an accurate average symbol error rate.

We first evaluate:

$$\begin{aligned}
\mathbb{P}\left(\mathbf{z}_{r,m} > 0 \middle| x_m = -1, \mathbf{H}\right) &= \mathbb{P}\left(\mathrm{Re}\{e_m\} > 1 \middle| x_m = -1, \mathbf{H}\right) \\
&= \mathbb{P}\left(\mathbf{E}_m^{(r)T}\mathbf{x} + \mathbf{u}_{r,m} > 1 \middle| x_m = -1, \mathbf{H}\right) \\
&= \mathbb{P}\left(E_{m,m}^{(r)}x_m + \mathbf{E}_{m,\not{m}}^{(r)T}\mathbf{x}_{\not{m}} + \mathbf{u}_{r,m} > 1 \middle| x_m = -1, \mathbf{H}\right) \\
&= \mathbb{P}\left(\mathbf{u}_{r,m} > 1 + E_{m,m}^{(r)} - \mathbf{E}_{m,\not{m}}^{(r)T}\mathbf{x}_{\not{m}} \middle| \mathbf{H}\right) \\
&= \mathbb{P}\left(\tilde{\mathbf{u}}_{r,m} > \frac{1 + E_{m,m}^{(r)} - \mathbf{E}_{m,\not{m}}^{(r)T}\mathbf{x}_{\not{m}}}{\sigma_{u_m}^{(r)}} \middle| \mathbf{H}\right) \\
&= \mathcal{Q}\left(\frac{1 + E_{m,m}^{(r)}(\mathbf{H}) - \mathbf{E}_{m,\not{m}}^{(r)T}(\mathbf{H})\mathbf{x}_{\not{m}}}{\sigma_{u_m}^{(r)}(\mathbf{H})}\right),
\end{aligned} \tag{5.61}$$

where $\tilde{\mathbf{u}}_{r,m} \sim \mathcal{N}(0,1)$, $\mathbf{E}_{m,\not{m}}^{(r)T}$ denotes the mth row of $E^{(r)}$ but for its mth entry knocked out. Similarly, $\mathbf{x}_{\not{m}}$ is the symbol vector with mth entry knocked out.

The average BER for BPSK symbols is, therefore, given by

$$P_e = \frac{1}{M}\sum_{m=1}^{M}\mathbb{E}_{\mathbf{H}}\left\{\mathcal{Q}\left(\frac{1 + E_{m,m}^{(r)}(\mathbf{H}) - \mathbf{E}_{m,\not{m}}^{(r)T}(\mathbf{H})\mathbf{x}_{\not{m}}}{\sigma_{u_m}^{(r)}(\mathbf{H})}\right)\right\}. \tag{5.62}$$

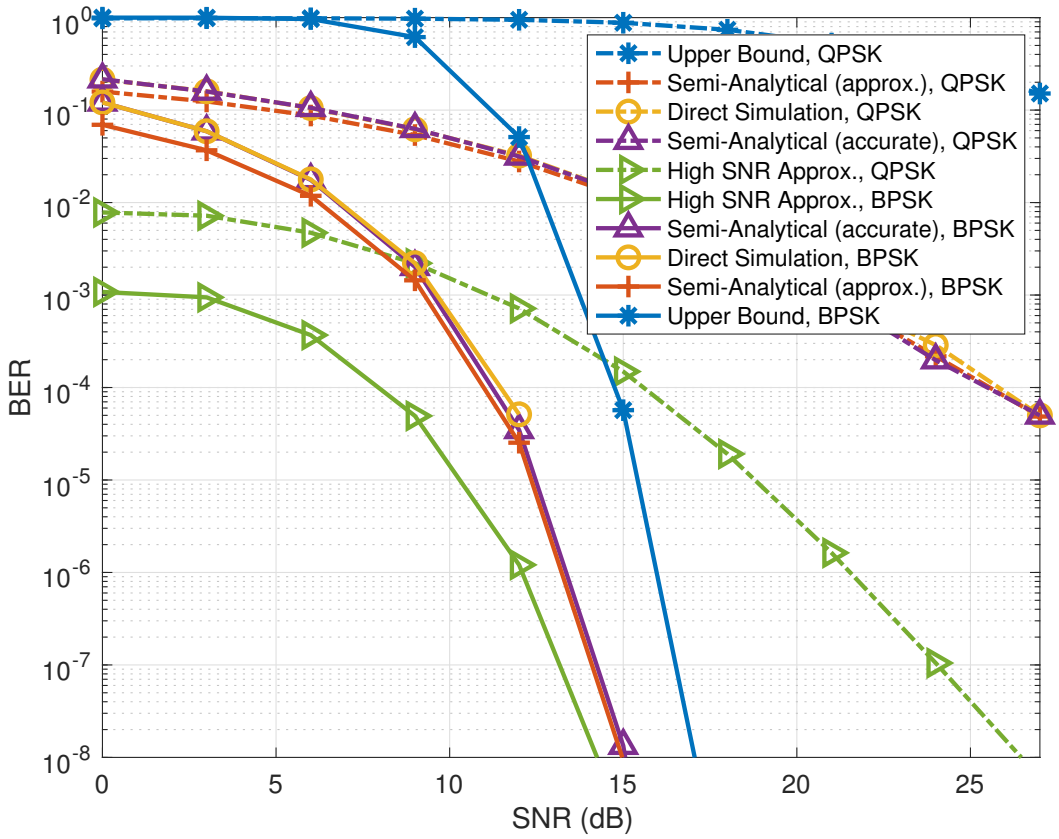

Figure 5.13: Bit error probabilities.

Similarly, the average BER for QPSK symbols can be shown to be:

$$P_e = \frac{1}{M}\sum_{m=1}^{M}\mathbb{E}_{\mathbf{H}}\left\{\mathcal{Q}\left(\frac{1+E^{(r)}_{m,m}(\mathbf{H})-\sqrt{2}\mathbf{E}^{(r)T}_{m,\not{m}}(\mathbf{H})\mathbf{x}^{(r)}_{\not{m}}+\sqrt{2}\mathbf{E}^{(i)T}_{m}(\mathbf{H})\mathbf{x}^{(i)}}{\sqrt{2}\sigma^{(r)}_{u_m}(\mathbf{H})}\right)\right\}. \quad (5.63)$$

Figure 5.13 shows the BER expressions in (5.52), (5.57), (5.59), and (5.62) evaluated and plotted for $N = 80$ BPSK/QPSK symbols, $N_{\text{trials}} = 10000$ simulation runs. Also plotted is the SEP obtained by direct numerical simulations and empirical bit error rate computation.We notice that upper bound is too loose and the high SNR approximation is approaching the true SEP as SNR increases. The SEP obtained through direct numerical simulations nearly coincides with the computed P_e (semi-analytical – accurate) plot.

Chapter 6

Conclusions

6.1 Summary

We developed algorithms suitable for underwater acoustic communications in an ocean medium that can be aptly characterized as *wideband* (due to high ratio of carrier waveform bandwidth to center frequency), highly *time-varying* (due to high Doppler), and highly *frequency-selective* (due to strong multipath propagation). Large delay spread due to long propagation times and high time-scale spread due to path dependent Doppler effect on a wideband transmitted signal require specialized algorithms to achieve a good communication performance. To that end, we first developed a sparsity exploiting iterative channel estimation and data detection scheme in a CP-OFDM communications system. Partial interval demodulation measurements were used to tackle the time-variation better which was shown to result in a larger number of effective measurements compared to the traditional full-interval demodulation. We developed a new variational Bayesian algorithm employing soft data symbol detection in the context of sweep spread carrier communication, which employs a chirp waveform. We then developed a new modulation scheme (ODSS) particularly suited for delay-scale spread wideband channels. We also presented a new multicarrier chirp based waveform (VBMC) whose subcarriers maintain their near orthogonality even after passing through a delay-scale channel. Finally, we developed a general framework based on the Shannon sampling basis to model a delay

and scale spread channel and introduced the notion of a waveform dictionary that can be used for evaluating a variety of multicarrier waveforms.

6.2 Directions for further work

We outline some interesting directions to explore in future work, in the order of increasing problem complexity, in the context of the work presented in this thesis.

1. Channel Estimation Schemes for ODSS and VBMC

   Our focus in the current work was to develop and demonstrate the promise of new waveforms suitable for data communications over a delay and scale spread wideband channel. We evaluated the performance of these waveforms using uncoded communications with perfect channel state information at the receiver (CSIR). New and practical channel estimation schemes that employ a low pilot overhead would be a useful direction for future work. Development of iterative data detection and channel estimation schemes for these waveforms together with coded communications would be of immense practical value.

2. Block Transmission Schemes for ODSS and VBMC

   In this thesis, we considered only one symbol per block transmitted for the newly proposed waveforms. Extending ODSS and VBMC to block transmissions where each block contains multiple symbols is essential for their use in real-world communications systems. Estimating and tracking the time-varying channel across symbols in the block is a natural requirement to address in practical receivers.

3. Optimum Waveforms for Delay-Scale spread Wideband Channel

   In this work, we developed a generic system model for communications over a delay and scale spread channel involving the notion of a waveform dictionary. An interesting direction to explore is the search for an optimum waveform dictionary for a delay-scale spread channel with suitable statistical properties.

4. Variational Soft Symbol Decoding in Coded Modulation Communication Systems

   We considered VSSD for uncoded communication systems in this work. Developing a variational soft symbol decoding framework for different waveforms using coded symbols would be an interesting future direction for research.

5. Theoretical Performance Analysis

   Analysis of the bit error rate performance of the proposed variational Bayesian soft symbol detection algorithm is another interesting but open problem. A rigorous analysis of the performance of iterative data detection and channel estimation scheme is also a possible direction of work requiring nontrivial effort.

Bibliography

[1] Evologics GmbH. Ackerstrasse 76, 13355 Berlin, Germany. [Online]. Available: https://evologics.de/acoustic-modems

[2] "Underwater acoustic MODEMS," in *Product Information Guide*. Evologics GmbH.

[3] S. Ahmed and H. Arslan, "Evaluation of frequency offset and Doppler effect in terrestrial RF and in underwater acoustic OFDM systems," in *IEEE MILCOM, San Diego, CA, USA*, 2008, pp. 1–7.

[4] A. Al-Sammna, M. Bin Azmi, and T. Rahman, "Time-varying ultra-wideband channel modeling and prediction," *Symmetry*, vol. 10, p. 631, Nov. 2018.

[5] K. P. Arunkumar and C. R. Murthy, "Variational soft symbol decoding for sweep spread carrier based underwater acoustic communications," in *IEEE 20th International Workshop on Signal Processing Advances in Wireless Communications*, Cannes, France, Jul. 2019.

[6] ——, "Orthogonal delay scale space modulation: A new technique for wideband time-varying channels," Nov. 2021. [Online]. Available: https://arxiv.org/abs/2111.10765

[7] Y. M. Aval and M. Stojanovic, "Differentially coherent multichannel detection of acoustic OFDM signals," *IEEE J. Ocean. Eng.*, vol. 40, no. 2, pp. 251–268, Apr. 2015.

[8] R. Balan, H. V. Poor, S. Rickard, and S. Verdu, "Time-frequency and time-scale representations of doubly spread channels," in *Proc. European Signal Processing Conf., Vienna, Austria*, September 2004, pp. 445–448.

[9] M. Bellanger, "FBMC physical layer: A primer," in *PHYDYAS FP7 Project Document*, Jan. 2010, pp. 1–31.

[10] Z. Ben-Haim and Y. C. Eldar, "The Cramér-Rao bound for estimating a sparse parameter vector," *IEEE Trans. Signal Process.*, vol. 58, no. 6, pp. 3591–3603, June 2010.

[11] C. R. Berger, J. P. Gomes, and J. M. F. Moura, "Sea-trial results for cyclic-prefix OFDM with long symbol duration," in *Proc. MTS/IEEE OCEANS Conf.*, June 2011.

[12] ——, "Study of pilot designs for cyclic-prefix OFDM on time-varying and sparse underwater acoustic channels," in *Proc. MTS/IEEE OCEANS Conf.*, June 2011.

[13] C. R. Berger, J. Huang, and J. M. F. Moura, "Study of pilot overhead for iterative OFDM receivers on time-varying and sparse underwater acoustic channels," in *Proc. MTS/IEEE OCEANS Conf.*, Sept. 2011.

[14] C. R. Berger, S. Zhou, J. C. Preisig, and P. Willett, "Sparse channel estimation for multicarrier underwater acoustic communication: From subspace methods to compressed sensing," *IEEE Trans. Signal Process.*, vol. 57, no. 5, pp. 2941–2965, May 2011.

[15] J. Bertrand, P. Bertrand, and J.-P. Ovarlez, *The Mellin Transform*, 2nd ed. Boca Raton: CRC Press LLC, 2000.

[16] J. Bertrand, P. Bertrand, and J. Ovarlez, "Discrete Mellin transform for signal analysis," in *International Conference on Acoustics, Speech, and Signal Processing*, vol. 3, May 1990, pp. 1603–1606.

[17] F. Campagnaro, R. Francescon, P. Casari, R. Diamant, and M. Zorzi, "Multimodal underwater networks: Recent advances and a look ahead," in *WUWNet 2017, Halifax, Canada*, Nov. 2019.

[18] D. Carlson, A. Ostrovskii, K. Kebkal, and H. Gildor, *Moored automatic mobile profilers and their application*. LAP LAMBERT Academic Publishing, June 2013, pp. 169–206.

[19] J. Davies, S. Pointer, and S. Dunn, "Wideband acoustic communications dispelling narrowband myths," in *MTS/IEEE OCEANS, Providence, RI, USA*, vol. 1, Sep. 2000, pp. 377–384.

[20] J. Dhanoa, R. Ormondroyd, and E. Hughes, "A robust digital communication system for doubly-spread underwater acoustic channels," in *Proceedings of MTS/IEEE OCEANS, Kobe, Japan*, vol. 1, 2004, pp. 9–13.

[21] M.-G. Di Benedetto, T. Kaiser, A. Molisch, I. Oppermann, C. Politano, and D. Porcino, *Ultra-wideband Communication Systems: A Comprehensive Overview*. Hindawi Publishing Corporation, 01 2006.

[22] T. Eggen, A. Baggeroer, and J. Preisig, "Communication over Doppler spread channels. Part I: Channel and receiver presentation," *IEEE Journal of Oceanic Engineering*, vol. 25, no. 1, pp. 62–71, 2000.

[23] M. Elad, "Sparse and redundant representations: From theory to applications in signal and image processing." Springer, 2010.

[24] P. Fan, E. Panayirci, H. V. Poor, and P. T. Mathiopoulos, "Special issue on broadband mobile communications at very high speeds," *EURASIP Journal on Wireless Communications and Networking*, no. 279, Aug. 2012.

[25] H. Franz and M. Gerald, *Wireless Communications Over Rapidly Time-Varying Channels*. Burlington, MA 01803, USA: Elsevier, 2011.

[26] A. Goldsmith, *Wireless Communications*. Cambridge University Press, 2005.

[27] R. Hadani and A. Monk, "OTFS: A new generation of modulation addressing the challenges of 5G," Feb 2018. [Online]. Available: https://arxiv.org/abs/1802.02623v1

[28] R. Hadani, S. Rakib, S. Kons, M. Tsatsanis, A. Monk, C. Ibars, J. Delfeld, Y. Hebron, A. J. Goldsmith, A. F. Molisch, and R. Calderbank, "Orthogonal time frequency space modulation," Aug. 2018. [Online]. Available: https://arxiv.org/abs/1808.00519v1

[29] R. Hadani, S. Rakib, A. Molisch, C. Ibars, A. Monk, M. Tsatsanis, J. Delfeld, A. Goldsmith, and R. Calderbank, "Orthogonal time frequency space (OTFS) modulation for millimeter-wave communications systems," in *IEEE/MTT-S International Microwave Symposium*, June 2017, pp. 681–683.

[30] R. Hadani, S. Rakib, M. Tsatsanis, A. Monk, A. Goldsmith, A. Molisch, and R. Calderbank, "Orthogonal time frequency space modulation," in *IEEE WCNC, San Fransisco, CA*, Mar. 2017, pp. 1–6.

[31] P. R. Halmos, "Finite dimensional vector spaces." Springer, 1958.

[32] R. He, Z. Zhong, b. ai, G. Wang, J. Ding, and A. Molisch, "Measurements and analysis of propagation channels in high-speed railway viaducts," *IEEE Transactions on Wireless Communications*, vol. 12, pp. 794–805, 02 2013.

[33] M. Helmling, S. Scholl, F. Gensheimer, T. Dietz, K. Kraft, S. Ruzika, and N. Wehn, "Database of Channel Codes and ML Simulation Results," www.uni-kl.de/channel-codes, 2019.

[34] J. Z. Huang, S. Zhou, J. Huang, C. R. Berger, and P. Willett, "Progressive inter-carrier interference equalization for OFDM transmission over time-varying underwater acoustic channels," *IEEE J. Sel. Topics Signal Process.*, vol. 5, no. 8, pp. 1524–1536, Dec. 2011.

[35] J.-Z. Huang, S. Zhou, and Z.-H. Wang, "Robust initialization with reduced pilot overhead for progressive underwater acoustic OFDM receivers," in *Proc. of MILCOM Conf.*, Nov. 2011, pp. 406–411.

[36] Y. Huang, L. Wan, S. Zhou, Z. H. Wang, and J.-Z. Huang, "Comparison of sparse recovery algorithms for channel estimation in underwater acoustic OFDM with data-driven sparsity learning," *Elsevier Physical Communication*, vol. 13, no. 3, pp. 156–167, Dec. 2014.

[37] R. Hunger, "Floating point operations in matrix-vector calculus," Technical Report, Version 3, https://mediatum.ub.tum.de/, Associate Institute for Signal Processing, Munich Univ. of Technol., Germany, 2007.

[38] X. Jiang, W.-J. Zeng, and X.-L. Li, "Time delay and Doppler estimation for wideband acoustic signals in multipath environments," *J. Acoust. Soc. Am.*, vol. 130, no. 2, pp. 850–857, Aug. 2011.

[39] Y. Jiang and P. Antonia, "Discrete time-scale characterization of wideband time-varying systems," *IEEE Trans. Signal Process.*, vol. 54, no. 4, pp. 1364–1375, April 2006.

[40] Y. Jiang and A. Papandreou-Suppappola, "Time-scale canonical model for wideband system characterization," in *Proc. IEEE Int. Conf. Acoustics, Speech, Signal Processing*, March 2005, pp. 281–284.

[41] M. Johnson, L. Freitag, and M. Stojanovic, "Improved Doppler tracking and correction for underwater acoustic communications," in *IEEE International Conference on Acoustics, Speech, and Signal Processing*, vol. 1, 1997, pp. 575–578.

[42] T. Jonathan, P. Dana, and D. Tse, "Prediction and modeling for the time-evolving ultra-wideband channel," *J. Sel. Topics Signal Processing*, vol. 1, no. 3, pp. 340–356, 2007.

[43] S. M. Kay, "Modern spectrum estimation: Theory and application." Prentice Hall Signal Processing, 1999.

[44] K. G. Kebkal and R. Bannasch, "Sweep-spread carrier for underwater communication over acoustic channels with strong multipath propagation," *J. Acoust. Soc. Am.*, vol. 112, no. 5, pp. 2043–2052, Nov. 2002.

[45] ——, "Method and devices for transmitting and receiving information," *U.S. Patent*, vol. 6,985,749 B2, Jan. 2006.

[46] K. G. Kebkal, O. G. Kebkal, and R. Bannasch, "Synchronisation of underwater communication receivers by means of swept pulses," in *Proc. of the 4th Int. Conf. on Underwater Acou. Measurements: Technologies and Results*, June 2011.

[47] K. G. Kebkal, V. K. Kebkal, O. G. Kebkal, and R. Petroccia, "Clock synchronization in underwater acoustic networks during payload data exchange," in *Proc. 2nd Int. Conf. Exhibit. Underwater Acoust.*, June 2014.

[48] K. Kebkal, A. K. Kebkal, and G. A. Ermolin, "Mathematic and experimental evaluation of phase errors when receiving hydro-acoustic PSK-signals with sweep-spread carrier in reverberant underwater environments," in *Proc. MTS/IEEE OCEANS Conf.*, June 2013.

[49] K. Kebkal, A. Kebkal, and V. Kebkal, "Synchronization tools of acoustic communication devices in control of underwater sensors, distributed antennas, autonomous underwater vehicles," in *Gyroscopy and Navigation*, vol. 5, no. 4. Pleiades Publishing, 2014, pp. 257–265.

[50] D. P. Kingma and M. Welling, "Auto-encoding variational Bayes," in *Proceedings of the 2nd International Conference on Learning Representations*, Apr. 2014.

[51] B. Li, S. Zhou, M. Stojanovic, L. Freitag, and P. Willett, "Multicarrier communication over underwater acoustic channels with nonuniform Doppler shifts," *IEEE J. Ocean. Eng.*, vol. 33, no. 2, pp. 1638–1649, Apr. 2008.

[52] ——, "Non-uniform Doppler compensation for zero-padded OFDM over fast-varying underwater acoustic channels," in *IEEE OCEANS, Aberdeen, UK*, 2007, pp. 1–6.

[53] W. Li and J. Preisig, "Estimation of rapidly time-varying sparse channels," *IEEE J. Ocean. Eng.*, vol. 32, no. 4, pp. 927–939, Oct. 2007.

[54] Y. Li, S. Wang, C. Jin, Y. Zhang, and T. Jiang, "A survey of underwater magnetic induction communications: Fundamental issues, recent advances, and challenges," *IEEE Commun. Surveys Tuts.*, vol. 21, no. 3, pp. 2466–2487, third quarter 2019.

[55] Y. Li, Y. Zhang, W. Li, and T. Jiang, "Marine wireless big data: Efficient transmission, related applications, and challenges," *IEEE Trans. Wireless Commun.*, vol. 25, no. 1, pp. 19–25, Feb. 2018.

[56] C. Liu, Y. V. Zakharov, and T. Chen, "Doubly selective underwater acoustic channel model for a moving transmitter/receiver," *IEEE Trans. Veh. Technol.*, vol. 61, no. 13, pp. 126–138, Mar. 2012.

[57] ——, "Doubly selective underwater acoustic channel model for a moving transmitter/receiver," *IEEE Transactions on Vehicular Technology*, vol. 61, no. 3, pp. 938–950, 2012.

[58] H. Lu, T. Xu, and H. Nikookar, *Cooperative Communication over Multi-scale and Multi-lag Wireless Channels*. Intech, 2012, pp. 103–126.

[59] Q. Lu, Y. Huang, Z.-H. Wang, and S. Zhou, "Characterization and receiver design for underwater acoustic channels with large doppler spread," in *Proc. of IEEE/MTS OCEANS conference*, Oct. 2015.

[60] L. Marchetti and R. Reggiannini, "An efficient receiver structure for sweep-spread-carrier underwater acoustic links," *IEEE J. of Ocean. Eng.*, vol. 41, no. 2, pp. 440–449, April 2016.

[61] A. R. Margetts, "Joint scale-lag diversity in mobile wideband communications," in *PhD thesis, The Ohio State University*, 2005.

[62] S. F. Mason, C. R. Berger, S. Zhou, and P. Willett, "Detection, synchronization, and Doppler scale estimation with multicarrier waveforms in underwater acoustic communication," *IEEE Journal on Selected Areas in Communications*, vol. 26, no. 9, pp. 1638–1649, 2008.

[63] "MATLAB Communications System Toolbox, version 6.3," The Mathworks, Inc., Natick, Massachusetts.

[64] A. Molisch and F. Tufvesson, "Propagation channel models for next-generation wireless communications systems," *IEICE Transactions on Communications*, vol. E97.B, pp. 2022–2034, Oct. 2014.

[65] A. F. Molisch, "Ultra-wideband propagation channels," in *Proceedings of the IEEE*, vol. 97, Feb. 2009, pp. 353–371.

[66] K. Murali and A. Chockalingam, "On OTFS modulation for high-Doppler fading channels," in *Information Theory and Applications Workshop*, Feb. 2018, pp. 1–10.

[67] J. Oberg, "Titan calling," *IEEE Spectrum*, vol. 41, pp. 28–33, 10 2004.

[68] A. V. Oppenheim, A. S. Willsky, and S. H. Nawab, *Signals and Systems*, 2nd ed. Englewood Cliffs, N.J.: Prentice-Hall, Inc., 1996.

[69] R. Otnes and T. H. Eggen, "Underwater acoustic communications: Long-term test of turbo equalization in shallow water," *IEEE J. Ocean. Eng.*, vol. 33, no. 3, pp. 321–334, July 2008.

[70] R. Otnes, P. A. van Walree, and T. Jenserud, "Validation of replay-based underwater acoustic communication channel simulation," *IEEE J. Ocean. Eng.*, vol. 38, no. 4, pp. 689–700, Oct. 2013.

[71] J. G. Proakis and D. K. Manolakis, *Digital Signal Processing (4th Edition)*. USA: Prentice-Hall, Inc., 2006.

[72] P. Qarabaqi and M. Stojanovic, "Statistical characterization and computationally efficient modeling of a class of underwater acoustic communication channels," *IEEE J. Ocean. Eng.*, vol. 38, no. 4, pp. 701–717, Oct. 2012.

[73] F. Qu, X. Nie, and W. Xu, "A two-stage approach for the estimation of doubly spread acoustic channels," *IEEE J. Ocean. Eng.*, vol. 40, no. 1, pp. 131–143, Jan. 2015.

[74] F. Qu and L. Yang, "Basis expansion model for underwater acoustic channels?" in *IEEE OCEANS, Quebec City, Canada*, 2008, pp. 1–7.

[75] P. Raviteja, Y. Hong, E. Viterbo, and E. Biglieri, "Practical pulse-shaping waveforms for reduced-cyclic-prefix OTFS," *IEEE Transactions on Vehicular Technology*, vol. 68, no. 1, pp. 957–961, 2019.

[76] ——, "Effective diversity of otfs modulation," *IEEE Wireless Communications Letters*, vol. 9, no. 2, pp. 249–253, 2020.

[77] P. Raviteja, E. Viterbo, and Y. Hong, "OTFS performance on static multipath channels," *IEEE Wireless Communications Letters*, vol. 8, pp. 745–748, June 2019.

[78] S. Rickard, "Time-frequency and time-scale representations of doubly spread channels," in *PhD thesis, Princeton University*, March 2005, pp. 281–284.

[79] D. Robb, J. Willners, N. Valeyrie, F. Garcia, A. Laskov, X. Liu, P. Patron, H. Hastie, and Y. Petillot, "A natural language interface with relayed acoustic communications for improved command and control of AUVs," in *2018 IEEE/OES Autonomous Underwater Vehicle Workshop (AUV)*. IEEE, Nov. 2018.

[80] H. M. Roudsari, J. Bousquet, and G. McIntyre, "Channel model for wideband time-varying underwater acoustic systems," *IEEE OCEANS, Aberdeen*, pp. 1–7, 2017.

[81] C. Schlegel, D. Truhachev, Z. Alavizadeh, and A. Vaezi, "Effective communications

over doubly-selective acoustic channels using iterative signal cancelation," in *Proceedings of the International Conference on Underwater Networks & Systems*. New York, NY, USA: Association for Computing Machinery, 2017.

[82] U. G. Schuster, *Wireless Communication Over Wideband Channels*. Series in Communication Theory, edited by Helmut Bölcskei, 2009, vol. 4.

[83] A. Sena and D. Rocchesso, "A fast Mellin and scale transform," *EURASIP Journal on Advances in Signal Processing*, vol. 2007, pp. 1–9, Jan. 2007.

[84] L. H. Sibul, L. G. Weiss, and T. L. Dixon, "Characterization of stochastic propagation and scattering via Gabor and wavelet transforms," *Journal of Computational Acoustics*, vol. 02, no. 03, pp. 345–369, 1994.

[85] A. Signori, F. Campagnaro, F. Steinmetz, B.-C. Renner, and M. Zorzi, "Data gathering from a multimodal dense underwater acoustic sensor network deployed in shallow fresh water scenarios," *Journal of Sensor and Actuator Networks*, vol. 8, no. 55, Nov. 2019.

[86] M. Stojanovic, "Recent advances in high-speed underwater acoustic communications," *IEEE J. Oceanic. Eng.*, vol. 21, no. 2, pp. 125–136, Apr. 1996.

[87] ——. Acoustic channel simulator. [Online]. Available: http://millitsa.coe.neu.edu/?q=research/simulator

[88] M. Stojanovic and L. Freitag, "Multichannel detection for wideband underwater acoustic CDMA communications," *IEEE J. of Ocean. Eng.*, vol. 31, no. 3, pp. 685–695, Jul. 2006.

[89] ——, "Multichannel detection for wideband underwater acoustic CDMA communications," *IEEE J. of Ocean. Eng.*, vol. 31, no. 3, pp. 685–695, Jul. 2006.

[90] M. Stojanovic and J. Preisig, "Underwater acoustic communication channels: Propagation models and statistical characterization," *IEEE Commun. Mag.*, vol. 47, no. 1, pp. 84–89, Jan. 2009.

[91] C. Studer, A. Burg, and H. Bölcskei, "Soft-output sphere decoding: Algorithms and VLSI implementation," *IEEE J. Sel. Areas Commun.*, vol. 26, no. 2, pp. 290–300, Feb. 2008.

[92] C. Studer, M. Wenk, A. Burg, and H. Bölcskei, "Soft-output MIMO detection algorithms: Performance and implementation aspects," in *Proc. of the 40th Asilomar Conference on Signals, Systems, and Computers*, Oct. 2006.

[93] B. L. Sturm and M. G. Christensen, "Comparison of orthogonal matching pursuit implementations," *20th European Signal Processing Conference (EUSIPCO 2012)*, pp. 220–224, Aug. 2012.

[94] S. S. Thoota and C. R. Murthy, "Quantized variational Bayesian joint channel estimation and data detection for uplink massive MIMO systems with low resolution ADCs," in *Proc. IEEE International Workshop on Machine Learning for Signal Processing, Pittsburg, PA, USA*, Oct. 2019.

[95] ——, "Variational Bayesian inference based soft-symbol decoding for uplink massive MIMO systems with low resolution ADCs," in *Proc. Asilomar Conference on Signals, Systems and Computers*, Nov. 2019.

[96] H. L. Van Trees, K. L. Bell, and Z. Tian, "Detection, estimation and modulation theory: Part I." John Wiley and Sons, 2013.

[97] P. A. van Walree, R. Otnes, and T. Jenserud, "The Watermark manual and user's guide version 1.0," in *Norwegian Defense Research Establishment (FFI)*, Nov. 2016.

[98] P. A. van Walree, F. Socheleau, R. Otnes, and T. Jenserud, "The watermark benchmark for underwater acoustic modulation schemes," *IEEE J. Ocean. Eng.*, vol. 42, no. 4, pp. 1007–1018, Oct. 2017.

[99] D. Vu, M. Xue, X. Tan, and J. Li, "A Bayesian approach to SAR imaging," *Digit. Signal Process.*, vol. 23, no. 3, pp. 852–858, May 2013.

[100] H. Wan, R.-R. Chen, J. W. Choi, A. Singer, J. Preisig, and B. Farhang-Boroujeny, "Markov chain Monte Carlo detection for frequency-selective channels using list channel estimates," *IEEE J. Sel. Topics in Signal Process.*, vol. 8, no. 5, pp. 1537–1547, Dec. 2011.

[101] Z.-H. Wang, S. Zhou, J. Preisig, K. R. Pattipati, and P. Willett, "Clustered adaptation for estimation of time-varying underwater acoustic channels," *IEEE Trans. Signal Process.*, vol. 60, no. 6, pp. 3079–3091, June 2012.

[102] Z. Wang, S. Zhou, G. B. Giannakis, C. R. Berger, and J. Huang, "Frequency-domain oversampling for zero-padded OFDM in underwater acoustic communications," *IEEE J. of Ocean. Eng.*, vol. 37, no. 1, pp. 14–24, Jan. 2012.

[103] J. Wu and P. Fan, "A survey on high mobility wireless communications: Challenges, opportunities and solutions," *IEEE Access*, vol. 4, pp. 450–476, 2016.

[104] T. Xu, Z. Tang, G. Leus, and U. Mitra, "Multi-rate block transmission over wideband multi-scale multi-lag channels," *IEEE Transactions on Signal Processing*, vol. 61, no. 4, pp. 964–979, 2013.

[105] L. Yang and G. B. Giannakis, "Ultra-wideband communications: An idea whose time has come," in *IEEE Signal Processing Mag.*, November 2004, pp. 26–55.

[106] S. Yerramalli, M. Stojanovic, and U. Mitra, "Partial FFT demodulation: A detection method for highly Doppler distorted OFDM systems," *IEEE Trans. Signal Process.*, vol. 60, no. 11, pp. 5906–5918, Nov. 2012.

[107] S. Yerramalli and U. Mitra, "Optimal resampling of OFDM signals for multi-scale–multilag underwater acoustic channels," *IEEE J. Ocean. Eng.*, vol. 36, no. 1, pp. 126–138, Jan. 2011.

[108] L. Zhao and A. Haimovich, "Performance of ultra-wideband communications in the presence of interference," *IEEE J. Select. Areas Commun.*, vol. 20, pp. 1684–1691, Dec. 2002.

[109] S. Zhou and Z. Wang, "Detection, synchronization and Doppler scale estimation," in *OFDM for Underwater Acoustic Communications*. Wiley, 2014, pp. 91–116.

[110] ——, "OFDM for underwater acoustic communications." Wiley, 2014.